2016

Advancing spaceborne tools for the characterization of planetary ionospheres and circumstellar environments

https://hdl.handle.net/2144/19717

Boston University

BOSTON UNIVERSITY

GRADUATE SCHOOL OF ARTS AND SCIENCES

Dissertation

ADVANCING SPACEBORNE TOOLS FOR THE CHARACTERIZATION OF PLANETARY IONOSPHERES AND CIRCUMSTELLAR ENVIRONMENTS

by

EWAN STREETS DOUGLAS

B.S., Tufts University, 2008
M.A., Boston University, 2011

Submitted in partial fulfillment of the
requirements for the degree of
Doctor of Philosophy
2016

Approved by

First Reader

Supriya Chakrabarti, PhD
Professor of Physics
University of Massachusetts Lowell
Visiting Professor of Astronomy
Boston University

Second Reader

Timothy A. Cook, PhD
Assistant Professor of Physics
University of Massachusetts Lowell
Adjunct Professor of Astronomy
Boston University

Third Reader

Catherine Espaillat, PhD
Assistant Professor of Astronomy
Boston University

Dedication

The greater our knowledge increases, the greater our ignorance unfolds.

John F. Kennedy,
speaking at Rice University on the Space Effort, September 12, 1962.

Acknowledgments

I would like to thank everyone through the years who has helped me learn physics and astronomy, and especially how to build telescopes. In roughly chronological order, some of these remarkable people include:

First my parents, Lynn and Bruce, for their Shackletonesque endurance throughout the endeavor of attempting to teach me how to learn. My sister Brianna, for her love and patience. My grandfather George, for teaching me how to develop images.

Everyone at the Vermont Astronomical Society and Stellafane for helping me build my first telescope.

Astronomy camp, and of course its tireless director Don McCarthy, gets much credit for cementing my interest in astronomy; and my fellow counselors, especially: Eric Hooper, Kate Follette, Tim Bowers, Vanessa Bailey, and all the Schlingmans for being such great mentors through many stages of my career.

Everyone at Tufts for expanding my opportunities and grounding me in physics, particularly Professor Tobin for the opportunities to break things in the lab.

Throughout the years, Molly has been an unmatchable inspiration as a hardworking student, a fierce athlete, and my dearest friend. I look forward to many more years of exploring together.

Everyone at LIGO Hanford, for teaching me how to work in a collaboration, hunt noise, and align an interferometer; especially Richard (Dick) Gustafson, Dani Atkinson, Nic Smith, and Mike Landry.

Without my hardworking colleagues, in one of the most topically diverse lab groups I know of, none of this research would have been possible. I would particularly like to thank Chris Mendillo for letting me adopt his rocket and for his astounding patience. Also Jason Martel, Kate Oram, and Paul Jung for all their help. Thanks to George Geddes, Kuravi Hewawasam, and Glenn Howe for so competently picking up where I left off on so many projects. And of course, Tim Cook and Supriya Chakrabarti for their support and willingness to entertain outlandish ideas.

Many thanks to my cohort of BU grad students, Ren Cashman, Chad Madsen, Dylan Morgan, Antonia Savcheva, and Laura Sturch. Also Sadia Hoq, Michael Malmrose, Nick MacDonald, Danielle Pahud, and the rest of the ever-hardworking BU Astronomy grads, you made long problem sets and exhausting practice talks bearable and fun.

Without my officemate and rocket-sister Meredith Danowski always fearlessly blazing the trail through graduate school and beyond I might have been left adrift. Instead, thanks to her brilliance, perseverance, and humor, we've made it!

Thanks to Alan Strahler and Crystal Schaaf, for letting me use "velcro" and their faith I would eventually find a tree in the forest with the Dual Wavelength Echidna Lidar.

Thanks to Andrew Stephan of the Naval Research Laboratory for the opportunity to work with data from Atmospheric and Ionospheric Detection System (RAIDS). My work with RAIDS was much eased by Phil Erickson's outstandingly clear and detailed answers to my questions about incoherent scatter radar.

Getting PICTURE off the ground required significant help from many hard working souls at White Sands Missile Range and Wallops Flight Facility, especially our mission managers: Christine Chamberlain and David Jennings. I would also like to thank FC1 Kwasi J. Smith for knowing exactly when to tell us to get some rest before we broke anything. Special thanks to Brian A. Hicks of NASA Goddard

Space Flight Facility, Laboratory, and Shanti Rao of the Jet Propulsion Laboratory for their support.

At the Space Telescope Science Institute: thanks to Nikole Lewis, for generously taking the time to guide the transition from graduate student to scientist; and Marshall Perrin, for making me a better coder.

Finally, I would like to thank the rest of my dissertation committee; Catherine Espaillat, for her excellent mentoring; Michael Mendillo, for his enthusiastic interventions; and Alan Marscher, for his steady guidance.

Portions of my work on the PICTURE missions were funded by NASA grants NNG05WC17G, NNX11AD53G, NNX13AD50G, NNX15AG23G, and through graduate fellowships awarded by the Massachusetts Space Grant Consortium. This research made heavy use of Astropy, a community-developed core Python package for Astronomy (The Astropy Collaboration et al., 2013); the IPython Interactive Computing architecture Perez & Granger (2007). Essential quantities were located in the SIMBAD database, operated at CDS, Strasbourg, France and the Exoplanets Encyclopedia, exoplanets.eu, operated by the Paris Astronomical Data Centre. Additional, data analyses were done using IDL (Exelis Visual Information Solutions, Boulder, Colorado).

ADVANCING SPACEBORNE TOOLS FOR THE CHARACTERIZATION OF PLANETARY IONOSPHERES AND CIRCUMSTELLAR ENVIRONMENTS

EWAN STREETS DOUGLAS

Boston University, Graduate School of Arts and Sciences, 2016

Major Professor: Supriya Chakrabarti,
Professor of Physics.

ABSTRACT

This work explores remote sensing of planetary atmospheres and their circumstellar surroundings. The terrestrial ionosphere is a highly variable space plasma embedded in the thermosphere. Generated by solar radiation and predominantly composed of oxygen ions at high altitudes, the ionosphere is dynamically and chemically coupled to the neutral atmosphere. Variations in ionospheric plasma density impact radio astronomy and communications. Inverting observations of 83.4 nm photons resonantly scattered by singly ionized oxygen holds promise for remotely sensing the ionospheric plasma density. This hypothesis was tested by comparing 83.4 nm limb profiles recorded by the Remote Atmospheric and Ionospheric Detection System aboard the International Space Station to a forward model driven by coincident plasma densities measured independently via ground-based incoherent scatter radar. A comparison study of two separate radar overflights with different limb profile morphologies found agreement between the forward model and measured limb profiles. A new implementation of Chapman parameter retrieval via Markov chain Monte Carlo techniques quantifies the precision of the plasma densities inferred from 83.4

nm emission profiles. This first study demonstrates the utility of 83.4 nm emission for ionospheric remote sensing.

Future visible and ultraviolet spectroscopy will characterize the composition of exoplanet atmospheres; therefore, the second study advances technologies for the direct imaging and spectroscopy of exoplanets. Such spectroscopy requires the development of new technologies to separate relatively dim exoplanet light from parent star light. High-contrast observations at short wavelengths require spaceborne telescopes to circumvent atmospheric aberrations. The Planet Imaging Concept Testbed Using a Rocket Experiment (PICTURE) team designed a suborbital sounding rocket payload to demonstrate visible light high-contrast imaging with a visible nulling coronagraph. Laboratory operations of the PICTURE coronagraph achieved the high-contrast imaging sensitivity necessary to test for the predicted warm circumstellar belt around Epsilon Eridani. Interferometric wavefront measurements of calibration target Beta Orionis recorded during the second test flight in November 2015 demonstrate the first active wavefront sensing with a piezoelectric mirror stage and activation of a micromachine deformable mirror in space.

These two studies advance our “close-to-home” knowledge of atmospheres and move exoplanetary studies closer to detailed measurements of atmospheres outside our solar system.

Contents

List of Tables

List of Figures

List of Abbreviations

N_m	F2-Region Peak density	xviii, xix, 56, 57, 72–74
ϵ Eri	Epsilon Eridani	viii, xiii, xv, xxvii, xxviii, 21, 25–29, 36, 82–84, 87, 106, 110, 114, 117, 119, 122–126, 139, 156–159
h_m	F2-Region Peak height	xx, 57, 73, 77
ACS	Attitude Control System	126, 127
AO	adaptive optics	29, 31, 32, 83, 137
AT	Angle Tracker	88
AU	Astronomical Unit [1.5e11 m]	xv, 26, 29, 86
CCD	charge-coupled device	xxi, 88–90, 96, 97
CFR	Complete Frequency Redistribution	54, 66, 67
CHARA	Center for High Angular Resolution Astronomy	25
CTE	Coefficient of Thermal Expansion	107
DIT	Discrete Inverse Theory	70
DM	deformable mirror	xxii, xxviii, 91, 92, 94, 95, 97–99, 113, 115, 120–123, 127, 128, 130, 139, 156, 157, 159, 165, 166, 172
DOF	degrees-of-freedom	159
EKB	Edgeworth-Kuiper belt	21, 22, 25–27, 87
EUV	Extreme-Ultraviolet	xiv, xvi, xxxiv, 7, 11, 12, 16, 17, 36–38, 42, 59
EUVS	EUV Spectrograph	xvi–xviii, xx, 37–42, 44–46, 52, 53, 76
FIR	far-infrared	21
FOV	field-of-view	xviii, 37, 52, 53, 68, 127

FPS	fine pointing system	xxix, xxxi, 83, 126, 129, 135–137, 148, 149, 154, 158
FSM	Fast Steering Mirror	93
FUV	far-ultraviolet	xiv, 11, 12
FWHM	Full-Width-Half Maximum	157
GPI	Gemini Planet Imager	32
GPS	Global Positioning System	7, 10, 11
HARPS	High Accuracy Radial velocity Planetary	27
HST	Hubble Space Telescope	xxi, 26, 29, 32, 33, 85, 103
IR	infrared	15, 22, 25, 27, 29, 30, 84–86
IRAC	Infrared Array Camera	25
IRAS	Infrared Astronomical Satellite	21, 25
IRS	Infrared Spectrograph	26
ISM	interstellar medium	16
ISR	Incoherent Scatter Radar	xviii, xx, 7–10, 36, 52, 53, 56, 59, 72, 73, 76
ISS	International Space Station	xvi, 37, 39, 46, 73
IWA	Inner Working Angle	xxiv, 88, 94, 101, 102, 125
JPL	Jet Propulsion Laboratory	87, 88
KIN	Keck Interferometer Nuller	86
LBTI	Large Binocular Telescope Inteferometer	86, 87
LITES	Limb-imaging Ionospheric and Thermospheric Extreme-ultraviolet Spectrograph	xxi, 78–81
LSI	Lateral Shearing Interferometer	34, 89, 166
MCMC	Marcov chain Monte Carlo	xix, xx, 48, 69, 71, 75, 78

MCP	Microchannel Plate	xvi, 38–40
MEMS	microelectromechanical systems	91, 92
MGHPCC	Massachusetts Green High Performance Computing Center	xii, 73
MIPS	Multiband Imaging Photometer for Spitzer	25
MMT	Multiple Mirror Telescope	34
MRF	Magnetorheological finishing	106, 119
MSIS	Mass Spectrometer Incoherent Scatter Radar	ix, 3, 59
NASA	National Aeronautics and Space Agency	xxxvii, 83, 126, 127
NIR	near-infrared	15, 16, 29
NPZT	Nuller Piezo Electric Transducer	xxx, 91, 94, 127–130, 138, 141–147, 157, 159, 166
OII	singly-ionized atomic oxygen spectroscopic state	48, 67, 79
OPD	optical path difference	xxii, xxxiii, 89, 94, 96, 129, 165, 168
OWA	Outer Working Angle	162, 163
PCA	Principal Component Analysis	xxiii, xxvii, 101–104, 118, 120, 124
PICTURE	Planet Imaging Concept Testbed Using a Rocket Experiment	xv, xvi, 28, 35, 36, 82–84, 87, 92, 106, 107, 122, 123, 125, 126, 128, 129, 131, 135, 137, 139, 141, 145, 158, 159
PID	Proportional-Integral-Derivative	146, 147
PSD	Power Spectral Density	xxviii, 120, 121
PSF	Point Spread Function	xxiii, xxviii, xxxii, 28, 29, 31, 33, 95, 98, 99, 101, 105, 113, 115, 122–124, 128–130, 135, 136, 151, 152, 154, 157, 160, 162, 163
PV	Peak-to-Valley	xxv, 32, 108, 110, 111

QE	quantum efficiency	39
RAIDS	Atmospheric and Ionospheric Detection System	xvi, xviii, xx, 36, 38–40, 46, 48, 52, 53, 73, 76, 78, 79
RMS	root mean squared	xxiv, 31, 32, 103, 165, 167
RMSE	root mean squared error	115, 119–121, 166, 167
RTD	Resistance Temperature Detector	108, 132, 135
SED	Spectral Energy Distribution	21, 26, 27, 84, 85
SHARPI	Solar High-Angular Resolution Photometric Imager	106
SI	Système international d'unités	8
SiC	Silicon Carbide	xxv, 110
SNR	signal-to-noise ratio	18, 19, 79, 138, 159
STIS	Space Telescope Imaging Spectrograph	xxi, 85
STIS	Space Telescope Imaging Spectrograph	25
SZA	Solar Zenith Angle	67, 68
TTP	tip, tilt, and piston	xxxi, 127, 128, 147, 150, 154
UV	ultraviolet	xiv, 11, 16, 17, 31
VNC	Visible Nulling Coronagraph	xvi, xxii, xxvii, 34–36, 83, 84, 87, 88, 92, 94–97, 106, 110, 112, 115, 117, 120, 123, 125, 127–129, 137, 139, 145, 153, 156–159, 162, 163
WFCS	wavefront control system	xxi, xxii, xxiv, 89, 91, 94–96, 98, 100, 103, 126, 127, 138, 146, 165, 172
WFE	wavefront error	xxii, 31, 32, 94, 96, 112, 119, 130, 142
WFF	National Aeronautics and Space Agency (NASA) Wallops Flight Facility	127, 131
WFIRST-AFTA	Wide-Field InfraRed Survey Telescope-Astrophysics Focused Telescope Assets	xvi, 30, 32

WFS	wavefront sensor xxii, xxx, xxxi, 83, 91, 94, 97, 127, 138–141, 143–146, 155, 158, 159, 172
WSMR	White Sands Missile Range . . . xxix, 83, 88, 126, 131, 132

Chapter 1

Introduction

This work focuses on the characterization of planetary atmospheres and their plasma environments, with high spectral, geographic and temporal resolution on Earth, and addresses some of the challenges facing imaging and spectroscopy of exoplanets. The science questions to be addressed are:

- What is the information content of terrestrial ionospheric plasma density profiles retrieved by inverting 83.4 nm emission measurements of O^+ scattering?
- What are requirements to image the distribution and brightness of a nearby extrasolar system's exozodiacal debris disk in scattered visible light?

The first half of this chapter will introduce the basics of ionosphere formation, setting the stage for understanding spectroscopy of the Earth's ionosphere. Motivating observations of exozodiacal debris disks, the latter half of this chapter provides a brief discussion of the atmospheric properties retrievable from exoplanet spectra and the limiting effect of dusty debris on exoplanet direct imaging and spectroscopy. Finally, the Epsilon Eridani (ϵ Eri) system will be introduced as a promising candidate for high-contrast imaging of exozodiacal dust with an interferometric Visible Nulling Coronagraph (VNC).

1.1 Ionospheres

The Earth's ionosphere is an ionized layer of plasma, primarily embedded within the thermosphere. Time variations in the density and vertical morphology of the ionosphere have considerable effect on radio communication, radio astronomy and space weather forecasting (Lawrence et al., 1964; Afraimovich & Yasukevich, 2008; Belehaki et al., 2009). Planetary ionospheres also play an important role in habitability, composing the interface between planetary atmospheres and stellar winds in planets with weak magnetic fields, such as Mars and Venus, and regulating atmospheric escape rates (Lammer et al., 2009).

1.1.1 Ionospheric Physics and Chemistry

Hydrostatic equilibrium provides the simplest description of the distribution of gas in a planetary atmosphere: the density distribution that arises from balancing the force of gravity with atmospheric pressure. In this brief introduction to the ionosphere, high order effects such as Coriolis forces, tides, and turbulence will be neglected. For a detailed overview of the Earth's ionosphere, see Risbeth & Garriott (1969); Kelley (2009) and for an introduction to Solar System ionospheres see Witasse et al. (2008) or Chapter 7 of Cravens (2004). An overview of some important processes, drawn primarily from Cravens (2004) and Risbeth & Garriott (1969), is presented below. For an isothermal atmosphere at temperature T, solving the momentum balance equation in hydrostatic equilibrium gives the number density n as a function of height, h,

$$n(h) = n_0 e^{-h/H} \tag{1.1}$$

and H is the scale height, $k_B T/\mu g$. Here k_B is Boltzmann's constant and μ is the mean molecular species mass in a well mixed atmosphere. μ should be replaced with individual species mass, m_s, for a heterogeneous atmosphere (above the turbopause).

Ionized gases exist at a higher energy state than their neutral counterparts, and most planetary atmospheres are predominantly neutral, lacking the energy input to maintain significant ionization. Conversely, driven internally by fusion, stars are highly ionized and heated to many thousands of Kelvins. Stars emit some of this energy in the form of ionizing photons. Incident on a planetary atmosphere, these photons with energy $h\nu$ strip electrons from neutral atmospheric species X by the process:

$$h\nu + X \rightarrow X^{+} + e^{-}. \tag{1.2}$$

The ion production rate, q, is proportional to the neutral number density n_X, the ionization cross section σ_X, and incident intensity I:

$$q = n_X \sigma_X I. \tag{1.3}$$

Some energetic photons travel deeper into the atmosphere where the densities are higher and their probability of collision with a neutral species and ionizing increases.

For a relatively dense atmosphere, such as the Earth or Mars, there exists a characteristic plasma density profile with a density peaking at high altitudes. At very high altitudes the plasma is rarified, since despite the intensity of incident ionizing radiation, the neutral density is low, keeping the production rate small. Few ionizing photons reach the surface of the planet because the probability they will collide with and ionize a neutral is high. Large densities also mean recombination occurs quickly and ions do not persist near the surface of the Earth. Thus, there exists a peak plasma density, dependent on the neutral atmosphere, the incident stellar flux, transport (diffusion) effects, and the recombination chemistry driving ion loss.

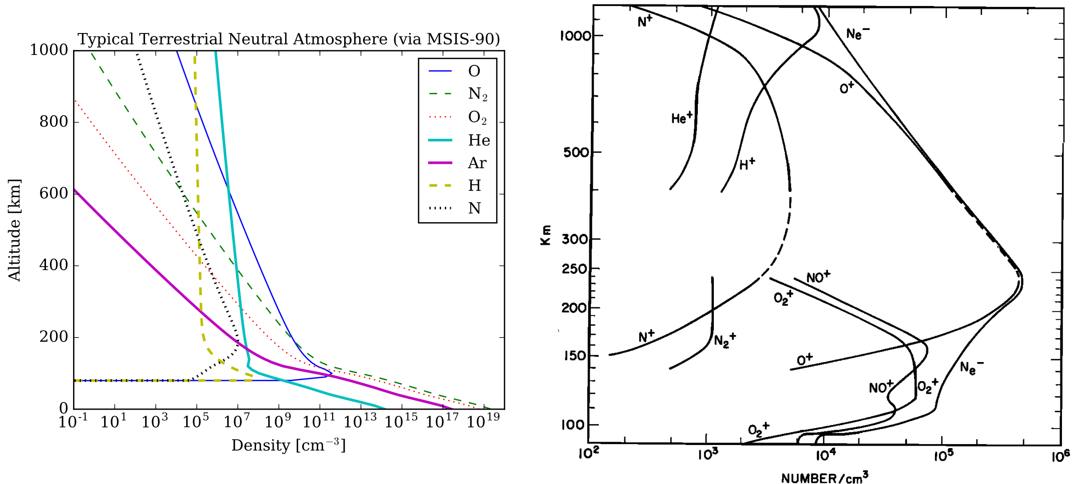

(a) Example Earth neutral densities generated using the MSIS-90 model (Hedin, 1991).

(b) Typical ionospheric constituent profiles measured from sounding rocket flights. Reproduced from Johnson (1966).

Fig. 1.1: Example altitude profiles of Earth's atmospheric constituents.

1.1.2 Vertical structure

Fig. 1.1a shows an example terrestrial density profile of neutral atmospheric species, generated with Mass Spectrometer Incoherent Scatter Radar (MSIS)-90[1]. N_2 and O_2 dominate where the atmosphere is well mixed below the turbopause and mesopause boundaries at approximately 100 km. Above the turbopause, the scale heights of each species are independent and density decreases faster for heavier species. Fig. 1.1b shows early in-situ measurements of the ionosphere via sounding rocket (Johnson, 1966). Many ionized species are present; however, in the so-called "E-region", between approximately 90 km and 150 km, NO^+ and O_2^+ ions dominate. While N_2 and O_2 are both readily ionized as in Eq. 1.2, N_2^+ doesn't persist because nitrogen ions are rapidly lost by one of two reactions:

$$N_2^+ + O_2 \rightarrow O_2^+ + N_2. \tag{1.4}$$

---

[1] `http://omniweb.sci.gsfc.nasa.gov/vitmo/msis_vitmo.html`.

or

$$\mathrm{N_2^+ + O \rightarrow NO^+ + N.} \tag{1.5}$$

These resulting ion molecules dissociatively recombine with electrons, e.g.:

$$\mathrm{NO^+ + e^- \rightarrow O + N.} \tag{1.6}$$

Assuming plasma quasi-neutrality, this loss rate is $l = -\alpha_2 n_e^2$. $\alpha_2 \approx 10^{-13}$ m^3/s and n_e is the electron number density. In the F-region, between approximately 160 km and 900 km, O$^+$ is the most common ion. The F-region is sometimes referred to as two separate regions, the F2 and F1 layers where the F2 is the portion that does not recombine during the night. Because O$^+$ cannot dissociatively recombine, the dominant F-region loss process is atom-ion interchange. If XY is some two species ion, such as O$_2^+$, one form of atom-ion interchange is:

$$\mathrm{O^+ + XY \rightarrow XO^+ + Y.} \tag{1.7}$$

This reaction is typically the rate limiting process in the recombination chain, and occurs at a reaction rate of $\beta n_{O^+} n_X$ and then XO$^+$ dissociatively recombines at a reaction rate orders of magnitude faster. $\beta \approx 10^{-17}$ m^3/s (Risbeth & Garriott, 1969, Table 1, p.106).

The O$^+$ lifetime, τ_{chem} is inversely proportional to density, and thus the F-region density increases until the lifetime equals the vertical diffusion timescale τ_{diff}. The ionospheric peak density is approximately where these two timescales are equal, and depending on conditions usually falls between 200 km and 500 km.

Chapman Theory

Chapman (1931) proposed a model of the previously observed ionospheric layers. Chapman assumed production (q) equals loss (l) locally. Thus, the production rate of ions is proportional to the loss of intensity due to ionization. Chapman also assumed:

- an isothermal neutral atmosphere,
- a single constituent species, X,
- one photon ionizes one atom into one electron-ion pair with an interaction σ,
- monochromatic light,
- Cartesian slab geometry with an angle from zenith, χ.

If the height is h and the path-length of an ionizing photon s, then $dh = ds \cos\chi$ and $ds = dh \sec\chi$. The brief derivation that follows assumes a noon-time ionosphere with χ=0. The neutral number density as a function of atmospheric height is described by hydrostatic equilibrium (Eq. 1.1). Assuming there is no spontaneous emission, we can solve the equation of radiative transfer (Eq. C.2) by integration:

$$\int_{I_\infty}^{I(h)} \frac{dI}{I} = -\sigma n_o \left(\int_{\infty}^{h} e^{-h/H} dh\right) \sec\chi \tag{1.8}$$

$$\rightarrow I(h) = I_\infty e^{\sigma n_o(-He^{-h/H})} \tag{1.9}$$

Assuming the production rate of electron-ion pairs q is equal to the number of incident photons, and neglecting secondary ionization, the production rate as a function of height (Risbeth & Garriott, 1969, Eq. 306) is:

$$q = \eta\sigma n_X(h) I(h) = \eta\sigma n_0 e^{-h/H} I_\infty e^{-\sigma n_0 H e^{-h/H}} \tag{1.10}$$

where η is a ionization efficiency factor. Setting the derivative of Eq. 1.10 equal to zero and solving for h gives the altitude of greatest density:

$$q_0 = \frac{\eta I_\infty}{e^1 H} \tag{1.11}$$

Assuming a constant scale height with a maximum at h_m and a reduced height of

$$z(h) = \frac{h - h_m}{H}, \tag{1.12}$$

setting $q = l = \alpha n_e^2$, and solving for n_e, gives the classic "Chapman$-\alpha$" density profile:

$$n_e(z) = (q_0/\alpha)^{1/2} e^{(1-z-e^{-z})/2} \tag{1.13}$$

This derivation neglects many critical aspects of ionospheric physics, including diffusion, wavelength dependence, and multiple species; however, as will be seen in later chapters, Eq. 1.13 provides a useful functional form to parameterize the terrestrial ionosphere.

1.1.3 Remote Sensing

This section describes techniques for measuring the Earth's ionosphere, particularly Incoherent Scatter Radar (ISR), Ionosondes, Global Positioning System (GPS) tomography and introduces the emerging field of Extreme-Ultraviolet (EUV) remote sensing.

An ionized layer was long suspected to be the mechanism of over-the-horizon radio communication in the Earth's atmosphere, and presence of this layer was first confirmed by Appleton & Barnett (1925). Their experiment relied on the difference in polarization between waves reflected from the atmosphere and waves refracted along Earth's surface. With a transmitter in London and a receiver in Cambridge, they found not only that the waves must be reflected off the upper atmosphere, they also observed a variation in the time-of-flight for waves during the day and night. On the other side of the Atlantic, Breit & Tuve (1926) used low frequency pulses to determine the virtual height of the ionosphere and calculated the real height due to the changing index of refraction. The electron density profile below the ionospheric peak altitude (h_m), the bottomside, is directly measurable by ionosonde, the modern equivalent of Breit and Tuve's experiment (Bibl & Reinisch, 1978), and equivalent radio sounding from orbit can be used to derive topside parameters (Thomas, 1963). Profiles of ion and electron densities and temperatures for the entire ionosphere are well resolved by ISR, which relies on Thomson scattering by ionospheric electrons (Evans, 1969). These techniques face several obstacles. ISR and ionosonde profiling from the ground are limited by the geographic distribution of facilities and their associated fields-of-view. Additionally, while more globally distributed, ionosondes cannot measure densities beyond the peak, because they measure the range to the nearest region of a given plasma frequency. Thus, determination of the entire ionospheric profile via ionosonde requires the assumption of topside ionospheric parameters or a coincident radio sounding from orbit. A variety of ionospheric models exist, which depend on solar and terrestrial inputs and chemistry (see the review by Belehaki et al. (2009)). However, modeling faces several challenges, including a lack of topside scale height accuracy in certain cases, as in the presence of strong neutral winds (Mikhailov et al., 2000), or validity limited to certain geographic locations for some empirically derived models (e.g. Zhang et al., 2005). Additional measures of the state of the ionosphere are needed to generate a truly global picture of the space environment.

Ionosondes

Early ionospheric observations depended on the reflection of radio waves below the plasma frequency. This frequency is a bulk property of the ionospheric plasma, responding to a slowly oscillating electromagnetic wave. Defined using Système international d'unités (SI) in radians per second, the plasma frequency is (Chen, 1984, Eq. 4-25) :

$$\omega_p^2 \equiv \frac{n_e e^2}{\epsilon_0 m_e}, \tag{1.14}$$

where e is the electron charge, m_e is the electron mass, and ϵ_0 is the electric permittivity of free space. The reflection frequency in Hertz is $f_p = 9\sqrt{n_e}$, where n_e is the electron density in cubic meters. For a typical terrestrial ionospheric peak density of 10^{12} $\mathrm{e}^-/\mathrm{m}^3$ the highest frequency reflection occurs at 9 MHz.

Modern ionosondes measure up to the ionospheric peak density by transmitting an increasing frequency chirp and measuring the return time-of-flight to probe the plasma modes both parallel and perpendicular to the Earth's magnetic field above the transmitter with multiple antennas (Reinisch et al., 2009).

Incoherent Scatter Radar

At frequencies well above the plasma frequency, rather than responding to the bulk plasma, radio waves interact with individual electrons in a manner well approximated by classical Thomson scattering. Thomson scattering arises from the interaction of a electromagnetic plane wave and a solitary electron, the $\vec{E}$-field accelerating the electron in an oscillatory motion. r_0 is the characteristic length scale of this classical interaction. For slow moving electrons ($v << c$) and a linearly polarized wave, with frequency ω_0, incident on the electron, the characteristic interaction length is the classical electron radius:

$$r_0 \equiv \frac{e^2}{mc^2}. \tag{1.15}$$

The Thomson scattering cross section is the integral of the differential cross section over solid angle (Rybicki & Lightman, 1979, p.91):

$$\sigma_T \equiv \frac{8\pi}{3} r_0^2. \tag{1.16}$$

Incoherent scatter radar measures the Thomson backscatter signal from electrons in the ionosphere by transmitting a highly collimated, high frequency beam into the ionosphere. Motions of the scattering electrons Doppler shift the return signal, imprinting the electron velocity spectrum on the ISR wave. The dominant frequency component of this velocity spectrum is the ion-accoustic mode of the plasma (Evans, 1969) – as ions move at the sound speed they drag electrons along with them. Thus, the frequency spectrum of ISR returns provides information about both the ion and electron populations. The terrestrial ionosphere is optically thin to probing ISR measurements and returns from both the top and bottom sides of the density profile are observable. However, the small cross section, and the height of the ionospheric F-region make ISR scattering energy intensive, limiting usage to a small but growing number of large apertures radars around the world (Kelly et al., 2006; Gillies et al., 2015).

GPS Tomography

Another method of measuring ionospheric plasma density, radio tomography relies on the phase delay of a wave propagating though a plasma. Given multiple lines-of-sight through the atmosphere, the line integral phase shifts can be inverted via computer tomography to estimate the plasma density (Bernhardt et al., 1998). While ground-based receivers and the GPS constellation provide sufficient coverage to determine the integrated plasma density (or “total electron content”) over particular locations (Rideout & Coster, 2006), the scarcity of satellite transmitters limits the potential of this approach to accurately measure vertical plasma density profiles.

1.1.4 Remote Sensing with Airglow

Fluorescent atmospheric emission processes divide into two primary categories: airglow and the aurora (the so-called Northern and Southern lights). These emissions share many of the same spectroscopic features, but they arise from different energetic processes. The aurora is driven by energetic particles which travel along magnetic field lines, concentrating the aurora around the poles. Airglow during the day (dayglow) is primarily driven by solar photons energizing the upper atmosphere, with additional collisional energy from ionized photoelectrons. At night, stored energy is released as photons during recombination, producing nighttime airglow (nightglow). The dayglow that arises from solar photons with ionizing energies offers a particularly useful probe of the state of the thermosphere, since most resonant emission lines are in the ultraviolet (UV) and the optical density of the atmosphere obscures background radiation from the surface.

The space-age made possible upper atmospheric and astronomical observations at far and extreme ultraviolet wavelengths that are absorbed by the terrestrial atmosphere (shortward of approximately 300 nm, Meier (1991)). The Apollo 16 far-ultraviolet (FUV) spectrograph recorded the first published spectra of the terrestrial airglow from 49 nm to 160 nm on April 21, 1972 from the Lunar surface (Carruthers & Page, 1972). Fig. 1.2 shows the cross-dispersion distribution of intensities from these early spectrographic observations. Variations in morphology indicate the differences between the photochemistry of each process and imply the potential for remote sensing of underlying atmospheric parameters.

Passive remote sensing relies on integrated line-of-sight observations and lacks the direct range information of radar; however, several approaches allow recovery of spatial information, including: assumption of a homogeneous plane parallel atmosphere (e.g. Douglas et al., 2012) or tomography analogous to the GPS inversion (e.g. Kamalabadi et al., 1999). Of particular interest was optically thick O^+ 83.4 nm emission, a resonant scattering transition which was clearly resolved at 4 nm resolution on the Apollo 16 spectroscopic films (Carruthers & Page, 1976).

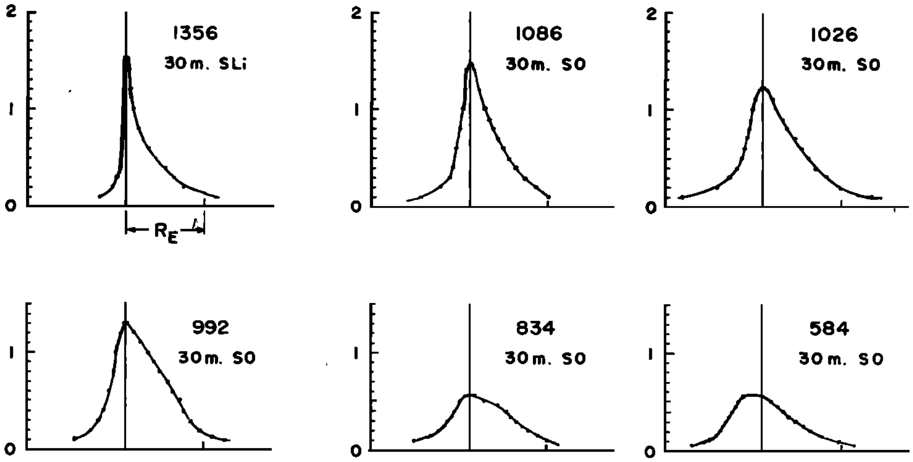

Fig. 1.2: Optical density distributions of EUV and FUV emission features observed from the lunar surface during Apollo 16. The vertical line indicates the sunward limb and the radius of the Earth is marked with a single x-axis tick mark. Asymmetries indicate the emission is resolved across the disk of the Earth. Reproduced from Carruthers & Page (1976).

Shortly after the first Apollo 16 results were published, Carlson & Judge (1973) published an altitude profile of the band from 75 nm to 105 nm using EUV photometer dayglow from an earlier sounding rocket flight. The observed profile peaked above 200 km and they found poor agreement with a forward model of the 83.4 nm emission process, these differences were attributed to other lines (N_2 at 99.2 nm and H at 102.6 nm). Subsequently, Feldman et al. (1981) used a sounding rocket to measure altitude profiles of EUV 83.4 nm emission with a 0.65 nm resolution on January 9, 1978. They found good agreement between the altitude profile and a forward model of O^+ 83.4 nm emission informed by ground-based ionosonde measurements. Retrieval of the ionospheric O^+ distribution was attempted shortly after forward model agreement was found: Kumar et al. (1983) inverted nadir and zenith measurements of 83.4 nm from the STP-78 satellite EUV spectrograph (Bowyer et al., 1981; Chakrabarti et al., 1983) by varying the ionospheric scale height and peak density to best-fit an in-situ ionospheric density measurement at 460 km from the Atmospheric Explorer AE-E satellite..

Measurement of the singly ionized oxygen (O^+) emission feature, OII 83.4 nm, has the potential to allow global monitoring of ionospheric parameters in regions where the upper atmosphere is sunlit. This emission is among the brightest features in the terrestrial EUV regime between 10 nm and 100 nm. Energetic solar photons (λ <45 nm) photoionize inner shell electrons of atomic oxygen via $O(^3P) + h\nu \rightarrow O^+(^4P) + e$ (Dalgarno et al., 1964), a process that peaks in the 150-175 km altitude range (Kumar et al., 1983; Anderson & Meier, 1985). This leads to an 83.4 nm photon from the $2s^1 2p^4\ ^4P \rightarrow 2s^2 2p^3\ ^4S$ transition, an allowed triplet. The emitted photon subsequently undergoes resonant scattering by ground-state O^+, the dominant ion in the F2 region of the ionosphere with a density profile that closely matches that of electrons. The peak density in the F2 region typically occurs at higher altitudes (200-500 km), where the effective recombination coefficient is lower due to diffusion (Yonezawa, 1959), setting up a separation between the photon production region and scattering region that allows these EUV photons to effectively illuminate the F2 region from below. The scattering optical depth, τ, is on the order of 1-10 (Meier, 1991), and this scattering leads to an observable altitude profile of 83.4 nm airglow that depends on the O^+ ion density. Thus, it is expected the distribution of O^+ is retrievable via inversion of this airglow profile (e.g. Kumar et al. (1983); McCoy et al. (1985)).

Given sufficient constraints, a “unique” O^+ density profile may be retrieved via radiative transfer analysis (Vickers, 1996; Picone et al., 1997; Picone, 2008; Stephan et al., 2012). For example, as discussed by Stephan et al. (2012) constraining the initial source intensity, due to photoionization, should allow inversion of an 83.4 nm emission profile to return a unique plasma density profile.

1.2 Circumstellar matter - Exoplanets and Debris Disks

I need not burden the reader with a litany of citations to past authors contemplating whether life on Earth is singular in the universe or a speck in a multitude of inhabited worlds. Discovery of extraterrestrial life will doubtlessly expand our understanding of biology, chemistry, and philosophy – along with numerous subfields and as-of-yet unknown disciplines. Yet, of all science questions, curiosity for whether there is life beyond Earth is one of the most self-evident.

Scientists are mammals: liquid water and gaseous oxygen dependent, carbon-based lifeforms on a rocky terrestrial planet. Thus, our natural inclination is to build instruments to search for life on other worlds “as we know it”. (For introductory reviews of planet habitability, and biomarkers see: Des Marais et al., 2002; Lammer et al., 2009). After millennia of speculation and slow progress, astronomical technology is advancing rapidly towards true remote sensing rocky terrestrial planet atmospheres around other stars. In 1992, the first exoplanets were detected around a pulsar (Wolszczan & Frail, 1992). Shortly thereafter, the first giant planet was detected via doppler motion of its host star (Mayor & Queloz, 1995) and via the dip in starlight during a transit (Charbonneau et al., 2000). Bond et al. (2004) reported the first gravitational microlensing (Einstein, 1936) of an exoplanet. Most recently, timing variations in Kepler transit data (Borucki et al., 2003) led to several new exoplanet discoveries (Steffen et al., 2012). Differences in transit depth with wavelength have provided the first look at the composition and structure of exoplanet atmospheres due to absorption during primary transit, for example sodium and hydrogen in the hot-Jupiter HD 209458b (Charbonneau et al., 2002; Ballester et al., 2007), and the emission features of hot planets in short-period orbits (e.g. Charbonneau et al., 2005; Bean et al., 2008; Lewis et al., 2010). Transmission spectroscopy in a transit only samples the optically thin ring of atmosphere along the terminator of the exoplanet. The geometry necessary for an exoplanet to pass through our line-of-sight to a star limits such transit spectroscopy to a narrow subset of planets. To date, 3434 exoplanet discoveries have been confirmed[2]. Early statistical analyses of the Kepler census show exoplanets are common: most stars have planets (Silburt et al., 2015) and the terrestrial planet occurrence rate within periods of 200 days is approximately 2.5 for late stellar types (Dressing & Charbonneau, 2013).

Direct imaging searches for planets close to stars will open our discovery space dramatically. Over the past two decades, direct imaging has progressed from large substellar objects (e.g. Lowrance et al., 2000) to giant exoplanets of a few Jupiter masses (e.g. Kalas et al., 2008). Direct infrared spectroscopy has started to reveal the diversity of massive exoplanets atmospheres, and has allowed detection of molecules such as methane (e.g. Lafrenière et al., 2008; Janson et al., 2010, 2013).

Cooler and smaller, rocky terrestrial planets have yet to be directly imaged – at any wavelength. While infrared (IR) light is more accessible from the ground, indicators of biology on Earth are most prominent at visible wavelengths (Seager, 2014). Some of these key markers are illustrated in Fig. 1.3, from Turnbull et al. (2006), a reflectance spectrum of the Earth at visible and near-infrared (NIR) wavelengths computed from "earthshine" observations of light reflected from the dark side of the moon. O_2, a particularly likely biomarker, is clearly seen in absorption at

---

[2] `http://exoplanets.eu` on June 13, 2016

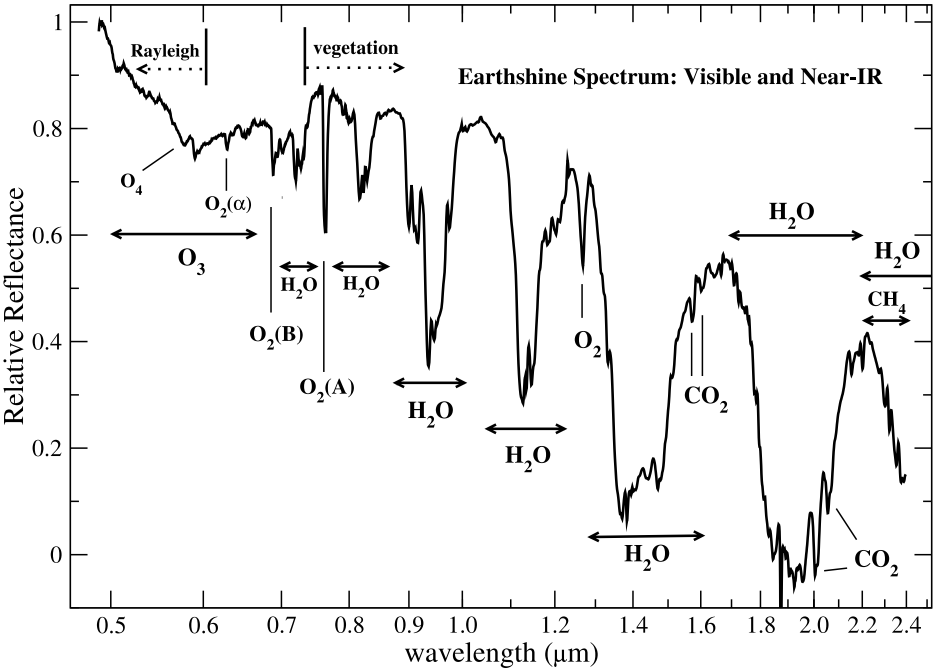

Fig. 1.3: Composite reflectance spectrum of Earth, calculated by dividing earthshine reflected by the night side of the moon by the full moon spectrum (Woolf et al., 2002; Turnbull et al., 2006) with some important features which indicate or enable life labeled, including O_2. Reproduced from Turnbull et al. (2006).

several visible and NIR wavelengths. Carbon dioxide, water, and methane dominate the longer wavelengths where the overall reflectance is lower. The high reflectance, spectral diagnostics, and increased flux from sun-like stars make visible wavelengths an appealing regime for exoplanet spectroscopy.

1.2.1 EUV Spectroscopy of Exoplanets

Ultraviolet observations provide an important probe of the upper atmosphere and space weather on Earth and Solar System planets (e.g. Earth's dayglow as described previously and Jupiter's aurora: Carruthers & Page, 1972; Broadfoot et al., 1979; Clarke et al., 1980). Observations of exoplanets in the UV and EUV will require long exposures and tight manufacturing tolerances.

However, since imaging resolution is proportional to both wavelength and aperture, future large UV telescopes should probe for planets closer to their host stars than visible wavelengths (Cook et al., 2012). Thus, UV direct imaging opens a new dimension or “trade-space” in exoplanet imaging mission design. Fig. 1.4 shows a terrestrial albedo at UV wavelengths. Fluorescence processes redistribute energy from x-ray photons (which would be obscured by hydrogen absorption in the interstellar medium (ISM) below the Lyman limit) to ultraviolet wavelengths, generating high apparent albedos.

UV imaging of exoplanets will be key to completing our understanding of stellar systems, exoplanets protective ionospheres, and holds some promise for detecting biomarkers such as O_3 absorption shortward of 334 nm by the Huggins band (Des Marais et al., 2002). However, visible light imaging requires lower manufacturing tolerances and is particularly sensitive to important spectral features such as H_2O and O_2. The remainder of this chapter and results presented in later chapters will focus on challenges facing visible light imaging of circumstellar environments, which serves as a stepping stone to direct EUV/UV imaging and spectroscopy of exoplanets.

1.2.2 Debris Disks in Extrasolar Systems

This section will describe the problem of exoplanet detection in a dusty stellar system. In most main-sequence stellar systems the inner primordial dust population has been cleared by a variety of processes, including planet formation, accretion, stellar winds, Poynting-Robertson drag, and photoevaporation (see review by Williams & Cieza, 2011). The small particles that remain form a *debris disk* of processed dust, replenished to various degrees by collisions, comets, and drag from the edges of the system. In the Solar System, this “zodiacal” dust lies in the plane of the ecliptic, scattering light and decreasing in density according to a power-law with

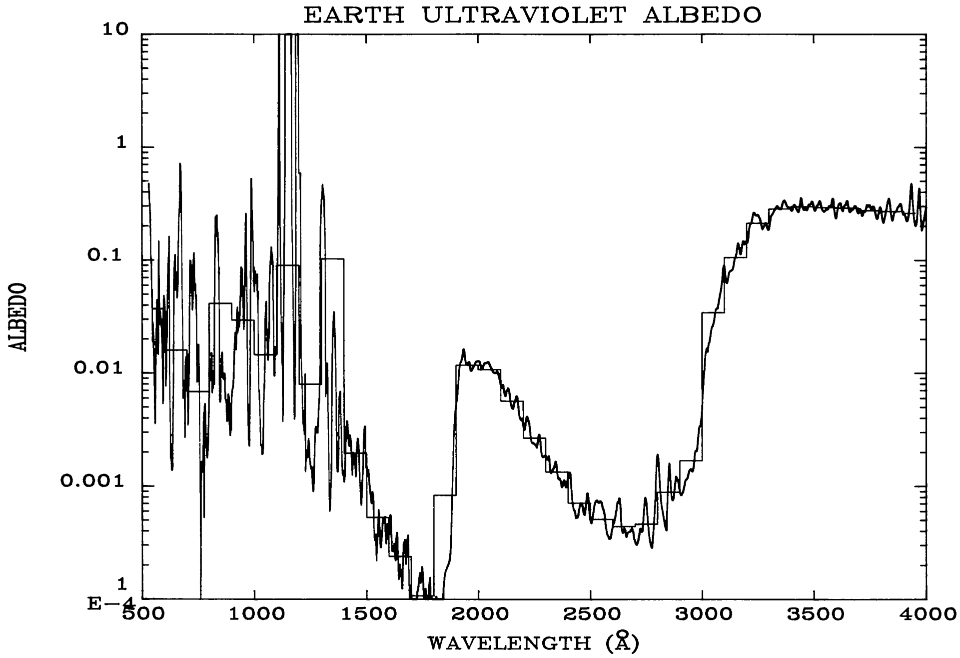

Fig. 1.4: Example Earth UV albedo shows strong fluorescent emission lines which decrease the Sun-Earth contrast. Reproduced from Meier (1991).

orbital radius (Kelsall et al., 1998; May, 2008, and references therein). This contributes a bright, resolved, background signal which must be overcome by future missions to image Earthlike exoplanets. A 2.4 meter aperture is the minimum necessary for the visible light from an exo-Earth to equal the surface brightness of the zodiacal light at 1AU (Traub & Oppenheimer, 2010). More challenging still, 1% of stellar Spectral Energy Distribution (SED)s imply exozodi (zodiacal light around other stars) exceeding 1000 solar zodi. (One zodi is typically defined as the zodiacal light surface brightness at one astronomical unit from the host star, though some authors set it equal to the integrated solar zodiacal brightness). The LBTI demographic survey will determine the frequency of bright exozodi in the IR (Roberge et al., 2012). Morphologically, the distribution of zodiacal dust has been proposed as a tracer of exoplanets (Stark & Kuchner, 2008) but will also contribute to false positives (Absil et al., 2010). Relatively unmeasured, visible wavelength exozodiacal brightness is particularly important since it includes many of the spectral features which are expected to indicate the presence of life (Kaltenegger et al., 2010), as well as important ionospheric features such as the OI 630.0 nm transition. Hence, direct measurements of exozodi brightness and morphology are critical to defining future visible light exoplanet imaging and spectroscopy missions.

Tantalizingly, while debris disk brightness adds challenges to direct imaging of exoplanets, it may also increase the probability a planet will be found around a star (Matthews et al., 2014, and references therein).

Impact of Exozodiacal Light on Exoplanet Observations

To answer the engineering question posed by exozodiacal light and estimate the telescope diameter required to image small exoplanets, a simple model for exoplanet detection is required. The signal-to-noise ratio (SNR) for ϕ_p photons per second from a planet observed for time t is given by:

$$SNR = \frac{\phi_p t}{\sqrt{(\phi_p + \phi_{bgnd})t}} \tag{1.17}$$

In the simplest case one assumes an ideal coronagraph, negligible solar and galactic backgrounds, and a noiseless detector, such that ϕ_{bgnd} is only composed of exozodiacal photons. As described by Stark et al. (2014), the background count rate is calculated from z zodis of exozodiacal light with a magnitude of m_z and a flux of $F_0 10^{-m_z/2.5}$, where F_0 is the zero magnitude flux. The solid angle observed by a telescope diameter D is $\Omega = \pi(X\lambda/D)^2$. X is the size of the photometric aperture, conservatively this is approximately one Rayleigh Criterion resolution element, $X = 1.22$. (Stark et al. (2014) suggests an optimum of $X = 0.7$). The count rate for SNR calculation also depends on the telescope and detector efficiencies, which are combined as an "effective quantum efficiency" of the system QE_{Eff}. Multiplying these quantities by the telescope area, $A = \pi(D/2)^2$, and bandwidth, $\Delta\lambda$, we find the photon rate per resolution element is independent of telescope diameter:

$$\begin{aligned} \phi_{exozodi} &= F_0 \; (z10^{-m_z/2.5}) \; A \; \Omega \; \Delta\lambda \; \mathrm{QE}_{eff} & (1.18) \\ &= F_0 \; (z10^{-m_z/2.5}) \; \pi^2 \; (X\lambda)^2 \; \Delta\lambda \; \mathrm{QE}_{eff} & (1.19) \end{aligned}$$

The flux from an unresolved exoplanet (ϕ_p) depends on the telescope diameter:

$$\begin{aligned} \phi_p &= F_0 \; (10^{-m_p/2.5}) \; A \; \Delta\lambda \; \mathrm{QE}_{eff} & (1.20) \\ &= F_0 \; (10^{-m_p/2.5}) \; \pi(D/2)^2 \; \Delta\lambda \; \mathrm{QE}_{eff} & (1.21) \end{aligned}$$

Given these expressions, for a particular SNR, planet magnitude and exozodiacal background surface brightness, Eq. 1.17 sets a limit on the minimum telescope diameter D. At elevated zodiacal dust levels, the telescope diameter required to detect a planet of a given magnitude also increases. This simple SNR model assumes a uniform exozodiacal light background, physical cases are expected to be clumpy due to dust dynamics and dust-planet interactions. A non-uniform exozodi will impart a residual which cannot be perfectly subtracted from the planet signal (e.g. modeling by Defrère et al. (2010)). Thus, this calculation merely represents a useful lower limit on sensitivity to exoplanets for an exoplanet imaging space telescope. Stark et al. (2014) presents an optimized visible light search for Exo-Earth candidates around nearby stars with a baseline 8 m space telescope with a realistic exozodiacal model. Using this model, the right panel of Fig. 1.5 shows the decrease in the number of targets at large distances in their notional target list due to a factor of thirty increase in background zodi around all targets. Stark et al. (2014) found the number of exo-Earth candidates detected decreases only weakly with average exozodi brightness,

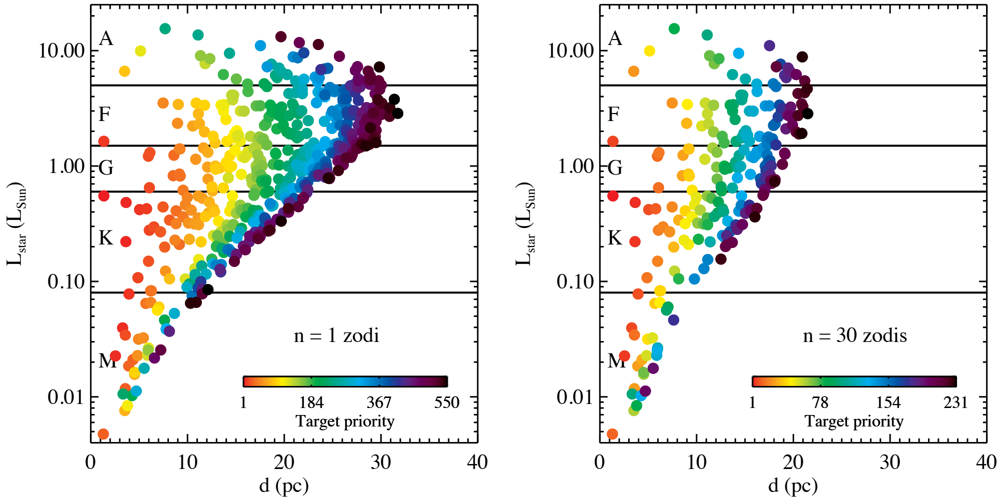

Fig. 1.5: Target star luminosity versus distance for an optimized Exo-Earth search. Target priority is indicated by color. The number of promising stars decreases when the zodiacal dust background increases from one zodi (left) to 30 zodis (right) for a hypothetical 8m telescope. The effect is relatively weak because more distant stars are already poor survey candidates. Reproduced from Stark et al. (2014).

since in a multi-parametric survey, otherwise weak targets will be dropped first. Nearby stars with high probability of terrestrial planets would still be well surveyed.

1.2.3 Past Observations

This section will sketch our understanding of dust and planetesimals in our Solar System (the zodiacal dust and the asteroid belt) and in extrasolar debris disks (e.g. Matthews et al. (2014); Wyatt (2008)) focusing on the nearby ϵ-Eridani system which is the target of the visible light PICTURE mission (Mendillo et al., 2012b). Our present understanding of debris disk morphology is determined by modeling (e.g. Stark & Kuchner (2008); Reidemeister et al. (2011)) and observations, including SEDs, sub-millimeter imaging (e.g. Greaves et al. (1998)) and IR imaging (e.g. Absil et al. (2008); Millan-Gabet et al. (2011); Defrère et al. (2013); Soummer et al. (2014))

and a very few cases of optical direct imaging from the Hubble Space Telescope (e.g. Schneider et al. (2006); Kalas et al. (2008)).

After star formation the primordial protoplanetary disk of gas and dust that did not form the star is cleared quickly, leaving a relatively rarified circumstellar environment. In the Solar System, this process left four commonly defined components: the inner zodiacal disk of dust transported into the inner Solar System (Nesvorný et al., 2010) and visible to the unaided eye along the plane of the ecliptic; the asteroid belt (see review by Asphaug, 2009), the Edgeworth-Kuiper belt (EKB) (see review by Luu & Jewitt, 2002), and the Oort cloud (Oort, 1950).

Early extrasolar debris disk observations

Aumann et al. (1984) inferred the first extra-solar debris disk from measurements of the far-infrared (FIR) excess in the SED of Vega (α-Lyra) with Infrared Astronomical Satellite (IRAS) (Aumann & Walker, 1977). Subsequent observations identified other stars hosting large excesses, including nearby β-Pictoris, α-Pisces, and ϵ Eri (Aumann, 1985). Ground-based follow-up readily detected light scattered by dramatic wings of debris around β-Pictoris (Smith & Terrile, 1984). Fig. 1.6 shows the original discovery image, the edge-on and somewhat asymmetrical β-Pictoris debris disk extends many arcseconds, making it a relatively easy target for imaging. The distant β-Pictoris disk is analogous to the cold Solar System EKB. Analogs of solar system's zodiacal dust have proven much more difficult to image due to their close proximity to host stars.

Debris Disk Effective Temperature

Measurements of IR excess provide us with information about the temperature of circumstellar material. Following the same approach as calculating a planetary equilibrium temperature, an estimate of the dust radius is found by assuming a stellar

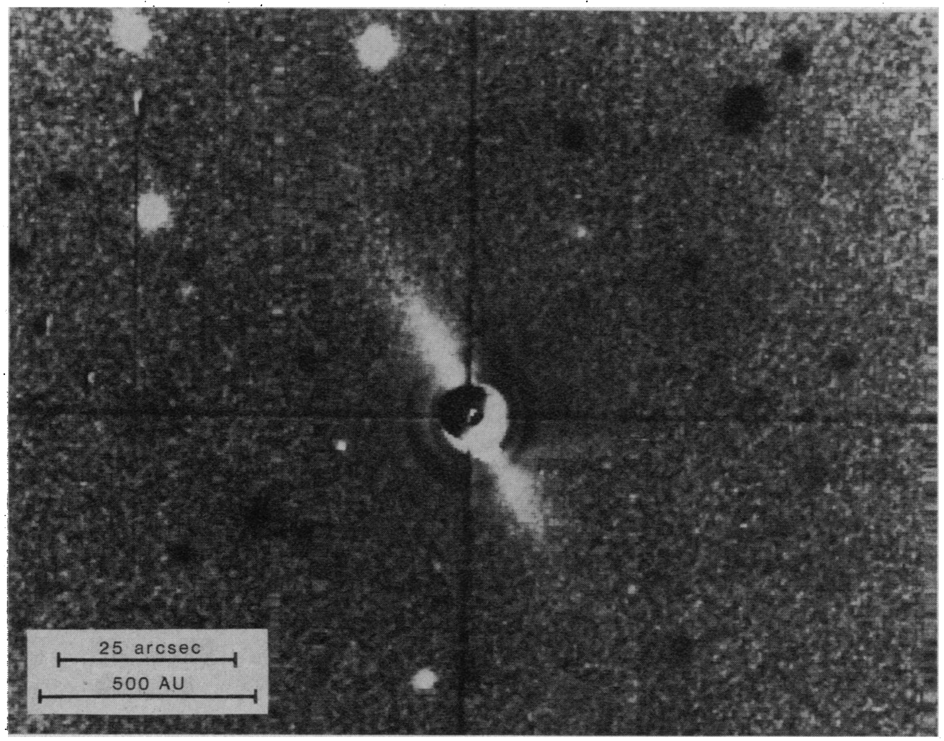

Fig. 1.6: Ratio image of β-Pictoris divided by α-Pictoris showing the scattered light from the β-Pictoris edge-on debris disk recorded with simple coronagraph on the 2.5 meter du Pont telescope at Las Campanas Observatory. Reproduced from Smith & Terrile (1984).

Planck spectrum and calculating the flux incident (F_{in}) on the circumstellar dust. For $T_\star$ and a wavelength independent albedo of a (the fraction of light reflected) at an orbital radius of r, and the absorbing cross-section of dust (or planet of radius R is) πR_p^2. The planet can be treated as a black-body planet with temperature T_p, re-emitting light with a flux $F_{emitted}$. Assuming radiative equilibrium allows us to equate the energy striking the orbiting body with the emission rate:

$$\pi R_p^2 F_{in}(1-a) = 4\pi R_p^2 F_{emitted} \tag{1.22}$$

$$\frac{L_\star}{4r^2}(1-a) = \frac{L_p}{R_p^2} \tag{1.23}$$

The Stefan-Boltzmann law relates the stellar energy output to temperature: $L_\star = 4\pi R_\star^2 \sigma_{SB} T_{eff}^4$. The luminosity of the dust or planetary body is: $L_p = 4\pi R_p^2 \sigma_{SB} T_p^4$, where σ_{SB} is the Stefan-Boltzmann constant . Upon substitution, R_p^2 cancels out, and we are left with:

$$T_p = T_\star (1-a)^{1/4} \left(\frac{R_\star^2}{4r^2} \right)^{1/4} \tag{1.24}$$

and the separation distance is

$$r = \left(\frac{T_\star}{T_p} (1-a)^{1/4} \left(\frac{R_\star^2}{4} \right)^{1/4} \right)^2 \tag{1.25}$$

This simple derivation rarely gives the actual temperature of a physical body orbiting a star. For planetary temperatures, this is because we neglected the heat trapping effects of the atmosphere (the "greenhouse effect", e.g. Arrhenius, 1896; Wildt, 1940) and internal heating. For dust grains, we have assumed the emission and absorption are reversible processes. However, measured debris disks consistently have larger radii than would be found by this simple black-body derivation (Matthews et al., 2014). This is illustrated by Fig. 1.7, which plots the resolved disk radius versus the black-body equilibrium radius for a large sample of known debris disks (Rodriguez & Zuckerman, 2012, Fig. 9, Table 7). Pawellek et al. (2014) found that this ratio increases with stellar luminosity.

For a more accurate distance-temperature relation, we need to account for variation in absorption efficiency with wavelength.

A more physically complete expression for radiative equilibrium balances the energy with the inclusion of a wavelength dependent emission/absorption coefficient Q_{abs}. Assuming isotropic thermal emission by spherical dust grains and thermal fluxes $B_\lambda(T)$ that depend on wavelength according to Planck's law:

$$\pi R_p^2 \int_\lambda \frac{4\pi R_\star^2}{4\pi r^2} Q_{\text{abs}}(\lambda) \pi B_\lambda(T_\star) d\lambda = 4\pi R_p^2 \int_\lambda Q_{\text{abs}}(\lambda) \pi B_\lambda(T_p) d\lambda. \tag{1.26}$$

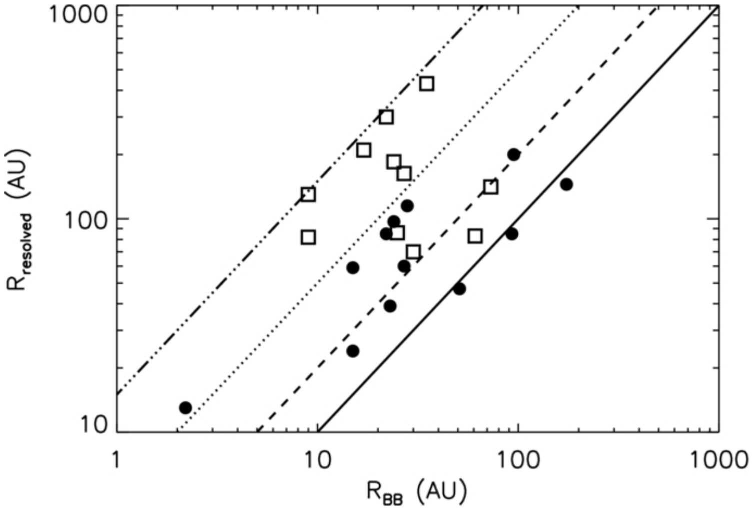

Fig. 1.7: The measured radii of imaged debris disks, particularly those imaged in scattered light, tend to be larger than their black-body equilibrium radii. Open squares indicate scattered light observations and filled circles are those resolved in thermal emission. The lines indicate the ratio between resolved and equilibrium radii, the solid line, a 1:1 ratio; the dashed line, a 2:1 ratio; the dotted line, a 5:1 ratio; and the triple-dot dashed line, a 15:1 ratio. Reproduced from Rodriguez & Zuckerman (2012).

Cancelling the (planet or dust) radius R_p and re-arranging gives:

$$r = \sqrt{\frac{\int_\lambda Q_{\text{abs}}(\lambda) R_\star^2 B_\lambda(T_\star) d\lambda}{4 \int_\lambda Q_{\text{abs}}(\lambda) B_\lambda(T_p) d\lambda}} \tag{1.27}$$

Or as a function of the observed stellar flux at Earth, $F_\star = \pi B_\lambda(T_\star) R_\star^2 / d^2$ from a star at distance d (Lebreton et al., 2013, e.q. 4):

$$r = \frac{d}{2} \sqrt{\frac{\int_\lambda Q_{\text{abs}}(\lambda) F_\star(\lambda) d\lambda}{\int_\lambda Q_{\text{abs}}(\lambda) \pi B_\lambda(T_p) d\lambda}} \tag{1.28}$$

A good approximation for Q_{abs} is unity at wavelengths below the circumference of a dust grain and a decreasing power law at longer wavelengths (the so-called “modified-black body” Backman & Paresce (1993) in Pawellek et al., 2014, Eq. 2). Using this approximation, measurements of the debris disk radius via direct imaging constrain the dust grain size via Q_ν and vice-versa.

1.2.4 ϵ Eri, a nearby dusty laboratory

Discovered by Aumann (1985) in an IRAS survey of nearby stars for IR excess, the ϵ Eri debris disk was one of the earliest detected extrasolar debris disks, due both to its proximity and significant dust population. The outer disk morphology was first resolved by Greaves et al. (1998) at 450 and 850 μm, finding a cool EKB analog from approximately 10" to 25" (30-75 AU). A subsequent search by Proffitt et al. (2004) with the Space Telescope Imaging Spectrograph (STIS) put a limit of 25 standard magnitudes per square arcsecond for scattered light from this outer ring while Di Folco et al. (2007) placed a limit on the total fractional scattered light brightness of the inner ring of 0.6×10^{-2} (or 5.5 magnitudes) using the Center for High Angular Resolution Astronomy (CHARA) array at 2 μm. Backman et al. (2009) broadly surveyed the system with the Spitzer Space Telescope, including: the Infrared Array Camera (IRAC) from 3.6-7.7 μm; the Multiband Imaging Photometer for Spitzer (MIPS) at 24, 70, and 160 μm; and SED observations from 55-90 μm. Spitzer Infrared Spectrograph (IRS) spectra were used to connect the calibration of the broadband mid-IR observations. Additionally, Backman et al. (2009) used the Caltech Sub-millimeter Observatory to observe the cool EKB analog and found a morphology inconsistent with previous observers, pointing to variation due to instrumental effects.

To explain the composite SED's IR-excess, shown in Fig. 1.8, Backman et al. (2009) proposed a four component disk system:

- a wide ice ring analogous to the EKB from 35-90 Astronomical Unit [1.5e11 m] (AU);
- a silicate ring and halo inclusive of the ice ring but extending further out to 110 AU;

- a warm, narrow, ring at 20 AU of indeterminate composition;
- and an innermost, narrow, warm belt of silicate material at 3 AU.

The inner warm belt dust was found to be best-approximated by $\sim 3\ \mu$m astrosilicate dust grains and the authors placed rough 25% certainty errors on the radius and width of the inner belt. Using the Submillimeter Array, MacGregor et al. (2015) resolved the outer ring and found no significant morphological features, seriously limiting the possible mass and orbits of outer planets in the ϵ Eri system. A planet candidate with a semimajor axis of 3.4 AU has been inferred from radial velocity and astrometric measurements (Hatzes et al., 2000). Using additional astrometric data from the Hubble Space Telescope (HST) *Fine Guidance Sensor 1r* (Benedict et al. (2007) report a mass of $0.78 M_J$ and an eccentricity of 0.70, which would pass through the Backman et al. (2009) warm ring. This orbit was expected to disrupt the inner ring, making either the planet orbit or dust ring untenable. Alternatively, using a variety of radial velocity observations Butler et al. (2006) reported a mass of $1.06 M_j$ and an eccentricity of 0.25 – which would not necessarily cross the inner ring.

The presence of a planet at 3.4 AU remains uncertain, while still “suggested”, no significant signal was found in a radial velocity search of both previously published data combined and new high precision observations from the High Accuracy Radial velocity Planetary (HARPS) instrument (Zechmeister et al., 2013). Numerous direct imaging searches for planet candidates have also failed to detect planets in the ϵ Eri system (e.g. Marengo et al. (2006); Janson et al. (2007); Nielsen et al. (2008); Marengo et al. (2009); Heinze et al. (2010); Janson et al. (2015)). While any values for the 3.4 AU planet candidate’s albedo and thermal emission brightness are highly speculative, none of these searches has reached contrasts likely to detect a Jupiter mass planet within a few arcseconds.

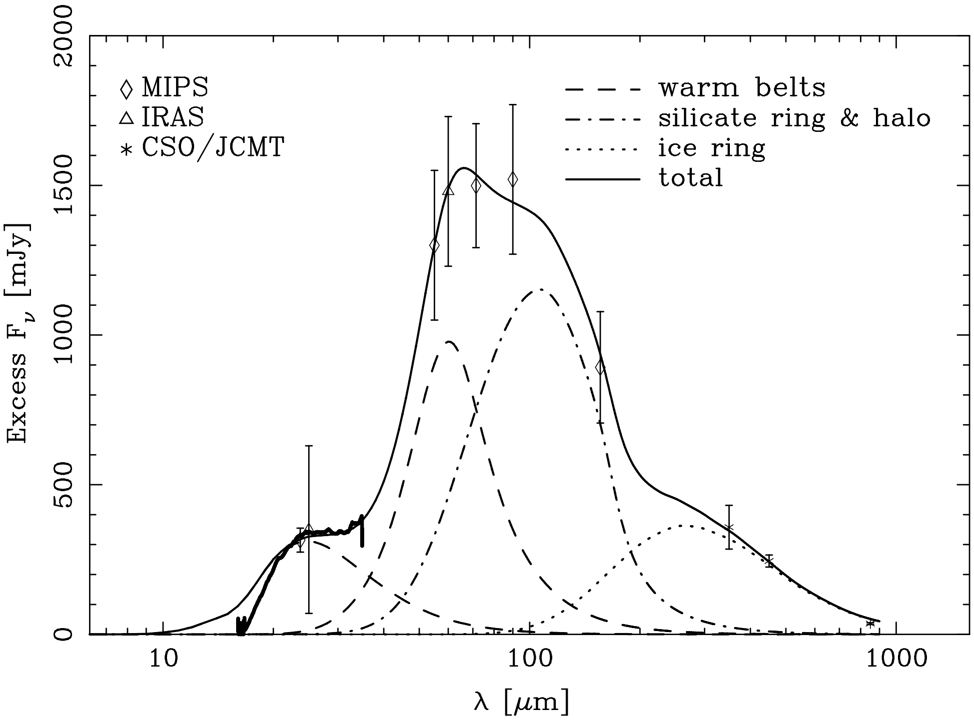

Fig. 1.8: The infrared excess of ϵ Eri after subtraction of a model photosphere. Dashed curves represent individual model components. Planet Imaging Concept Testbed Using a Rocket Experiment (PICTURE) sought to test for the scattered light from the warm ring component, a possible explanation of the excess at 22 microns. Reproduced from Backman et al. (2009).

Reidemeister et al. (2011) proposed that pseudo-Poyinting-Robertson drag due to ϵ Eri's strong stellar wind (Wood et al., 2002) could sustain the innermost ring, independent of an inner planet's orbit. They showed that the SED is reproduced by an outer EKB-analog with a 70/30 ice/dust volume ratio, which would stream inward at a sufficient rate to sustain the IR excess at short-wavelengths. The presence of a planet hollows out an otherwise flat surface brightness distribution but would not be discernible from existing SED observations. Fig. 1.9 shows how the 3.4 AU planet with an eccentricity of 0.7 would sculpt the brightness distribution close to the star in the Reidemeister et al. (2011) model.

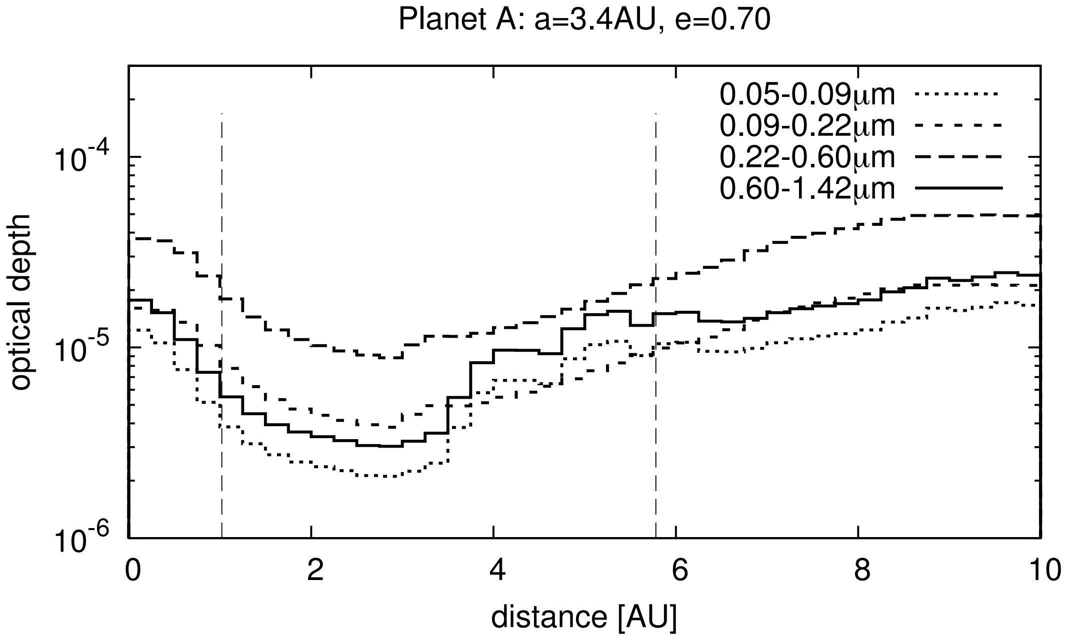

Fig. 1.9: The optical depth of the inner region of the ϵ Eri system if dust dynamics is driven by strong stellar wind in the presence of a highly eccentric planet with a semi-major axis of 3.4AU and eccentricity of 0.70. Reproduced from Reidemeister et al. (2011).

Solar zodiacal dust is thought to be dominated by efficiently scattering 1-100 micron grains (Grogan et al., 2001). Such grains should scatter visible wavelengths with a high albedo, $\omega \gtrsim 0.5$ (Kennedy et al., 2014); however, observed extrasolar zodiacal albedos have been much smaller and both Backman et al. (2009) and Kennedy et al. (2014) both assume a conservative $\omega = 0.1$.

This well studied system, with two significantly different hypotheses to explain the observed SED, provides a scientifically exciting test target for direct exoplanet imaging instruments.

1.2.5 Coronagraphs – High Contrast Imaging and Wavefront Control

High-contrast visible light imaging is required to evaluate the distribution and intensity of exozodiacal light. Such imaging shares much in common with the problem of detecting a dim exoplanet, an observer must determine the probability that the light measured in a pixel is due to a exoplanet or exozodiacal source and not stellar light. Even with perfect subtraction of the stellar Point Spread Function (PSF) in post-processing, stellar photon noise limits detection of faint sources, motivating the separation and removal of starlight before it reaches the imaging detector. Such removal of stellar contamination at the 10^{-5} level or better is commonly referred to as *high-contrast imaging* (Oppenheimer & Hinkley, 2009) and devices designed for the removal of starlight are commonly termed *coronagraphs.* Recent advances in coronagraph technology, coupled with adaptive optics (AO) and image processing, have permitted ground-based measurement of large gaseous extrasolar planets at NIR and IR wavelengths (e.g. Beuzit, 2006; Macintosh et al., 2008; Hinkley et al., 2011; Males et al., 2014). At optical wavelengths, the extreme stability of the HST PSF has allowed detections of bright planets and debris disks (e.g. Schneider et al., 2006; Kalas et al., 2008; Schneider et al., 2014) and powerful PSF subtraction routines have allowed high-contrast measurements at the Poisson-noise limit (Schneider & Stobie, 2002; Lafrenière et al., 2007; Soummer et al., 2012; Fergus et al., 2014; Amara & Quanz, 2012; Choquet et al., 2014).

While numerous techniques have been developed to attenuate or subtract starlight, they all rely on the instrument maintaining a stable influence on the phase and amplitude of that light. Seeming exceptions, such as lucky dark speckle observations (Labeyrie, 1995) rely on the stellar wavefront randomly matching the desired phase, an inefficient form of control by elimination. Ground-based coronagraphy in the IR (e.g. Poyneer & Dillon (2008); Hinkley et al. (2011); Jovanovic et al. (2015))

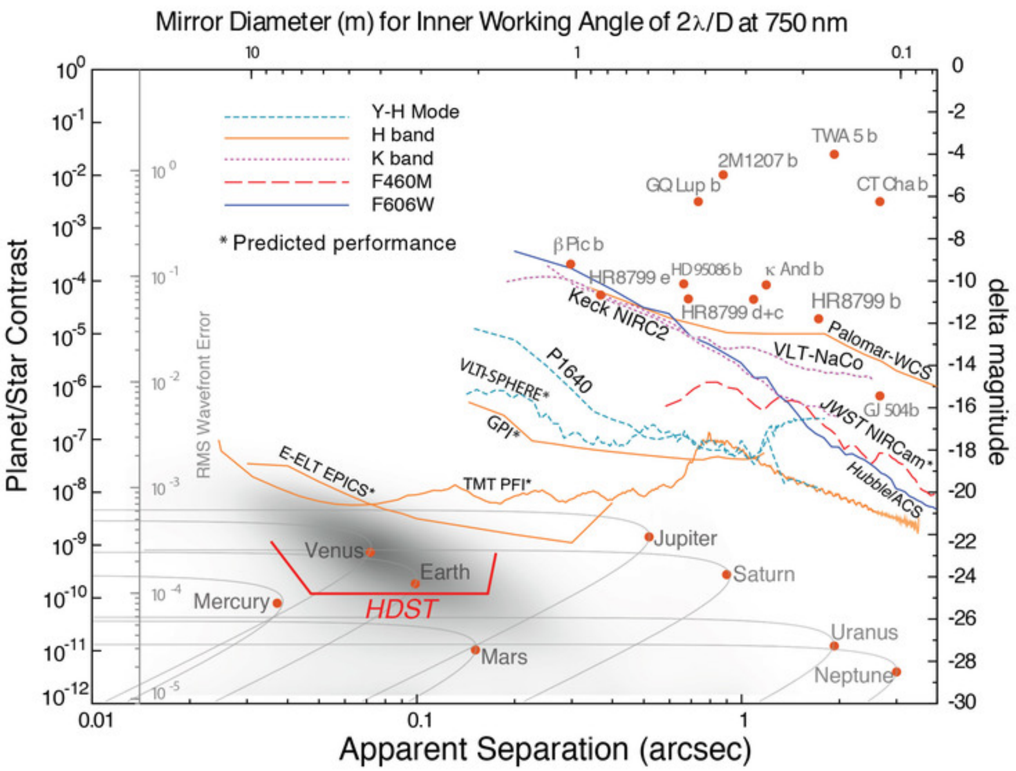

Fig. 1.10: Contrast curves for existing and planned exoplanet imaging observatories. A notional High-Definition Space Telescope (HDST) capable of imaging Exo-Earths with a 12-meter class primary mirror is shown in red. Reproduced from Dalcanton et al. (2015).

relies on wavefront sensing and control to correct both atmospheric turbulence and optical disturbances.

Starlight contamination in a coronagraphs arises from imperfections in the optical system which manifest as *speckles* – spurious diffraction patterns in the image plane. For example, ripple polishing errors in the Hubble Space Telescope scatter light into the PSF wings, these speckles then evolve over time, changing in brightness and location in the image plane, as the optical assembly temperature varies (Krist, 2004). Minimum speckle size corresponds to the telescope resolution (Perrin et al., 2003), leading to confusion between speckles and true off-axis point sources. By the time a spherical stellar wavefront has covered several parsecs and is incident on a space telescope, or the atmosphere, it is planar or approximately "flat" on the scale of telescope diameter. Thus, the challenge of wavefront control is to measure and minimize the variation from a planar wavefront. These errors can be both internal and external to the optical system. AO comprises the field of wavefront error sensing and control. The speckle-limited contrast achievable due phase errors with average amplitude h_{rms} is (Traub & Oppenheimer, 2010, Eq. 124):

$$C = \pi \left(\frac{4h_{rms}}{N\lambda} \right)^2 \tag{1.29}$$

N is the number of control points across the wavefront, and λ is the wavelength of observation. The inverse dependence of contrast on λ^2 drives the tighter manufacturing tolerances for visible and UV direct imaging. For example, with a state-of-the-art 48x48 actuator deformable mirror, for $h_{rms} = 0.1$ nm at λ=1 μm the contrast is $\sim 2 \times 10^{-10}$; however, at 100 nm the residual speckles in the same system is $\sim 2 \times 10^{-8}$.

The primary challenge faced by ground-based AO systems is external atmospheric turbulence, which necessitates rapid correction across many spatial scales.

Atmospheric turbulence is typically approximated as a Kolmogorov spectrum, where the root mean squared (RMS) wavefront error (WFE) between two points separated by a distance, r, follows a power law:

$$\Delta\phi \propto \left(\frac{r}{r_o} \right)^{5/6}, \tag{1.30}$$

where r_0 is a scaling constant which represents the quality of the atmospheric seeing. Larger telescopes with a greater separation between points thus experience larger wavefront errors.

Additionally, for a wind shear velocity v and an exposure time τ, the sampled atmosphere is changing and $r = v\tau$, introducing a time dependence which requires wavefront correction at a wide range of spatial scales and times. For derivations of the relation above and further discussion see: Fried (1965); Martin (1987); Sarazin & Roddier (1990); Hill (1990). r_0, the "Fried Parameter" depends on wavelength, $r_0 \propto \lambda^2$; thus, as wavelength increases the challenge of diffraction limited imaging through the atmosphere lessens. In the field, atmospheric turbulence requires fast measurement and correction loops. For example, the state-of-the-art ground-based Gemini Planet Imager (GPI) AO wavefront sensing system operates at 1000 hz between 700-900 nm (Thomas et al., 2012) and in good seeing conditions on a bright star (β-Pictoris, $m_v = 3.9$), the internally measured RMS wavefront sensing error is small ($\approx$ 6 nm) but servo lag still limits the corrected wavefront to 25 nm RMS (Poyneer et al., 2014).

Space-based telescopes circumvent time varying atmospheric disturbances, enabling diffraction limited imaging even at short wavelengths. This effect is dramatically illustrated in Fig. 1.10 by the many orders-of-magnitude improvement in contrast between a state of the art coronagraph GPI and the planned Wide-Field InfraRed Survey Telescope-Astrophysics Focused Telescope Assets (WFIRST-AFTA) coronagraph, a 2.4 m coronagraphic space-mission which is expected to reach a 10^{-10} contrast level at 0.2 arcsec (Spergel et al., 2015) and the notional 12 meter High-Definition Space Telescope which might reach 10^{-10} at seperations as little as 0.05 arcsec (Dalcanton et al., 2015). In space, time-varying WFE arises from the coupling of mechanical perturbations of the spacecraft structure to the surfaces of optical components. The HST was designed with a highly stable "optical bench" with expected $\lambda/20$ stability ($>$2 μm primary-secondary mirror despace at λ =633 nm) over 24 hours (McCarthy & Facey, 1982) via an athermalized composite metering structure design (McMahan, 1982). Despite these efforts, on-orbit variations in the HST wavefront error are significant. The despace variation amplitude is 5 μm Peak-to-

Valley (PV) per orbit, which results in variable wavefront errors $>$ 100 nm PV on ninety-minute time scales, while astigmatism and coma vary by approximately 5 nm and 11 nm PV, respectively (Lallo et al., 2006). These variations significantly limit repeatability of PSF measurement and inhibit PSF subtraction for high-contrast image post-processing. The HST secondary mirror can be commanded to new positions, but each correction requires human-in-the-loop determination of best focus and command from the ground. Consequently, focus has only been corrected a few dozen times over the course of the multi-decade mission (Lallo et al., 2006). Future space-based imaging of rocky planets with internal coronagraphs requires sub-nanometer wavefront stability, much lower than that exhibited by the passive HST design, and active control presents a natural solution which will be further discussed in Chapters 4 and 5.

1.2.6 Nulling Interferometry

The goal of extrasolar coronagraphy is the suppression of starlight before it reaches the detector while still transmitting planet light from small angles. Many approaches to extrasolar coronagraphy have been proposed and compared theoretically (Guyon et al., 2006), and various designs have been prototyped and tested in the lab. See Lawson et al. (2013) for a recent review of the state-of-the-art. In the nulling coronagraph architecture (or "nuller"), proposed by Bracewell (1978), two equal components of starlight, collected by apertures separated by a baseline (interferometer "arms") with a π phase shift between them are combined to form a fringe pattern on the sky. When recombination occurs at a beamsplitter, the π phase shift due to reflection splits the light into two output fringes: one where starlight is destructively interfering (or "nulling") with itself, the so-called "dark fringe" or "dark output," and a second where light constructively adds, the "bright fringe" or "bright output". Path length through the interferometer depends on angle with respect to the optical axis;

when the fringe pattern is centered on a star the light from exoplanets at close angles is partially transmitted, lowering the effective contrast in the dark output and thereby improving the likelihood of detection of a dim companion. Nulling interferometry was first demonstrated from the ground at infrared wavelengths in 1998 with the Multiple Mirror Telescope (MMT) (Hinz et al., 1998, 1999) and has been employed to measure exozodi brightness in the infrared by the Keck Interferometer Nuller (Millan-Gabet et al., 2011). Pupil apodization via various techniques to detect exoplanets, including a broadband Mach-Zehnder interferometer was proposed in the Lockheed Martin Apodized Telescope report (Lockheed, 1979).

The PICTURE VNC, the focus of this work, is a uni-axial Mach-Zehnder Lateral Shearing Interferometer (LSI) design (Shao et al., 2004; Lyon et al., 2006; Levine et al., 2006; Lozi et al., 2011).

The LSI design allows a single telescope to feed the nuller. Shearing the input wavefront in a pupil plane allows a single telescope to function in manner analogous to a two-telescope nulling interferometer. Interference occurs between collimated beams, each a copy of the input pupil, and the interfered wavefront travels along a single axis before imaging. Other variations on the visible nulling interferometer include the Rotational Shearing Interferometer (Serabyn et al., 1999; Wallace et al., 2000; Hicks et al., 2009, 2013) and multi-axial designs where interference occurs in the image plane (Haguenauer & Serabyn, 2006).

The first order nuller transmission pattern, $T(b, \theta, \lambda)$, is a function of baseline (b); angle on the sky along the shear axis (θ); and wavelength (λ). The fringe pattern for two apertures is bar-like, analogous to the interference generated by Young's double slit experiment:

$$T(b, \theta, \lambda) = T_a \left[1 - \cos\left(\frac{2\pi}{\lambda} b \sin(\theta) \right) \right] \tag{1.31}$$

where T_a is the transmission of a single aperture. Fig. 1.11 shows the on-sky transmission map for b = 0.3 m at λ=675 nm. For an instrument fed by a single telescope, T_a is at most one-half of the input aperture.

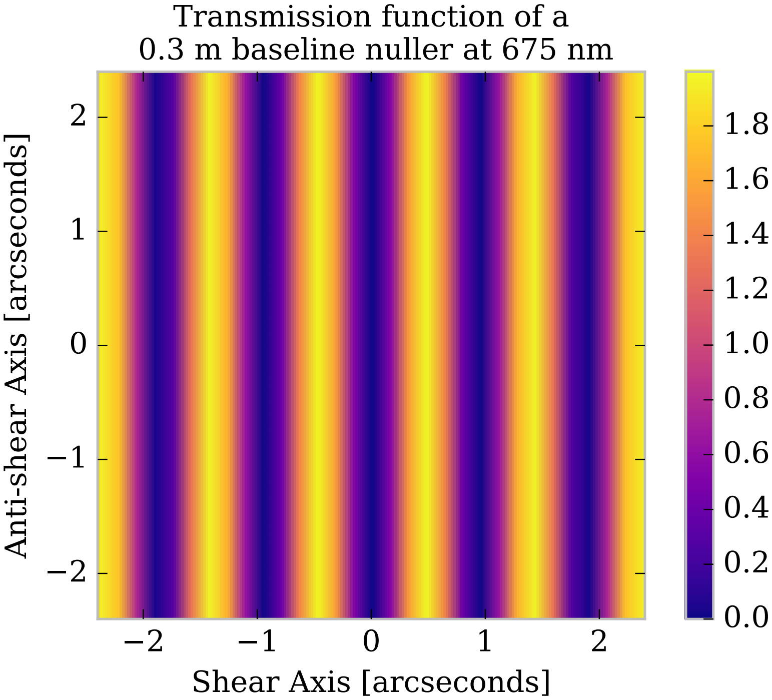

Fig. 1.11: Ideal transmission function of a nuller with the baseline and central wavelength of the PICTURE VNC .

Both external and instrument-induced errors contribute to deviations from the ideal transmission pattern. On a space platform, atmospheric turbulence can be neglected. For stratospheric balloons, atmospheric turbulence is expected to limit achievable contrasts to approximately 10^{-9} (Traub et al., 2008). Starlight incoherence due to the finite stellar radius and pointing stability place additional limits on coronagraph contrast. Internal to the instrument, asymmetries in phase and amplitude, pupil rotation, dispersion, and polarization all contribute to leakage of starlight into the dark output. Time varying environmental errors include thermal variation, vibration, pointing error, and atmospheric turbulence. Details of these errors and their contribution to nulling interferometer leakage are given in Appendix B.

1.3 Summary

This chapter has introduced the terrestrial ionosphere and its remote sensing as well as the challenges of exoplanet detection and spectroscopy to evaluate the atmosphere of planets around other stars. Additionally, the limitations placed on these observations by exozodiacal light, and the interesting properties of the nearby ϵ Eri debris disk were discussed. From this foundation, this work will next explore two experiments and two sets of results:

- The Atmospheric and Ionospheric Detection System (RAIDS) EUV Spectrograph, described in Chapter 2, provides continuous observations of the limb profile of 83.4 nm dayglow, greatly expanding on the previous observations of this emission by sounding rocket (Cleary et al., 1989; Dymond et al., 2000, 2001; Yamazaki et al., 2002) and satellite (Kumar et al., 1983; McCoy et al., 1985).
- A new study, using the RAIDS EUV Spectrograph, presented in Chapter 3, demonstrates the sensitivity of 83.4 nm emission to ionospheric parameters by comparison to simultaneous ISR measurements as "ground truth". EUV Spectrograph altitude profiles from 15 January 2010 and 10 March 2010 are compared to a model derived from both geophysical parameters and ionospheric plasma density measured at the mid-latitude Millstone Hill Incoherent Scatter Radar (42.6° N geodetic latitude, 288.5° E geodetic longitude; 54 Λ; L $\sim$ 3.5).

- Chapter 4 describes the PICTURE payload in greater detail, characterizes the laboratory performance of the flight VNC and shows that the integrated payload had the potential to test for a debris disk around ϵ Eri.

- Chapter 5 describes the flight performance of the PICTURE payload, the first successful wavefront sensing with a VNC in space, as well as payload stability in light of unexpected anomalies in optical alignment.

Chapter 2

The RAIDS EUV Spectrograph

This chapter describes the EUV Spectrograph (EUVS) aboard the Remote Atmospheric and Ionospheric Detection System (RAIDS), its design, on-orbit performance and data reduction. RAIDS is a suite of instruments spanning from the EUV to the near-infrared wavelengths (< 800 nm) launched in September 10, 2009. Observing from 55 to 115 nm the EUVS provides a unique view of ultraviolet emission in the thermosphere from a vantage on the Japanese Experiment Module (Kibo) - Exposed Facility (JEM-EF) on the International Space Station (ISS). Much of this description was previously presented in Douglas et al. (2012).

2.1 Instrument Design

This section details the design of the RAIDS EUVS grating spectrograph and its photon counting micro-channel plate detector (MCP), which provides continuous observations of the limb profile of 83.4 nm dayglow, greatly expanding on the previous observations of this emission by satellite (Kumar et al., 1983; McCoy et al., 1985) and sounding rocket (Cleary et al., 1989; Dymond et al., 2000, 2001; Yamazaki et al., 2002).

2.1.1 EUV Spectrograph

A spectrograph requires a means of selecting the field-of-view (FOV), typically a slit or optical fiber, and means of dispersing light. While prisms and diffraction

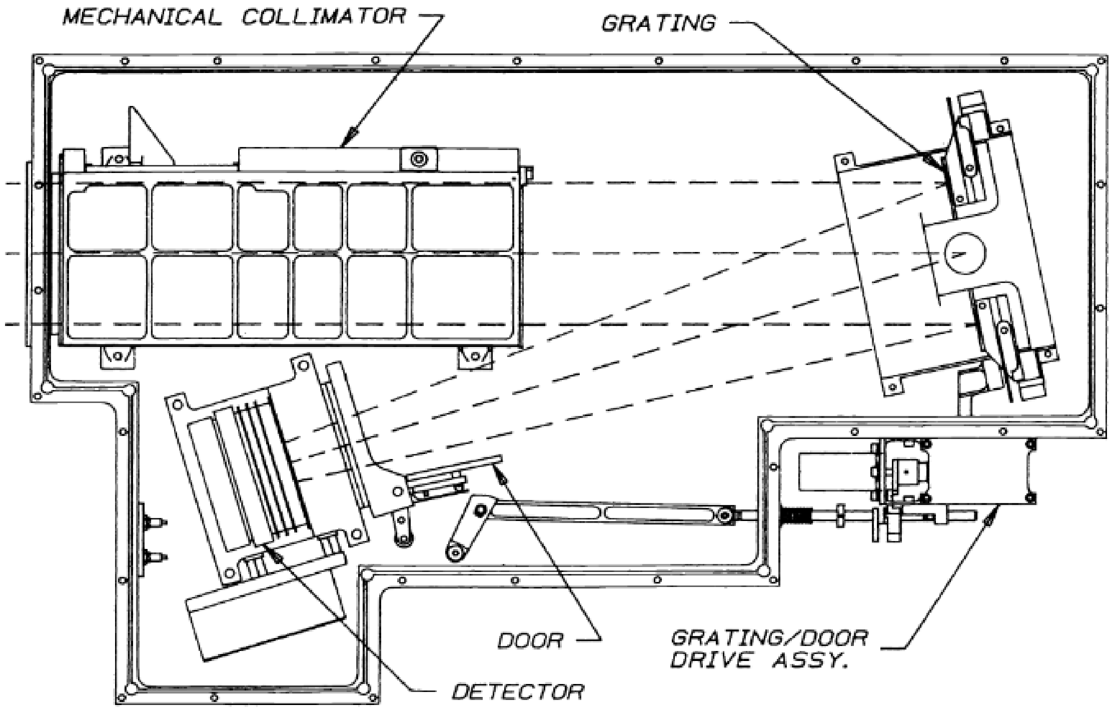

Fig. 2.1: A schematic of the RAIDS EUVS instrument. Photons (dashed lines) enter from the upper left and pass through the mechanical collimator, strikes the diffraction grating in the upper right and is dispersed across the Microchannel Plate (MCP) detector in the lower left. Reproduced from Christensen et al. (1992).

gratings are both effective dispersive elements in visible light, the EUVS requires a reflective diffraction grating due to the lack of transparent materials at EUV wavelengths. To minimize the number of optical surfaces, the RAIDS diffraction grating also serves as the powered optic and focuses light directly onto the detector. The earliest concave grating spectrographs were developed by Rowland and consisted of a source, grating, and output each positioned at points on the Rowland Circle, whose diameter is the radius of curvature of the diffraction grating (Rowland, 1882). With the detector on the circle observing light off the grating the Roland spectrograph images the slit.

The RAIDS EUVS f/4 spectrograph (Fig. 2.1) uses a Wadsworth design (Wadsworth, 1896; Christensen et al., 1992), which is similar to a Rowland spec-

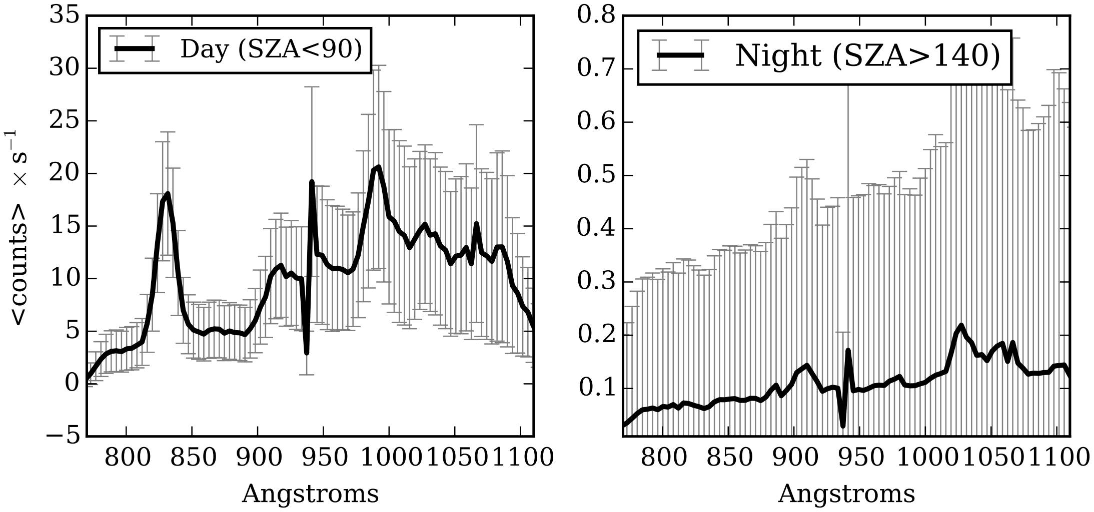

Fig. 2.2: Mean unprocessed RAIDS EUVS spectrum during sunlit and nighttime conditions for an entire day of ISS orbits. Error bars indicate the standard deviation. The 83.4 nm OII feature is clearly evident in the daytime spectrum.

trograph except the source is collimated and the detector is placed at the focus of the grating, allowing spectroscopic imaging of astronomical targets (spectrography). The EUVS has two different grating settings: a short-wave setting that covers 55 nm to 85 nm and a long-wave position that observes from 77 nm to 111 nm. These ranges were chosen to ensure that the 83.4 nm OII emission is always observed (Christensen et al., 1992).

2.1.2 Microchannel Plate Detectors

The RAIDS EUVS relies on a windowless MCP detector to count energetic photons. Arrays of small photomultipliers, MCPs depend on the photoelectric effect (Einstein, 1905). The conversion rate of photons to photoelectrons is given by the quantum efficiency (QE), which for the bare MCPs used for EUVS is approximately 10% at 83.4 nm (Christensen et al., 1992). At other wavelengths, photocathodes with different work functions provide increased QE. For a review of photocathode efficiency see Siegmund (2003). In a photomultiplier, a photon incident on a photocathode releases a single high kinetic energy “primary” electron which then strikes a metallic surface and generates a cloud of “secondary” electrons which are then accelerated by a potential. The production of secondary electrons was discovered by Austin & Starke (1902). Bruining (1962) describes the essentials physics of secondary electron emission. When accelerated by a strong electric field, the secondary electrons striking a second metallic “dynode” surface liberate additional electrons (as proposed by Farnsworth (1934)). The charge of a single primary electron can thus be amplified by many orders of magnitude by harnessing this cascade effect with an extended chain of dynodes. Typical MCPs consists of lead glass plates within a potential of several kilovolts with conducting faces connected by many small through-holes (the channels), each of which is a miniature photomultiplier with the channel wall acting as dynode surfaces. A single photon produces many secondary electrons within a single MCP channel and the large potential accelerates the secondary electrons to high kinetic energies. A two-dimensional anode localizes the position of the initial photoelectron by the centroid of the charge cloud at the output of the MCP stack. The resulting charge is then measurable as a significant voltage via a transimpedence amplifier. Thus, MCP are efficient arrays for two dimensional sensing of high energy particles (Wiza (1979) and references therein). MCPs have been employed in astronomical space telescopes for X-ray (Giacconi et al., 1979) and UV imaging (e.g. Bohlin et al. (1980); Sirk et al. (1997); Mende et al. (2000); Vallerga et al. (2001); Postma et al. (2011)) as well as medical applications (e.g. Williams et al. (1998)).

The RAIDS EUVS employs a wedge-and-strip array anode (Martin et al., 1981) and three bare microchannel plates in a “Z" configuration to prevent ions from traveling up the MCP stack (known as “ion feedback”). The RAIDS readout electronics sum the counts in detector “pixels” perpendicular to the spectrograph dispersion axis,

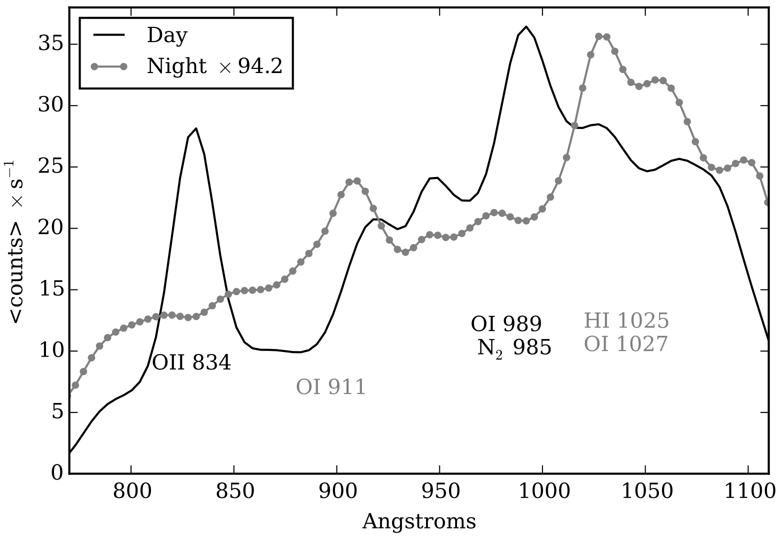

Fig. 2.3: Day and night spectra from Fig. 2.2 smoothed by the instrument resolution (1.2 nm). The nightside spectra has been rescaled to match the dayside peak intensity. The 83.4 nm emission feature is clearly visible in the sunlit spectra. At night, OII features are absent while the OI feature at 91.1 nm and the OI/HI feature at 102.7 nm become prominent.

generating a single, one dimensional, spectrum every half second (Siegmund et al., 1986; Kayser et al., 1989).

2.2 Data Reduction

This section will describe the data reduction process for transforming discrete EUVS spectra from the RAIDS limb scanning instrument into useful tangent point and zenith angle emission profiles, which provide practical coordinate systems for evaluation of vertical structure.

RAIDS views the anti-ram direction, observing the Earth's trailing limb and nodding between tangent points from 75 to 310 km. The EUVS began observations in late-October 2009. The instrument has a field-of-view of 0.1° (altitude) by 2.3° (azimuth) and a stepper motor vertically scans across 16.5° in altitude, corresponding to observation of tangent point altitudes from approximately 75 km to 325 km. The pre-launch instrument characterization showed a responsivity of 0.54±0.11 counts/sec/Rayleigh at 83.4 nm and a spectral resolution of 1.2 nm (Stephan et al., 2009). This resolution is insufficient to resolve the individual components of the 83.4 nm triplet: 83.28 nm, 83.33 nm, and 83.45 nm (Meier, 1991).

Fig. 2.2 shows mean day and night spectra with the EUVS in the long wavelength configuration. Error bars indicate the standard deviation. The small error in the 83.4 nm emission during the day implies the feature is omnipresent in daytime spectra regardless of look direction. However, as will be shown subsequently, the 83.4 nm intensity is not constant with altitude. Fig. 2.3 shows these same spectra smoothed with a gaussian kernel to the instrument resolution to minimize background noise. The night-time spectrum was rescaled for ease of comparison. The total EUV flux from the limb is nearly a factor of 100 dimmer at night and OII features appear absent from the night-time spectra, reinforcing the expectation that the OII features are driven by energetic solar photons.

2.2.1 83.4 nm Intensity Measurement

To extract 83.4 nm limb profiles, EUV spectra within an 80.0 nm to 84.8 nm window were averaged into 20 km tangent point altitude bins. Instrument counts in each pixel of the spectrograph were converted to Rayleighs by applying the calibration described in Stephan et al. (2011). A linear background was fit to the baseline of each altitude's mean spectrum. An example averaged spectrum and baseline are shown in Figure 2.4. The baseline-subtracted signal within the window was summed to derive the total line column emission rate in Rayleighs. Error bars represent $\pm 1\sigma$ Poisson counting uncertainty, including the uncertainty in the degradation rate of each bin via the equation of propagation of uncertainty (Ku, 1966).

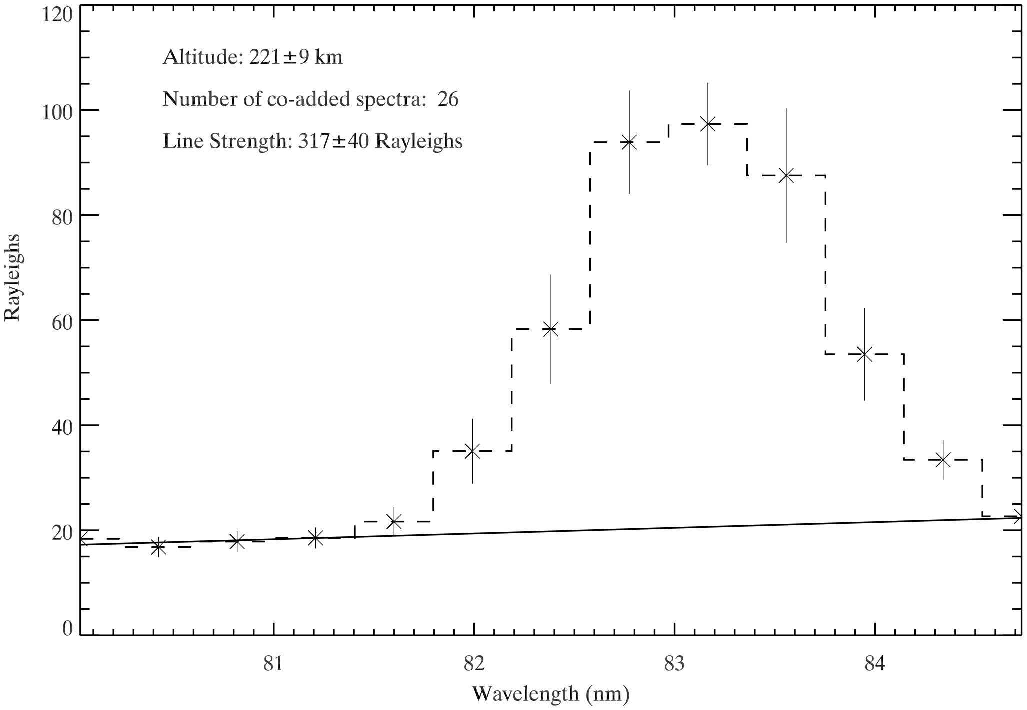

Fig. 2.4: Example mean 83.4 nm line profile of observations within a 20 km altitude range from the 10 March 2010 overflight of Millstone Hill. Calculated emission in Rayleighs in each pixel is shown with combined $\pm 1\sigma$ uncertainty in observation and calibration. The best-fit background level subtracted to yield the line strength is indicated by a solid line. Reproduced from Douglas et al. (2012).

2.2.2 Degradation in Sensitivity

The original instrument sensitivity to photons versus wavelength was measured by Christensen et al. (1992) after instrument integration. This measurement is shown as a dashed line in Fig. 2.6. After extended storage, the sensitivity was remeasured before flight at several wavelengths by Stephan et al. (2009), these preflight measurements are shown as solid dots with capped error bars representing the expected ±20% calibration uncertainty. The calibration at turn-on was assumed to be equal to the preflight measured value of 0.54 Rayleighs per count for the bins composing the 83.4 nm emission feature.

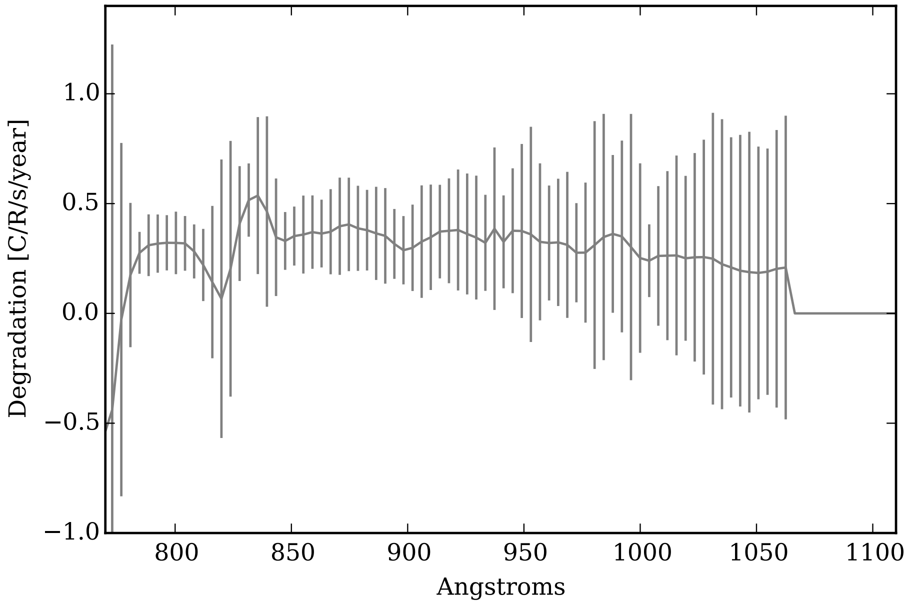

Fig. 2.5: The per pixel change in EUVS sensitivity per year for the long-wave grating position, derived from the best linear fit to each pixel from the observations described in Stephan et al. (2011) and as discussed and applied in Douglas et al. (2012).

Analysis performed early in the mission showed a time-averaged relative 0.20%/day degradation rate of the sensor responsivity over all wavelengths. Dedicated responsivity tests in early 2011 found that the rate of change was dependent on the measured photon flux through the sensor, suggesting a pixel-dependent effect caused by gain changes on the microchannel plate detector and the valid-count pulse height filter implemented in the onboard processing (Stephan et al., 2011).

Thus, the degradation rate of a bright feature on the detector, such as the OII 83.4 nm line, is expected to differ from that of neighboring regions on the detector. We found the initial responsivity near turn on, 27 October 2009, and degradation rate by applying a linear regression to each pixel's responsivity to ionospheric emissions from comparable look directions under similar solar conditions. This method and the days of comparison are the same as those used by Stephan et al. (2011) to find

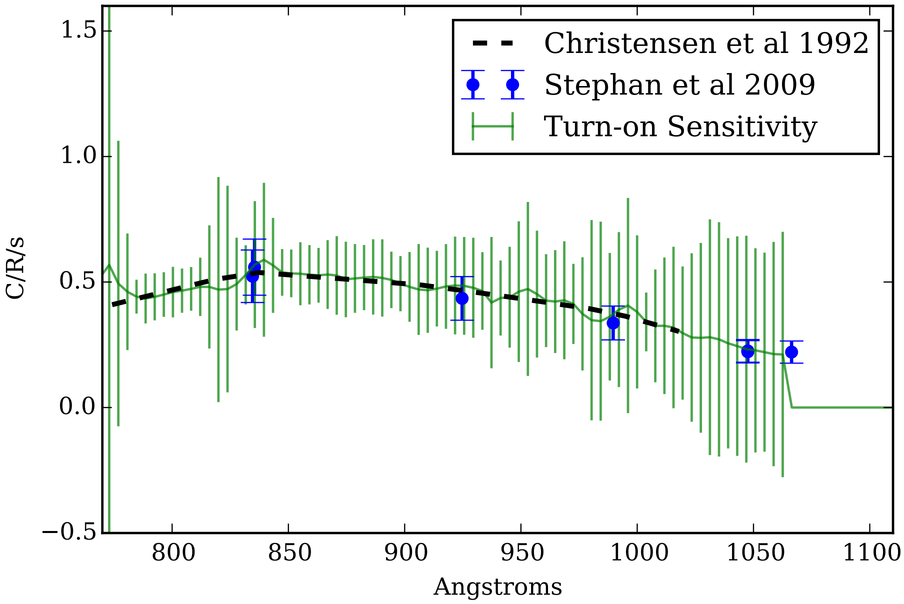

Fig. 2.6: Hybrid turn-on calibration (uncapped-error bars) for the long-wave grating position. Laboratory measurements (dashed line and dots with capped error bars) were used to rescale the sensitivity found from in-flight sensitivity measurements.

the integrated detector responsivity degradation. This responsivity change, shown in Fig. 2.5, is applied to the pre-flight calibration, enabling conversion from instrument counts to Rayleighs for each spectral component on any given day.

Back-projecting the degradation calculation to EUVS turn-on provides a useful illustration of the uncertainty in our knowledge of the calibration. The solid line in Fig. 2.6 shows a hybrid calibration: the linear best-fit degradation rate normalized to unity at EUVS turn-on was multiplied by the pre-flight calibration measurements (from Stephan et al. (2009), shown as dashed lines and error bars as they were originally presented), and linearly interpolated onto each pixel's wavelength measurement. The uncapped-error bars are derived from the uncertainty in the degradation rate and *neglect* the systematic and statistical errors in the initial calibration. Thus, the large uncertainties in the degradation rate drives the error in the limb intensity profile.

2.3 Conclusions

From an aft-facing vantage on the ISS, the RAIDS EUVS provides a unique view into the energetic processes of the terrestrial ionosphere at low altitudes. The nominal mission started on 27 October 2009. Routine station keeping and docking operations on the ISS periodically prevented limb scans. Green days in Fig. 2.7 shows when the instrument was scanning normally and the hexadecimal key indicates which instruments were operating. During periods of normal operation, the orbital ephemeris was used to search for times when the EUVS passed over ground-based ionospheric observatories for instrument validation. Such comparison, using the 83.4 nm emission process as a probe of electron density, will be detailed in the next chapter.

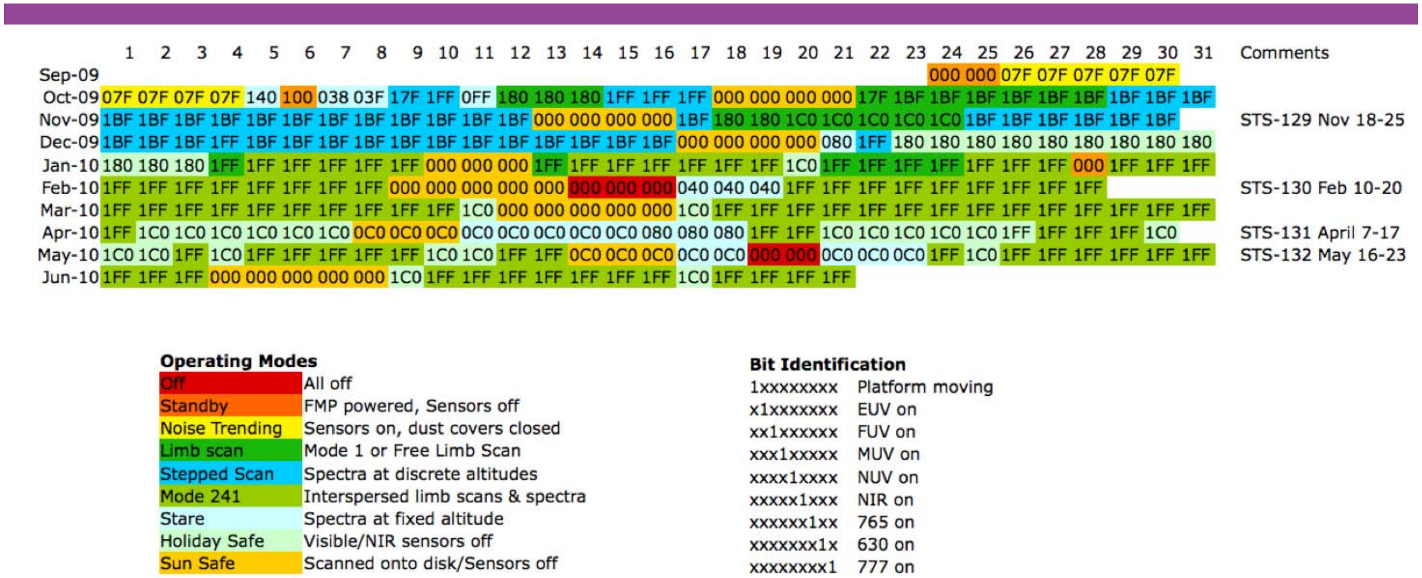

	1	2	3	4	5	6	7	8	9	10	11	12	13	14	15	16	17	18	19	20	21	22	23	24	25	26	27	28	29	30	31	Comments
Sep-09																								000	000	07F	07F	07F	07F	07F		
Oct-09	07F	07F	07F	07F	140	100	038	03F	17F	1FF	0FF	180	180	180	1FF	1FF	1FF	000	000	000	000	17F	1BF	1BF	1BF	1BF	1BF	1BF	1BF	1BF	1BF	
Nov-09	1BF	1BF	1BF	1BF	1BF	1BF	1BF	1BF	1BF	1BF	1BF	1BF	000	000	000	000	1BF	180	180	1C0	1C0	1C0	1C0	1C0	1BF	1BF	1BF	1BF	1BF	1BF		STS-129 Nov 18-25
Dec-09	1BF	1BF	1BF	1FF	1BF	1BF	1BF	1BF	1BF	1BF	1BF	1BF	1BF	1BF	1BF	1BF	000	000	000	000	080	1FF	180	180	180	180	180	180	180	180	180	
Jan-10	180	180	180	1FF	1FF	1FF	1FF	1FF	1FF	000	000	000	1FF	1FF	1FF	1FF	1FF	1FF	1FF	1C0	1FF	1FF	1FF	1FF	1FF	1FF	1FF	000	1FF	1FF	1FF	
Feb-10	1FF	1FF	1FF	1FF	1FF	1FF	1FF	1FF	000	000	000	000	000	000	000	000	040	040	040	1FF	1FF	1FF	1FF	1FF	1FF	1FF	1FF	1FF				STS-130 Feb 10-20
Mar-10	1FF	1FF	1FF	1FF	1FF	1FF	1FF	1FF	1FF	1FF	1C0	000	000	000	000	000	1C0	1FF	1FF	1FF	1FF	1FF	1FF	1FF	1FF	1FF	1FF	1FF	1FF	1FF	1FF	
Apr-10	1FF	1C0	1C0	1C0	1C0	1C0	1C0	0C0	0C0	0C0	0C0	0C0	0C0	0C0	0C0	080	080	080	1FF	1FF	1C0	1C0	1C0	1C0	1C0	1FF	1FF	1FF	1FF	1C0		STS-131 April 7-17
May-10	1C0	1C0	1FF	1C0	1FF	1FF	1FF	1FF	1FF	1C0	1C0	1FF	1FF	0C0	0C0	0C0	0C0	0C0	000	000	0C0	0C0	0C0	1FF	1C0	1FF	1FF	1FF	1FF	1FF	1FF	STS-132 May 16-23
Jun-10	1FF	1FF	1FF	000	000	000	000	000	1C0	1FF	1FF	1FF	1FF	1FF	1FF	1FF	1C0	1FF	1FF	1FF	1FF											

Operating Modes

Off	All off
Standby	FMP powered, Sensors off
Noise Trending	Sensors on, dust covers closed
Limb scan	Mode 1 or Free Limb Scan
Stepped Scan	Spectra at discrete altitudes
Mode 241	Interspersed limb scans & spectra
Stare	Spectra at fixed altitude
Holiday Safe	Visible/NIR sensors off
Sun Safe	Scanned onto disk/Sensors off

Bit Identification

1xxxxxxxx	Platform moving
x1xxxxxxx	EUV on
xx1xxxxxx	FUV on
xxx1xxxxx	MUV on
xxxx1xxxx	NUV on
xxxxx1xxx	NIR on
xxxxxx1xx	765 on
xxxxxxx1x	630 on
xxxxxxxx1	777 on

Fig. 2.7: RAIDS suite status matrix, as of June 2010, from the RAIDS Update newsletter (NRL, 2010).

Chapter 3

OII 83.4 nm emission as a measure of ionospheric electron density

This chapter describes the process by which 83.4 nm photons, generated by the ionization of neutral oxygen by sunlight and photoelectrons, resonantly scatter off O^+ ions and are imprinted with information regarding the distribution of ionized oxygen in a planetary atmosphere. This scattering is expected to reveal the distribution of O^+ in a process analogous to a thick mist illuminated from below. Comparison of RAIDS observations of O^+ emission scattering to forward models driven by ground-based radar measurements reveals the potential of the scattering process. An Marcov chain Monte Carlo (MCMC) parameter retrieval elucidates some of the limitations of this effect as a plasma remote sensing tool. Much of this analysis was previously presented in Douglas et al. (2012).

Measurement of the singly-ionized atomic oxygen spectroscopic state (OII) emission feature at 83.4 nm has the potential to allow global monitoring of ionospheric parameters in regions where the upper atmosphere is sunlit. This emission is among the brightest features in the terrestrial extreme ultraviolet (EUV) regime between 10 nm and 100 nm. Energetic solar photons (λ <45 nm) photoionize inner shell electrons of atomic oxygen via $O(^3P) + h\nu \rightarrow O^+(^4P) + e$ (Dalgarno et al., 1964), a process that peaks in the 150-175 km altitude range (Kumar et al., 1983; Anderson & Meier, 1985; McCoy et al., 1985). This leads to an 83.4 nm photon from the $2s^12p^4\ ^4P \rightarrow 2s^22p^3\ ^4S$ transition, an allowed triplet at 83.28 nm, 83.33 nm, and 83.45 nm. The emitted photon subsequently undergoes resonant scattering by ground-state O^+, the dominant ion in the F2 region of the ionosphere with a density profile that closely matches that of electrons. Fig. 3.1 shows the energy level diagram of oxygen with a ground-state neutral atom in the first column, a ground-state ion in the second column, and excited singly-ionized atoms in the remaining columns. The F2 layer is primarily composed of singly-ionized oxygen atoms and the peak density typically occurs at higher altitudes (200-500 km), setting up a separation between the photon production region and scattering region that allows these EUV photons to effectively illuminate the F2 region from below. Since the optical depth, τ, is on the order of 1-10 (Meier, 1991), scattering leads to an observable altitude profile of 83.4 nm airglow that depends on the O^+ ion density, and thus it is expected that the distribution of O^+ is retrievable via inversion of a measured airglow altitude profile (Carlson & Judge, 1973). Fig. 3.3 summarizes the scattering process, where photons generated at low altitudes from the ionization of neutrals, scatter off ionized oxygen at higher altitudes.

3.1 Transitions and scattering cross sections

This section will review the radiative transfer and interaction cross sections pertinent to a discussion of 83.4 nm emission. Following the treatment of Meier (1991), the volume excitation rate at a particular point $\mathbf{r}$, species is given by

$$j[\mathbf{r}] = n[\mathbf{r}]g[\mathbf{r}], \tag{3.1}$$

where $n[\mathbf{r}]$ is the density and $g[\mathbf{r}]$ is the excitation rate, which depends the excitation cross-section, σ and the incident solar photon flux $F_\odot(\mathbf{r}, \lambda)$ integrated over all wavelengths:

$$g[\mathbf{r}] = \int_0^\infty \sigma(\lambda)\pi F_\odot(\mathbf{r}, \lambda)d\lambda. \tag{3.2}$$

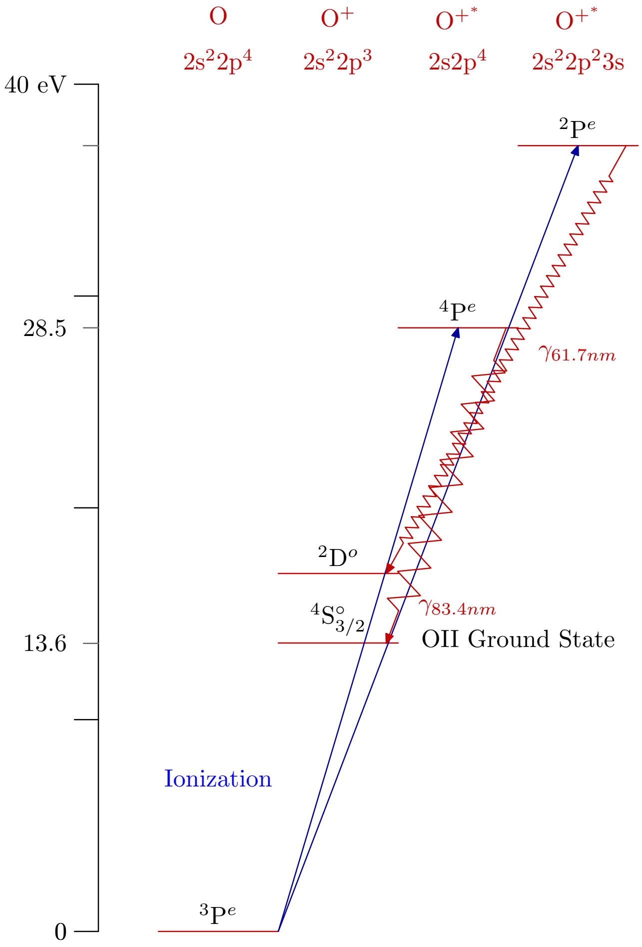

Fig. 3.1: Abridged energy level diagram for oxygen showing the 83.4 nm scattering process. Straight lines with arrows indicated ionization transitions while jagged lines with arrows indicate emission.

In our study of the 83.4 nm emission process, three classes of cross-section are of greatest importance: I) the ionization cross-section of neutral oxygen $\sigma(\lambda)$, shown in Fig. 3.2; II) the absorption cross-section of other atmospheric species, primarily molecular oxygen and nitrogen; and III) the scattering cross-section of O^+. The values of these cross-sections are summarized in Table 3.1 for each wavelength of the resonant scattering triplet.

The mean free path (l), the distance between scattering or absorption events, at a particular wavelength allows us to determine the important species in a radiative

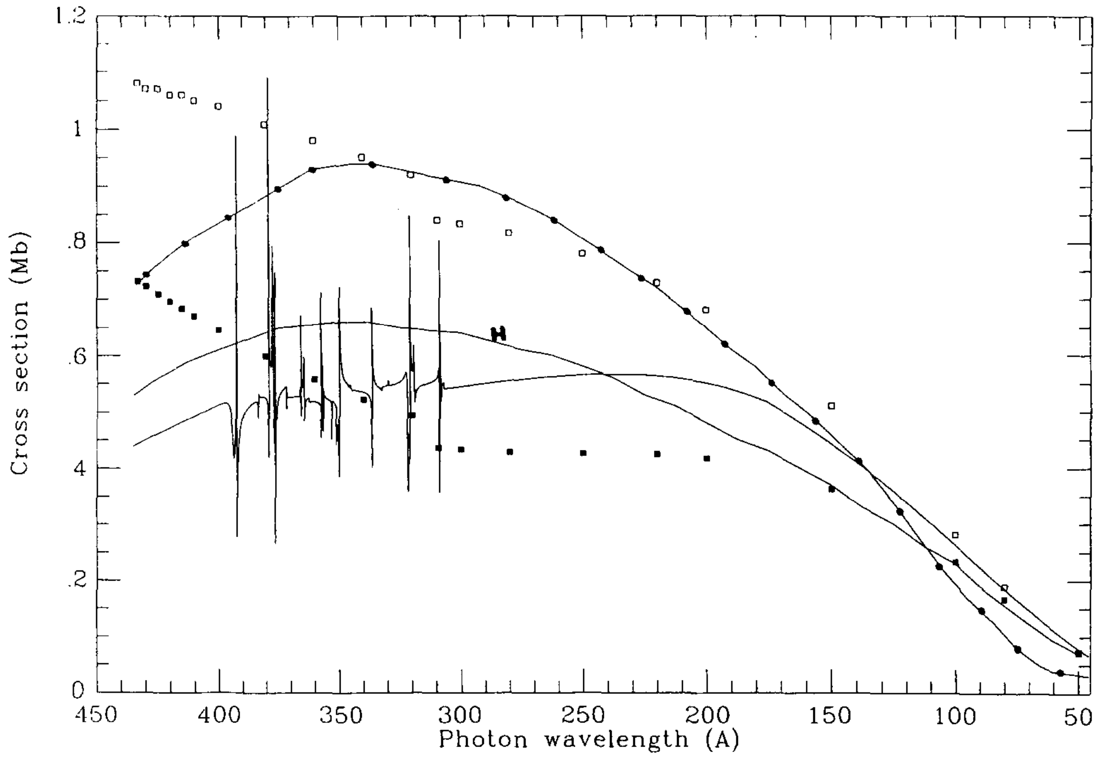

Fig. 3.2: Theoretical calculations of the photoionization cross-section of neutral oxygen left in the $2s^1 2p^4\ ^4\mathrm{P}$ state. The dominant solar emission driving this ionization process within the terrestrial atmosphere is the HeII 30.4 nm line (Woods et al., 1998). Reproduced from (Bell & Stafford, 1992, p. 1421) with data from Kirby et al. (1979); Henry (1967); Smith (1976).

Table 3.1: Cross-sections of important species at each of the resonant scattering wavelengths of the O^+ triplet. All cross sections are in units of megabarns (10^{-18}cm^2). Data from Link et al. (1994).

Constituent	σ(83.28 nm)	σ(83.33 nm)	σ(83.45 nm)
O^+ (scattering at 1000K)	1.68×10^5	1.12×10^5	5.61×10^4
O (absorption)	3.89	3.90	3.90
N_2 (absorption)	0.05	0.29	10.1
O_2 (absorption)	31.8	14.4	10.44

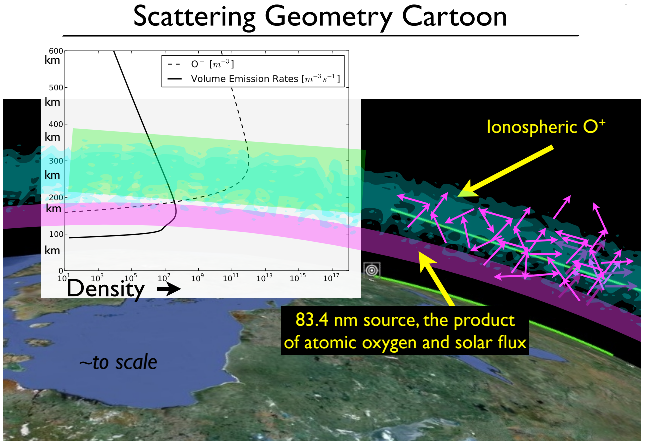

Map credit: Google Earth

Fig. 3.3: A cartoon of the O^+ 83.4 nm emission and scattering process showing generation of 83.4 nm photons at low altitudes by photoionization and their scattering off ionospheric O^+ atoms at higher in the thermosphere.

transfer process. The inverse of the mean free path, is the attenuation coefficient α, which is equal to the product of number density and cross section, $n\sigma$. For typical ionospheric conditions, at 83.4 nm the attenuation coefficients of molecular nitrogen and molecular oxygen are of order the scattering coefficient of O^+ at 200 km. Above this altitude scattering dominates, and below this altitude absorption tends to dominate. Thus, since the ionization which creates to 83.4 nm photons primarily occurs below 200 km, and the peak plasma density is typically above 200 km, both scattering and absorption processes must be accounted for in our radiative transfer model.

3.1.1 Coincident Millstone Hill Observations

After several months of operation a retrospective study was undertaken to find times when the RAIDS FOV passed over operating ISR facilities. Early in the mission, two coincident overflights of the Millstone Hill ISR (the tracks of which are mapped in Fig. 3.5) were found via a Madrigal database search of ISR for electron density profiles when RAIDS was recording EUVS limb scans.

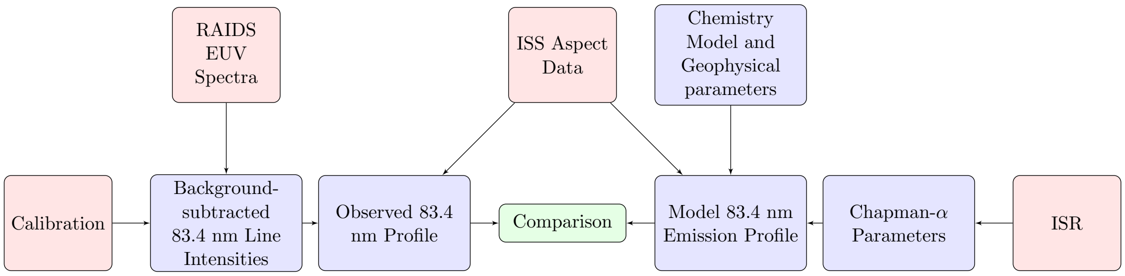

Fig. 3.4: Flow chart of procedure for comparison of ISR driven forward model to RAIDS EUVS 83.4 nm limb profiles. Reproduced from Douglas et al. (2012).

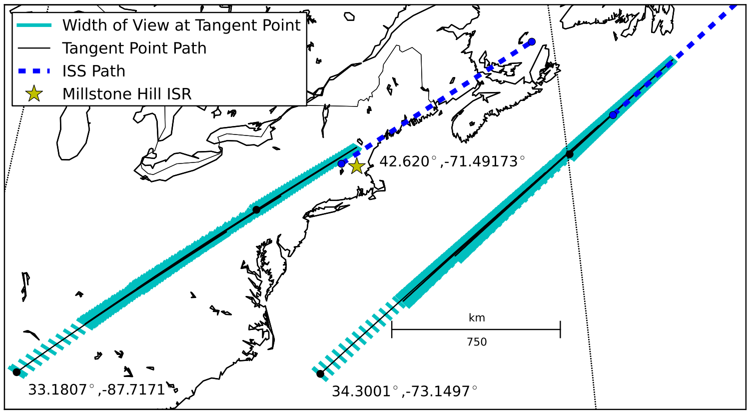

Fig. 3.5: The paths of the observed tangent point and the ISS ground track on 10 March (Left) and 15 January (Right) are indicated by dashed lines. The latitude and longitude of the furthest measurements and of the Millstone Hill Observatory Incoherent Scatter Radar are specified. The width of each bar corresponds the EUVS FOV width at the tangent point. Reproduced from Douglas et al. (2012).

3.1.2 Radiative Transfer Forward Model

The relation between O^+ density and measured limb profiles is a multifaceted and non-linear problem. The non-linearity is illustrated by Fig. 3.6, which in the left panel shows ionosphere models of increasing density with all other terms held constant and the corresponding emission profile on the right. As the plasma density increases, photons are scattered out of the line-of-sight and the total emission decreases until the profiles become nearly indistinguishable. Forward modeling this process has been the subject of numerous studies and the two forward models employed in this work to compute 83.4 nm emission profiles will be described subsequently.

Picone et al. (1997) describes the forward model of 83.4 nm emission developed at the Naval Research Laboratory (henceforth the NRL Model) and Vickers (1996) described an alternative matrix based radiative transfer model (henceforth the Matrix Model). The NRL model is detailed below and the Matrix Model will be discussed in Section 3.5 and applied to computationally intensive retrieval tests in Section 3.5.2.

The NRL model was used "as-is" for this study but highlights will be described below. Using the formalism of Picone et al. (1997) and following the comparable derivations in Anderson & Meier (1985) and Meier (1991), the NRL Model volume emission rate with scattering as a function of altitude (z) is:

$$j_k(z) = j_{0k}(z) + \sigma_{0k} N_{\mathrm{O}^+}(z) \int_{z_0}^{\infty} j_k(z') \mathrm{H}(|\tau_k' - \tau_k|, |t_k' - t_k|) dz' \tag{3.3}$$

$j_{0k}(z)$ is the initial source function, due to both resonant scattering of solar photons by O^+ and emission by inner shell ionization of neutral oxygen atoms. t is the pure absorption optical depth and τ is the pure scattering optical depth. Optical depth depends on the scattering cross section and the optical path $\vec{r'} - \vec{r}$. $\mathrm{H}[\vec{r'}, \vec{r}]$ is the probability a photon from dr' will be absorbed in a volume element dr, assuming isotropic scattering and Complete Frequency Redistribution (CFR). CFR assumes the incident frequency (within the broadened line shape) is independent of the output frequency, scattering with a classic Voigt profile (Rybicki & Lightman, 1979, p.291) and greatly simplifying the radiative transfer problem. CFR is a good assumption for a smoothly varying source function and optical depths less than $\tau \sim 200$ (Meier, 1991, p.47 and references therein). H is the plane parallel transport kernel, an approximation of the general Holstein probability function **G** (Holstein, 1947; Meier, 1991, p.50). This relation can be derived from the solution to the equation of radiative transfer and the conservation of photons, or the condition of radiative equilibrium – the emissivity of a volume must equal the sum of local production rate and the scattering rate (Strickland & Donahue, 1970, Equations 11-27): For the case of both resonant scattering and pure absorption, H takes the form:

$$\mathrm{H}(|\tau_k' - \tau_k|, |t_k' - t_k|) = \frac{1}{2\sqrt{\pi}} \int \phi(x)^2 E_1(|\tau - \tau'|\phi(x) + |t - t'|)dx \tag{3.4}$$

$\phi(x)$ is the lineshape as a function of x, the number of Doppler widths $(\Delta\nu)$ from line center frequency ν_0, that is: $x = (\nu - \nu_0)/(\Delta\nu)$. $E_1(x)$ is the first exponential integral (Abramowitz & Stegun, 2012):

$$E_1 = \int_1^\infty \frac{e^{-xt}dt}{t} = \int_x^\infty \frac{e^u du}{u} \tag{3.5}$$

The integral is solved by numerical integration as described in the Appendix of Picone et al. (1997). Given the volume emission rate, found by plugging Eq. 3.4 into Eq. 3.3, the column emission rate can be computed by integrating along a line-of-sight vector $(\hat{e})$:

$$4\pi I(\vec{r}, \hat{e}) = 10^{-6} j_k(z) \int \sum_k j_k[\vec{r}'(s)] T_k(\vec{r'}, \vec{r}) ds, \tag{3.6}$$

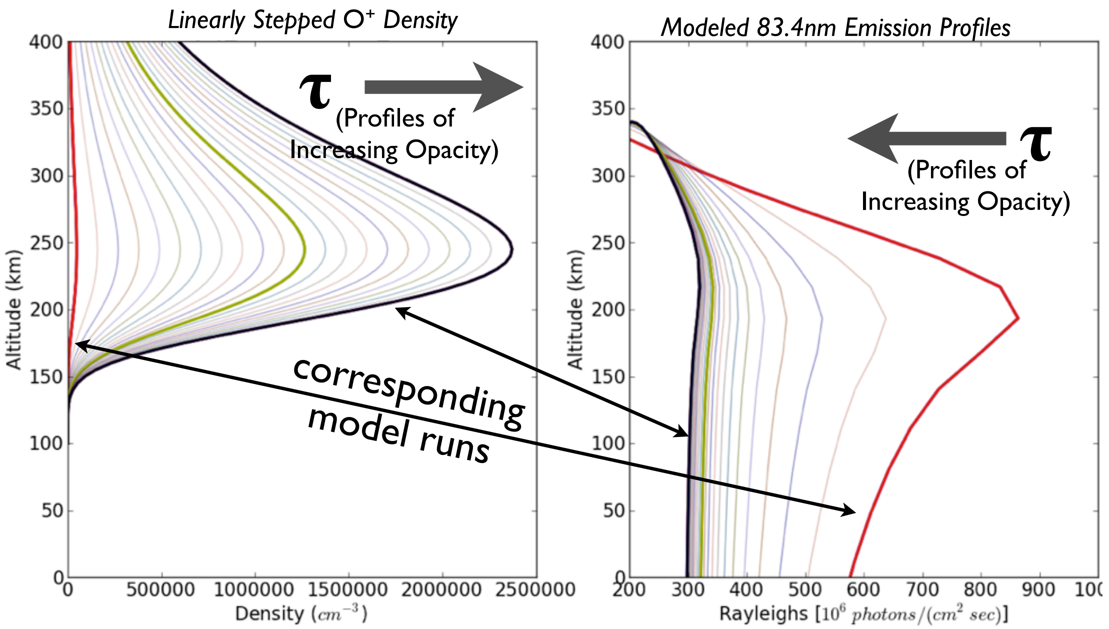

Fig. 3.6: Multiple scattering forward Matrix Model runs of 83.4 nm limb profiles (right), for ionospheric profiles of varying F2-Region Peak density (N_m) (left) with all other variables held constant.

where $T[\vec{r'},\vec{r}]$ is atmospheric transmission function, the probability of a photon from $\vec{r'}$ reaching the sensor at $\vec{r}$ rather than being absorbed or scattered. The radiance, I has units of megaphotons per cm^2 per second per steradian, multiplying it by 4π gives the column emission rate in units of Rayleighs (Hunten et al., 1956).

$$T_k[\vec{r'},\vec{r}] = \frac{1}{\sqrt{\pi}} \int \phi[x'] e^{-\tau[\vec{r'},\vec{r}]\phi[x']} e^{-t[\vec{r'},\vec{r}]} dx' \tag{3.7}$$

To get intensity, substitute the volume emission into Eq. 3.6 along with Eq. 3.7. Now that we have developed a model of scattering, we need a measurement of the density of O$^+$ to define the model scattering medium. While energy intensive to operate, ISR facilities provide “gold-standard” measurements of the both the topside and bottomside ionospheric plasma densities. The sequence of analysis which leads to the comparison of this ISR driven emission model with the RAIDS observation is summarized as a flow chart in Figure 3.4.

3.1.3 ISR measurement of Plasma Density

For the study intervals, the Millstone Hill ISR was operating a standard zenith profiling experiment using interleaved alternating and long pulse codes designed to monitor the E and F regions of the ionosphere. The alternating pulse is used in this analysis for its higher resolution in the lower ionosphere, where the signal-to-noise ratio is high. The alternating code measurements have characteristic time resolution of 4 minutes and altitude resolution of 4.5 to 58.5 km. Electron density, range (altitude), and associated statistical uncertainty from measurements processed by Millstone Hill's standard INSCAL ISR analysis program were obtained from the Madrigal database (Holt et al., 2006). There is an additional uncertainty in measured N_e of up to 10% arising from uncertainty in the ISR's calibration constant, which was not included in the calculations or figures.

In order to compare expected emission to the observed RAIDS emission profiles, a Chapman function (Section 1.1.2) was fit to ISR electron density measurements. ISR data was selected to span from the lowest observed tangent point to above the ISS orbit, altitudes (h) from 100 km to 390 km. While lacking physical processes such as diffusion, the analytical Chapman function provides a straightforward analytic representation of the ionospheric density profile. The simplest form of this function consists of three parameters, N_m, F2-Region Peak height (h_m), and scale height (H) as described by Risbeth & Garriott (1969). The Chapman-α function (Eq. 1.13) has the form:

$$N_e(z) = N_m e^{(\frac{1-z-e^{-z}}{2})} \tag{3.8}$$

Where

$$z(h) = \frac{h - h_m}{H} \tag{3.9}$$

This canonical function with three constant parameters has been preferred for inversion because it provides a well constrained function as discussed by Stephan et al. (2012). However, a five-parameter fit of a Chapman-α model with linearly varying scale heights on the top (A_1) and bottom (A_2) of the F2 profile provides a better fit to the ISR measurement, as it accounts for variations in diffusion rate and temperature with height (Fox, 1994). This function provides an excellent approximation of the variation in the constituent scale height and is tested and discussed extensively by Lei et al. (2004). The constant scale height H is replaced by the variable $H(h)$, where

$$H(h) = \begin{cases} A_1(h - h_m) + H_m & \text{if } h > h_m \\ A_2(h - h_m) + H_m & \text{if } h < h_m \end{cases} \tag{3.10}$$

Anderson et al. (1986) proposed a similar model with six free parameters; however, Fox (1994) found better results with Equation 3.10, which constrains the scale height to equal H_m at h_m. Since the goal was an accurate recovery of ionospheric density, the scale height, peak height and peak density were all left as free parameters. These two analytic functions were fit to ISR electron density measurements with statistical errors provided by the Madrigal database from the INSCAL incoherent scatter autocorrelation function analysis program. The fit was optimized using the Levenberg-Marquardt algorithm to minimize χ^2 in the Sherpa modeling and fitting application (Refsdal et al., 2011) in Python. Figures 3.7(a) and 3.7(d) compare the radar profile and the two Chapman-α models. The fits were performed on ISR electron density measurements in 10 km bins using the $\pm 1\sigma$ uncertainty in the electron density (represented by horizontal error bars). The range resolution of the ISR was not included in the fitting but is represented by vertical error bars for completeness. The five-parameter fit clearly exhibits better matching of the profile (reduced-$\chi^2 =$ 6.9 and 7.7 on 15 January and 10 March, respectively) on both days, recovering both

h_m and N_m, whereas the classic three-parameter Chapman$-\alpha$ fit recovers h_m to 10% but underestimates N_m by nearly 25% on 10 January 2011 and 35% on 15 March (reduced-$\chi^2 = 34$ and 56 on 15 January and 10 March, respectively).

3.1.4 MSIS Atmospheric Models

Equipped with species dependent ionization and scattering cross-sections and measurements of EUV emission and plasma density we still lack density profiles of neutral species necessary to complete our radiative transfer model of the 83.4 nm process. The MSIS empirical analytic model (Hedin et al., 1991; Picone et al., 2002) completes this picture using ISR measurements of temperature profiles to solve the equations of hydrostatic equilibrium as a function of latitude, longitude time, time season and space weather conditions for each the major thermospheric species. MSIS is valid from temperature and density boundary conditions set at an altitude of 120 km to the exobase. The NRL-MSIS model was used for forward modeling with the NRL Model (Picone et al., 2002) while the more accessible MSIS-90 model was used for retrieval studies with the Matrix Model (Hedin et al., 1991). While NRL-MSIS is based on an updated dataset, MSIS-90 provides largely comparable accuracy for the RAIDS observing altitudes and has been made readily accessible by Natalia Papitashvili and Dieter Bilitza via the Virtual Ionosphere, Thermosphere, Mesosphere Observatory (VITMO) at NASA Goddard[1].

3.2 Response Validation by comparison to Millstone Hill Incoherent Scatter Radar

This section describes the study presented in Douglas et al. (2012) which compared incoherent scatter radar driven forward modeling of 83.4 nm emission profiles

---

[1] `http://omniweb.gsfc.nasa.gov/vitmo/msis_vitmo.html`

Table 3.2: Observation Details for Millstone Hill Overflights. Reproduced from Douglas et al. (2012).

	15 January 2010	10 March 2010
Local time	13:59 to 14:02 UT	16:42 to 16:44 UT
Latitude	34.3° N to 45.6° N	33.2° N to 43.4° N
Longitude	-73.2° to -53.3°	-87.7° to -71.5°
Solar Zenith Angle	62.1° to 80.6°	64.1° to 79.9°
F10.7 Flux[a]	85	80
Ap Index[a]	3	7

---

[a] Information from the Space Weather Prediction Center, Boulder, CO, National Oceanic and Atmospheric Administration (NOAA), US Dept. of Commerce.

to RAIDS observations and showed a response in 83.4 nm emission to changes in ionospheric density but did not place constraints on the inverse problem.

The EUV observations analyzed here were collected on 15 January 2010 from 18:59:37.0 UT to 19:02:29.0 UT and 10 March 2010 from 21:42:9.0 UT to 21:44:32.0 UT. The range of observed tangent point Solar Zenith Angle (SZA)s in each period spans from 60 to 90 degrees. Details for each observation, including the position of the tangent point and geophysical parameters are shown in Table 1. During these RAIDS overflights, the line-of-sight tangent point passed within 500 km of the Millstone Hill ISR (i.e. within ~2.5 degree latitude or longitude), allowing for approximate comparisons of the observed column emission rate profiles to the expected column emission rate from "ground truth" measurements via modeling. F10.7 values were also comparable for these solar minimum times. This similarity in geophysical conditions leads one to expect that the observed EUV profile will be driven by changes in the F2 region profile. The tracks of the ISS and the RAIDS EUV line-of-sight tangent point are shown with respect to MIT Millstone Hill Observatory (Local Time = UT −5 hours) in Figure 3.5.

3.3 Results of Comparison to Forward Model

Calibrated observations and modeled emissions are shown as altitude profiles in Figure 3.8. The three-parameter fit constants were fed into the Picone model to compute expected 83.4 nm column emission rate, shown as a solid lines. The statistical uncertainty in the RAIDS data arising from Poisson noise and degradation is propagated through the averaging and background subtraction, with error bars representing the uncertainty in the observed emissions and the extent of vertical altitude bins.

The dashed lines represent the model output using the molecular fraction corrected O^+ profiles as an input, while the solid line represents a one-to-one electron to O^+ density relation and used the ISR electron density directly. On both days, the molecular fraction corrected model is comparable to the electron measurements at the certainty level of the RAIDS data. On 15 January, the increased difference between the profiles may be attributable to the particularly low h_m ($\sim 200km$), partially embedding the F2 region in the molecular ion layer. On both days measurements are consistently below both model output emission profiles and the morphology is comparable. Compounding calibration errors make this absolute column emission rate comparison difficult. The ISR electron density input has up to ±10% calibration error and significant range uncertainty. The EUV Spectrograph absolute calibration error is ±20%, and the degradation rate changes non-linearly with time, as it is driven by observing conditions and is negligible during times when the sensor is not in operation (Stephan et al., 2011). Moreover, the absolute scale of the modeled column emission rate profile depends on measurements of solar irradiance, and the total column density of neutrals.

To mitigate these uncertainties in the calibrated column emission rate and allow comparison of model and observations, the calibrated column emission rate was rescaled via a χ^2 fit of a constant factor to the modeled emission. These rescaled observations are shown in Figures 3.7 (b, c, e, and f). The rescaling factors for the three-parameter fed model, as a ratio of modeled Rayleigh per observed Rayleigh are 1.12±0.07 and 1.16±0.10 for 10 March. The five-parameter model rescaling factors, are 1.16±0.07 and 1.21±0.10 for 10 March. (These rescaling factors are within the absolute instrument calibration uncertainty.) On both days the topside profiles agree well and the overall shape is well approximated. The e-folding scale height on 15 January is clearly much shorter than on 10 March. Comparison of the two days shows that the observations are morphologically responsive to changes in ionospheric parameters as the observed shape closely tracks the expected emission profile, particularly on the topside. Low altitude emissions vary from one altitude to the next, however, the uncertainty in the column emission rate profiles preclude further interpretation of this possible variability.

Figure 3.7(b and e) show modeled emissions using each day's three-parameter Chapman-α fit as input. Figure 3.7(c and f) shows the result of modeling with five-parameter Chapman-α fits. Comparison of these profiles show that the three-parameter fit provides sufficient ionospheric information to generate a model which well approximates the 83.4 nm observations in shape. The differences in column emission rate between the three and five-parameter fit models are small compared to the observational $\pm 1\sigma$ error bars for these two solar minimum days. This is in agreement with the finding of Picone et al. (1997), that a constant ionospheric scale height is sufficient for 83.4 nm modeling. However, this study examined a narrow range of altitudes at low precision in solar quiet conditions. It is likely that higher precision measurements would be more accurately represented by a varying topside scale height.

3.4 Discussion of Forward Model Validation

The preceding sections demonstrated the sensitivity of the 83.4 nm scattering process to ionospheric parameters, indicating that it may be a practical means of recovering global ionospheric parameters during the daytime. Future observations of OII 83.4 nm airglow emission will serve to quantify the ionospheric plasma parameters, particularly the more infrequently measured topside profile, which have importance in ionosphere-magnetosphere coupling and satellite communications. As seen in Figure 3.7 and as discussed by Vickers (1996), the best-fit three-parameter Chapman-α function accurately captures the expected emission profile morphology. Additionally, despite the difficulties in calibration, the column emission rate profiles generated from forward modeling come within 21% of the calibrated observations (Figure 3.8). This approach shows considerable potential, especially considering the 10% calibration error of the ISR profile and the 20% calibration error of the EUV instrument. By adding free parameters, inversion to recover a five-parameter model would decrease the number of constraints on the uniqueness of an inverted model. However, the potential exists for constraining the inversion with bottom side sounding. The accuracy to which the topside was modeled and the insensitivity to low altitude density differences between O^+ and electron densities both suggest that the 83.4 nm is most sensitive to high altitude morphology and integrated plasma density. This result might be expected since the bulk of photons scattering off O^+ ions in the lower altitudes are obscured by absorption along the path to the sensor. Thus, besides its global coverage, RAIDS also provides an ideal complement to ground-based ionospheric radio sounding methods discussed previously which are limited to measuring bottomside densities in restricted geographic regions.

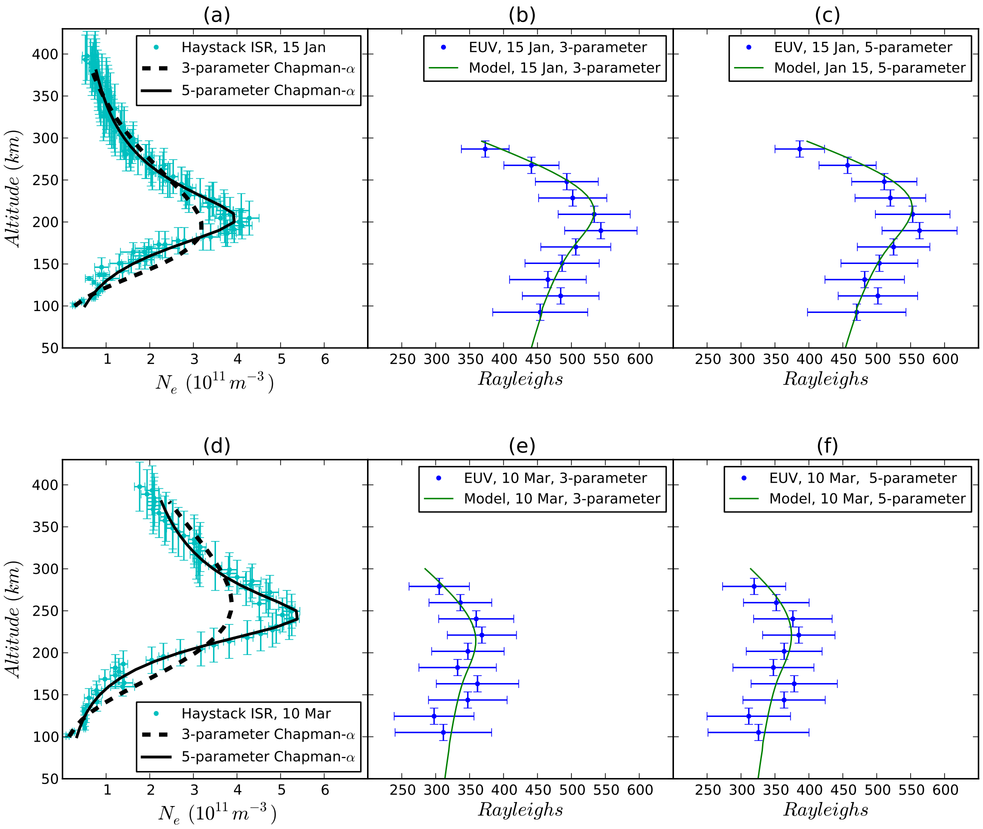

Fig. 3.7: (a) shows the Millstone Hill ISR electron density profile and Chapman-α fits on 15 January 2010. The three-parameter fits were used as the prescription ionospheric density profile in (b), which shows the observed 83.4 nm column emission rate and modeled profiles. The solid line represents modeled emission, using the Chapman-α profiles as inputs. The five-parameter fit was used as the prescription ionospheric density profile in (c). (d-f) are the same as (a-c) but for 10 March 2010. Reproduced from Douglas et al. (2012).

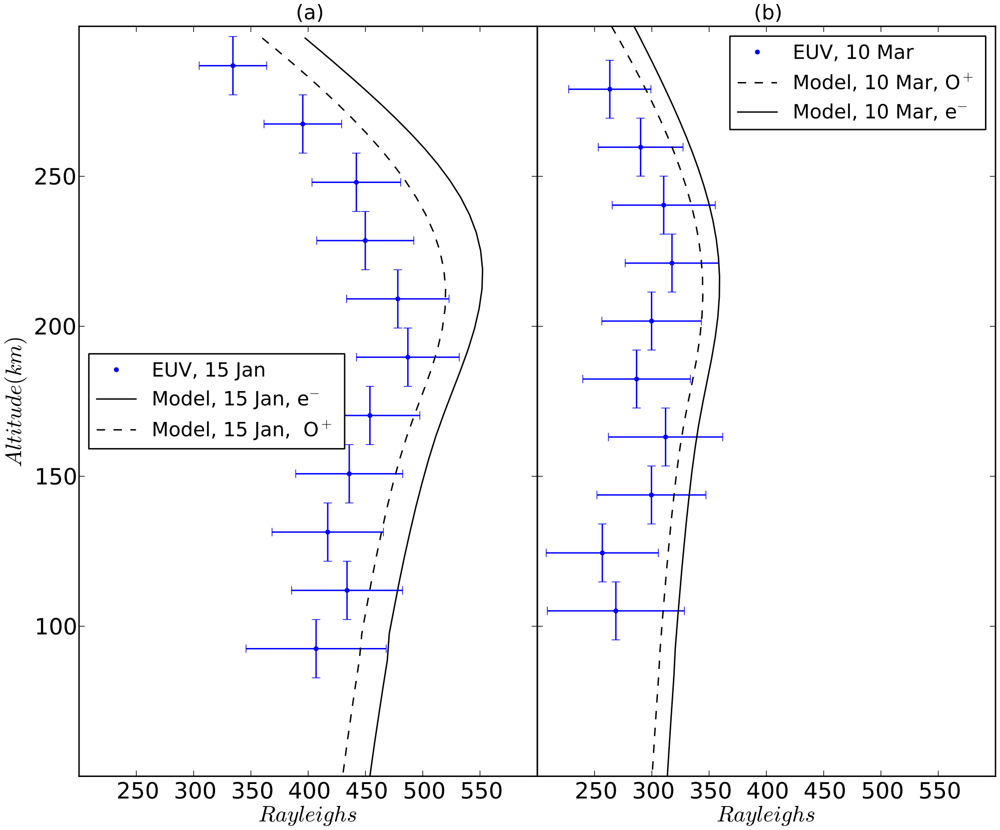

Fig. 3.8: The observed and modeled 83.4 nm column emission rate profiles. Error bars show 20 km altitude bins and the $\pm 1\sigma$ count statistics, degradation and calibration uncertainty in the EUV line measurements within each altitude bin. The solid line represents the electron density derived column emission rate profile, using the three-parameter Chapman-α ISR profiles as inputs. The dashed line represents the modeled emission profile adjusted to account for the expected differences between O^+ and electron density. Reproduced from Douglas et al. (2012).

3.5 Inversion of source and scattering

This section will discuss the uniqueness of inverting 83.4 nm emission to determine the scattering O^+ density profile. Given sufficient constraints, a unique O^+ density profile may be retrieved via radiative transfer analysis but prior studies (such as Vickers (1996); Picone et al. (1997); Picone (2008)) have not had multiple EUV profiles or ground truth measurements available. Modern computing power has also allowed a wide model parameter space to be more thoroughly explored. Various studies, (e.g. Kumar et al. (1983); Meier (1991); Link et al. (1994) and Picone et al. (1997)), have shown examples of expected observations for various scattering and absorption optical depths from different viewing geometries using comparable emission models. Picone et al. (1997) and Vickers (1996) both developed approaches to retrieve the ionospheric plasma density from 83.4 nm emission profiles. Picone et al. (1997) employed discrete inverse theory to determine a maximum likelihood by reducing χ^2 and assuming gaussian uncertainties in data and parameters. While providing a useful test of the forward model given ground truth, these two days were expected to be poor candidates for inverted retrieval of the ionospheric density from airglow observations, as Picone et al. (1997) found that for h_m below 300 km the uncertainty in retrieved parameters prevented a "unique" inversion. However, as will be shown subsequently, the information content of 83.4 nm limb profiles, even on solar minimum days, constrains the range of ionosphere morphologies.

3.5.1 Matrix Radiative Transfer Model

This section describes a computationally efficient multiple scattering matrix radiative transfer model applied to 83.4 nm emission by Vickers (1996). This approach follows from treating the radiative transfer problem as a Markov Chain process whose future behavior is independent of past events and which can be analytically discretized (Esposito & House, 1978). The matrix approach allows cross sections to vary as a function of altitude, thus relaxing the isothermal assumption of the NRL Model used in Picone et al. (1997) and Douglas et al. (2012).

The Matrix Model assumes each line of the triplet is independent with a Gaussian line shape and CFR. First I will define the initial conditions, the radiative transfer approach, and finally discuss an approach which treatments the radiative transfer problem as matrix multiplication of a viewing matrix on a vector of altitudes, producing a vector of angles, corresponding to spacecraft look direction.

Initial Conditions

The initial 83.4 nm source as a function of height, arising from solar photoionization and photoelectrons (j_0), is computed using AURIC (Strickland et al., 1999). AURIC is a photochemical model of upper atmospheric airglow emission from 80-1000 nm which calculates j_0 for each line of the OII 83.4 bm triplet seperately as function of geographical location, SZA, geomagnetic activity level (via daily mean Ap index), using F10.7 as a proxy for the solar EUV spectrum on the day of interest (Hinteregger et al., 1981). To calculate neutral molecular densities, we assume MSIS-90 atmospheric profiles (Hedin, 1991).

Scattering Matrices

Vickers (1996)[2], similarly to Esposito & House (1978), solved the equation of radiative transfer for a discrete grid of matrix cells and applied linear algebra techniques to simplify the computation of multiple scattering events. This section presents an abbreviated derivation following the notation of Vickers (1996) and Geddes et al. (2016, *submitted, JGR-Space Physics*) to highlight some of the key features of the

---

[2] as well as the unpublished manuscript, A matrix-based solution to radiative transfer within media of moderate optical depth, by J. S. Vickers and S. Chakrabarti

matrix approach. The single scattering matrix, $\mathbf{M_S}$, is a square matrix with dimensions corresponding to the number of altitude bins N. The elements of the single scattering matrix, m_{ij} (Vickers, 1996, eq. 4.31), correspond to the fraction of light scattered in altitude cell i from cell j, derived from the equation of radiative transfer assuming CFR, azimuthally constant scattering, and a single scattering albedo as function of altitude and frequency that includes absorption.

Multiplying a source function, S_0, of intensity as a function of altitude by $\mathbf{M_S}$ gives the distribution of photons after a single scattering event per cell. Vickers (1996) showed a multiple scattering matrix, $\mathbf{M_M}$ equals $(I - \mathbf{M_S})^{-1}$, by taking the limit for an infinite series of single scattering events where each single scattering matrix is less than one (conserving flux). Thus, the final distribution of emission with altitude is:

$$\vec{S_F} = \mathbf{M_M}\vec{S_0} = \begin{bmatrix} 1 - m_{00} & m_{10} & ... & m_{i0} \\ m_{01} & 1 - m_{11} & ... & m_{i1} \\ ... & ... & ... & ... \\ m_{0j} & m_{1j} & ... & 1 - m_{ij} \end{bmatrix}^{-1} \times \begin{bmatrix} I_0(z_0) \\ I_0(z_1) \\ I_0(...) \\ I_0(z_N) \end{bmatrix}$$

Viewing Matrix

If the viewing matrix is defined as $\mathbf{V}$, built up of elements v_{ij}, where i is the look direction (angle) and j is the altitude bin. Each altitude of $\mathbf{M_M}$ corresponds to a column of $\mathbf{V}$, but the number of look direction bins can be varied to match the instrument FOV and spatial resolution.

Each element is the attenuated integral of intensity along a zenith angle from the viewer. Multiplying the scattered source function by viewing matrix returns a vector of scattered light intensity as a function of SZA, $\mathbf{Z}$, for comparison to observations.

$$\vec{Z} = \mathbf{I}(SZA) = \mathbf{V}\mathbf{S_F} = \mathbf{V}\mathbf{M_M}\vec{S_0}$$

where $\mathbf{M_M}$ is the multiple scattering matrix, $\mathbf{V}$ is the viewing matrix and $\vec{S_0}$ is the source vector. It is necessary to repeat the radiative transfer computation for each of the triplet lines independently and sum their contributions, denoting lines by their last digit, 83.**2** nm, 83.**3** nm, and 83.**4** nm, the final weighted solution is: $\mathbf{Z_T} = \mathbf{Z_2} + \mathbf{Z_3} + \mathbf{Z_4}$. Which are statistically weighted by the probabilities of the transitions. Assuming equal production rates, $\mathbf{Z_4}$ for example, is given by

$$\mathbf{Z_4} = \mathbf{V_4}\mathbf{M_{M-4}}(\frac{6}{6+4+2}\vec{S_0})$$

These statistical weights are the multiplicity of quantum states $(2J + 1)$ where J is the total angular moment.

Vickers (1996) implemented this matrix based radiative transfer in the C programming language for a simple test case. In order to streamline comparison and parallelization, I wrapped Vickers (1996) implementations of the Matrix Model source code into Python functions using the Cython module (Behnel et al., 2011). These wrapped functions permit easy interaction with Python parallelization, statistics, and plotting libraries, thereby greatly streamlining analysis.

3.5.2 Uniqueness of the Inverted Profile

This section will describe my work implementing the Vickers (1996) model and quantifying the bounds on ionospheric density (in terms of Chapman parameters) placed by comparison of the model to RAIDS 83.4 nm limb profiles and Millstone Hill observations previously presented.

The Douglas et al. (2012) study comparing the NRL forward model to data for two limb profiles implied a causal relation between the ionospheric profile and the ionospheric plasma density. Thus, modulo a constant scaling factor, the forward model accurately described a probable state of the system. This forward model comparison, while useful, failed to measure the information content of our observation, merely illustrating the correlation between model and observation. To assess the information content of the example observations shown previously (Fig. 3.8) I implemented the *emcee* affine-invariant MCMC sampler (Foreman-Mackey et al., 2013). Since each radiative transfer calculation is computationally intensive, a short algorithm convergence time, minimizing the number of forward model runs is important for future efforts to parameterize the ionosphere in realtime via 83.4 nm observation. Goodman & Weare (2010) found a affine-invariant sampler which converges more rapidly than the more common Metropolis-Hastings MCMC method for skewed datasets where the likelihood is asymmetrical in parameter space. The *emcee* implementation of this algorithm is parallelized, which allowed straightforward computation on a multicore machine or cluster via IPython (Perez & Granger, 2007). Tests were performed on the Boston University Scientific Computing Cluster, an interface to the Massachusetts Green Computing Facility (Brown, 2012).

Bayesian Retrieval of Chapman Parameters

The Discrete Inverse Theory (DIT) approach of Picone et al. (1997) is a robust method to invert a physical system when uncertainties in model parameters and measurements are both approximately gaussian. However, given poor quality data or cases where significant non-linearities between data and model exist DIT or the iterative methods used by Vickers (1996) can retrieve a local minima or fail to converge.

Retrieval, the process of determining the likelihood of parameters in a physical model given a set of measurements, is an extensively studied topic in Bayesian statistics. An alternative to parametric retrieval via iteration often paired with Bayesian statistics, Monte Carlo techniques randomly sample a parameter space and thus are stable to anomalies and local minima (for a review of the history of Monte Carlo techniques in geophysics see Sambridge & Mosegaard (2002)). From Bayes law (MacKay, 2003) we can see the relation between probability of a hypothesis relates to the probability of a dataset:

$$P(H|E) = \frac{P(E|H)P(H)}{P(E)} \tag{3.11}$$

where $P(H|E)$ is the probability of the model or hypothesis given the evidence. $P(E|H)$ likelihood, or the probability of the evidence given the model. P(H) is the probability of the evidence, also known as the *prior*. P(E) is the marginal likelihood, a constant evidence for the model between evaluations. Thus, for a constant *prior* and a constant marginal likelihood, the set of parameters which maximize $P(E|H)$ represent the most probable realization of the physical model given the evidence.

Since the limb profile measurements are expected to be dominated by Poisson noise and the number of counts per bin is relatively large (> 100), we assume Gaussian errors for the measurements composing an 83.4 nm emission profile. Given a proposed three-parameter Chapman profile, $\hat{y}(z_i|N_m, H_m, h_m)$ we compute $P(E|H)$ from the set of N discrete intensities as a function of altitude $y(z_i)$ that makeup a limb profile by multiplying the probabilities of each data point given the model: (VanderPlas, 2014):

$$P(E|H) = \prod_{i=1}^{N} \frac{1}{\sqrt{2\pi\sigma_i^2}} \exp\left[-\frac{(y(z_i) - \hat{y}(z_i|N_m, H_m, h_m))^2}{2\sigma_i^2}\right] \tag{3.12}$$

This framework lends itself to random sampling of the Chapman parameters (N_M, H_m, and h_m) via MCMC – assessing the underlying probability distribution via many model realizations. *emcee* expects a log-likelihood, which we find by taking the natural logarithm of Eq. 3.12:

$$ln(P(E|H)) = -\frac{1}{2}\sum_{i}^{N}\left(\ln(2\pi\sigma_i^2) + \frac{[y_i - \hat{y}(z_i|N_M, H_m, h_m)]^2}{\sigma_i^2}\right) \tag{3.13}$$

While faster convergence could be expected with a *prior* based on solar conditions or ground-based measurements, we begin with the un-informed case of a uniform *prior* of Chapman parameters. The convergence time can be seen in Fig. 3.9 where the value of the Chapman-α parameters are shown for each walker as a function of step number. The *emcee* configuration used for retrieval is shown in Table 3.3. The total runtime was limited to 15 minutes due to system constraints, the configuration shown well sampled the parameter space with 26,400 forward models (the product of the number of walkers and the number of MCMC steps). The chosen time to convergence or "burn-in" is shown as a vertical dashed line, values preceding the burn-in time do not reflect the underlying distribution and were excluded from subsequent analysis. Fig. 3.13 shows 100 randomly drawn forward models after the burn-in time, showing each realization is a qualitatively plausible fit at the level of the forward models presented in Douglas et al. (2012). Figures 3.12 and 3.11 shows the posterior probability distributions for the same two observations as forward modeled from the Millstone Hill radar. In these "corner" plots (Foreman-Mackey et al., 2014) each histogram corresponds to a Chapman$-\alpha$ parameter and two-dimensional plots show show parameters plotted against each other. The ground-truth Millstone Hill ISR measurements of the corresponding Chapman-α parameters are shown as vertical lines in each histogram and intersecting lines in the density plots. Since there is a large uncertainty in the instrument calibration (see Section 2.2.2) the magnitude S_0 has been adjusted by an altitude constant scale factor such that peak of the retrieved N_m matches the ground-truth measurement. (While similar and analogous to rescaling the final profile in the forward model comparison, adjusting S_0 rather than the final profile is biased toward correction of the volume excitation rate than the instrument calibration). In the figures shown, the multiplicative scaling factor for the 15 January observation is 1.7 and on 10 March the scaling factor is 1.25. While manual rescaling prohibits the single dataset retrieval of all three Chapman parameters without an external calibration, it shows that $NmF2$ can be retrieved given h_mF2 or an external calibration. Thus, this observation provides information constraining the ionosphere to a range of scale heights and peak altitudes.

While a degeneracy between the probable peak height and peak density is clearly observed (first column, middle row of Figures 3.11 and 3.12) there is a well localized region of high probability slightly offset from the radar parameter peak for the 15 Jan 2010 dataset, while the scale-height (bottom row) is poorly constrained but peaked near the true value. With so few observations, it is not possible to definitively determine whether the distinct offset between retrieved values and ground based measurements is due to differences in the ionospheric volume space sampled by the ISR and RAIDS observations or deficiencies in the forward model. The more uniformly bright limb profile on 10 March 2010 provides less constraint on the probable scale height, implying the topside morphology (the decline in intensity at high altitudes visible on 15 Jan) drives the information content of the observation. An instrument which measures 83.4 nm emission at a wider range of tangent-point altitudes, either by observing from a higher altitude than the ISS (Geddes et al., 2015) or by slowly rotating (Cotton et al., 2000) would better constrain the morphology and narrow the retrieved parameter probabilities. However, the ISS provides a flexible and convenient platform for atmospheric studies and future missions are expected to share the RAIDS observing geometry. Thus, another means of breaking the degeneracy between Chapman parameters is required.

Table 3.3: *emcee* inputs used for retrieval tests. The walker number and step length were tuned to keep the runtime below 15 minutes while still achieving good coverage of parameter space. Runtime is for a *Intel(R) Xeon(R) CPU E5-2670 v2* at 2.50GHz with 10 cores and a maximum of 20 threads per core on the Boston University Scientific Computing Cluster-Lite at the Massachusetts Green High Performance Computing Center (MGHPCC) (Brown, 2012).

Parameter	Value
Dimensions	3
Walkers	48
Steps	550
n_{burn}	50
Typical Runtime [min.]	14.5
Threads	30
H Initial Guess range [km]	20-60
h_m Initial Guess range [km]	200-300
N_m initial Guess range [m^3]	$5 \times 10^7 - 5 \times 10^{11}$

3.5.3 Breaking the degeneracy between parameters

This section describes how lessons learned from the preceding studies of 83.4 nm limb profiles inform future work to better constrain ionospheric density profiles. Previous studies of 83.4 nm emission have emphasized the “uniqueness” of the ionospheric density retrieved in the narrow sense of whether a single “best-fit” exists and closely approximates the expected ionosphere. The best-fit approach breaks down for low-information content data such as the presented RAIDS EUVS profiles. The results of the preceding MCMC retrieval analysis of RAIDS data shows additional information is required under some conditions to constrain the retrieved ionosphere to the underlying physical parameters. A Bayesian approach permits integrative analysis of the ionosphere, maximizing the leverage of even a poor measurement via straightforward addition of data sources. External data sources could provide electron density priors, such as global ionospheric models (Schunk et al., 2004; Galkin

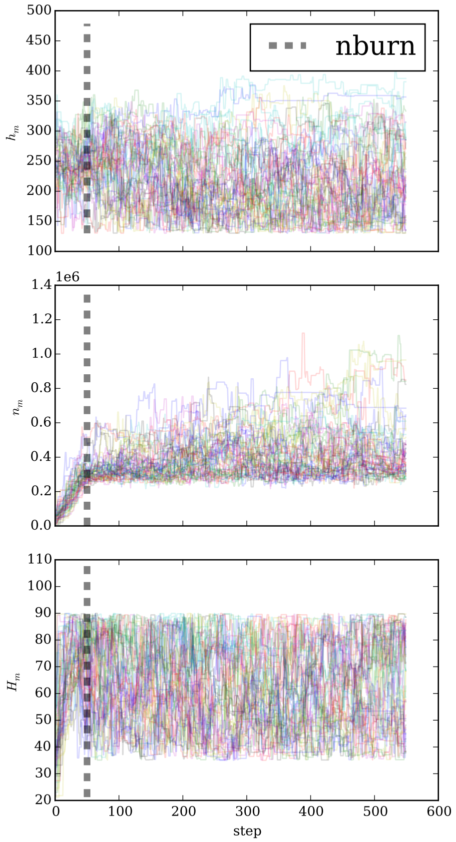

Fig. 3.9: Time evolution of Chapman-α parameters for each *emcee* walker while sampling the parameter space underlying the 15 January profile. For this example, N_m (Table 3.3) was underestimated, and the walkers can be clearly seen to rapidly climb towards the probable range of values. Model parameters prior to burn-in, indicated by a dashed vertical line, are excluded from subsequent probability density estimation.

et al., 2014, e.g.) or total electron content measurements from GPS (Rideout & Coster, 2006).

Improved Calibration and Higher Sensitivity Observations

Retrieval informed by external data sources suffer from mismatches in calibration, thus there is also an incentive to increase the information recovered from a single EUV measurement. The absolute calibration of the RAIDS instrument is of order twenty-percent (Stephan et al., 2009; Christensen et al., 1992) while MSIS neutral

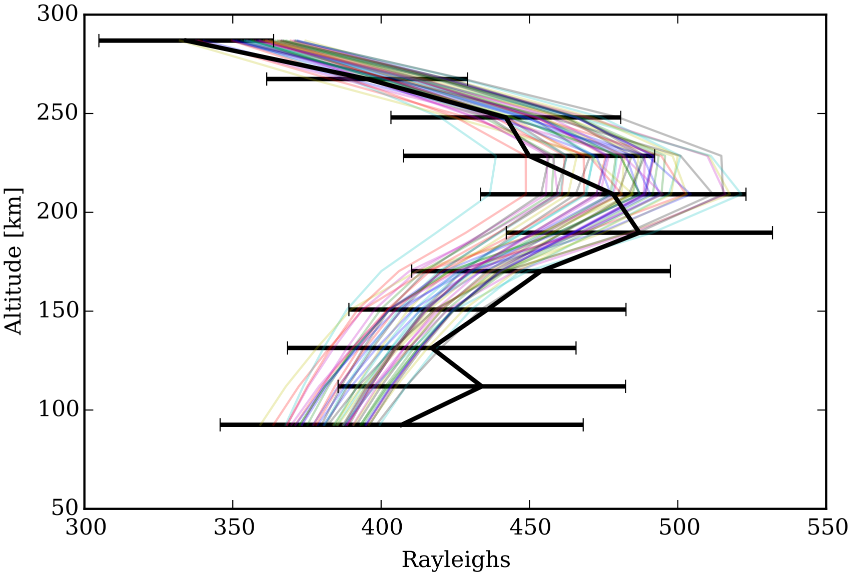

Fig. 3.10: Comparison of the 15 January profile with 100 randomly drawn forward models after burn-in of the MCMC sampler.

oxygen densities have uncertainties exceeding twenty-percent (Bennett & Omidvar, 2001). This uncertainty, coupled with uncertainty in the solar irradiance explains the difficulty in determining the source function intensity. As presented previously, forward modeling of RAIDS data found a calibration error of up to 21% (Douglas et al., 2012).

Whereas the RAIDS instrument is mounted on a nodding platform and measures one zenith angle per exposure, the soon-to-be-launched Limb-imaging Ionospheric and Thermospheric Extreme-ultraviolet Spectrograph (LITES) (Stephan et al., 2015) employs a toroidal Cotton spectrograph (Cotton et al., 1994) which allows continuous spectral observation of multiple zenith angles. This will increase the sensitivity to 83.4 nm emission by large factor and coupled with a higher sensitivity detector, LITES is expected provide an order of magnitude increase in sensitivity to 83.4 nm emission (Geddes et al., 2015). Assuming photon noise dominates the uncertainty of both RAIDS and LITES, the SNR will increase by $\sim \sqrt{10}$. Fig. 3.14 shows the effect

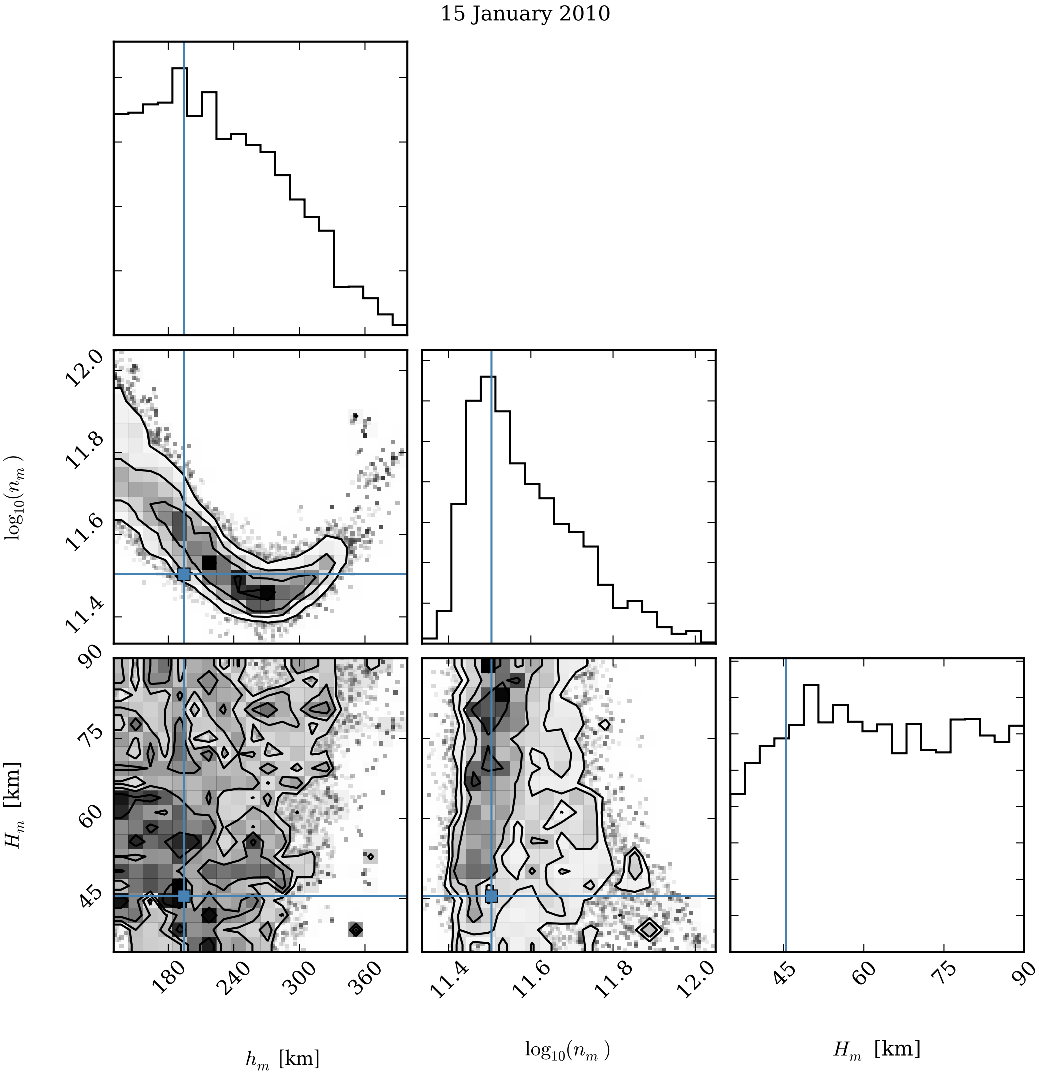

Fig. 3.11: Posterior probability distributions for a three-parameter Chapman-α ionosphere given the 15 January 2010 RAIDS EUVS profile illustrating the morphological information content of 83.4 nm emission profiles. Distributions were generated by *emcee* sampling of parameter space and forward modeling with the Matrix Model. Ground truth Millstone Hill ISR best-fit Chapman-α parameters are show as vertical lines in each histogram. The source function was rescaled by a constant multiplicative calibration factor until the plasma density approximated the ground truth ISR best-fit value from Douglas et al. (2012). (A rescaling factor of $1.7\times S_0$ was used to generate this figure). The plasma density vs. peak height relation is well constrained and the peak of the scale-height probability agrees well with the ground based measurement, but the uncertainties is large and the individual parameters are not uniquely determined.

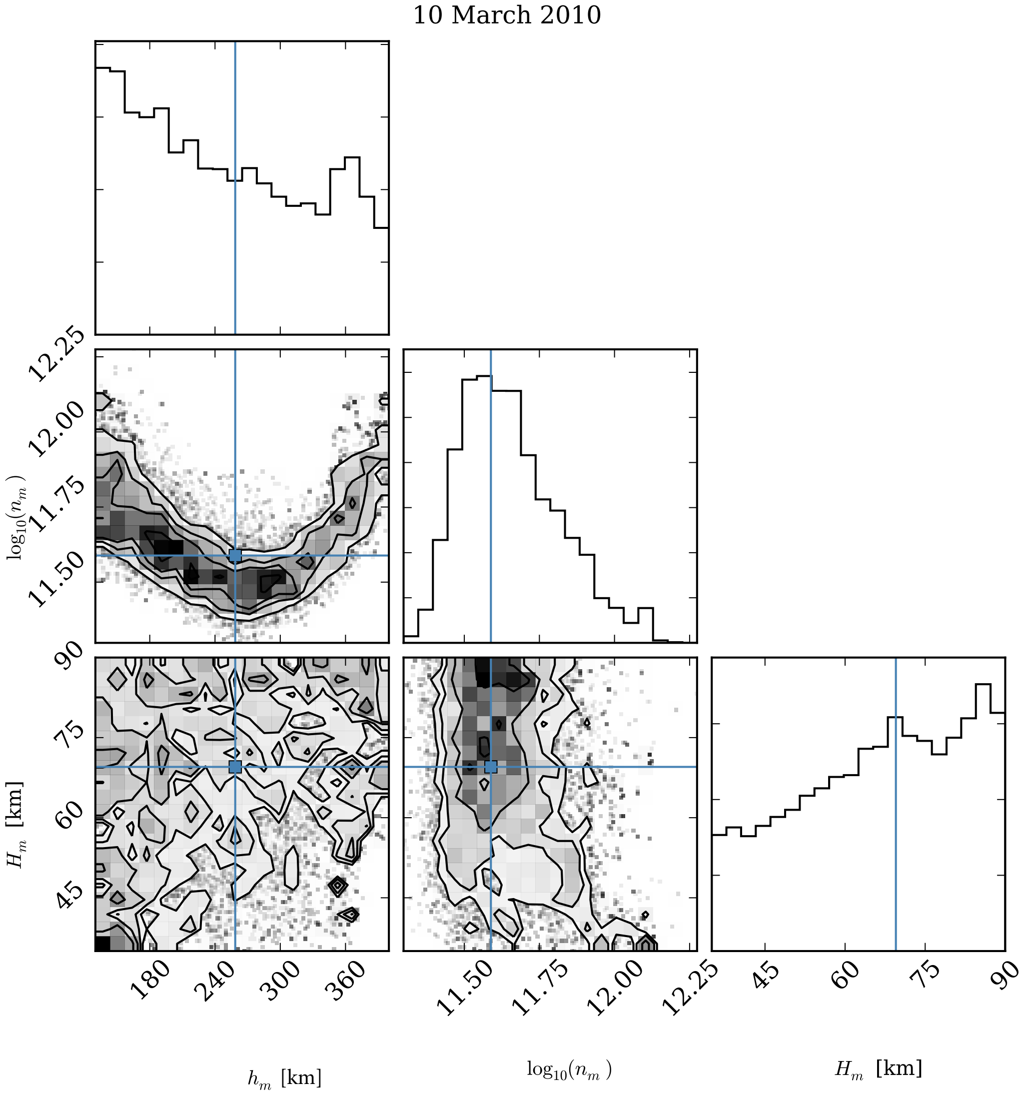

Fig. 3.12: The same as Fig. 3.11 for the 10 March 2010 Millstone Hill overflight and a $1.25\times S_0(z)$ adjustment of the source function, which is of order the instrument calibration error, neglecting the source function and neutral density uncertainties. While a peak height versus density relation is still visible, the flatter emission profile shows increased degeneracy with the equiprobability region poorly localized compared to the 10 January example and lacks a single peaks in the H or h_m probabilities across expected values.

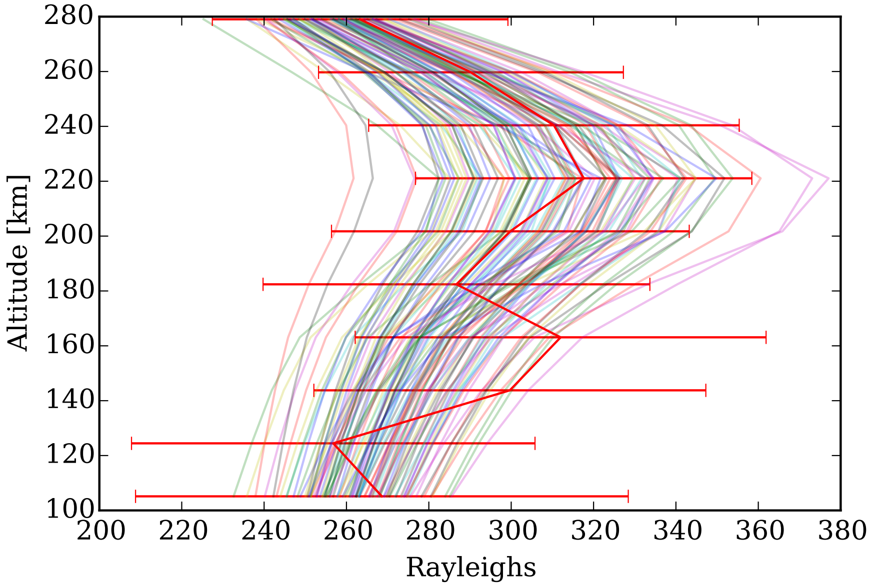

Fig. 3.13: Comparison of the 10 March limb profile with 100 randomly drawn forward models after burn-in of the MCMC sampler.

of decreasing the uncertainty in the RAIDS 10 Jan 2010 limb profiles observation by $\sqrt{10}$. Each Chapman parameter is well localized in probability density, without the extended degeneracy between parameters seen in Fig. 3.11 and the offset between retrieved values and ground based measurements mirrors that of the original retrieval.

The co-adding of RAIDS measurements to generate profiles requires including measurements over a wide geographic range. Thus, alternatively, the increased LITES sensitivity allows binning observations to SNR equal to that of RAIDS for increased spatial resolution. A LITES measurement of the same signal-to-noise as these RAIDS observation would cover a much shorter ground track and corresponding ionospheric volume, reducing the variability in measured emission rate due to small scale structure such as spread-F "bubbles" (Christensen et al., 2003).

The increased precision tightly constrains the morphology, suggesting value in revisiting the five-parameter Chapman$-\alpha$ with LITES but leaves open the questions of source function uncertainty and instrument absolute calibration. This uncertainty may be mitigated by observation of additional OII lines.

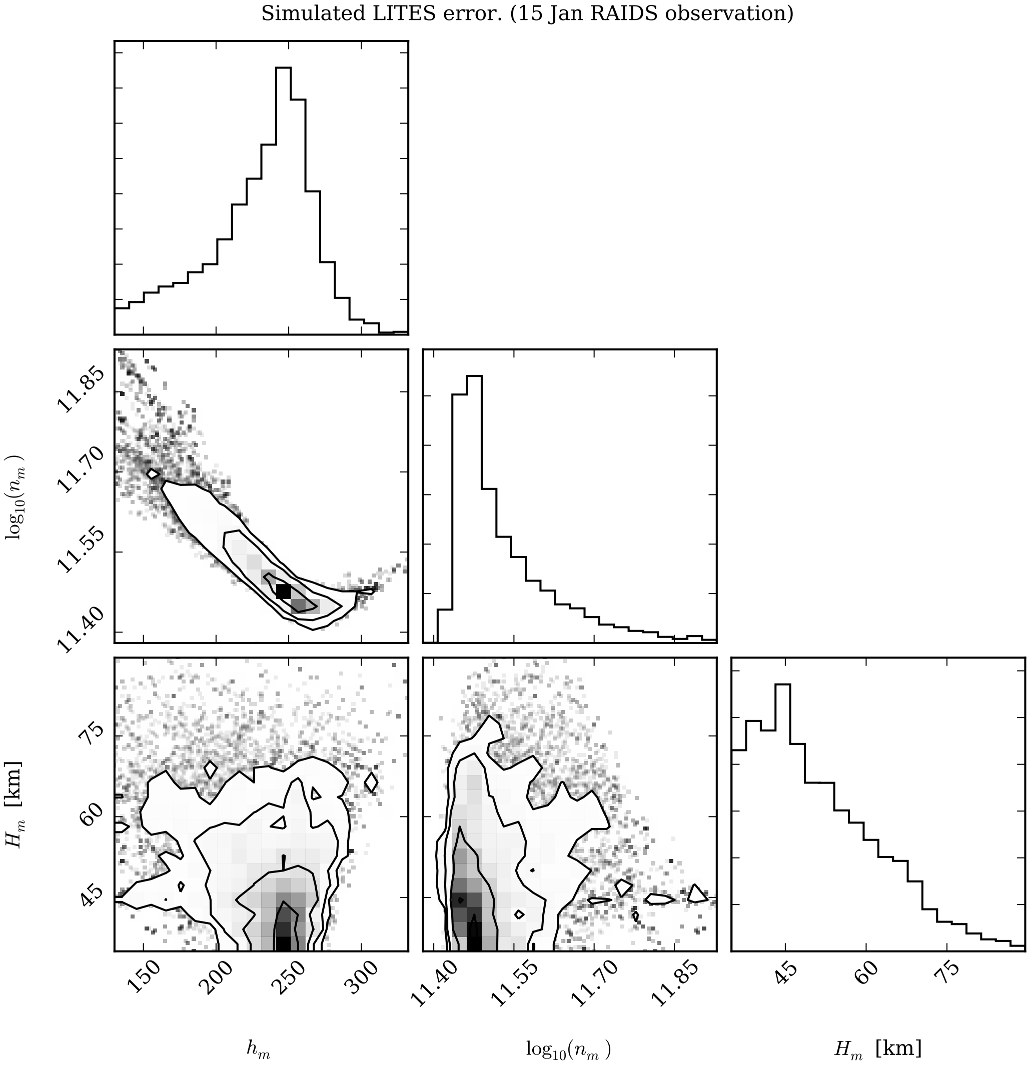

Fig. 3.14: The same as Fig. 3.11 with uncertainties in each limb measurement divided by $\sqrt{10}$ to simulate expected LITES sensitivity at 83.4 nm.

Observing other OII processes

Observation of OII 61.7 nm emission ($3s^2P \rightarrow 2p^3\ {}^2D$, Fig. 3.1) with LITES holds the potential to lessen the calibration uncertainty both the incident solar radiation and remove the assumption of an MSIS neutral oxygen density. This optically thin feature depends on the same ionization processes as 83.4 nm emission, solar radiation and photoelectrons (Stephan et al., 2012). However, unlike the 83.4 nm triplet, the 61.7 line nm is not an allowed transition from the ground state of O^+. Thus, 61.7 nm photons do not resonantly scatter off O^+ atoms. Since both processes originate from neutral, ground state oxygen atoms, the volume excitation rate can be treated as a constant. Furthermore, Stephan et al. (2012) assumed that the g-factor ($g[\mathbf{r}]$, Eq. 3.1) is approximately equal for the two processes. Using this assumption, coupled with knowledge of the lower atmospheric molecular densities and absorption cross sections (Conway, 1982; Link et al., 1994, tabulated in Stephan et al. (2012)), the volume emission rate of 61.7 nm allows estimation of the 83.4 nm source function volume emission rate without requiring an assumed solar flux or atomic oxygen profile. This approach still requires accurate specification of the neutral molecular density profiles to quantify the relative absorption at 61.7 nm and 83.4 nm, motivating further refinement of empirical neutral atmospheric models. While RAIDS observes 61.7 nm, the grating was in the long-wave position for the test observations presented previously. Thus, it is not possible to test this particular approach on these Millstone Hill overflights.

The upcoming LITES mission will not suffer from this lack of 61.7 nm observations and will continuously observe a wide EUV-FUV band, from 60-140 nm, simultaneously observing of OII 83.4 nm and 61.7 nm emission. Coupled with higher sensitivity, simultaneous observation of 61.7 nm should enable LITES to well retrieve ionospheric density profiles profiles.

Chapter 4

PICTURE: A Sounding Rocket for the Direct Imaging of Exozodiacal Light

Despite many indirect detections of extrasolar planets by radial velocity (RV) (Struve, 1952; Mayor & Queloz, 1995) and transit methods (Charbonneau et al., 2000), very few (∼2%[1]) have been directly imaged. While RV and transit measurements are highly informative, direct imaging is important to characterizing other worlds as it allows direct spectroscopy of emitted and reflected light. Additionally, since it does not rely on observing a candidate over multiple orbital periods, direct imaging greatly increases our discovery space to large orbital periods. With reflected light from Earth-sized rocky planets in stellar habitable zones approximately 10 orders of magnitude dimmer than light from parent stars, direct exoplanet imaging presents a significant technological challenge to the astronomical community. Further increasing the challenge of detecting planets, zodiacal light from dust in stellar systems (exozodi), contributes a significant background brightness. The Planet Imaging Concept Testbed Using a Rocket Experiment (PICTURE) is a sounding rocket payload to directly measure optical exozodiacal light scattered by the debris disk around nearby exoplanet candidate host star Epsilon Eridani (ϵ Eri), constraining

---

[1] 69 of 3422 confirmed planets imaged versus total confirmed, http://exoplanets.eu, 31 May 2016

the disk morphology and brightness, while placing limits on the future detection of exoplanets in this system.

4.1 PICTURE Experiment

The following sections describe the design and implementation of the PICTURE payload. PICTURE mission was devised to demonstrate a variety of technologies essential to future space exoplanet and exozodiacal science missions, including active wavefront correction, fine pointing, and high-contrast visible light coronagraphy with a Visible Nulling Coronagraph (VNC). Directly measuring $\phi_{exozodi}$ (Eq. 1.18) quantifies the scattered light background from exozodiacal dust which must be overcome to observe exoplanets around ϵ Eri at visible wavelengths.

The first PICTURE payload launched aboard National Aeronautics and Space Agency (NASA) sounding rocket 36.225 UG (the 225th Black Brant IX University Galactic Astronomy mission), on 8 October 2011 from White Sands Missile Range (WSMR) with an observing time on Rigel of up to 350 seconds (preset by timers on the payload shutter door)(Mendillo et al., 2012a,b; Hicks, 2012; Mendillo, 2013). This first flight suffered a telemetry failure approximately seventy seconds after launch. Data recorded onboard showed the fine pointing system (FPS) demonstrated first order adaptive optics (AO), allowing sensing and control of tip-tilt to approximately 5×10^{-3} arcseconds RMS (a 12 nm PV error across a 0.5 m telescope) at an update rate of 200 hz (Mendillo et al., 2012a). Unfortunately, limited wavefront sensor (WFS) data was transmitted before telemetry failure and no interference fringes were observed. A second mission, 36.293 UG, detailed herein and renamed PICTURE-B (Planet Imaging Coronagraphic Technology Using a Reconfigurable Experimental Base) re-flew the same payload with minor modifications in the fall of 2015 with the same science goals as the original flight.

The reflight includes several improvements, including a new deformable mirror and a state-of-the-art silicon carbide telescope primary mirror which was expected to provide improved image-stability from the laboratory to space.

This chapter's purpose is to demonstrate the PICTURE payload's efficacy: Section 4.1.1 motivates the imaging of scattered light as a test of the dust distribution measured via thermal emission. Section 4.2 describes the PICTURE VNC, Section 4.3 presents laboratory high-contrast imaging measurements of the interferometer. Section 4.4 presents surface measurement of the aligned telescope. Finally, 4.5 combines the telescope surface error, the measured VNC contrast and numerical modeling of a proposed exozodiacal dust ring around ϵ Eri to show that the science goals were within reach of the payload in a short sounding rocket flight.

4.1.1 Science Background

This section will describe the scientific impact of the PICTURE measurement of surface brightness and morphology at 600-750 nm of the ϵ Eri system between 1.5 AU and 20 AU. The close proximity of ϵ-Eridani (3.2 pc), a main sequence K2V star, with a particularly bright dust Spectral Energy Distribution (SED) make it the ideal candidate for a short sounding rocket observation. A thin, bright ring ($2\times10^{-4}L_*$) of "warm" ($\approx 150K$) dust is inferred at 3AU from excess infrared (IR) emission at 24μm (Section 1.2.4 and Backman et al., 2009). Testing for this ring and constraining the scattered light properties of this system address the primary science question of the PICTURE observations: *What is the distribution and brightness of scattered light (exozodi) in a nearby extrasolar system?*

The quantification of debris disks has both scientific and engineering ramifications. Scientifically, characterizing debris disk morphology and brightness illuminates the underlying processes in stellar system evolution and dust migration. As was discussed in 1.2.2, the surface brightness of zodiacal light also helps answer an engi-

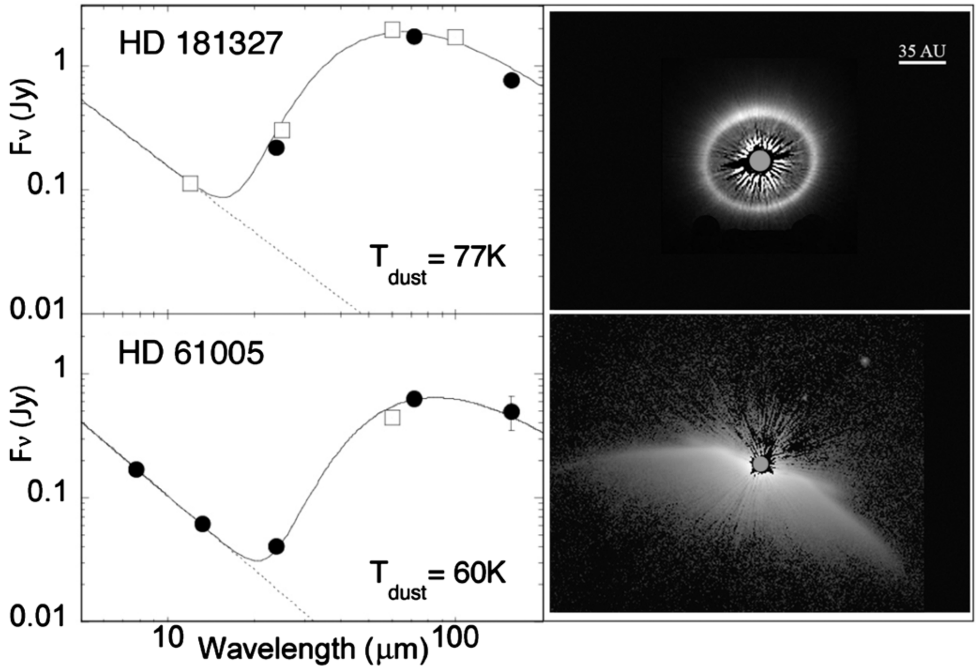

Fig. 4.1: Example of two debris disks with nearly identical infrared excesses (left) which exhibit radically different scattered light morphologies when imaged in scattered light with Hubble Space Telescope (HST) Space Telescope Imaging Spectrograph (STIS) (right). Temperatures are single temperature black body fits to the excess. Reproduced from Schneider et al. (2014).

neering question: what diameter of space-telescope is required to observe Earth-size exoplanets?

Exozodiacal dust levels increased by a factor of 10 times the solar zodiacal light would halve the exo-Earth detection rate for a 8m telescope with a visible light coronagraph (Stark et al., 2014, Fig. 9). Without knowledge of the dust emissivity, the equilibrium temperature derived from IR excess in the SED does not constrain the radial distribution of dust from a host star. For example, Fig. 4.1 from Schneider et al. (2014) shows two debris disks with similar SEDs and vastly different morphologies. Thus, high-contrast imaging of scattered light in nearby systems is necessary to constrain the telescope apertures needed to image rocky planets embedded in debris disks.

From ground-based observatories, the spatial distribution of dust is probed by IR imaging of dust grain thermal emission. Following on the thermal exozodiacal brightness limits placed on nearby stars by the Keck Interferometer Nuller (KIN) (Millan-Gabet et al., 2011), over the next several years the Large Binocular Telescope Inteferometer (LBTI), a two aperture nulling interferometer with a 22m baseline, will resolve thermal emission from exozodi as dim as 1/3 solar at scales of 0.4-1 Astronomical Unit [1.5e11 m] (AU) for stars 10 parsecs distant (Hinz, 2009). Kennedy et al. (2014) describes the LBTI team's model of exozodiacal thermal emission as a function of radius from the star (r) for a black body intensity, $B_\lambda(T)$:

$$S_{Thermal,\lambda}(r) = \frac{1\text{AU}^2}{1\text{pc}^2}\Sigma_M(r)B_\lambda(T), \tag{4.1}$$

with units of Jy/as^2 and one $\text{AU}^2\text{pc}^{-2} = 2.3504431 \times 10^{-11}$. Debris disks are generally assumed to be optically thin. For example, the solar zodiacal dust optical depth is 7.1×10^{-8} at 1 AU (Schneider, 2014). An optical depth analog, Σ_M (the measured "surface density of cross sectional area") could take many morphological forms: Kennedy et al. (2014) defines a radial power-law: $\Sigma_M(r) = \Sigma_{m,0}\left(r/r_0\right)^{-\alpha}$ in units of zodis, z, and r_0 is defined in terms of host star luminosity, $r_0 = \sqrt{L_* L_\odot^{-1}}$ AU.

$\Sigma_{m,0}$ is a normalization constant defined either by the integrated solar zodi brightness or the brightness at one AU. The LBTI team prefers the latter definition as an interferometer's central fringe may obscure the bulk of the exozodiacal emission in a general survey. These conventions may be equivalent in the ϵ Eri system, where the bulk of the inner dust population is predicted to be well outside of 1 AU.

More realistic "gray-body" dust grains with emissivity < 1 will not be at the equilibrium temperature but will still follow the same functional form while emitting at higher temperatures than ideal blackbodies and increasing the orbital radius of a debris disk (see Section 1.2.3).

In the simple case of a wavelength and grain independent albedo, ω, the thermally measured surface density, Σ_M, is related to the true optical depth by: $\Sigma_M = \Sigma_{True}[1 - \omega]$. (Debris disk optical depths range from the solar zodiacal dust and Edgeworth-Kuiper belt (EKB) at $\tau < 10^{-6}$ to $\tau \sim 10^{-4}$ for β-Pictoris). Given an assumed visible light albedo and a map of thermal emission, the scattered light intensity can be found:

$$S_{Scat,\lambda}(r) = \frac{F_{*,\lambda}}{4\pi} \left(\frac{r}{d}\right)^2 \omega \Sigma_{True}(r). \tag{4.2}$$

$F_{*,\lambda}$ is the parent star flux and d is the distance from Earth. Thus, direct images of scattered light at visible wavelengths coupled with future LBTI observations of $S_{Thermal}$ provide a test of this relation by directly measuring the intensity of scattered light for a particular system. The resulting relation between visible light and thermal emission would be extensible from ϵ Eri to other systems with similar dust properties.

4.2 Visible Nulling Coronagraph

4.2.1 PICTURE Instrument

High-contrast imaging from space requires the advancement of a variety of technologies, including active wavefront control, precision pointing and coronagraphic starlight suppression at visible wavelegnths. The PICTURE mission matures these technologies via a brief suborbital flight of a VNC with a phase shifting wavefront sensing system and fast steering mirror.

The PICTURE payload was designed and built as a collaboration between Boston University, the Massachusetts Institute of Technology, and the Jet Propulsion Laboratory (JPL). The VNC was assembled at JPL Rao et al. (2008). The nuller is a thermally ultra-low expansion (ULE) glass “sandwich," the optical components permanently bonded between two parallel plates of ULE. Fig. 4.2 shows a schematic of the nuller assembly and a photograph with the optical schematic overlaid. Samuele et al. (2007) and Rao et al. (2008) describe instrument prototyping, optical layout, and laboratory measurements prior to payload integration. Mendillo et al. (2012b) describe the original PICTURE sounding payload architecture, the active-wavefront control system, and the telemetry failure during the first launch in October 2011 – which precluded the collection of science data. The milliarcsecond pointing system was successfully demonstrated during the flight (Mendillo et al., 2012a).

Following the initial launch at WSMR, the payload was recovered, refurbished and tested. The following sections will describe the post-flight performance tests conducted at the University of Massachusetts Lowell in preparation for the second sounding rocket flight of PICTURE in Nov. 2015. The next platform for the PICTURE VNC is currently under construction, a stratospheric balloon with an unobscured telescope of similar aperture (Cook et al., 2015).

4.2.2 Optical layout

In laboratory testing, the VNC was fed by the fore-optics from the sounding rocket payload (Fig. 4.3) with a retro-reflecting spherical mirror replacing the telescope. Fig. 4.2 shows the VNC layout after low-order wavefront correction and beam compression. After the compressor optics, the collimated VNC input beam diameter is approximately one centimeter. First, a dichroic short-pass filter transmits light shortward of 600 nm to the Angle Tracker (AT) CCD. The first 50/50 beamsplitter (labeled 1) separates the beam into two arms. A series of mirrors in a bow-tie pattern offset the beams by 0.3 aperture diameters ($0.3D$), giving a 15 cm baseline. Given this shear, the effective baseline of the interferometer, we define the Inner Working Angle (IWA) as $1.7\lambda/D$, the angle from the first dark fringe to the first bright fringe

Fig. 4.2: A schematic and photograph of the PICTURE nuller showing the path of light through the instrument. Light shortward of 600 nm passes through the first dichroic beamsplitter to the angle tracker (AT), while long wavelengths are split into to interferometer arms (1), which are phase matched by the PZT and deformable mirror. The recombined beam (2) is split again by a 50/50 beamsplitter (3), one arm going to the wavefront control system (WFCS) imaging the pupil plane, and the other to the science camera (SCI) assembly, not shown, which focuses light onto a charge-coupled device (CCD) and rejects light longward of 750 nm.

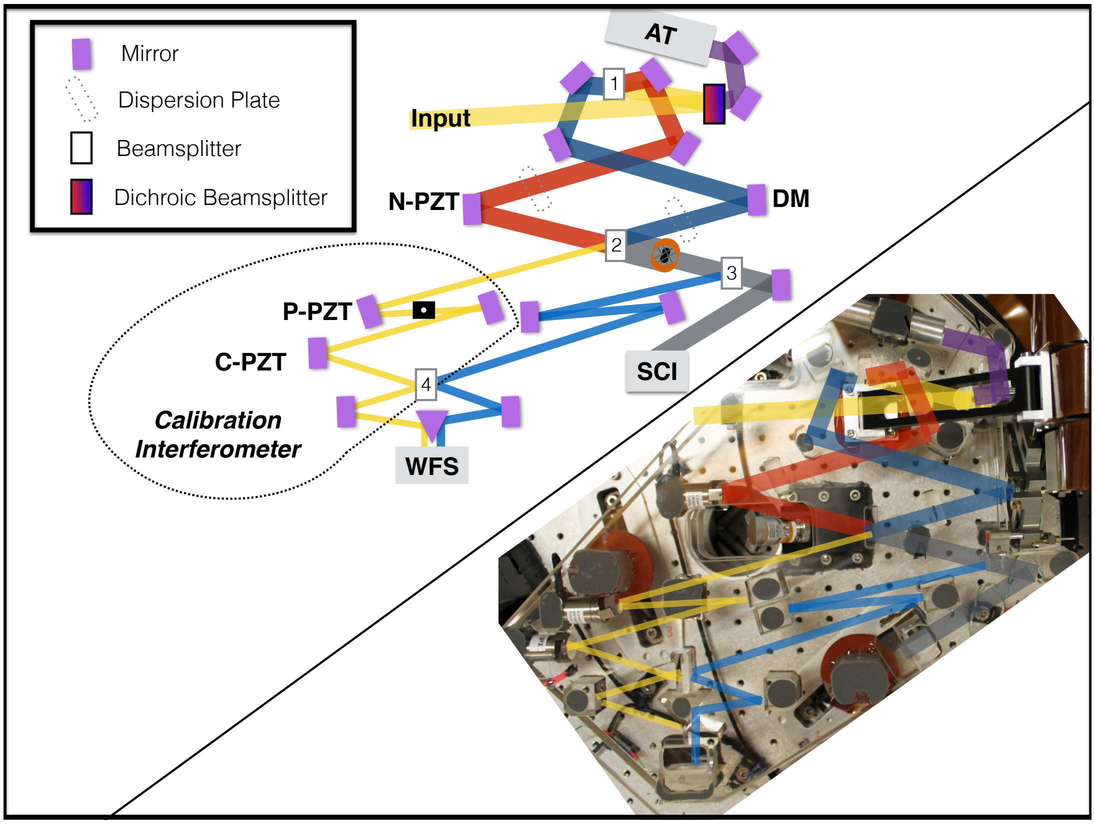

along the axis normal to the fringe direction (Mendillo, 2013). In a reflective Lateral Shearing Interferometer (LSI) design, the phase delay of the two arms can only be offset by π at a single wavelength. In order to operate over a broad band of "white light", the PICTURE nuller employs 10.0 mm dispersive phase plates (dotted rectangles) in each arm, before the active mirrors, which act to normalize the pathlength across a range of wavelengths – analogously to an achromatic lens. The optical path difference (OPD) between these plates, set by introducing a tilt relative to the optical axis, allows first order correction of the linear dependence of pathlength on wavelength (Morgan et al., 2003). At the recombining beamsplitter (2), the bright fringe is transmitted to the calibration interferometer (Wallace et al., 2006), whose optics are enclosed by the dashed line in the lower left and which was not employed in this work. A Lyot mask in the dark output blocks transmission of light from outside the pupil overlap region. The masked beam is finally split by another 50/50 beamsplitter (3) between the pupil imaging wavefront sensor and the science camera. Short-pass filters before the wavefront sensor (WFS) and science (SCI) cameras block wavelengths longward of 750 nm, combined with this input dichroic, this sets the science bandwidth to 22% of the central wavelength (675 nm).

4.2.3 Cameras

The WFS and SCI cameras both incorporate CCD cameras developed for the Astro-E2 X-ray Imaging Spectrometer (Bautz et al., 2004). These 1024 x 1024 pixel MIT Lincoln Laboratory model CCID41 detectors are cryogenically cooled with liquid nitrogen to $-70\,^{\circ}$C and provide low read and dark noise levels, essential to the short observing times available to the PICTURE sounding rocket. The camera plate scale is 0.57 λ/D/px, or 0.16 arcseconds/px for a 0.5 m telescope at 675 nm.

In order to allow short exposure times, only small subregions are read-out from each camera. The WFS readout area is 76x76 px and the science detector readout area is 138x138 px. The measured RMS read noise rate is 2.3 e^- /px/exposure. The cooled dark noise levels approach 1 e^-/s/px at flight temperatures. The laboratory noise rate is increased by time varying video crosstalk noise from cable extensions required for pre-integration testing and is visible as diagonal striations in both panels of Fig. 4.6.

4.2.4 Active Wavefront Control

Wavefront errors (WFE) between the two beams in the interferometer arise from spatial variations in optical path and amplitude in both the input beam before shearing (i.e. telescope optical errors) and between the two arms after shearing. Minimization of WFE is essential to minimizing leakage of light at the recombining beamsplitter and thereby maximizing contrast. Two active elements control phase error ($\Delta\phi$). In the left arm of Fig. 4.2 a flat mirror mounted on the Nuller Piezo Electric Transducer (NPZT) corrects tip, tilt, and piston. In the right arm, higher order phase errors are corrected by a first-generation Boston Micromachines Kilo-DM, a square 32 x 32 actuator microelectromechanical systems (MEMS) deformable mirror (DM) with a $340\mu m$ pitch across a continuous polysilicon phase sheet.

Amplitude errors are not actively controlled in the PICTURE VNC; however, the deformable mirror and NPZT mirror were coated as a pair to minimize amplitude mismatch to below 1%. Before nulling, the WFCS performs the calibration sequence described in Mendillo et al. (2012b) to align the system and correct for wavefront errors. After calibration, the PICTURE WFCS corrects path length differences at DM-controllable spatial frequencies (below one-half the actuator frequency, f_a) via a closed loop. The NPZT steps through four relative phase shifts: 0, $\pi/2$, π, $3\pi/2$. The WFS records an image at each position. The slope between these intensities allows measurement of the phase error in the pupil plane (Wyant, 1975) and is given as

$$\Delta\phi = tan^{-1}\left(\frac{I(0) - I(\pi)}{I(\pi/2) - I(3\pi/2)}\right). \tag{4.3}$$

This provides an error signal to drive the DM actuator pistons until the wavefront error converges to a minimum limited by the actuator print-through wavefront error of the deformable mirror ($\sigma \approx 13$ nm) and control loop noise.

4.3 Laboratory Measurements

Subsequent sections will describe the integration and testing of the refurbished PICTURE VNC at the Lowell Center for Space Science and Technology at UMass Lowell and the fabrication and testing of a lightweight 0.5 meter silicon carbide primary mirror in collaboration with AOA Xinetics/Northrop Grumman. The PICTURE nuller was designed by JPL as a demonstration instrument for the Terrestrial Planet Finder Coronagraph (TPF-C) mission to provide starlight suppression ("null depth") at levels below 10^{-4} (Rao et al., 2008). These laboratory measurements will assess flight instrument performance in a vibration isolated, thermally controlled environment, which was not available before the first flight. Pre-flight measurements include instrument thermal sensitivity, wavefront and science CCD noise levels, wavefront error correction and broadband nulling contrast.

4.3.1 Refurbishment

The cabling to the DM was damaged during the assembly of the payload for the first flight of PICTURE and new polyimide flex cable assembly was manufactured and installed along with a new Kilo-DM (S.N. 11W310#002). Manufacturing irregularities during the forging of the polysilicon MEMS can lead to unresponsive mirror elements. However, MEMS DM actuator yield has improved greatly: early Kilo-DM models had yield as low as 96.9% (Evans et al., 2006), whereas this new DM has only two inactive actuators ($\sim$ 99.8% active). Fortunately, both were positioned behind the Lyot mask allowing active phase control across the entire output pupil.

4.3.2 VNC Testing Setup

The VNC was tested on a vibration suppressing pneumatic optical table and inside an opaque acrylic glass enclosure to minimize air currents and background light. Room air filtration minimized dust to between Class 1,000 and 10,0000. Fig. 4.3 shows a schematic of the fore-optics used to feed the nuller. An NKT model NL-1.4-775-945 single mode crystal fiber with a manufacturer specified mode-field-diameter of 1.36 μm provides an starlike laboratory light source with a small angular size (FWHM $\approx$ 0.026”). The fiber tip is placed in the image plane of the telescope facing away from the instrument. A 150mm focal length spherical mirror is used in place of the telescope, functioning as a retroreflector, returning the beam to the image plane where it is collimated by an off-axis-parabola (OAP1). This mirror functions as the telescope tertiary mirror in the flight configuration and re-images the telescope pupil to the Fast Steering Mirror (FSM) – a piezoelectic tip-tilt mirror that maintains fine pointing control (Mendillo et al., 2012a). Compressor optics following the FSM (OAP 2 - OAP 3) decrease the beam diameter to match the deformable mirror active area.

Fig. 4.3: Schematic of the fore-optics used during laboratory testing of the nuller. The input fiber and retroreflecting spherical mirror simulate a star from an f/12.3 telescope. Both the tertiary (OAP1) and compressor optics are the flight fore-optics from the sounding rocket payload.

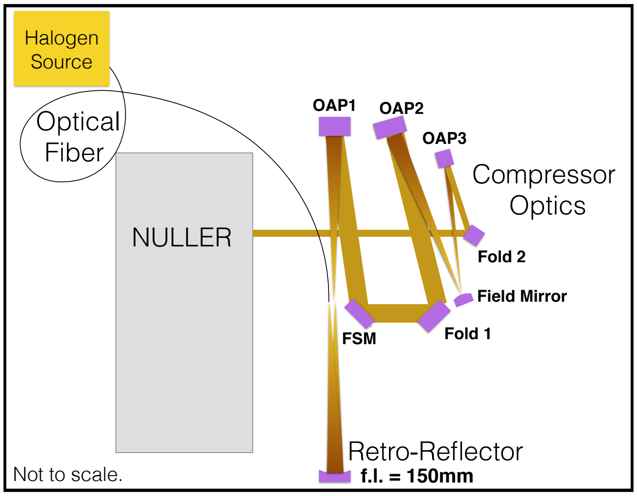

4.3.3 Wavefront Control Tests

Fig. 4.4 shows the average OPD after correction for a typical calibration sequence. The OPD is calculated from measured phase error at the central wavelength of the instrument passband (675 nm). The top row shows the total measured OPD error (left) and the expected image plane contrast (right), modeled with a simple forward model of Fraunhofer diffraction (Douglas et al., 2015). The middle row shows the same WFS measurement after low-pass filtering to the Nyquist frequency of the DM via a 2D boxcar with a width of $f_a/2$. The greatly decreased OPD at correctable spatial frequencies indicates the WFCS system effectively controls phase error near the IWA. The bottom row of Fig. 4.4 shows the residual wavefront error measurement. The Fraunhofer diffraction model of the high frequency residual underestimates the contrast at small angles due to aliasing of higher-order surface features by the WFS pixels.

The PICTURE sounding rocket observing window lasts under five minutes. Since science images are saturated during alignment, this requires rapid wavefront error (WFE) measurement and correction to maximize the high-contrast imaging time on target. Fig. 4.5 shows that the wavefront error converges to the residual print-through error of the DM in under 15 seconds. After WFE is minimized, the NPZT is moved to the center of the dark fringe. The WFCS sequence ends with the instrument in the “null” state, where the SCI and WFS cameras both observe the dark fringe of the interferometer, enabling high-contrast imaging.

Fig. 4.4 shows the median OPD map generated from a typical WFCS phase measurement and corresponding contrast maps from a Fraunhofer diffraction model of the VNC. Pixels behind the Lyot stop are masked. **A1**: the average OPD between the nuller arms during ABCD measurements after the total error converged. **A2**: a forward model of the contrast due solely to the measured phase error. **B1**: the same

WFCS measurement filtered to the spatial frequencies correctable by the deformable mirror, this residual indicates the performance of the WCS. The RMS value of this wavefront error allows approximation of the leaked starlight in the science image due to phase errors. **B2**: a forward model (Section 4.5) of the contrast due to the uncorrected error below $f_a/2$. **C1**: the residual high frequency error after correctable frequencies are subtracted. This is a measure of intrinsic optical path differences in the system (e.g., DM surface features and other high order surface errors). **C2**: a forward model of the contrast due to uncorrected error above $f_a/2$ shows a higher contrast at small inner working angles. This extrapolation of the limiting contrast of a single DM VNC with an ideal WFCS providing perfect control of phase error is limited by WFS sampling.

4.3.4 Contrast Measurement

This work reports on PICTURE nuller performance and measurements are reported in units of contrast per pixel, both as two-dimensional maps and as one-dimensional (1D) curves of the pixel-to-pixel standard deviation (σ) as a function of radius. At a particular angular separation from the star (r), the 1D contrast in the nulled image I_d from the dark interferometer output is given by

$$C = \frac{\sigma(I_d(r))}{\max I_b} \tag{4.4}$$

where I_b is the Point Spread Function (PSF) of the bright fringe of the instrument, a measure of the coronagraph-less throughput of the system.

Fortunately, the quasistatic nature of speckles on a space platform represents a systematic error, which evolves due to small changes in instrument optics. This allows datasets to be speckle subtracted (or “whitened”) using reference observations via various optimized speckle subtraction routines. After speckles have been removed

Fig. 4.4: Median OPD map generated from a typical WFCS phase measurement. and corresponding contrast maps from a Fraunhofer diffraction model of the VNC. The first row corresponds to the median WFE, the second row is low pass filtered to controllable spatial frequencies and the bottom row is the high-frequency residual.

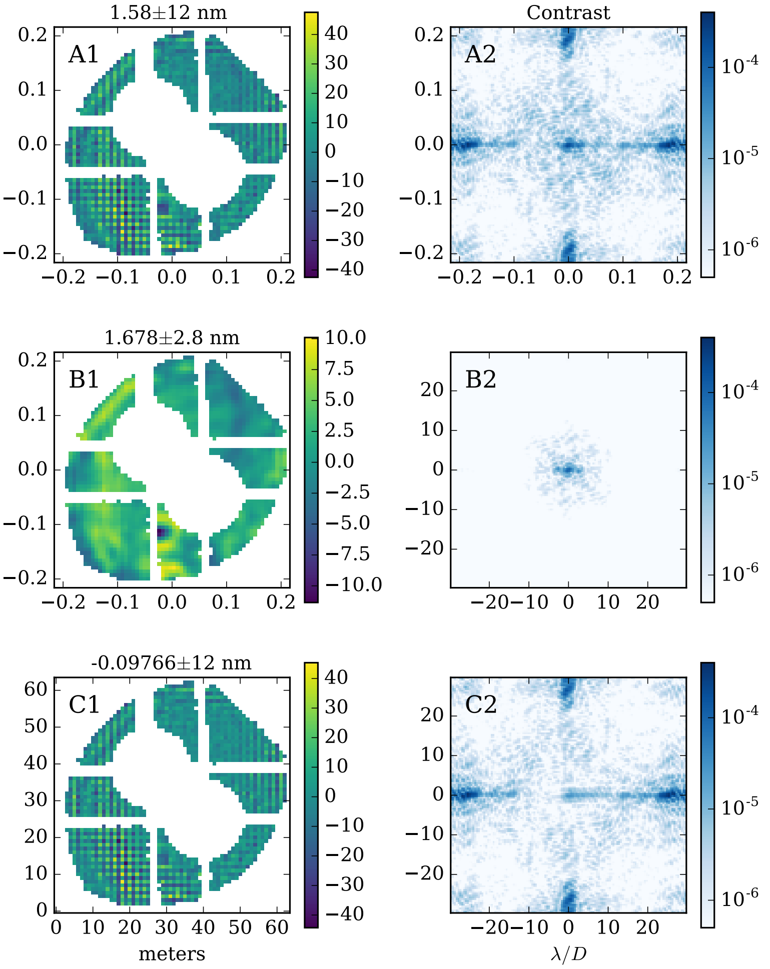

optimally, the remaining per-pixel uncertainty follows approximately Gaussian statistics, driven by detector and Poisson noise (a function of speckle brightness).

Characterizing a high-contrast coronagraph necessarily requires a total dynamic range exceeding a million to one. The PICTURE science camera dynamic range is limited to three orders of magnitude by the CCD readout saturation level of 4095 counts and by detector noise. A common method for overcoming detector dynamic

Fig. 4.5: Wavefront error correction as a function of time for a typical VNC phase up sequence in the laboratory. Dots indicate the root mean square of the total phase error for the measurement and the solid line shows the standard deviation of the phase measurement. The large jump at approximately 9 seconds is due to a fixed pattern briefly applied to the DM to confirm the WFS image to actuator mapping.

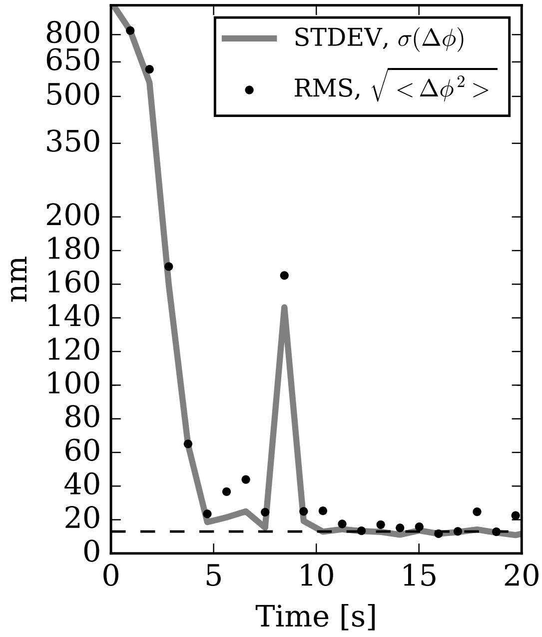

range is a photometry ladder based on exposure time (Trauger & Traub, 2007). However, the CCD readout-speed-limited minimum exposure time is 0.5 seconds for the science detector, and measuring a factor of 1000 contrast at a constant CCD well depth by varying the exposure time would require exposures of 500 seconds. This is significantly longer than the thermal stability of the nuller assembly in the laboratory environment. Thus, we independently measure the input brightness to construct an alternative photometry ladder.

This ladder relies on the stability of the deformable mirror print-through, which acts as a diffraction grating at high-spatial frequencies. This "scalloping" at the actuator frequency (f_a) of the deformable mirror results in bright "spikes" in the image plane. Since the high-spatial frequency DM print through pattern is unchanged by the WFCS and small phase perturbations about the bright and dark fringes have equal intensity, the spike brightness is conserved between the fringes and serves as a photometric fiducial. These four diffraction spikes are visible in both the median bright and dark fringe PSFs, Fig. 4.6. Diffraction spike brightness is at the 10^{-3} level versus the central bright PSF, comparable to the central leakage in the dark fringe PSF, illustrating that the VNC attenuates by approximately three orders of magnitude.

A bright PSF was observed by finding the dark fringe and then shifting the PZT arm by π radians. Adjusting the fiber coupling efficiency, the bright fringe intensity was decreased until the science camera was unsaturated and short science frames were recorded. The median of these science camera frames provides a standard bright image. The ratio of a DM diffraction spike brightness (boxed in lower right in both frames of Fig. 4.6) and the brightest pixel in bright fringe PSF provide a constant contrast scale factor. The position of the PSF relative to the pixel spatial pattern is arbitrary. Thus, the maximum observed pixel brightness may be reduced by distribution of the PSF core across several pixels. To determine the peak bright fringe pixel, the recorded PSF was computationally shifted in subpixel increments, via third-order spline interpolation, to maximize the single-pixel intensity using the Powell minimization algorithm (Powell, 1964) as implemented by SciPy (Jones et al., 2001). The maximum of the bright fringe PSF was increased 11% by this optimal recentering process. Using the ratio of the bright PSF peak to the diffraction spike, we are able to measure contrast directly from the spike brightness in a nulled image.

4.3.5 VNC Test Observations

Data were collected in flight-like sequences at the UMass Lowell Center for Space Science and Technology (LoCCST) following the phase correction steps described in section 4.3.1 and Mendillo et al. (2012b). The laboratory test environment for these

Fig. 4.6: The raw median nuller point spread functions imaged by the science camera and plotted on a logarithmic scale. The left frame shows the bright fringe output and the right frame shows the dark frame output, with the input intensity adjusted to prevent detector saturation in each case. The four faint diffraction spikes near the edges of each image provide a constant photometric scale factor between the two images, allowing calculation of contrast in dark fringe output via comparison to peak of the bright image. The spike used for photometric calibration is boxed in each frame and connected by a dashed line.

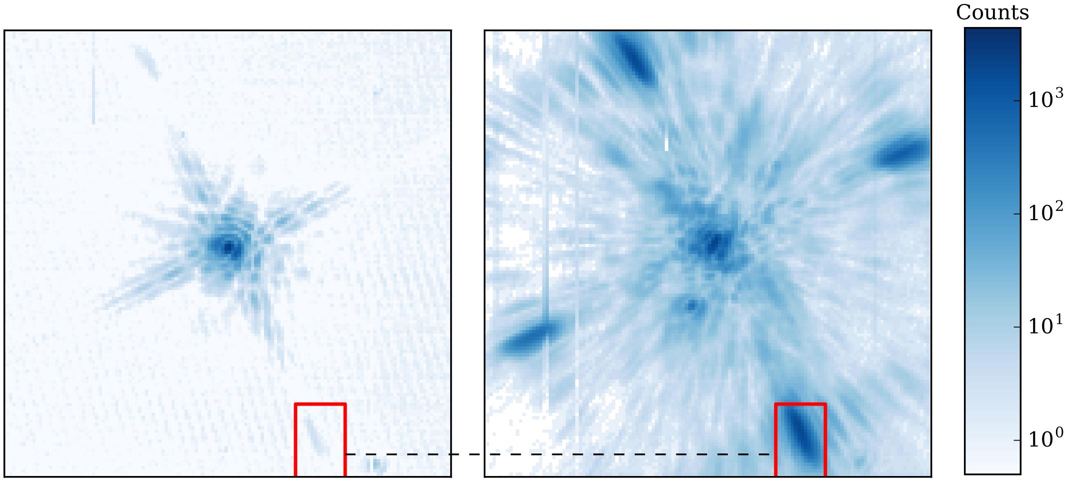

measurements was designed to minimize air currents and vibration, both of which contribute to the measurement noise floor. Thus, superior path-length stability might be expected in a space environment.

A total of 630 nulled frames were collected over five separate simulated flight sequences with the laboratory heating, ventilating, and air conditioning system disabled to minimize acoustic noise; and the slow nitrogen purge for prevention of DM humidity corrosion (Morzinski et al., 2012) paused to minimize air turbulence. Individual observations were terminated if the relative humidity near the deformable mirror exceeded 30% or the contrast was observed to have worsened significantly due to thermal drift. In order to mitigate systematic bias due to environmental drift between runs, two random sets of 315 non-redundant frames were drawn for PSF subtraction analysis. One set makes up the measurements used for leakage mea-

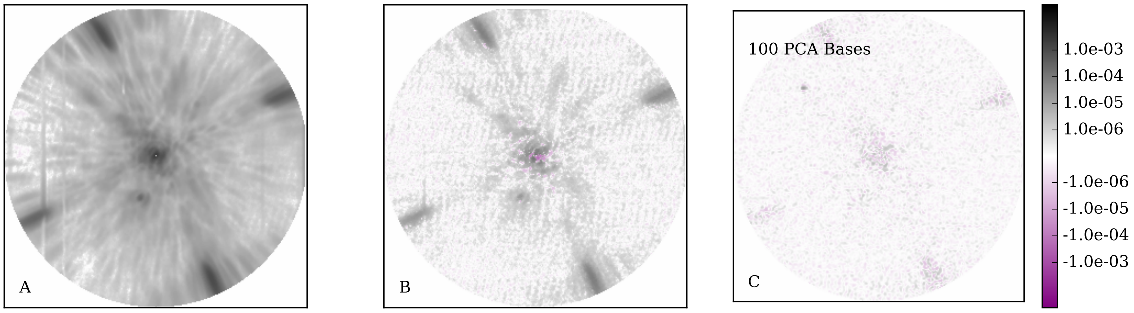

Fig. 4.7: Raw and PSF subtracted contrast measurements from laboratory data. Contrast is calculated by dividing the peak of the bright PSF from nulled science camera images. **A** shows the median raw contrast image for a sequence of science images. **B** shows the difference between median images from two different sequences of science images. Since both images are taken from the instrument in a comparable state, both sequences represent subsets of the true instrument state. **C** shows the optimally speckle subtracted residual of the same science image after projection on a set of empirical basis vectors generated by principal component analysis (PCA) of the reference dataset.

surement and the second set serves as a reference for tests of speckle stability and subtraction. Of the 630 images recorded, 253 contain no saturated pixels.

Wavefront Correction Test Results

The mean closed loop wavefront phase error of 5.7 nm at WFCS controllable spatial frequencies, shown in Fig. 4.10, is significantly above the 0.54 nm RMS error previously measured with a Kilo-DM in other wavefront control systems (Evans et al., 2006; Rao et al., 2008). Limitations on closed loop wavefront correction with a MEMS deformable mirror include: irregular actuators (one is clearly visible in the lower left corner of Fig. 4.4**B1**) and edge effects due to scattering and diffraction in the WFCS optical path (Evans et al., 2006). Additionally, while the WFCS sequence is running, acoustic disturbances, vibrations, and thermally driven motions are not corrected above the control bandwidth of 0.5 Hz, so these are also integrated into the phase error measurement.

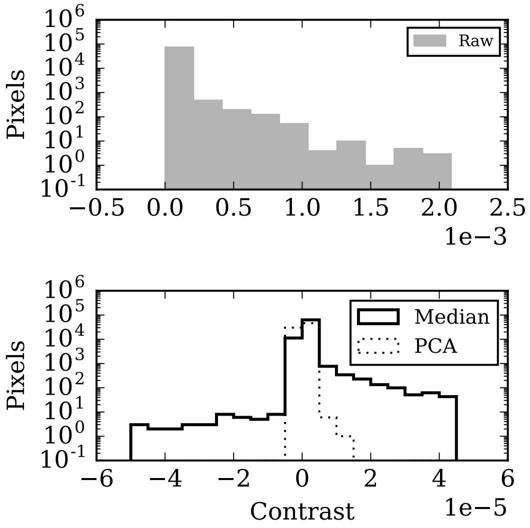

Fig. 4.8: Histograms of the number of pixels with a given contrast. The top panel shows the median raw contrast in the nuller output image. After subtraction of a reference PSF made up of the median pixel values of a comparable observation, the residual contrast distribution (solid line, bottom panel), decreases two orders of magnitude, becomes quasi-Gaussian. The residual after speckle subtraction via Principal Component Analysis (PCA) using the same set of reference images (dotted line) decreases the number of outlier pixels, further contracting the distribution of contrasts and approaching the unbiased noise level.

High-Contrast Imaging Test Results

At the IWA of the median nulled frames, the contrast of the radially averaged intensity (dashed gray line) in Fig. 4.9 is 3×10^{-4}, showing the coronagraph attenuates starlight by more than two orders of magnitude versus the average bright fringe PSF (thin dash-dot line, Fig. 4.9). The radial standard deviation at the IWA is approximately equal to 10^{-4}. The simplest post-processing step for speckle removal from a high-contrast image is subtracting a reference PSF made up of the median pixel values from the second randomly selected non-redudant subset of nulled frames. Before subtraction, each frame is oversampled and centered using the Pynpoint-Exoplanet routines developed for PCA (Amara et al., 2015). Median subtraction removes static

Fig. 4.9: Contrast curves showing the coronagraph performance and the increase in contrast achieved by speckle subtraction. The average bright curve illustrates the raw system PSF without a coronagraph. The IWA is indicated by the vertical dashed line at $1.7\lambda/D$. At the IWA the $2{\times}10^{-4}$ standard deviation of the raw dark fringe contrast is three orders of magnitude lower than for the bright fringe. PCA subtraction improves the contrast by two additional orders of magnitude for a contrast of $\approx 2 \times 10^{-6}$ at the IWA.

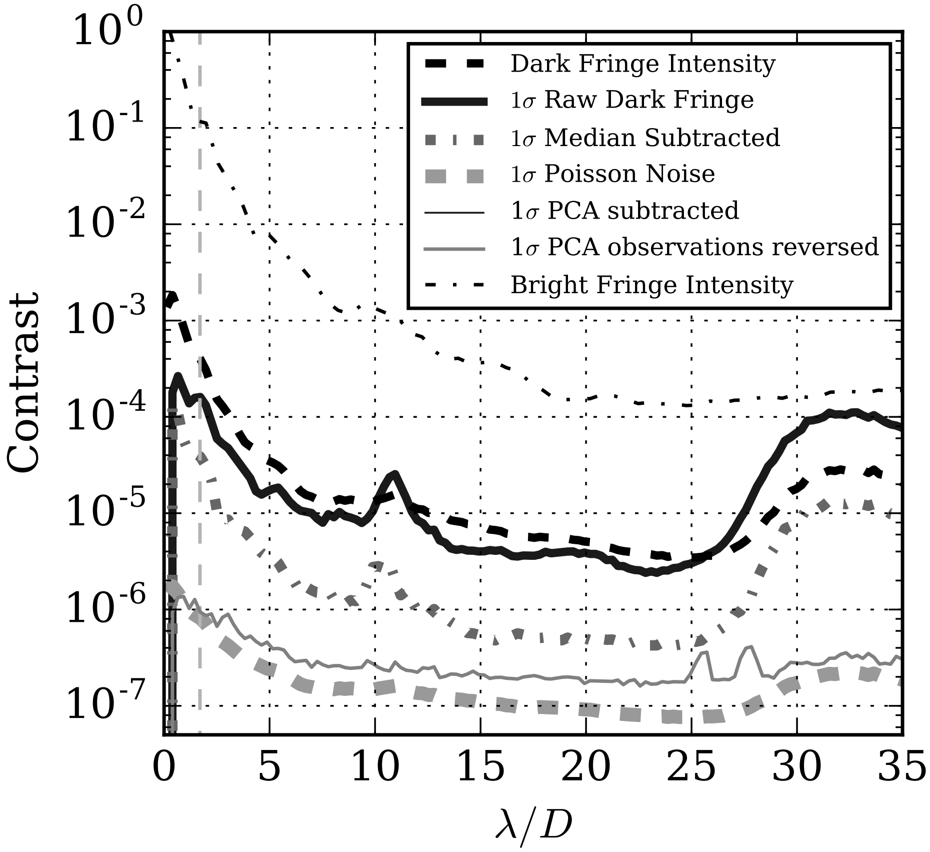

speckles and provided a further improvement in contrast of nearly an order of magnitude. Fig. 4.7 **B** shows the residual speckle pattern after subtraction of the median of the second dataset.

Principal Component Analysis

To demonstrate instrument sensitivity given state-of-the art speckle subtraction techniques, we apply the PynPoint-Exoplanet PCA speckle subtraction Python pack-

Fig. 4.10: Left: time-series of mean wavefront phase error filtered to low spatial frequencies from multiple WFCS fine calibration sequences (one sequence per trace). Right: Histogram of mean low spatial frequency error. The average root mean squared (RMS) wavefront error is 5.7 nm.

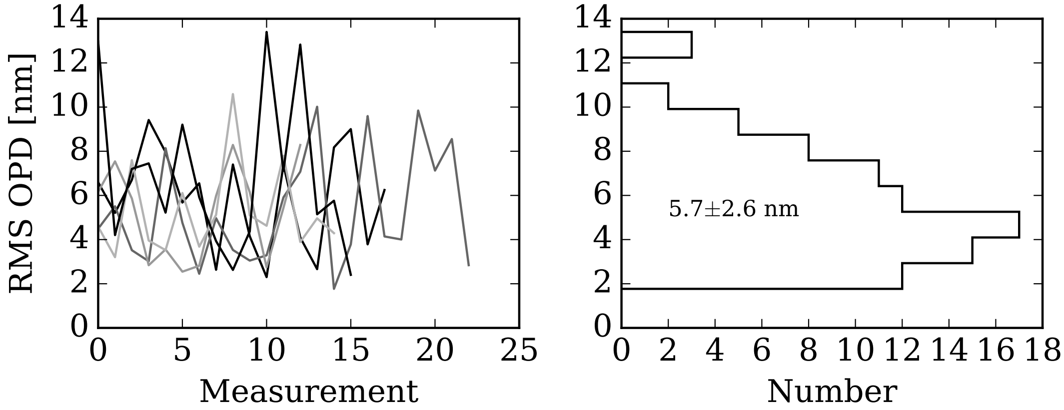

age (Amara & Quanz, 2012; Amara et al., 2015). PCA techniques permit high-fidelity characterization of astronomical instrument state, and have been used previously for space telescope data analysis, e.g. to quantify gravitational lensing with the HST Advanced Camera for Surveys (Jee et al., 2007) and for exoplanet and debris disk detection in the HST Near Infrared Camera and Multi-Object Spectrometer archive (Choquet et al., 2014). A singular value decomposition (SVD) implementation of PCA, PynPoint builds on prior applications of PCA to telescope PSFs. Also called the Karhunen-Lo'eve transform, PCA allows determination of the most probable realizations of a noisy PSF given a random sampling, and allows semianalytic determination of algorithm throughput, thereby preserving photometric accuracy. Given N PSF observations, sampling the underlying PSF with a set of M pixels, PCA is the empirical retrieval of a set of orthogonal basis vectors efficiently describing the subspace encompassed by N points in M-dimensions. The principal component set corresponds to a sequence of vectors in decreasing order of maximum variance (Abdi & Williams, 2010), thus the PCA basis set can be truncated to the number of vectors that accurately recovers the speckle pattern, typically significantly less than N.

The PCA basis mitigates time-dependent variations in the speckle pattern not captured by subtracting a median reference image. To maximize diversity and best approximate on-sky observation, frames with individual saturated pixels were not discarded. Once a PCA basis has been determined, each frame is individually projected against the basis set. A residual is composed of those components of the science image which are orthogonal to each basis vector. Averaging the residuals of the science images produces a final science image with speckles well-subtracted. Fig. 4.7 **C** shows the mean residual pixel values after application of a PCA basis composed of 100 coefficients (the number found to be optimal four groundbased PCA (Amara & Quanz, 2012)). Throughput losses are neglected in this analysis and are expected to be small for point sources and under one hundred coefficients.

The basis was generated from the same set of observations as the set used for median subtraction. Time-varying video crosstalk noise pattern is visible as diagonal striations in the median subtracted image but is absent in the PCA subtracted image, demonstrating the PCA basis provides a superior empirical model of instrument noise. Both the median subtraction and PCA methods "whiten" the dataset; Fig. 4.8 shows the number of low contrast pixels decreases dramatically after subtraction of a median PSF, and decreases further still after PCA. Fig. 4.9 shows the radial intensity contrast versus separation for a raw high-contrast image (thick dashed line), the radial standard deviation (thick solid line), and the standard devation after subtraction of a median reference (dot-dash). The curves after PCA subtraction (thin solid lines) represent the radial standard deviation for each set of observations after subtraction of a basis formed from the second set of observations. The inner working angle is indicated by a vertical dashed line. The PCA subtraction is most effective at the smallest innerworking angles, reaching a Poisson noise limited radial standard deviation contrast of 2×10^{-6} at $1.7\lambda/D$. At larger angles, the PCA subtraction

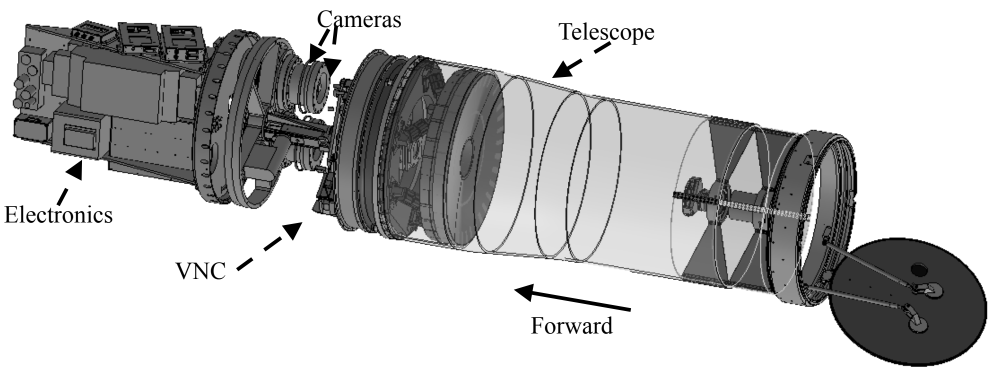

Fig. 4.11: Rendering of the PICTURE payload with the skins and nuller enclosure removed for clarity and the carbon telescope tube made transparent to reveal the telescope internals. The forward arrow indicates the direction of travel of the rocket upon launch and indicates the coordinate system used to describe temperature sensor positions (Section 5.2).

approaches the median subtracted contrast, except at the diffraction spikes, which are also well subtracted by the PCA basis.

4.4 PICTURE Telescope

Independent of the coronagraph contrast, image quality depends on telescope resolution. A sounding rocket platform severely limits the available aperture and, at the 0.5 m, PICTURE telescope is believed to have one of the largest collecting areas flown on a Black Brant IX. This aperture's diffraction limited resolution of 0.34 arcseconds would readily resolve a one arcsecond diameter exozodiacal ring at 675 nm. Surface and alignment errors in the telescope optical assembly lead to aberrations in the PSF, decreasing the resolution from the diffraction limit. The following sections will describe the replacement PICTURE-B primary mirror and the final telescope assembly, with particular attention to system wavefront error and thermal sensitivity.

Manufacturing

The original PICTURE/Solar High-Angular Resolution Photometric Imager (SHARPI) primary mirror (Antonille et al., 2008) flown on 36.225 UG did not survive to recovery. A new light-weighted silicon carbide primary mirror with a silicon cladding was designed by AOA Xinetics/Northrop Grumman to survive the rigors of launch and provide a surface quality sufficient to demonstrate the VNC in space and measure the predicted ϵ Eri inner warm dust ring.

Final figuring of the mirror was performed via Magnetorheological finishing (MRF) (Golini et al., 1999), which provided efficient material removal, essential to preserving the thin, approximately 40μm thick, cladding. Fig. 4.12 shows a single fringe measurement and a phase measurement of the aligned telescope surface with only wavefront tilt removed. Significant astigmatism due to gravity can be observed, as well as mid-frequency ripple due to the MRF finishing (Sakao et al., 2014).

Alignment

Due to prior high-quality measurements of the telescope secondary mirror, primary mirror acceptance testing and telescope alignment were carried out as a single step. Telescope focus was mechanically set relative to the telescope mounting structure with a pinhole. The pinhole was matched to the focus of a fused silica positive bestform lens at the output of a phase-shifting interferometer and a full-aperture retroreflecting flat mirror was used to measure the system wavefront error. Because tests were performed in a reflective double pass arrangement, surface errors were magnified by a factor of four. Errors reported herein represent single-pass reflective wavefront error as would be measured by the VNC in flight. For comparison to surface metrology, the wavefront errors should be halved. The left panel of Fig. 4.13, reproduced from Chakrabarti et al. (2016), shows the gravitationally induced

Fig. 4.12: Telescope surface measurements in the laboratory. (The examples were collected at different roll angles and the handles of three micrometers used temporarily to translate the secondary mirror are visible as radial obscurations in frame (a)).

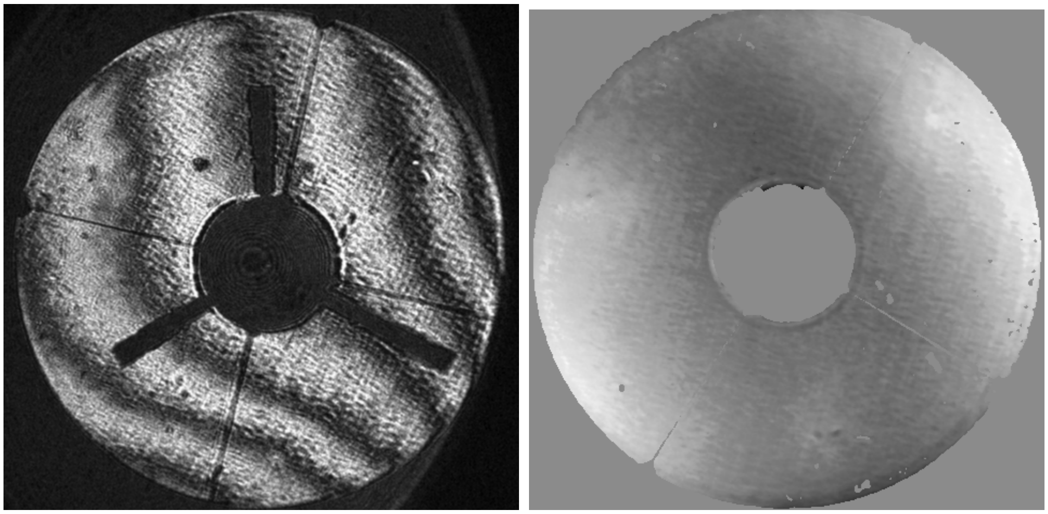

(a) Example of phase a single set of shifting interferometer fringes recorded during telescope alignment.

(b) Unprocessed phase shifting interferometer measurement showing astigmatism due to gravity sag.

astigmatism and the right panel shows the expected residual aberration expected in free-fall. Table 4.1 shows the final telescope wavefront error expected in flight after the secondary was aligned in translation, tip, tilt, and piston to minimize errors other than the unavoidable gravitationally dependant aberrations.

Thermal Sensitivity

The PICTURE telescope was designed to be athermal, maintaining constant metering between the telescope focal plane and the primary and secondary mirrors. This was attempted using a low-Coefficient of Thermal Expansion (CTE) carbon fiber composite tube, a titanium secondary mirror spider, an athermalized titanium bipod design and Invar mounting hardware.

Despite these measures, a significant variation in telescope focus and astigmatism was observed as a function of temperature. Fig. 4.14 shows the dependence

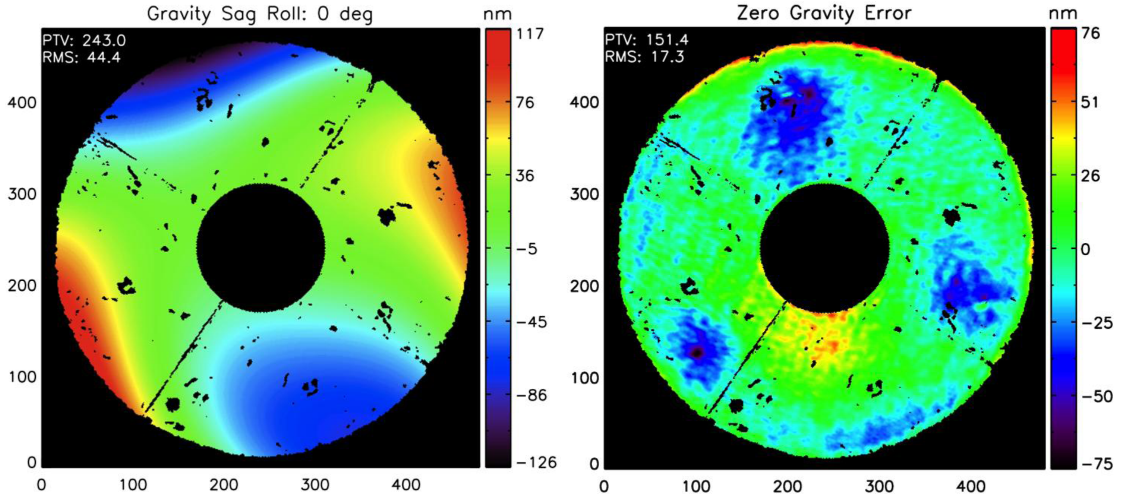

Fig. 4.13: Averaging surface measurements taken at 24 roll angles to find gravity sag. The left panel shows a map of the gravity sag and the right panel shows the static residual. Print-through of the three titanium mounting inserts is clearly visible as depressed regions. Units are nanometers of surface error. Reproduced from Chakrabarti et al. (2016).

of the Peak-to-Valley (PV) focus on temperature, as measured by fitting of the Zernike power coefficient to phase shifting interferometer errors using the Durango software package[2]. The temperature is calculated from Resistance Temperature Detector (RTD) measurements at the base of the carbon fiber and epoxy composite tubular metering structure nearest the primary mirror (T_b) and from two sensors on both the inside (T_i) and outside (T_o) of the tube at the secondary mirror end of the tube. Since focus is driven by differences in the separation of the optics not the gradient from the inside to the outside of the tube, the tube temperature was calculated as a weighted mean: $\bar{T} = 0.5(T_b + 0.5(T_i + T_o))$.

The left panel of Fig. 4.14 shows focus measurements which were made with the telescope laying horizontal and rotated such that a line between two of the three mounting bipods would be oriented parallel to the floor and the third bipod was at

---

[2] Diffraction International, `http://www.diffraction.com`

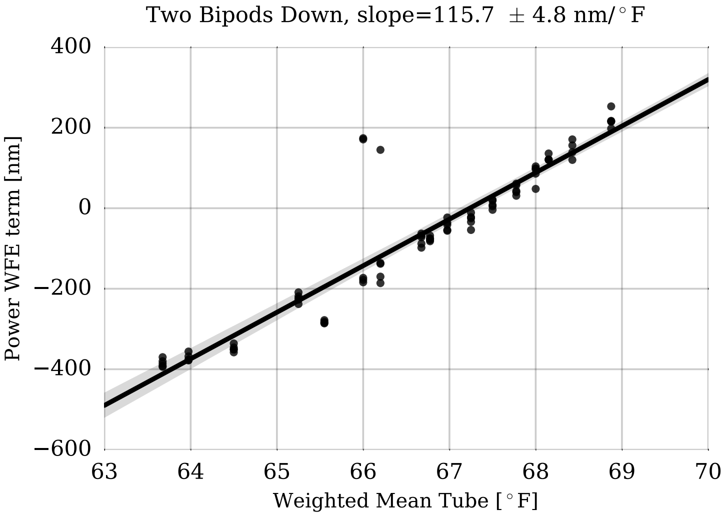
Two Bipods Down, slope=115.7 ± 4.8 nm/°F

(a) Focus wavefront error as a function of the carbon fiber tube temperature for the integrated PICTURE primary and secondary mirror assembly.

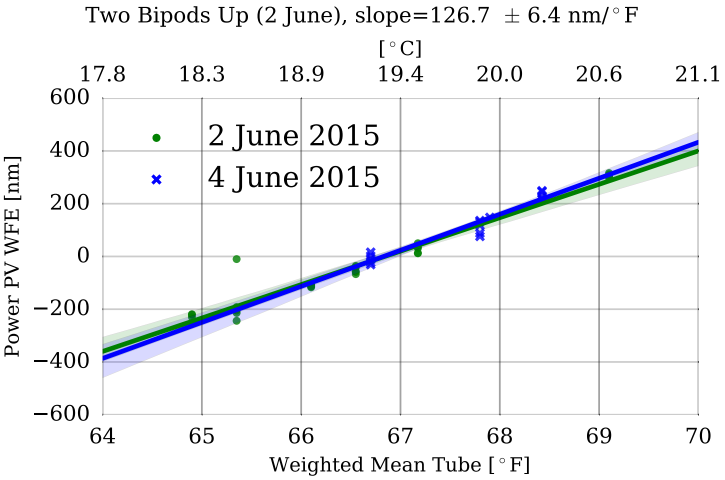
Two Bipods Up (2 June), slope=126.7 ± 6.4 nm/°F

(b) Focus wavefront error amplitude as a function of temperature, for the telescope rolled 180 degrees about the horizontal axis with respect to Fig. 4.14a. Data collected on separate days shows measurement stability.

Fig. 4.14: Focus wavefront error amplitude as a function of the carbon fiber tube temperature for the integrated PICTURE-B telescope. The PV wavefront error dependency on temperature is approximately 240 nm/°F. Shaded regions indicate the 95% confidence intervals of the linear regression (Waskom et al., 2016).

the top of the primary mirror. There is no discernible difference in the dependence on focus with bipod orientation: the right panel shows two datasets from the opposite configuration, with the two bipods at the top and the third closest to the floor. The strong temperature dependence observed in Fig. 4.14 drove a very tight payload temperature stability requirement (±0.25°F) on the launch pad. The nominal focus was adjusted to a mean tube temperature of 67.5°F. Fig. 4.15a shows the strong temperature dependence of the vertical astigmatism term, while the 45 degree term (4.15b) shows no significant trend.

Unlike focus, the proportionality of the astigmatism to mean tube temperature was not stable day-to-day, as seen by comparing two day different day's best-fit lines, plotted in Fig. 4.16. This variation in slope suggests the titanium and aluminum mounting structure drives the variation in astigmatism, which is expected to respond to changes in room temperature with a different time constant than the carbon tube where temperatures were measured.

Cumulative Wavefront Error

Table 4.1 shows the telescope wavefront error amplitudes in units of PV Zernike polynomial terms, approximated from measurements using the phase shifting interferometer at multiple roll angles assuming a small focus error and gravity release. These values were used as inputs to a diffractive VNC model to validate that the as-built telescope could detect the 3 AU debris disk around ϵ Eri proposed by Backman et al. (2009).

Fig. 4.15: Zernike wavefront error coefficients as a function of the mean carbon fiber tube temperature for the integrated PICTURE-B Silicon Carbide (SiC) primary and secondary mirror assembly measured in double pass with a phase shifting interferometer. Approximately 300 nm PV of astigmatism due to gravitational sag was expected on the ground. The magnitude and orientation of the sag depends on the bipod orientation with respect to the gravitational vector. The system was aligned such that the observed astigmatism matched the gravity sag prediction at the temperature of best-focus.

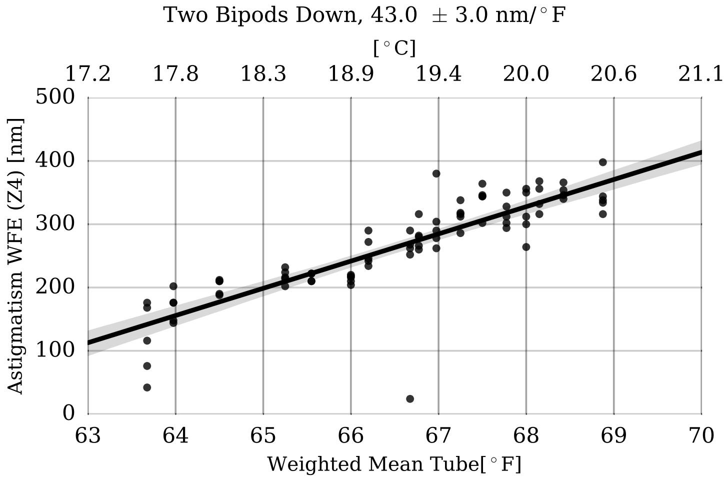

(a) Vertical astigmatism coefficient shows a strong temperature dependency. Shaded regions indicate the 95% confidence interval of the linear regression.

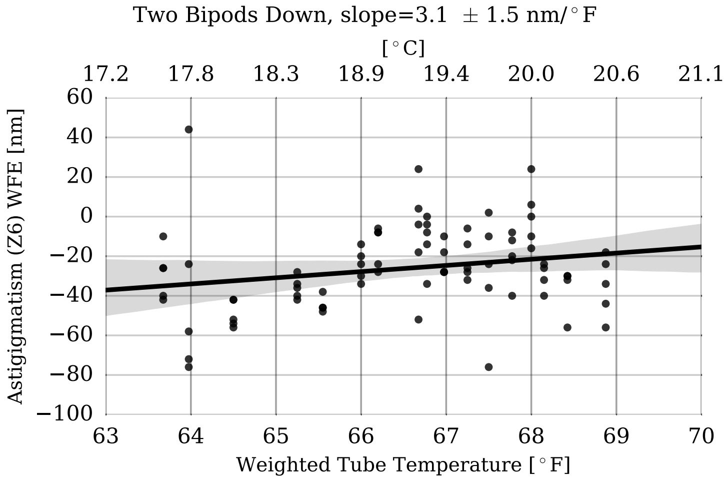

(b) The second astigmatism Zernike coefficient does not show a significant temperature dependence.

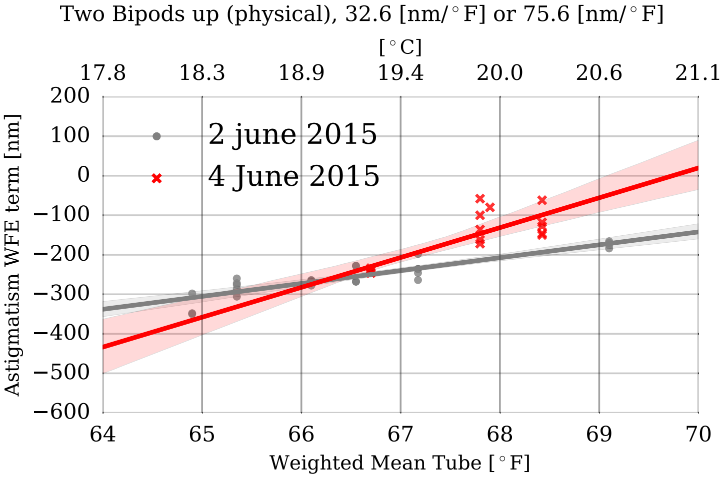

Fig. 4.16: Two separate days of measurement show variation in the relation between astigmatism and carbon fiber tube temperature.

Table 4.1: Peak-to-valley estimates of Zernike polynomial terms representing the telescope output for the coronagraph forward model. These values assume successful gravity release of astigmatism and a deviation in telescope tube temperature of ≈ 0.6°F. Coma and astigmatism are primarily residual errors from alignment, while spherical error is the dominant low-order residual from manufacturing.

Aberration	PV [nm]
Focus	150
Astigmatism	100
Coma	80
Spherical	100
Trefoil	50
Total peak-to-valley OPD	320 nm

4.5 Coronagraph Modeling

Diffraction Simulators

Testing of the assembled payload in the laboratory required double-pass end-to-end testing with a flat half-meter retro-reflector, doubling the effective wavefront error in the lab. This factor of two, coupled with the excess astigmatism under gravity (Fig. 4.12), meant that laboratory errors far exceeded expected on-sky errors and the contribution of telescope WFE on VNC performance was best performed via detailed coronagraph simulations.

Prior space-based astronomical observatories have used lightweight PSF modeling libraries for simulating science results both before and after launch (Krist, 1995; Perrin et al., 2012). Maximizing the science return of missions requires careful management of design parameters. Such as trade-offs between wavefront error at different spatial frequencies, or the signal-to noise ratio change from switching to potentially less uniform, but more reflective, coating. Similar trade-offs present themselves to the observer. For example, the choice between a distant star with a relatively bright dust ring versus a higher contrast dust ring around a nearby star. Computationally efficient modeling of such subtle effects, in a robust and repeatable manner, allows easy tracking of expected science yield versus manufacturing realities. Expensive commercial software packages aimed at the optical engineer provide important information for the system mechanical layout and tolerancing, but would be unnecessarily complicated for specification of optical quality and science result simulation. One approach is to generate flexible models of the telescope and coronagraph using diffraction-based optical models in programming languages commonly used for data analysis, such as IDL or Python, thereby minimizing the divide between instrument engineering and the final science product.

First the astrophysical properties of the target are defined (flux, stellar type, angular size) and the expected target spectrum is combined with the system spectral response using the pysynphot Python package (STScI development Team, 2013). This spectrum is next decomposed into a series of wavefronts. A wavefront of the appropriate wavelength, tilt, and intensity is then propagated through a diffraction model, which is defined by the coronagraph and telescope opto-mechanical design.

4.5.1 Instrument Modeling Methods

This section will describe the PICTURE instrument response to targets at various angular separations and roll angles, the sensitivity to errors in the deformable mirror surface, and to mismatches in color. This modeling has been carried out by extending the POPPY package[3], an open source Python module originally written to simulate JWST PSFs without requiring proprietary software (Perrin et al., 2012).

While an understanding of Fresnel diffraction effects is important for high-contrast imaging, in the PICTURE VNC the intra-instrument propagation beam covers a short distance. Both the DM and telescope primary are in conjugate pupil planes and the aperture is masked at the edges by a Lyot stop, and PICTURE operates in a mid-contrast regime ($\sim 10^{-3}$). Therefore, Fraunhofer propagation from an effective instrument pupil plane to the science camera approximates first order system deviations – useful for the purpose of determining the influence of telescope and deformable mirror surface quality on the science goals.

4.5.2 Spectral Throughput

To model wavelength dependent diffractive effects accurately, quantifying the PSF and simulating speckles, requires both input stellar spectra and spectral throughput curves. Additionally, to calculate signal-to-noise ratios photon rates are

---

[3] https://github.com/douglase/poppy-nulling, https://github.com/mperrin/poppy

required. The target star visible magnitude provides flux calibration of the model spectra. The pysynphot synthetic photometry package (STScI development Team, 2013) was used to generate input spectra from an empirical stellar flux library (Pickles, 1998). Using pysynphot's interpolation and unit conversion functions, bandpasses were generated by multiplying by the responses of the spectral throughput of each element. These modeled responses include protected silver, gold and antireflection coatings and detector quantum efficiency for each type of surface preceding each detector. These were applied to the input stellar spectra: a B8I spectral-type star (shown in Fig. 4.17) , which closely approximates Rigel, the planned calibration target of the PICTURE sounding rocket flight and ϵ Eri. Curves are shown for a blue band (shortward of 600 nm) which feeds the angle tracker (AT) to maintain payload pointing (Mendillo et al., 2012a) and for the science band (600-750 nm). The decreased detector quantum efficiency and coating reflectivity at short wavelengths combine for a dramatic decrease in photons measured at the angle tracker.

Surface Error

Deviations from ideal surface geometry aberrate the telescope PSF and also lead to mismatch between the VNC arms which must be corrected with the deformable mirror to maintain a deep null of the target star. At large spatial scales, Zernike polynomials provide a convenient measure of surface error components by describing aberrations in terms of an orthogonal basis in polar coordinates (Noll, 1976). The PICTURE-B telescope required a total wavefront error within the 1.5 μm stroke of the deformable mirror, and with a PSF sufficiently compact that the proposed ϵ-Eri warm ring would be easily distinguished from the "wings" of the PSF. This was expected to correspond to a surface quality of approximately $\lambda/4$ root mean squared error (RMSE) at 633 nm ($\lambda/2$ surface error) at deformable mirror correctable spatial frequencies ($< 15\lambda/D$). Additionally, in order to minimize speckles from high-

Fig. 4.17: Example of using pysynphot to generate synthetic spectra for speckle modeling and count rate predictions. Modeled responses accounting for coating transmission and quantum efficiency are shown opposed to a flat 100% throughput for a B8I star, the short wavelength band (< 600 nm) corresponds to the PICTURE sounding rocket angle tracker camera (AT). The science band (600-750 nm) is also shown, indicating the flux reaching the pupil imaging wavefront sensor (WFS). Reproduced from Douglas et al. (2015).

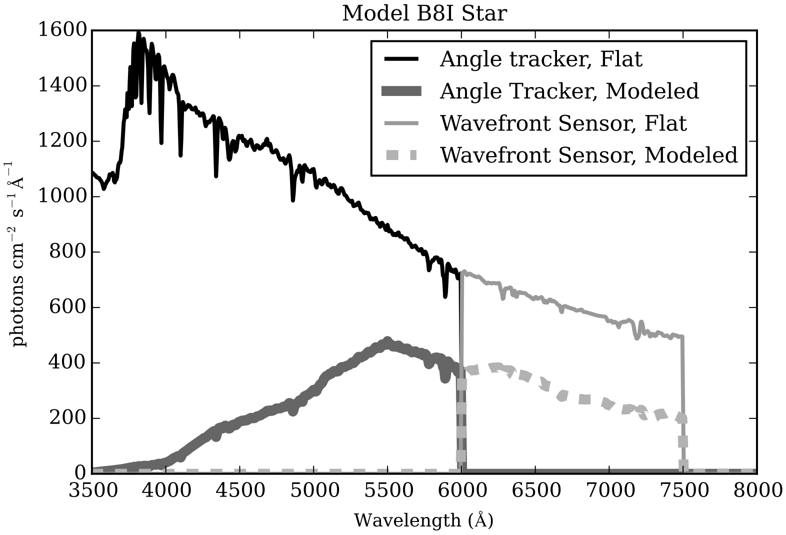

frequency error, a 5 nm RMS surface quality was specified. Due to the difficulty of manufacturing a lightweight mirror to survive the rigors of a sounding rocket flight, these requirement were revisited frequently and deviations in the surface quality were individually modeled and compared to the desired science outcome. The final aligned telescope optical quality at low spatial frequencies was approximated by the wavefront error terms in Table 4.1.

To estimate the influence of telescope manufacturing errors on the science image, a simple VNC model where the dominant sources of surface error are the telescope and DM surfaces was assumed. Since the DM and primary mirror are located in conjugate pupil planes, a simple Fraunhofer diffraction model is sufficient to quantify their effects on the instrument PSF. Using *POPPY*, a complex input wavefront is sheared,

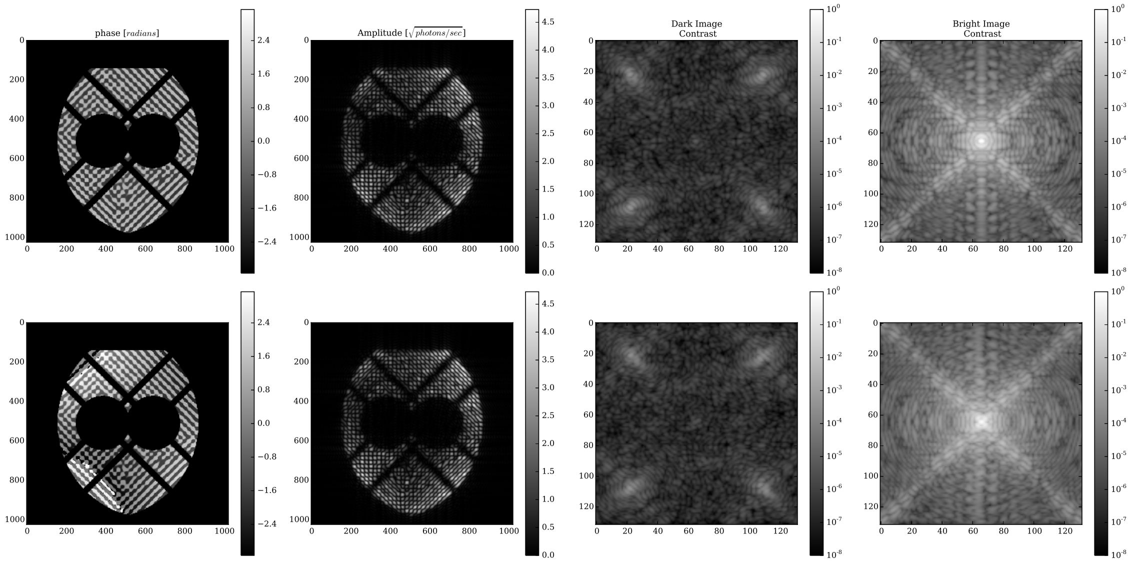

Fig. 4.18: Example simulation of monochromatic interference for the sounding rocket telescope with a realistic uncorrectable deformable mirror surface print through and intensity leakage. The leftmost column shows the pupil plane phase (without unwrapping) in radians after interfering the two complex wavefronts. The second column shows the dark output amplitude, the third column shows a focal plane image of the science camera contrast in the dark fringe output, and the rightmost column shows the corresponding bright fringe output. The top row corresponds to an ideal telescope and the lower row corresponds to an astigmatic telescope with an unacceptable 280 nm of PV surface astigmatism. The distribution of leaked starlight is slightly changed without changing the total leakage. The telescope Strehl ratio, seen in the bright fringe, decreases with the addition of this excessive astigmatism. Reproduced from Douglas et al. (2015).

and the DM surface error at uncorrectable spatial frequencies is optionally added to one arm. After the beams are combined, a binary transmission Lyot mask applied to block regions where the two pupils do not overlap and the wavefront is multiplied by the sheared telescope wavefront, simulating correction of relative WFE between the interferometer arms. The left two columns of Fig. 4.18 show the variation in phase and amplitude of ideal (top) and extremely astigmatic (bottom) example interfered post-Lyot wavefronts. From this final pupil plane, Fraunhofer propagation is carried out for each wavefront. The third column of Fig. 4.18 shows the wavefront difference at the image plane for each case, corresponding to the interferometer dark output, while the right-most column shows the bright output PSF.

To simulate a realistic source, a single bright wavefront with zero tilt (a central star) and a set of lower amplitude tilted wavefronts (composing a number of faint companion sources, N_S) are individually propagated through a simple nuller model for a number of wavelength bins (N_λ). After propagation to the image plane, each wavefront is added incoherently. This process is repeated at each wavelength of interest. *POPPY* implements the Matrix Fourier Transform (Soummer et al., 2007), which does not require equal array sizes in the pupil, and permits significant speed gains when a small number of focal plane pixels is required relative to the sampling of the pupil plane. If the propagation time per wavefront is t_p the total simulation time is $t_P \times N_\lambda \times N_S = 615 t_p$. For a 1024×1024 pupil array and a 132×132 pixel image, oversampled 10×, and $N_\lambda = 15$, $N_S = 41$, on a Core i5 laptop processor, t_p is of order five seconds. Thus, such a simulation requires nearly an hour of processing time. However, since each wavefront is independent, the problem was parallelized via the *IPython IPCluster* module (Perez & Granger, 2007). The total processing time for such a set of 615 wavefronts is approximately 4.4 minutes using a 40 node IPCluster, across 20 physical E5-2670 Intel Xenon(R) Cores at 2.50 GHz at the Boston University Shared Computer Cluster. Decreasing the image plane array size to sample only the central 35 pixels, oversampled to 345x345, decreases simulation time to 1.3 minutes.

Simulated Sounding Rocket VNC Science Image

Nearby and dusty, the ϵ Eri system has one of the brightest known debris disks, making it an ideal target to demonstrate high-contrast imaging in a short-duration observation (Section 1.2.4). We illustrate the PICTURE payload expected science results in Fig. 4.19a using the simplest model of the inner warm debris disk: a face-on ring, of radius one arcsecond, with infinitesimal thickness, and an integrated brightness of $2\times10^{-4}L_{\star}$. Fig. 4.19b shows a final science image with idealized speckle subtraction. The count rate and stellar color are approximated using pysynphot as described previously. The debris disk is truncated by the VNC transmission pattern, yet clearly visible as four peaks at 1 arcsecond radius. Fig. 4.20 shows the transmission function weighted radial average of a dustless image and the inner warm debris disk model. The clear separation between the 1σ error bars in the two models indicates the $\lambda/4$ low-spatial frequency surface figure of the sounding rocket telescope (Table 4.1) was sufficient to recover the predicted debris disk.

Fig. 4.21 shows the same radial average of the modeled 3 AU debris disk along with the laboratory measured raw contrast and PCA residuals (Section 4.3.5) and exhibits a similar detection level, validating the numerical model.

High-Spatial Frequency Telescope Ripple

MRF figuring of large optics imparts a high-frequency ripple due to the small size of the polishing tool and the finite acceleration of the electromechanical stage which controls the dwell-time of the MRF. The MRF removal rate is constant, so the dwell-time is directly proportional to material removal. The primary prescription called for high frequency surface error below 5 nm RMSE (or 10 nm WFE). MRF figuring delivered an approximately 10 nm RMSE average surface. The left two frames of Fig. 4.22 show the wavefront error of the primary mirror surface prior to final figuring collected by AOA Xinetics with a *4D Technology*[4] interferometer and an Offner Null lens (Offner, 1963). The center frame of Fig. 4.22 shows the residual uncontrollable by the DM. This residual was calculated by subtracting a low-pass spatially filtered copy of the map. (The filtered map was calculated via convolution

---

[4] http://www.4dtechnology.com

Fig. 4.19: Simulated 210 second sounding rocket observation of the predicted inner warm ring of ϵ-Eridani (Backman et al., 2009) using the PICTURE VNC, a $\lambda/4$ surface figure primary telescope, the flight deformable mirror, and a 5% intensity mismatch between the interferometer arms. Deformable mirror print through errors at the actuator frequency are shown as four bright spikes defining the outer working angle. Poisson, detector dark, and detector read noise are included.

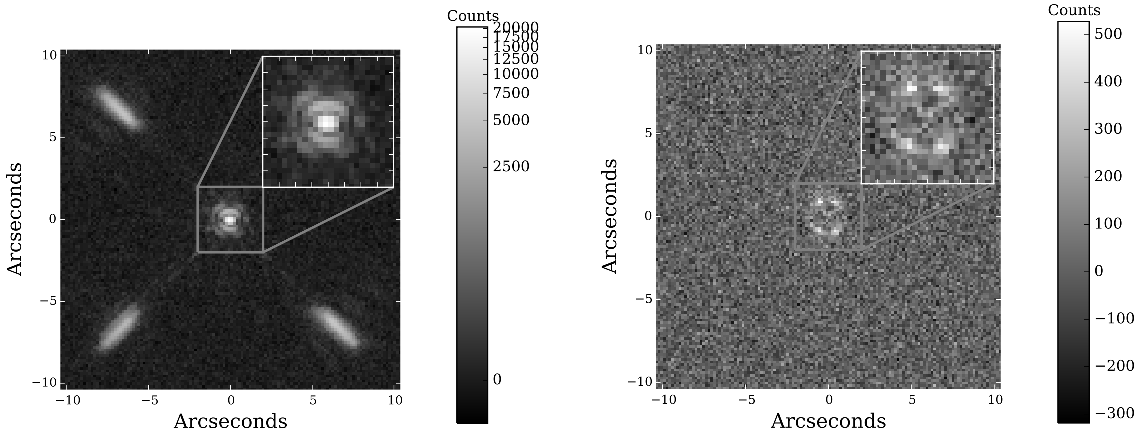

(a) Simulated average image as will be recorded during the PICTURE sounding rocket flight. The debris disk is nearly lost in the wings of the leaking PSF.

(b) After ideal PSF subtraction only noise and the predicted inner ring are visible. The expected face on ring is truncated at zero and 1" by the vertically oriented nuller fringe pattern.

of the measured map with a $15\lambda/D$ box kernel.) The synthetic map shown in the rightmost frame of Fig. 4.22 was created from a random two-dimensional PSD in *PROPER* (Krist, 2007), with 20 nm RMSE with power evenly distributed from 0 to 100 λ/D. The high frequency residual shown was generated by subtracting a boxcar convolved copy of the map in a manner identical to the measured map (Sec. 4.3.3). The synthetic map, based on the reported RMSE high-frequency error, was used for mirror acceptance modeling. The measured residual has a lower standard deviation than the synthetic map. However, the random PSD fails to capture systematic errors such as quilting or the ripple seen in measured wavefront error.

Fig. 4.23 shows the expected contrast curves generated with the Fraunhofer VNC model discussed previously. The contrast from three simulations is shown: the

Fig. 4.20: Radial average of noisy simulated observations after ideal speckle subtraction, with and without a 2×10^{-4} dust ring at 1" around ϵ Eri. Simulation is the same as the image shown in 4.19b. The dusty curve is weighted by the on-sky transmission function of the nuller. The ring is clearly detected at 1". Numerical model includes aberrations from low order telescope wavefront errors and a 5% intensity mismatch in the interferometer, approximating laboratory performance.

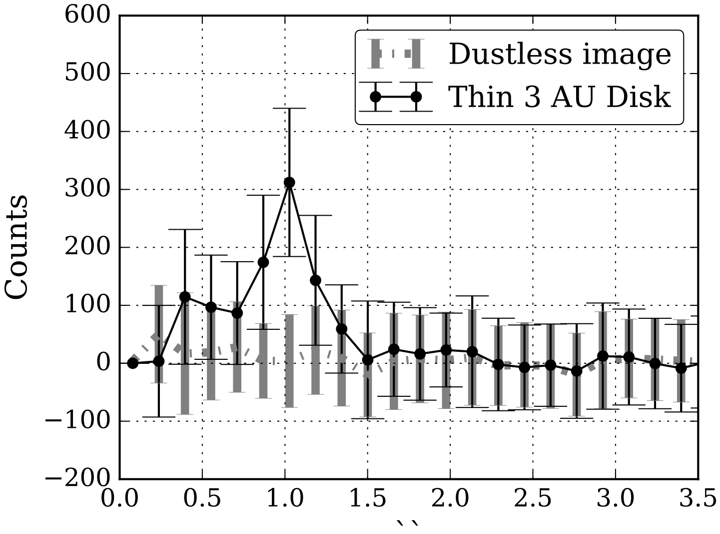

prescribed 10 nm RMSE wavefront above $15\lambda/D$ (dashed line), as well as a synthetic random 20 nm RMSE wavefront (thin solid curve), and the measured surface (gray dotted line). All three models include a modest 2% intensity mismatch between the arms and a high spatial frequency error map of the DM, whose actuator scalloping contributes the strong peak between 30 and 40 λ/D. These curves are monochromatic, polychromatic simulations would smooth and extend the diffraction peaks.

Despite filtering, the measured surface provides much worse high-contrast imaging performance near the central star (low to mid-spatial frequencies), than either of the synthetic surfaces. This maybe attributable to the mid-spatial frequency ripple, which unlike the DM scalloping is present in both arms of interferometer and thus presents a significant mismatch between interferometer arms when sheared, even af-

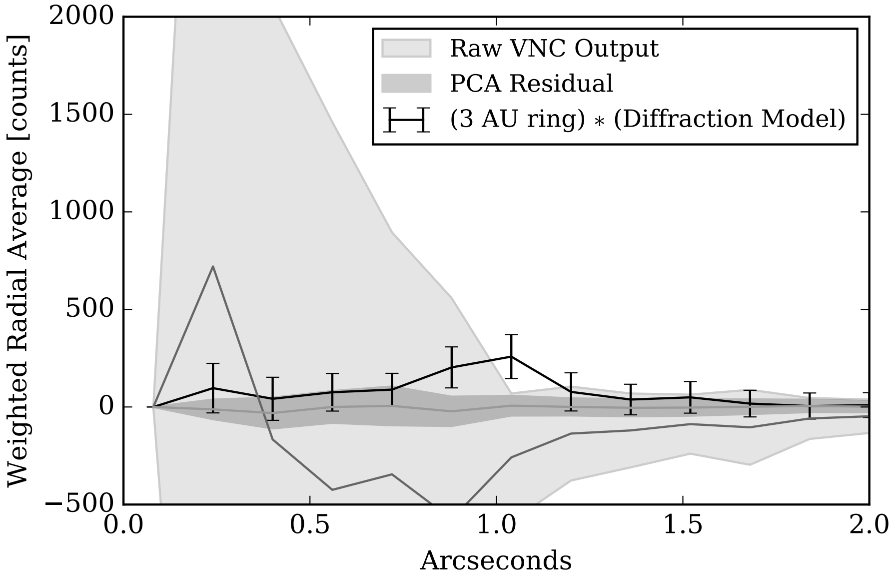

Fig. 4.21: Error bars show the transmission weighted radial averages of the modeled noisy dust signal. Shaded regions indicates the measured 1σ broadband VNC contrast reported in earlier sections: before post-processing (light gray) and after PCA subtraction (dark gray).

ter DM correction. This worsened contrast, however, is still below the 1σ laboratory contrast floor (shown in Fig. 4.9). Unlike the low frequency errors examined previously, the ripple does not significantly alter the appearance of the imaged debris disk itself, minimizing the contribution to the on-sky performance.

Spectral Type Effects

Since PICTURE observes a relatively wide passband, the dramatically different spectral types of Rigel (B8I) and ϵ Eri (K2V) add an additional dimension to speckle subtraction. As a diffractive effect, the position of speckles in the image plane is proportional to wavelength. Essentially parasitic spectrometers, speckles vary in shape and brightness with the stellar spectra. Fig. 4.24a is a noiseless, high resolution image of the telescope aberrated dust signal from Fig. 4.19b. The same dust signal, recovered by subtracting a much bluer calibration star (Rigel) from a leaked ϵ Eri

Fig. 4.22: **Left:** An interferometric surface measurement of the SiC primary mirror including significant spherical aberration. **Middle:** The interferometric measurement filtered to uncontrollable spatial frequencies (above $15\lambda/D$). **Right:** A synthetic controllable surface error from *PROPER* generated Power Spectral Density (PSD). Despite the similar standard deviations (σ) the synthetic surface shows more high frequency error while most of the power in the real measurement is visible as mid-frequency ripple. Note: color scale extents were chosen to show structure and do not represent data extrema.

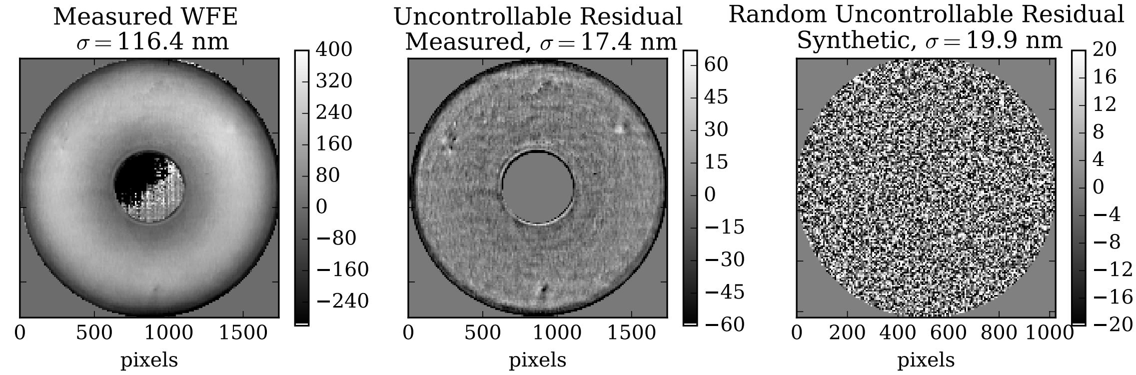

PSF in Fig. 4.25 shows artifacts due to the difference in the spectra of the two stars. In this simple model the only aberrations arise from the DM surface and the low-order telescope error in Table 4.1. Subtraction of the numerous speckles visible in dark frame of Fig. 4.6, from the as-built instrument, will each manifest similar color dependent error. The DM diffraction spikes enable a straightforward first-order correction: “zooming" or stretching the reference star image by interpolation onto new coordinate system such that the center-of-mass of the spikes matches the science target.

Fig. 4.25 illustrates PSF zooming with laboratory VNC data. Different color stars were simulated by varying the temperature of the OSL1 halogen light source in the VNC test setup shown in 4.3. The “center-of-mass” of the diffraction spike shifted by 1 percent, comparable to the “center-of-mass” difference between the Rigel spectrum and the ϵ Eri spectrum in the PICTURE science bandpass. The bottom right frame shows the diffraction spikes are more evenly subtracted and the central

Fig. 4.23: Monochromatic contrast curves for the measured, prescribed, and expected high spatial frequency wavefront error.

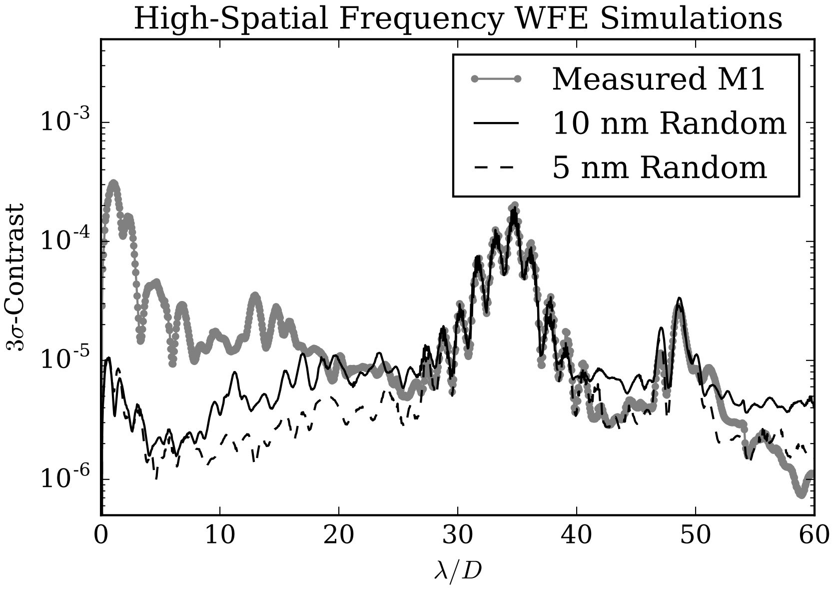

PSF standard deviation (σ printed within inset) decreased slightly. Future work to combine and optimize reference PSF stretching and PCA techniques is required to approach Poisson noise limited imaging.

4.6 Summary

Given the need for observations of exozodiacal scattered light to relate reflected light to thermal emission and test models of the structure of the ϵ Eri system, the PICTURE payload design fills a unique niche. The telescope resolution and the VNC contrast were found to be sufficient to image scattered light from the proposed narrow warm inner ring. These observations will constrain the aperture of a telescope needed to survey the ϵ Eri system for reflected light from small exoplanets. Through laboratory tests, the PICTURE VNC was found to reach 1σ contrasts as low as 10^{-6} after optimal speckle subtraction (Fig. 4.9). Even without speckle subtraction, the 3σ sensitivity at the IWA of $\approx 6\times10^{-4}$ exceeds the 6×10^{-3} sensitivity of previous 2μm

Fig. 4.24: Noiseless, oversampled models of a nulled dust ring around a K2V star, approximating ϵ Eri after subtraction of an ideal (a) PSF. Subtraction of the expect calibration PSF (b) shows the systematic error in speckle subtraction arising from stellar spectral type mismatch.

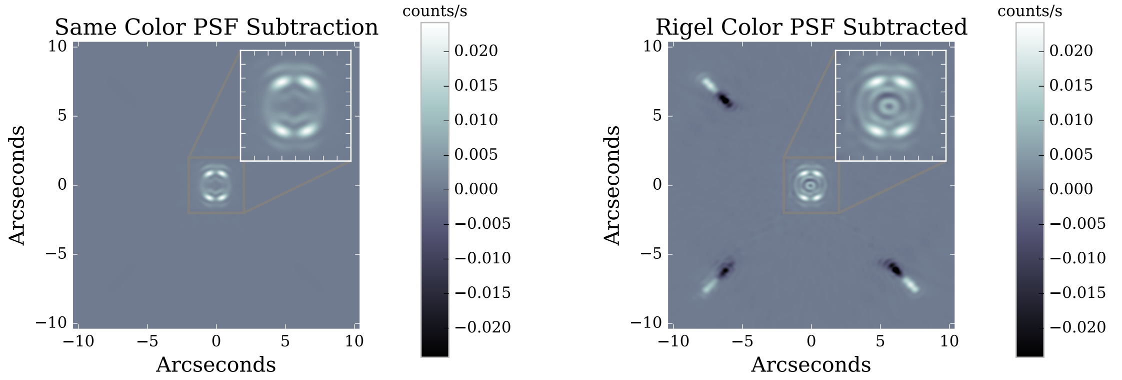

(a) Dust signal after propagation through the telescope and VNC model and perfect subtraction of the leaked ϵ Eri stellar PSF.

(b) Flight-like residual, when a Rigel-like B8I PSF observation is used as a speckle reference the dust signal is contaminated by mismatch in the PSF wings. Differences between the spectra are particularly pronounced in the four diffraction grating spikes.

studies of ϵ Eri (Di Folco et al., 2007). The speckle subtracted 3σ VNC sensitivity of $\approx 3 \times 10^{-6}$ is more than four orders of magnitude more sensitive. Challenges which remain include the optimal subtraction of stellar spectra of different colors and the effect of high-spatial frequency polishing ripple.

Laboratory tests of the PICTURE telescope showed that the assembly is highly sensitive to changes in temperature and requires tight temperature control to stay maintain focus. Numerical modeling of the VNC performance with an approximation of the as-built, near-focus telescope showed the integrated PICTURE payload was capable of imaging the narrow inner ring proposed by Backman et al. (2009) (Fig. 4.19b, also shown as a transmission weighted radial average in Fig. 4.20).

Fig. 4.25: Example of improving PSF subtraction for different color stars. Nulled images of cool and warm laboratory light sources are shown in the left column. The top image in right column shows the difference between the two nulled images. The difference in the color is most visible in the uneven subtraction of the four diffraction spikes. The bottom of the right column shows the difference between the images after the warm image was demagnified to better match the cooler image.

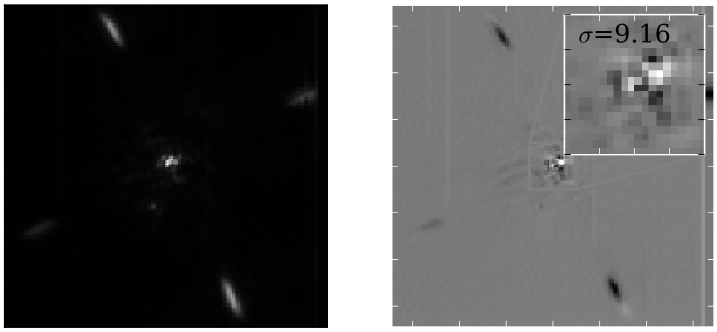

Cool Spectra

Cool-Warm

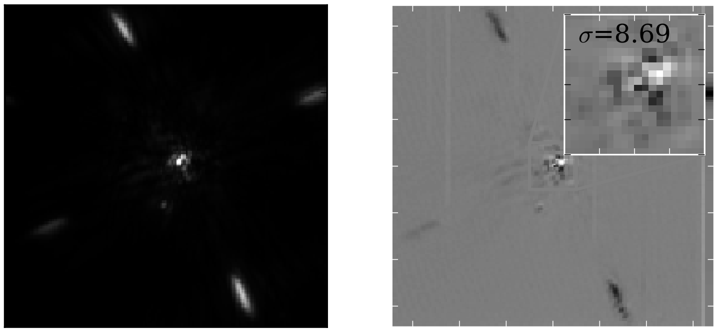

Warm Spectra

Cool-zoom(Warm)

Chapter 5

PICTURE Flights

The first Planet Imaging Concept Testbed Using a Rocket Experiment (PICTURE) payload launch, aboard National Aeronautics and Space Agency (NASA) sounding rocket 36.225 UG (a Black Brant IX University Galactic Astronomy mission), launched on 8 October 2011 from White Sands Missile Range (WSMR) with an observing time on Rigel of 350 seconds (preset by timers on the payload shutter door). The results are detailed in Mendillo et al. (2012a,b); Mendillo (2013). After extensive refurbishing, the payload was relaunched on a Black Brant IX as NASA 36.293 UG from WSMR on 25 November 2015 at 0417 UTC (9:17 PM MST on 24 November).

Three Attitude Control System (ACS) maneuvers were planned:

- Nuller alignment and 10 seconds of speckle observations on Rigel (β Orionis, m_v=0.13),
- Slew to Epsilon Eridani (ϵ Eri) and observe the circumstellar environment,
- Roll payload during the ϵ Eri observation to characterize speckles.

During ascent, the fine pointing system (FPS) computer, which also performs temperature datalogging, was powered on at t+47 seconds. The wavefront control system (WFCS) and telemetry processing computer was powered on at t+50 seconds. The FPS camera controller was powered on at t+74 seconds. After initial acquisition of

Rigel by the NASA Wallops Flight Facility (WFF) ACS, the payload Xybion® camera, with an approximately 10 arcminute circular field-of-view (FOV), was used to measure the pointing offset between the angle tracker camera (15 arcsecond circular FOV) and the ACS system. During both missions, a manual uplink successfully provided the pointing correction to ACS, placing Rigel on the angle tracker camera near the nominal t+105 second observing start time. Additional minor uplinks allowed centering of the star on the angle tracker to the ACS accuracy of approximately 1 arcsecond within the first twenty seconds on target. Once Rigel was centered, the fine pointing control loop locked, providing pointing precision error of approximately five milli-arcseconds Mendillo et al. (2012a). Flight 36.225 could not be observed to advance beyond this initial pointing due to the failure of a relay in the onboard telemetry system Yuhas (2012). The 36.293 telemetry system performed as designed and additional data was stored onboard the flight computers.

Two cameras observe the VNC output, a science camera which produces an image of the sky and a wavefront sensor (WFS) camera which images the output pupil plane. During the reflight the WFCS advanced to the VNC *coarse mode* or “phase-up" stage: locating the white light fringe packet, applying a predetermined map to approximately flatten the DM using a saved map (Fig. 5.1b) and attempting to flatten the wavefront error (eliminating optical path differences in tip, tilt, and piston (TTP) between the interferometer arms). In the planned flight sequence, coarse mode was followed by fine correction of higher spatial frequencies with the DM and finally a transition to *nulling mode* with the Nuller Piezo Electric Transducer (NPZT) shifted to the dark fringe for high-contrast “nulling” science imaging over the remainder of the flight.

Flight 36.293 did not achieve null because the wavefront could not be flattened. The closed loop correction of wavefront mismatch between the arms with the DM

Fig. 5.1: Open-loop flat map applied to deformable mirror (DM) during coarse alignment to compensate for stress induced surface curvature of the mirror.

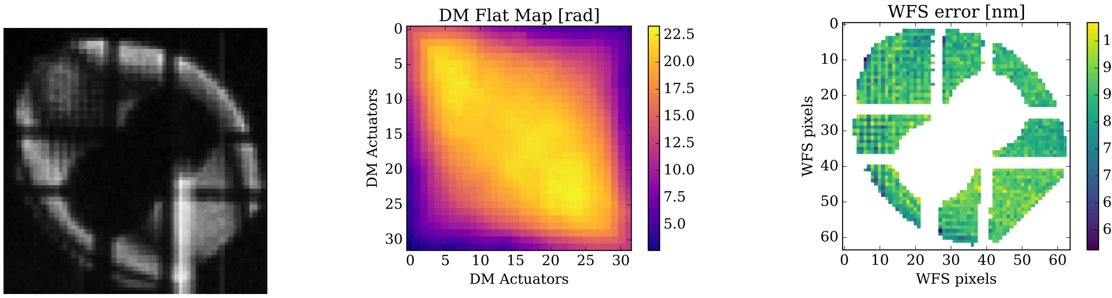

(a) Unpowered DM fringe pattern through Visible Nulling Coronagraph (VNC) (without telescope), showing more than a wave of curvature without the flat map. The light vertical bar is excess dark noise.

(b) The previously saved flat map applied to the DM in flight.

(c) A laboratory measurement of the VNC phase error with the flat map correction applied. This measurement was recorded in white light without the telescope.

was not initiated because the center of the white light fringe packet was outside the range of the NPZT to correct TTP errors.

The 36.293 telemetry system worked as designed and additional data was stored onboard the flight computers, providing significantly improved knowledge of flight performance. As will be detailed subsequently, this new dataset provides the opportunity to assess operation of the VNC in space. In addition to active measurements of wavefront, temperature sensor data and the telescope Point Spread Function (PSF) provide important insight into the condition of the PICTURE payload in space - answering the questions: *how well did the VNC sense wavefront errors in space? Was the telescope metering structure stable? And what was the thermal environment the payload experienced?*

A significant portion of the wavefront sensing results presented herein are also presented in Douglas et al. (2016).

5.1 Flight Performance

The following sections will quantify available information regarding telescope and instrument performance, including telescope PSF, wavefront correction, and achievable null depth. Section 5.2 describes thermal control requirements of the payload and the temperature data recorded on the launch rail and in flight. Section 5.3 details the angle tracker camera measurements of the telescope PSF as a function of time as well as the measured precision of the FPS. Section 5.4 motivates the need for precision wavefront sensing in space and describes wavefront sensor measurements performed with the PICTURE VNC. Section 5.6 details how the telescope PSF deteriorated over the course of the flight while Section 5.5 shows tube telescope temperature evolved during the flight. Section 5.7 compares the flight wavefront sensor precision to the theoretical expectation. Finally, Section 5.8 summaries the impact of these results on the intended science.

5.2 Temperature Measurements

5.2.1 Temperature Control Requirements

During the 36.225 flight, the telescope was significantly out of focus in-flight (Mendillo et al., 2012a), and the telescope temperature was significantly below nominal laboratory temperatures. As discussed previously, the 36.293 telescope, much like the 36.225 telescope (Mendillo, 2013, Fig. 5.13, p. 200)), showed a strong temperature dependency under laboratory conditions. Additionally, the optical path difference (OPD) between the nuller arms depends on temperature, bringing the white-light fringe position toward the NPZT by approximately 0.4 μm/°C (Mendillo,

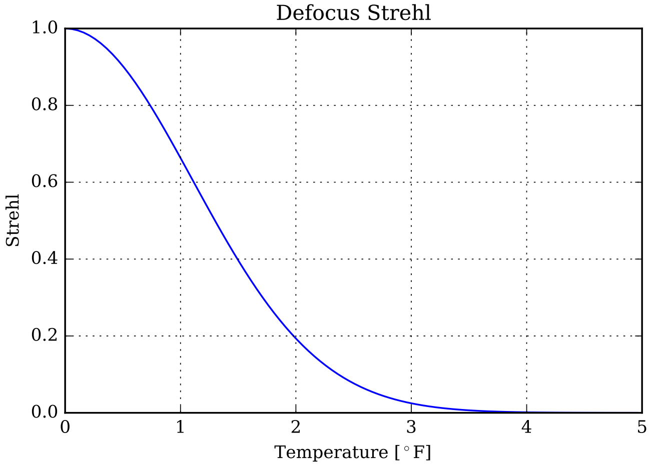

Fig. 5.2: Relation between Strehl ratio and mean tube temperature using the proportionality between temperature and the focus Zernike measured from laboratory data (e.g. Fig. 4.14b).

2013, Fig 5.14, p. 201). The NPZT and DM interferometer arm path lengths were matched by flattening the central white-light fringe with shims at the base of the NPZT mirror while the nuller deck temperature was approximately 67.5 degrees Fahrenheit.

The change in the peak pixel value provides a simple way of assessing PSF evolution. The Strehl ratio is the peak intensity of an aberrated PSF divided by the maximum intensity of the PSF for the corresponding diffraction limited aperture. Inspection of Fig. 5.2 shows the relation between the Strehl ratio of a telescope spot and the mean tube temperature, assuming 120 nm PV of pure-focus surface error per degree Fahrenheit, as found in laboratory testing. Mahajan (1983)[1] found an approximation for the Strehl ratio, S, from the variance of the wavefront error (WFE):

$$S \approx \frac{1}{e^{(\sigma(WFE))^2}} \tag{5.1}$$

---

[1] see also: `http://www.telescope-optics.net/Strehl.htm`

Fig. 5.3: The assembled PICTURE-B mission, 36.293 UG, mounted on the Athena launcher rail at WSMR. Image courtesy WSMR.

For pure defocus (Z_4), the variance of the wavefront, $\sigma(WFE) = Z_4/\sqrt{12}$ [radians].(Wyant & Creath, 1992, Table IV). Thus, for a pure focus error, the conventional "diffraction-limited" Strehl (> 0.8) is only maintained within a tube temperature range of approximately three quarters of a degree Fahrenheit. Due to the presence of other aberrations, a conservative temperature requirement of stability within ±0.25°F of 67.5°F, the laboratory focused temperature.

To meet these requirements, a new launch rail temperature control system was developed to monitor and control both the internal nuller temperature and the payload enclosure temperature for flight 36.293.

5.2.2 Thermal Control System

Radiative cooling of the monolayer-insulation-wrapped PICTURE telescope was assumed to be slow over the short flight. Thus, all thermal control was ground-based to optimize the temperature on launch, thereby minimizing the payload mass and

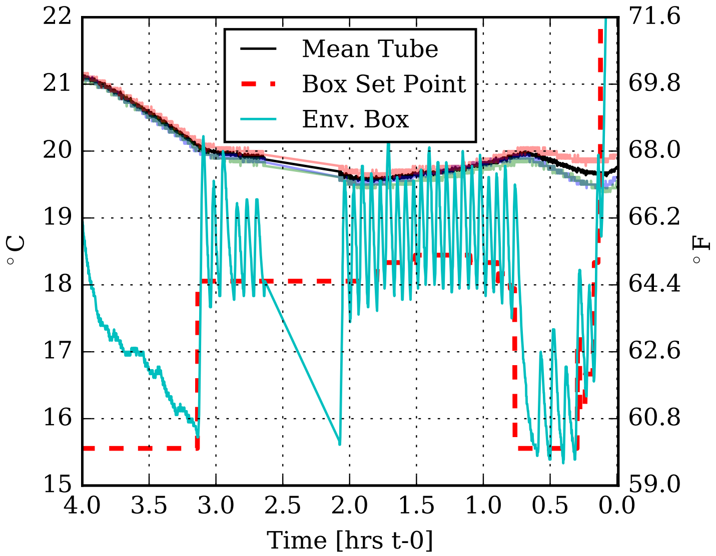

Fig. 5.4: Flight 36.293 launch rail temperature control and monitoring directly preceeding launch. The rapidly oscillating gray line shows the environment box temperature, driven by the WSMR external heater, and the control software setpoint (dashed line). The mean tube temperature is shown as a solid black line, calculated from the three measured tube temperatures (ticker pale colored thick lines).

complexity. An electric heater provided by WSMR provided a fast moving warm air input to a white polystyrene box enclosing the payload from the WFF telemetry section to the base of the second stage booster (Fig. 5.3). A four-wire RTD provided temperature sensing in the box and allowed the experiment team to command payload temperature via closed loop "bang-bang" (on-off) control of the heater. The loop allowed control of the mean temperature of the carbon fiber tube to small fraction of a degree: Fig. 5.4 shows the set-point, control temperature and telescope tube temperature versus time during the pre-countdown period. After aggressive cooling until nearly *t*-three hours, the telescope tube temperature was stabilized by controlling the environment box temperature (thin pale blue line) by manually varying the control set point (dashed line). The environment box cooling rate (discernible as the period of the heater oscillations) depends on the temperature gradient between the payload and the box, the external temperature, and the payload orientation. From

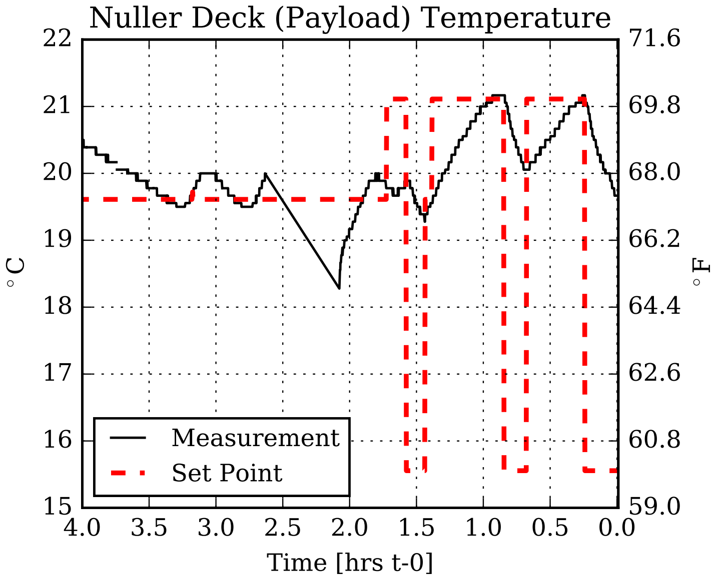

Fig. 5.5: Flight 36.293 instrument section temperature control and monitoring directly preceding launch. The last measurement before launch was 67.4 degrees Fahrenheit.

t-three to 2.5 hours, warmer ambient temperatures and a shelter shielded the box. After the sensor blackout of motor arming, completed at approximately *t*-two hours, the payload was elevated (to near vertical) and exposed to gusts of evening desert air, requiring an increased heater duty-cycle. The weighted-mean tube temperature at launch was 67.6 ± 0.3 degrees Fahrenheit. This temperature was within the window of 67.25-67.75 degrees Fahrenheit expected to maintain diffraction limited telescope focus.

Additionally, a 600 watt heating element was added to an N_2 gas purge line which entered the payload at the electronics bulkhead and provided closed loop control of the nuller deck temperature on the launch rail. Fig. 5.5 shows the air temperature in the instrument section, recorded by a Omega Engineering Inc. *iTH*-model temperature and humidity probe (manufacturer specified ±0.5 Celsius accuracy) mounted on the nuller deck.

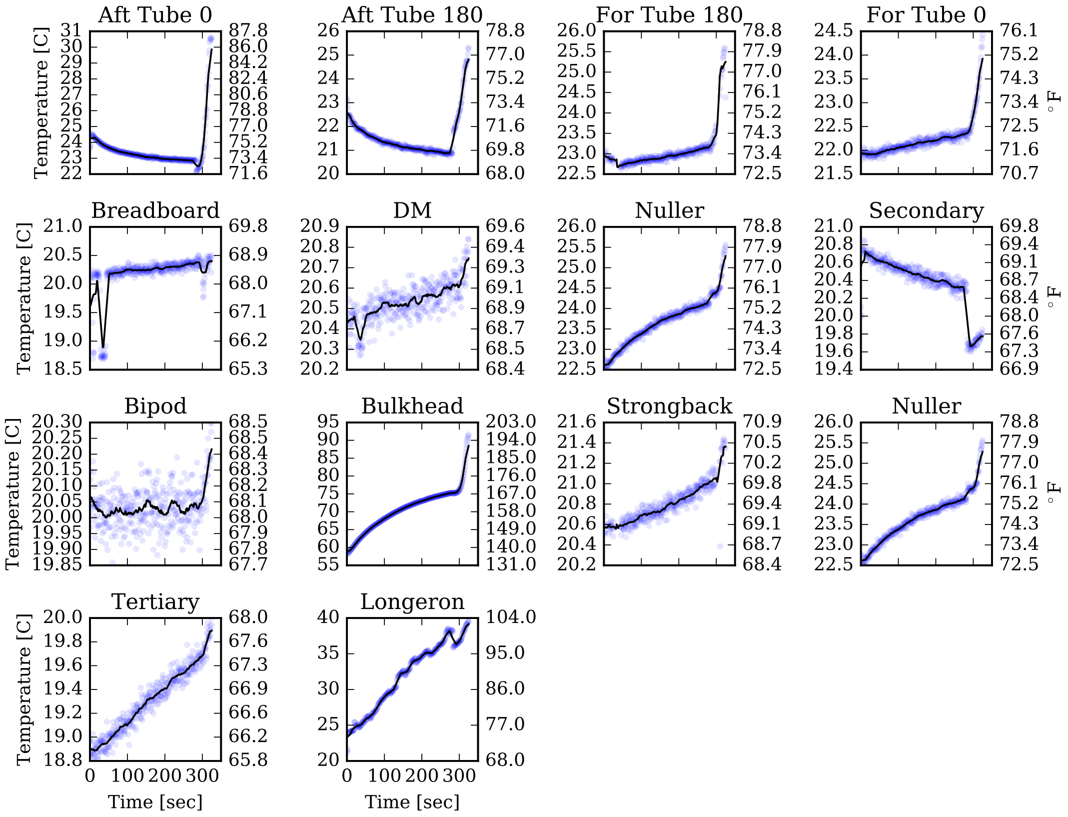

Fig. 5.6: Temperatures recorded onboard flight 36.293. Solid line shows the 20 measurement running average. Payload warming on re-entry occurs near 300 seconds from the start of temperature recording. These time series have been filtered to remove large outliers due to data dropouts. Unlike the 4-wire Resistance Temperature Detector (RTD) measurements shown in Fig. 5.5 and 5.4, these measurements were made with integrated circuit temperature transducers. The flight measurements shows significant offsets from the pre-flight temperatures. This mismatch is due to variations in calibration and sensor location as well as the launch thermal inputs (skin heating and adiabatic escape).

5.2.3 Onboard Temperature Measurements

A launch rail temperature monitoring system was added to the payload for flight 36.293 and readout via a direct connection between controllers and experiment section skins. Since these new temperature sensors were unreadable via the flight telemetry, the original temperature monitoring system from 36.225 was enabled both on the ground and in flight.

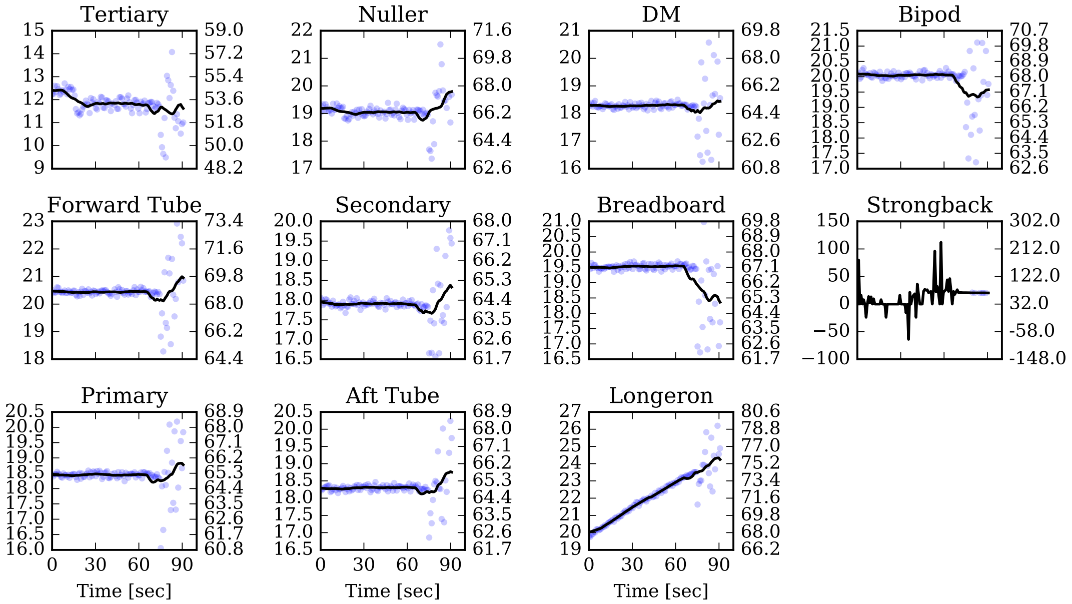

Fig. 5.7: Temperatures recorded onboard flight 36.225. The strongback temperature sensor values are erroneous.

Fig. 4.11 shows a rendering of the payload with the skins removed for clarity and the telescope carbon tube partially transparent. The four telescope temperature sensors were positioned in pairs at either end of the carbon tube, one on each side, 180 degrees apart. The forward pair of sensors is near the primary mirror and the aft sensors are just forward of the secondary mounting vanes. Fig. 5.6 shows the temperatures measurements recorded for optic and metering structures during flight. These measurements were all made using Analog Devices AD590 2-terminal integrated circuit temperature transducers, with the exception of the "Aft Tube 180" sensor, a Minco 2-Wire RTD. A twenty second running average (solid line) smooths the sensor noise to illustrate the trends in each optic. For comparison, Fig. 5.7 shows temperature data recorded during flight 36.225. Unfortunately, due to glitches in the FPS computer, the temperature data for the complete 36.225 observing window is not available.

Fig. 5.8: Full frame angle tracker images of Rigel showing the deterioration of focus over the course of flight 36.293, from when the star was initially acquired by the FPS (left) to the last frame before the shutter door closed (right). Both images are shown on a linear scale normalized to the maximum intensity of the initial image.

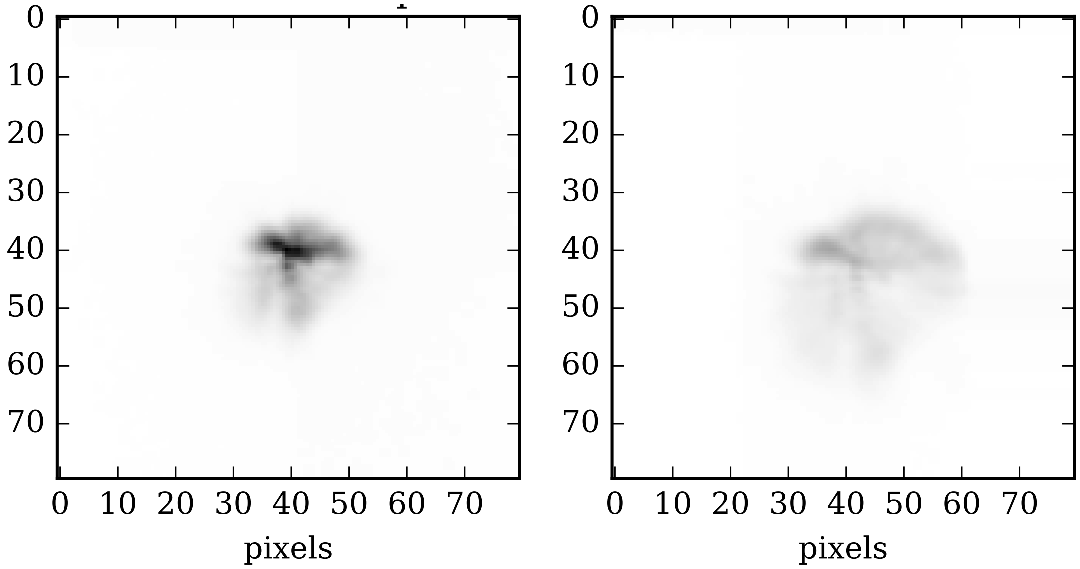

5.3 Angle Tracker Measurement

Besides the primary role of the angle tracking camera providing precision attitude sensing for the FPS, full-frame images from the e2v CCD39 (80x80 pixels at ≈0.19”/pixel) stored onboard provide a monitor of the evolution of the PSF during flight 36.293. This is the first time the full PICTURE telescope PSF has been observed during flight as full-frame images were not stored during 36.225. Images are recorded at a 1 second cadence to onboard solid state storage. Post-processing consisted of dark subtraction. Fig. 5.8 shows the first and last frame of the angle tracker image; the initial spot is moderately well focused but the final PSF occupies nearly a third of the frame.

A preliminary analysis of the 36.293 pointing precision (C.B. Mendillo, private communication) shows pointing precision surpassing the 5.1 milliarcsecond precision reported for a 30 second window of flight 36.225 in Mendillo et al. (2012a). Fig. 5.9

Fig. 5.9: Fine pointing system error, each point represents an angle tracker centroid. The circles show the total enclosed error, with the innermost circle indicating 1σ. (figures provided by C.B. Mendillo, private communication).

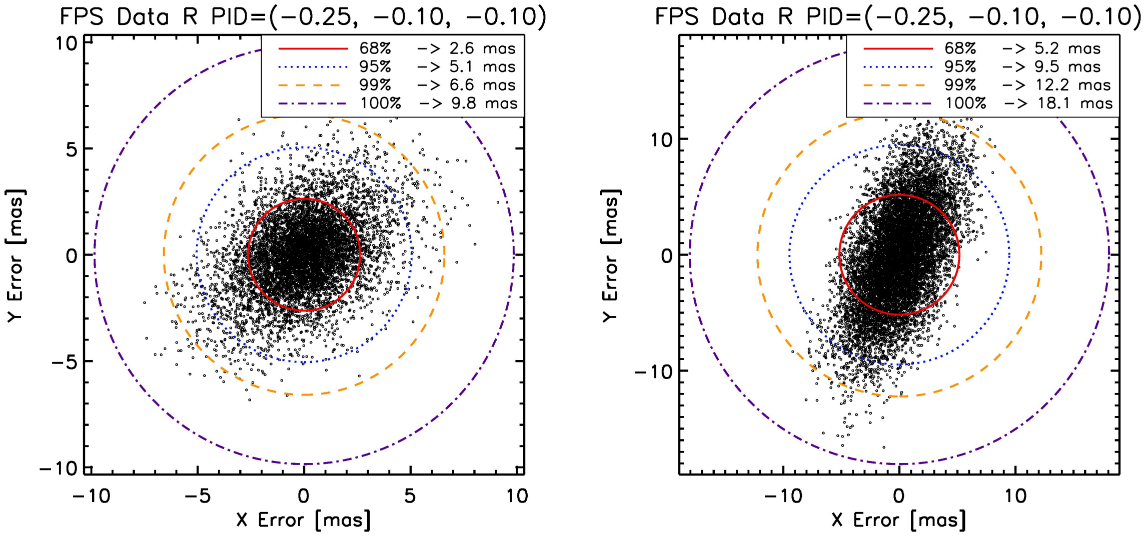

(a) First 34 seconds of FPS data on Rigel.

(b) Last 47 seconds of FPS data on Rigel.

shows the pointing error measured from centroid positions in detector coordinates. The innermost circle shows the total enclosed error for each period of observation, for the first half minute of flight, Fig. 5.9b shows 2.6 millarcsecond pointing precision immediately following Rigel acquisition. For the final 47 seconds of observing, Fig. 5.9b the FPS precision decreased to 5.2 milliarcseconds, on par with flight 36.225.

5.4 Wavefront Sensor Measurements

This section will detail the collection and processing of wavefront sensor data during the 36.293 flight. Wavefront sensing and control is the cornerstone of high-contrast imaging.

The 36.225 flight of PICTURE demonstrated first order adaptive optics (AO), allowing sensing and control of tip-tilt to approximately 5×10^{-3} arcseconds RMS (12

Fig. 5.10: Four step “ABCD” Phase Measurements.

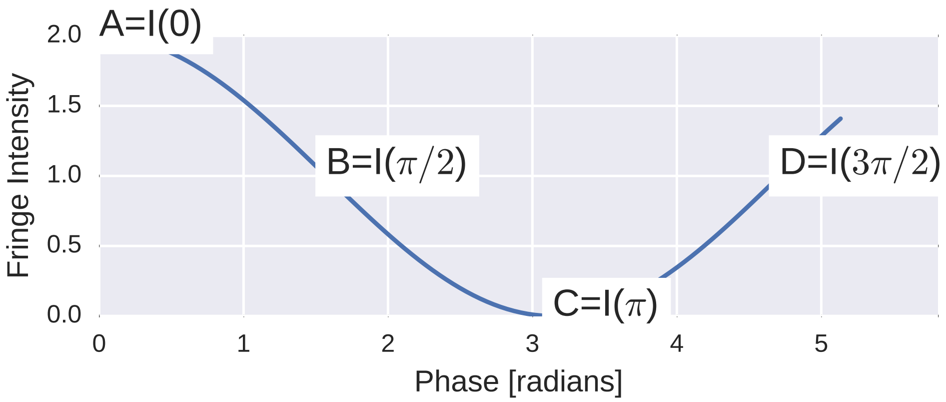

(a) Ideal phase curve with four measurements labeled.

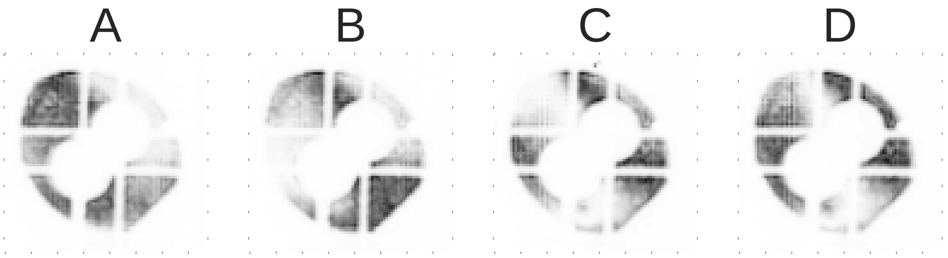

(b) Example of flight WFCS measurements at four NPZT steps from 36.293 flight data.

nm PV across a 0.5 m telescope) at an update rate of 200 hz (Mendillo et al., 2012a). Laboratory tests of the PICTURE VNC without the telescope (Section 4.3) found a 5.7 ± 2.6 nm phase error at controllable spatial frequencies with a 1 hz update rate. High precision, end-to-end laboratory testing of the assembled payload including the telescope was limited by environmental disturbances (atmospheric turbulence and optical bench vibration) as well as the double pass nature of the test setup (described in detail by Mendillo et al. (2012b)). Flight of 36.293 did not achieve null because the wavefront could not be flattened within the range of the NPZT mirror. The initial coarse flattening was initiated and accurate measurements of the wavefront phase error were recorded. Thus, the mission did return valuable wavefront sensing measurements of phase at an approximately one second cadence.

Throughput

The instrument throughput drives both the wavefront sensing budget and the science signal-to-noise ratio (SNR). Fig. 5.11a shows the per pixel number of electrons per second incident on the WFS during flight 36.225. Background pixels behind the Lyot stop are masked. Fig. 5.11b shows the same map for flight 36.293. A low count rate, 30% below the prediction (Section 4.5.2), during flight 36.225 was attributed to primary mirror coating degradation; however, the average flux per pixel is indistinguishable between the two flights. The total number of active pixels is approximately fifty percent larger for flight 36.293, increasing the expected science camera flux significantly. This increase is because prior to flight 36.225 the Lyot stop mask was enlarged to cover DM actuators that became unresponsive due to damaged cables. The flight 36.293 refurbishing included a new deformable mirror and drive cables, allowing mask transmission of nearly the complete overlap region of the two beams, increasing the throughput by maximizing the effective area. Table 5.1 shows the *pysynphot* throughput model predicted total on-sky WFS count rates. The WFS gain is approximately $4e^{-1}$/count while the science gain is near unity. The ratio of the predicted and observed count rate per pixel on the WFS was used to correct the throughput values in the bottom row. The corrected SCI values provide a best-estimate of the ϵ Eri count rate incident which would have been observed in flight.

5.4.1 Wavefront Sensing

The PICTURE design leverages the interferometric nature of a nulling coronagraph to directly measure wavefront error at the science output of the VNC. Subsequent sections describe and compare two approaches to retrieving phase information from the data recorded in flight.

Fig. 5.11: WFS intensity maps from Rigel observations during each flight of the PICTURE payload. Both maps are placed on axes with equal areas to illustrate the increased total throughput of flight 36.293. A single color scale was also chosen inclusive of all values in both images for ease of comparison.

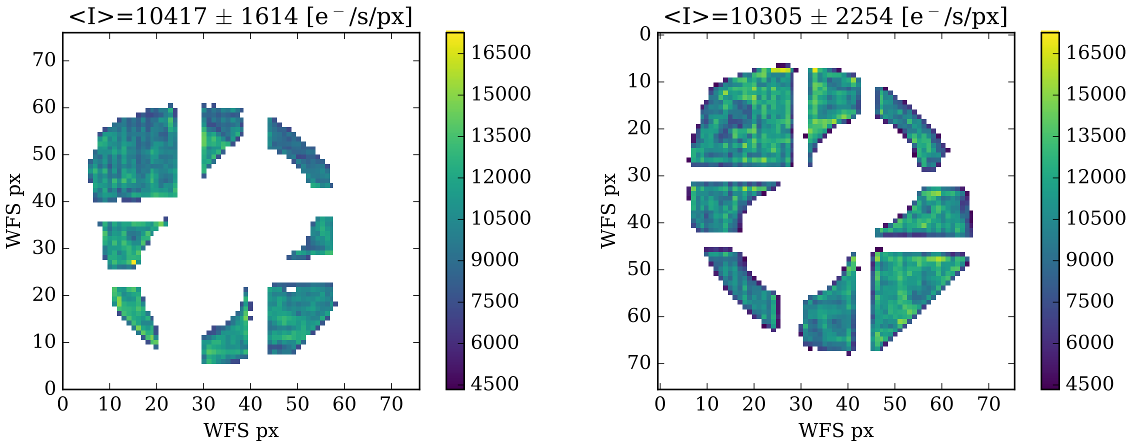

(a) Mean wavefront sensor intensity from the 16 sets of ABCD frames transmitted before loss of telemetry in flight 36.225.

(b) Mean wavefront sensor intensity from five sets of ABCD frames acquired before the central fringe packet was located in flight 36.293.

Calculating the phase

Simplifying the interference equation (Born & Wolf, 1980, p. 503) by assuming two beams of equal intensity (I) gives a relation between fringe intensity, $I(\Delta\phi)$, and phase difference, $\Delta\phi$, between the beams:

$$I(\Delta\phi) = 2I + 2I\cos(\Delta\phi)\mu. \tag{5.2}$$

μ is the coherence between the two beams. μ is near unity for measurements at the center of the white-light fringe packet. For a discussion of the spatial coherence, see Section B. The total phase difference can be written as $\Delta\phi = \delta + \Delta\phi'$ where $\Delta\phi'$ is the phase error we seek to measure and δ is the phase step between each frame. This allows expansion of the cosine term: $\cos(\Delta\phi) = \cos\delta\cos\Delta\phi' - \sin\delta\sin\Delta\phi'$. Defining

Table 5.1: Science camera and per pixel wavefront sensor count rates (in e^-/second) for both Rigel and ϵ Eri. The first row shows the predicted values based on the *pysynphot* model of the payload throughput and the middle row is corrected for the observed on-sky wavefront sensor count rates. The bottom row shows the measurements available from flight 36.293. N/A indicates flight values that are not available due to detector saturation or because ϵ Eri was not observed.

	Rigel SCI	eEri SCI	Rigel WFS, per px	eEri WFS, per px
Predicted	1e+08	6.8e+06	1.5e+04	1e+03
Predicted w/ 36.225 correction	7e+07	4.6e+06	1e+04	6.7e+02
36.293 Observed	N/A	N/A	1e+04	N/A

three new variables allows us to simplify the relation, $a_0 = 2I$, $a_1 = a_0 \cos \Delta\phi'$, and $a_2 = -a_0 \sin \Delta\phi'$, such that: $I(\Delta\phi) = a_0 + a_1 \cos \delta + a_2 \sin \delta$. The PICTURE payload was designed to recover phase by recording WFS intensity measurements at a sequence of four measurements separated by $\pi/2$ as shown in Fig. 5.12. For convenience, we rename each of these intensities: **A**$= I(\Delta\phi', \mu, \delta = 0)$, **B**$= I(\Delta\phi', \mu, \delta = \pi/2)$, **C**$= I(\Delta\phi', \mu, \delta = \pi)$, **D**$= I(\Delta\phi', \mu, \delta = 3\pi/2)$. Solving the system of equations composed of the four intensity measurements and the known phase step values permits calculation of the phase error of each pixel for a set of ABCD measurements (Wyant, 2011, 1975):

$$\Delta\phi' = \arctan(\frac{A-C}{B-D}). \tag{5.3}$$

The fringe visibility, V, shown in the rightmost column of Fig. 5.12, is a measure of the degree of coherence in an interference pattern,

$$V \equiv \frac{I_{max} - I_{min}}{I_{max} + I_{min}}. \tag{5.4}$$

The left panel of Fig. 5.13 shows a phase measurement made by applying Eq. 5.3 to the flight measurements in Fig. 5.12b. Despite the low visibility of the measurement, phase is recovered across the interferred pupil.

Fig. 5.12: Examples of Rigel wavefront sensor observations during flight 36.293. The first four columns correspond to the four wavefront sensing frames, A, B, C, and D. The position of the each of the three NPZT actuators is shown in microns in the title of each frame. The first actuator is observed to be railed at the full range (~8.5 μm) for each frame in the top and bottom rows. The far right column shows the fringe visibility for the corresponding row of measurements.

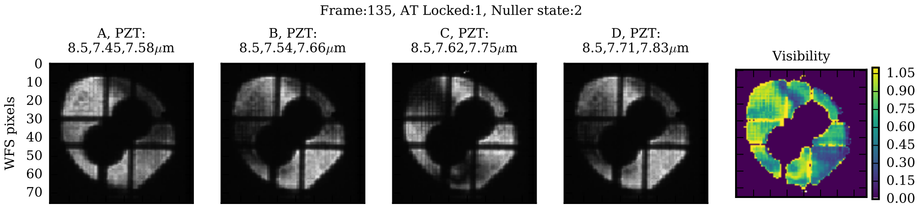

(a) The first measurement recorded in coarse alignment mode.

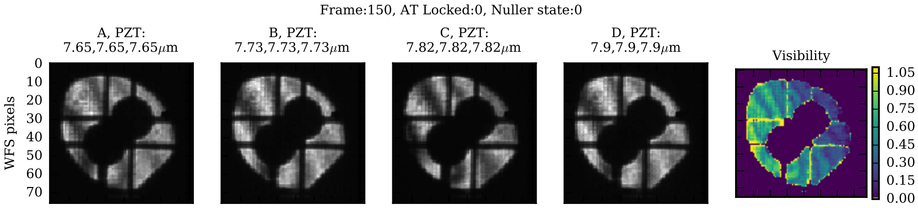

(b) Example of low visibility fringes with complete phase steps while the pointing system was unlocked.

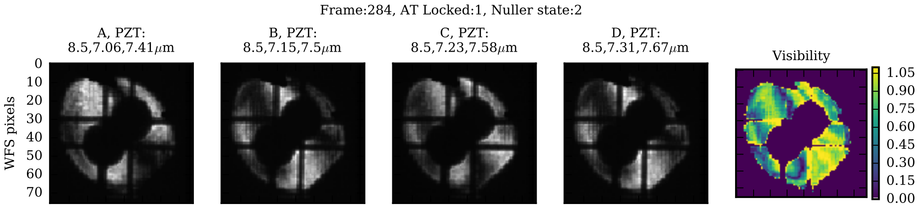

(c) The final WFS measurement with the pointing system locked. The number of fringes across the pupil has increased from Fig. 5.12a because the telescope focus degraded over the duration of the flight.

Phase Unwrapping

Due to the cyclic nature of the arctan function in Eq. 5.3, the phase measurement in the left panel of Fig. 5.13 appears as an extended two-dimensional sawtooth pattern, limited to a range of 2π. We know that the optical surfaces do not follow this sawtooth pattern, so additional processing in the form of "unwrapping" is required before we can visualize the wavefront phase. That is, the measurements are *modulo*

2π, and the phase must be reconstructed to eliminate the apparent saw-tooth pattern and measure the true WFE. As shown in the right panel of Fig. 5.13, phase measurements were successfully unwrapped in post-processing via the Herráez et al. (2002) method. This method is robust to noisy data and many fringes across the pupil plane but must be performed across a contiguous phase measurement, requiring manual optimization of unwrapping boundaries making. This manual adjustment makes the Herráez et al. (2002) method less useful for highly time-constrained sounding rocket flight. The PICTURE flight code (Mendillo et al., 2012b) used an iterative Picard method to globally unwrap the phase (Ghiglia & Romero, 1994; Ghiglia & Pritt, 1998). This unwrapper works well for fewer than approximately three fringes across the WFS pupil plane, but was found to fail and introduce discontinuities when correcting larger errors, presumably due to limited and varying phase information in regions of the complicated pupil plane mask.

Least Squares Fitting of the Phase

Due to the large path difference, during flight 36.293 one of the three piezo actuators translating the NPZT mirror was railed high (out of range) for many of the ABCD measurements, while the other two actuators moved the mirror in $\pi/2$ steps, causing an varying phase shift (δ) across the pupil image. Moreover, this is true of the high visibility measurements (e.g. Fig. 5.12a and Fig. 5.12c) where the path length between the arms was best matched, meaning the railed frames are also the measurements with the most phase information.

To compensate for this uneven shifting of the NPZT mirror, an alternative approach to measuring phase was applied. For varying values of δ, the phase error ($\Delta\phi'$) was recovered by least squares fitting of the intensity ($I(\Delta\phi)$) versus phase step size (δ). Allowing for variation in coherence, we fit a model of three unknowns:

$$I(\Delta\phi) = a_0 + (a_0 \cos \Delta\phi' \cos \delta - a_0 \sin \Delta\phi' \sin \delta)\mu. \tag{5.5}$$

δ values for each WFS pixel were calculated from commanded NPZT positions using a laboratory calibrated transformation matrix of NPZT actuator positions to surface tip-tilt. To constrain the problem, bounds were set requiring a coherence between 0.01 and unity and a phase shift between 0 and 2π, and this least squares bound-constrained minimization was solved using the subspace trust region interior reflective algorithm (Branch et al., 1999).

To validate this new approach, it was first tested on a low visibility measurement where four $\pi/2$ phase steps were taken as designed (Fig. 5.12b). Fig. 5.14a shows the results of this fitting, the total wavefront error agrees well with the results of Eq. 5.3 shown in Fig. 5.12, *modulo* a constant offset. Quantitatively, Fig. 5.15a shows excellent agreement between the mean subtracted wavefront errors calculated via both methods for one row of WFS pixels. The error bars on the constant δ derived phase curve (black line) are the theoretical minimum error, calculated via propagation of Poisson estimated shot noise (Wyant, 1975). The error bars on the least squared fit (gray line) are the 1σ uncertainty in the fit.

Least squares fitting of each pixel was repeated on the four frames of the first railed measurement (Fig. 5.12a) with varying values of δ and the resulting phase map is shown in Fig. 5.14b. Comparison of cross sectional slices of the phase across a row of WFS pixels shows indistinguishable results between the two methods in Fig. 5.15b.

The flight control software (Mendillo et al., 2012b) required all four ABCD measurements to determine the phase using Eq. 5.3. Given the good agreement in Fig. 5.15b and the computational efficiency of the original approach, the prelimi-

Fig. 5.13: Pupil plane phase measurement example. **Left:** the phase ($\Delta\phi$) calculated from the WFS frames shown in Fig. 5.12. The decreased visibility due to the NPZT actuator railing in flight is visible as phase noise on the upper right side of the pupil. **Right**: the unwrapped phase.

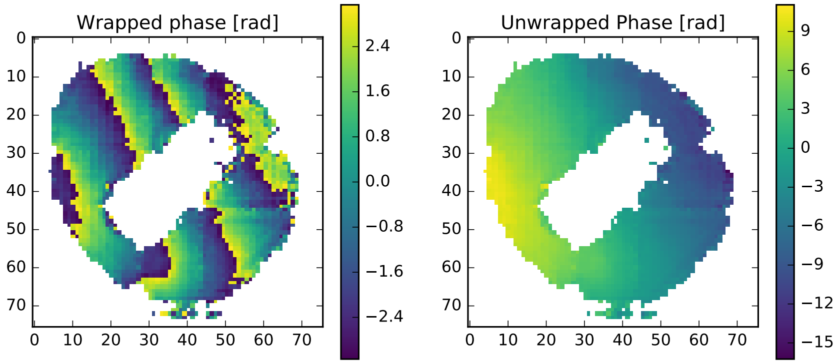

nary results presented below continue the assumption of constant δ to illustrate the wavefront sensing stability and provide an estimate of the sensing precision.

Fig. 5.14: Wrapped (left) and unwrapped (middle) pupil plane phase measurements from least squares fitting of four wavefront sensor measurements and corrected NPZT positions. The error (right panel) is 1σ fitting error.

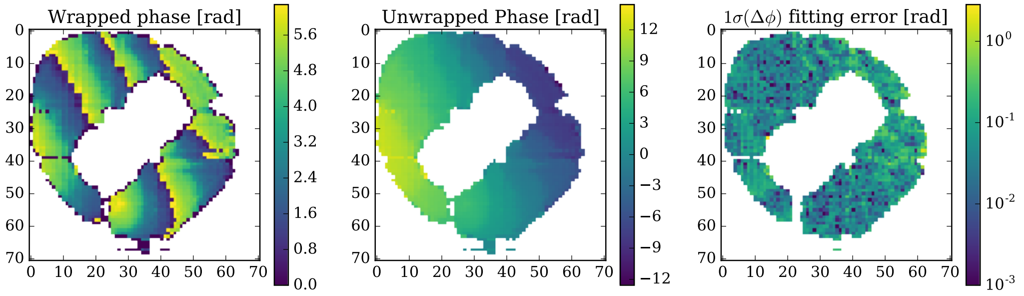

(a) Demonstration of least squares fitting technique on a low fringe visibility measurement where each piezo actuator moved $\pi/2$ (Fig. 5.12b).

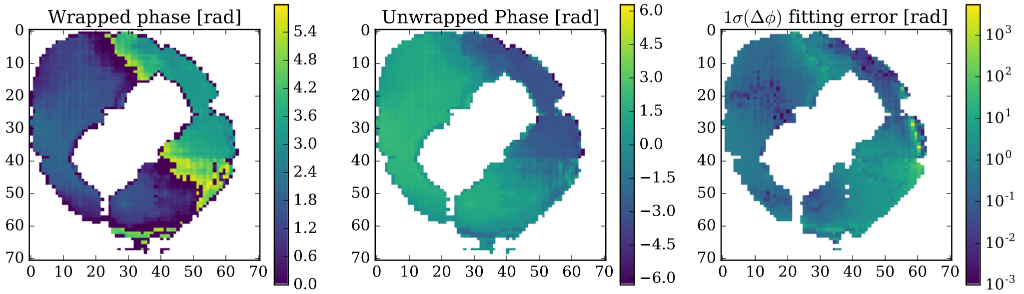

(b) Example of least squares phase data from wavefront sensor frames where one piezo actuator railed (Fig. 5.12a).

Modal Fitting

Zernike polynomials provide a convenient basis to describe low spatial frequency wavefront aberrations and are commonly used to characterize the surface figure of circular optics. Since the PICTURE VNC shears a copy of the pupil plane before interfering the beams, the wavefront error measured at the WFS is not directly mappable to errors in the surface of telescope optics. Fig. 5.17 shows the first 30 interfered Zernike polynomials sheared by 30% of the aperture, equivalent to the 0.5 m PICTURE baseline of 0.15 meters. Each map is created by generating a standard Zernike wavefront error map (Fig. 5.16) in POPPY (Perrin et al., 2016), shearing a copy of the map and subtracting it from the standard map. This set of phase maps

Fig. 5.15: Cross-sectional slices of the phase maps in Fig. 5.14 measured via the standard method (Eq. 5.3) and by least squares fitting showing the equivalence of the two methods. Calculated by taking slices at WFS pixel row eleven. Error bars on constant δ measurements (gray) are the photon limited 1σ error for ideal wavefront sensing. Error bars on least squares fits (black) are 1σ fitting errors.

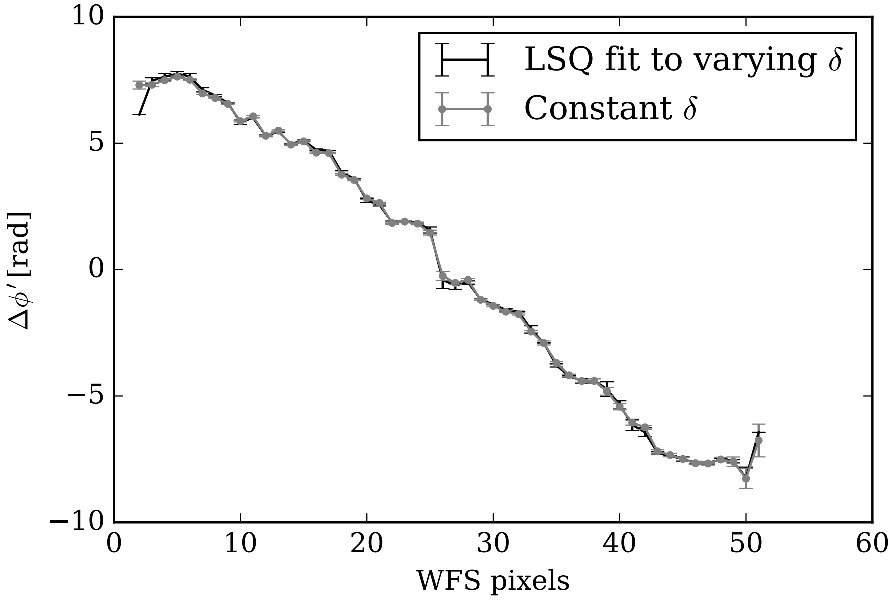

(a) Demonstration of least squares fitting technique on a low fringe visibility measurement where each piezo actuator moved $\pi/2$ (intensities shown in Fig. 5.12b).

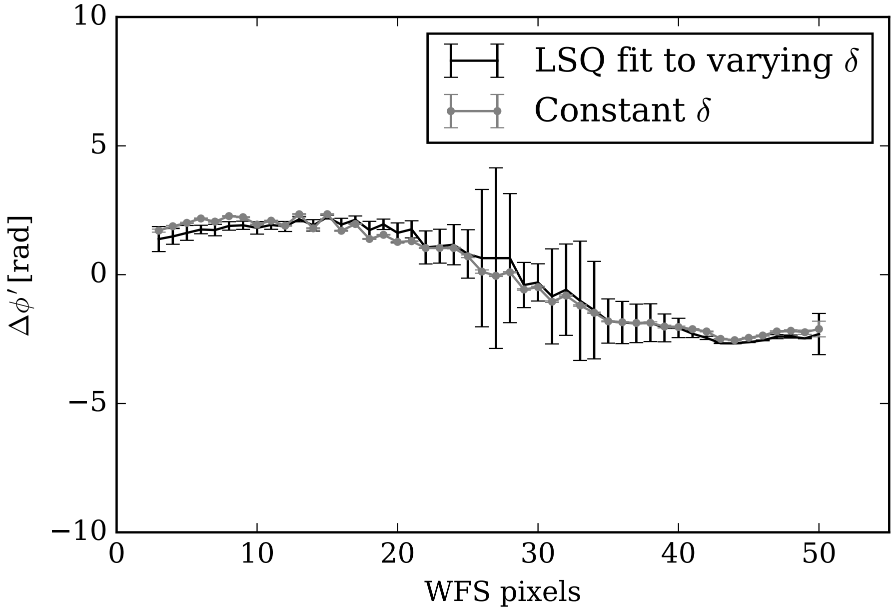

(b) Example of phase calculated by fitting to wavefront sensor frames where one piezo actuator railed (intensities shown in Fig. 5.12a).

Fig. 5.16: Phase maps of standard Zernike polynomials, generated with POPPY (Perrin et al., 2016).

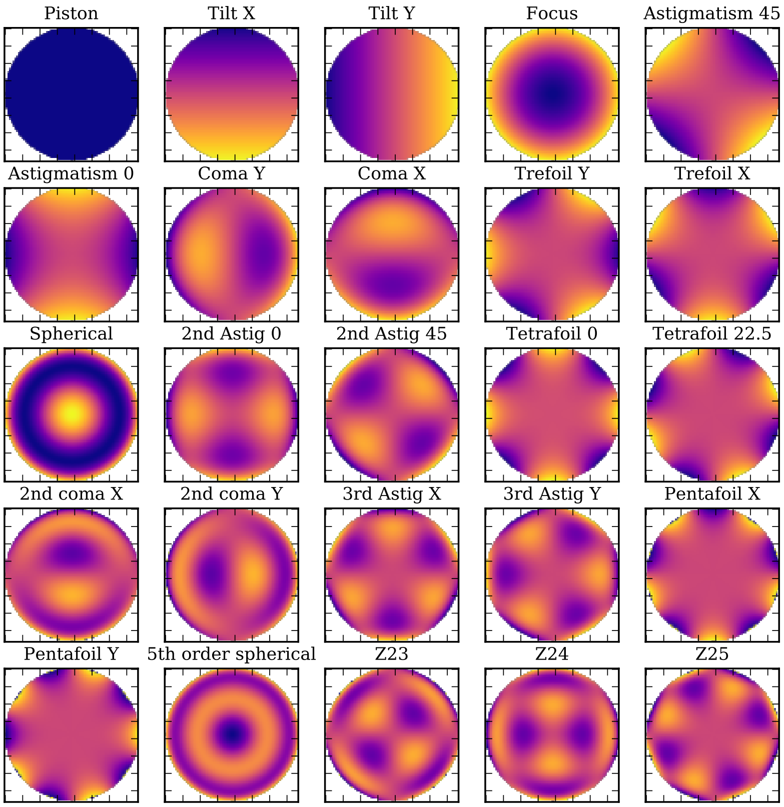

defines a vector representing conventional wavefront aberrations which can be fit to the WFS data to measure the dominant modes of the system. Some of the new basis vectors are degenerate, for example, as seen in Fig. 5.17, the focus and astigmatism 0 both manifest as y-axis tilts. This approach has been used previously using two orthogonally sheared measurements to minimize degeneracy (Harbers et al., 1996).

Subtraction of the best-fit sheared Zernike phase maps removes time-varying biases from each frame (such as changes in focus), allowing characterization of the per-pixel sensing precision of the WFCS. Fitting was performed by minimization, with Powell's method (Powell, 1964), of χ^2 between each unwrapped phase measurement and the sheared Zernike basis with a phase variance calculated from the Poisson limited per-pixel uncertainty.

Fig. 5.17: Phase maps of interfered Zernikes polynomials after a 30% shear, as would be observed after the PICTURE VNC. See Fig. 5.16 for maps of the un-interfered polynomials.

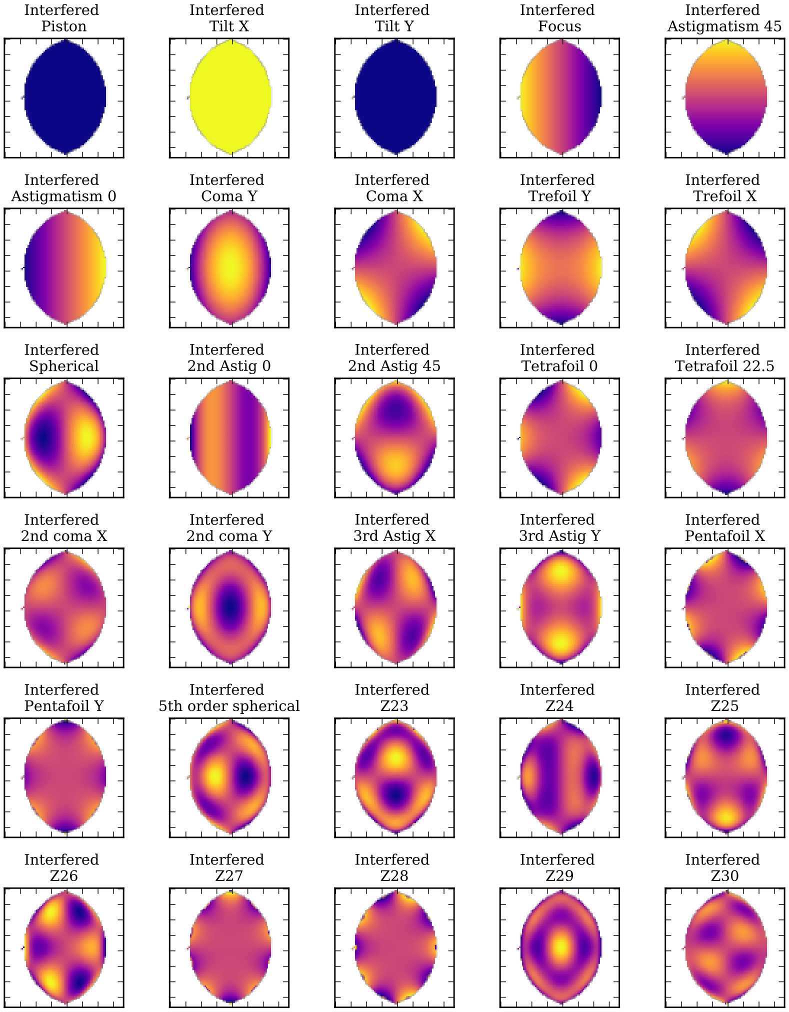

5.4.2 Instrument States and Best Measurements

The flight WFCS initially hunts for the white light fringe packet by stepping through the full range of NPZT values until a peak in the visibility (Eq. 5.4) is located. The fringe packet is then flattened by the "coarse-mode" Proportional-Integral-Derivative (PID) loop correcting the TTP error in the measured wavefront. At the end of this mode each pixel should approximately follow the *ABCD* curve (Fig.

Fig. 5.18: Time series of Zernike coefficient polynomial fits to each of the 11 initial consecutive coarse mode phase measurements. Focus and astigmatism dominate and the defocus is drifting steadily negative. An increase in defocus was also observed in FPS camera images. The mean fit residual is shown in Fig. 5.19

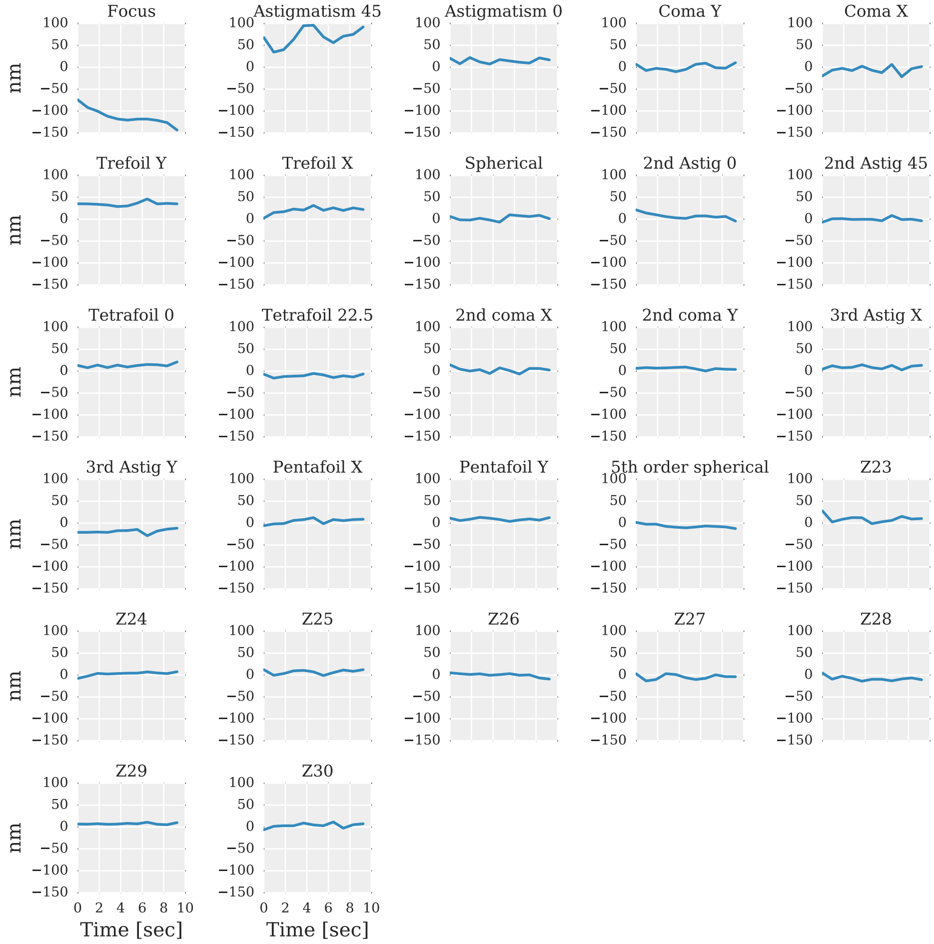

5.10a) with all pixels on the bright fringe on the first step (A) and the third step (C) on the dark fringe. As described in Mendillo et al. (2012b) the next mode maximizes the visibility, confirming that the NPZT was flattened on the central fringe of the white light packet before deformable mirror corrections are applied. During 36.293, the PID was unable to flatten the wavefront phase tilt as the required position was beyond the range of the NPZT and the control system did not advance to maximizing the visibility. Several attempts to re-run the coarse mode were made with Rigel placed

Fig. 5.19: Zernike subtracted residual maps for the first consecutive set of coarse mode observations. The top left map shows the full extent of the mean residual after subtraction of just the sheared focus and astigmatism Zernikes (which manifest as TTP in the sheared map), while the top right map shows the frame-to-frame standard deviation of the residual. All the fit Zernike maps were subtracted to generate the bottom left mean residual map, and the bottom right map shows the frame-to-frame standard deviation after subtraction.

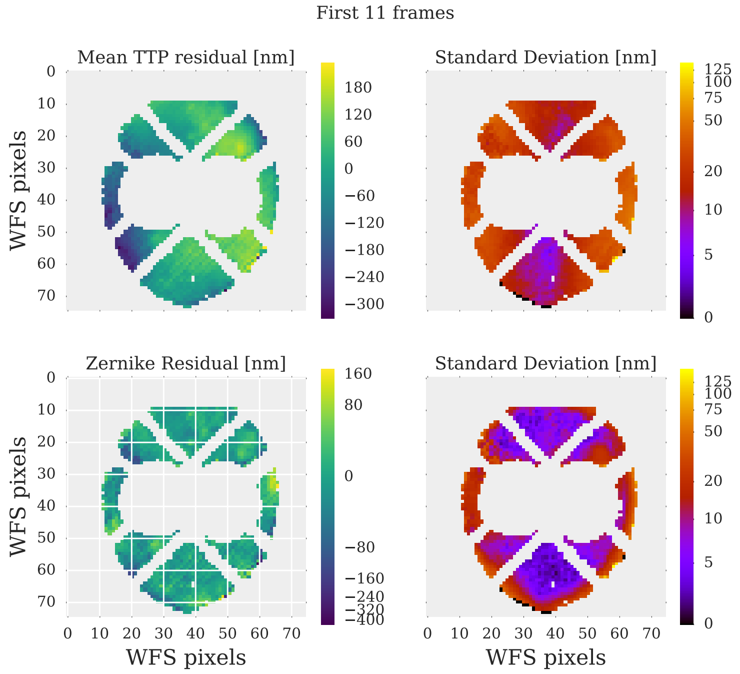

on different sides of the angle tracker, in an effort to tilt the wavefront sufficiently to bring the net piston into range.

Since the focus was worsening during the flight, the number of fringes across the wavefront sensor increased, the FPS precision deteriorated significantly and the attempts at repointing were unsuccessful. Thus, the first coarse flattening mode phase observations are the best measure of the interferometer state. This dataset, comprised of 11 phase measurements recorded in the initial instrument calibration sequence, allows a detailed assessment of active wavefront sensing performance in space.

Fig. 5.20: Histogram of the standard deviation of the phase residual in wavefront sensor pixels. Solid lines indicate gaussian kernel-density estimates of the underlying distribution. σ_{ABCD} is calculated from Poisson uncertainty in the A,B,C, and D intensity measurements assuming $\pi/4$ phase steps. $\sigma(\phi(t))$ is the frame-to-frame standard deviation after removal of the sheared Zernike modes.

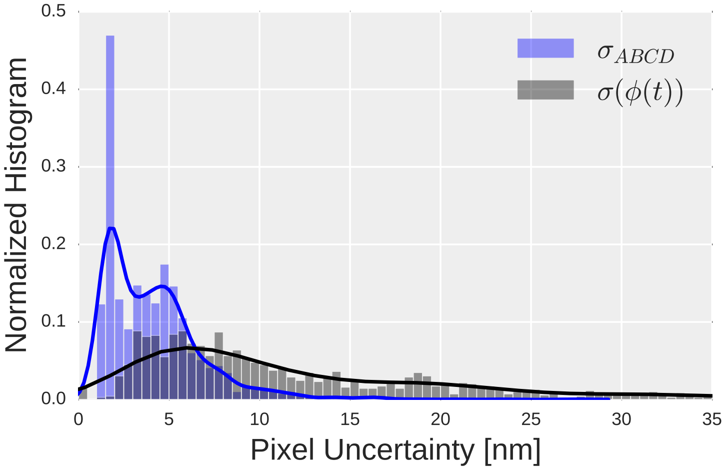

5.5 Temperature Sensor Results

Fig. 5.21 shows the mean tube temperature cooled approximately half a degree Celsius in the first 50 seconds of datalogging, likely due to the adiabatic escape of dry nitrogen out of the “scupper” holes in the sounding rocket skin during ascent. (For a detailed discussion of spacecraft “cabin” depressurization see Roth (1964).) The mean temperature is relatively stable over the remainder of the flight, with the the aft sensors nearer the entrance aperture cooling over a degree while the forward sensors nearer the telescope bulkhead warming about half a degree Celsius.

The likely source of this energy is conduction of heat generated by the friction of atmospheric drag on the rocket skin during ascent. This would require conduction from the skins to the bulkhead, which is coupled to the telescope strongback by insulating G10 washers. Indications of heating are also seen on other sensors in the instrument section, such as the nuller deck breadboard and the tertiary mirror sensor.

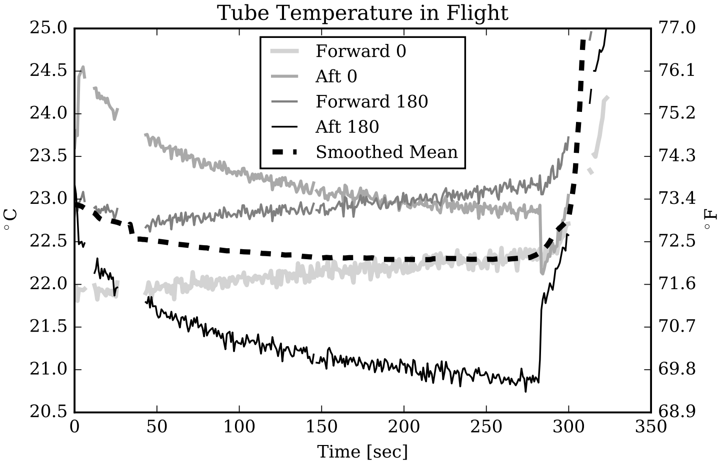

Fig. 5.21: Measurements of tube temperature during flight 36.293. The mean temperature curve is smoothed with a 20 measurement running average and shows little change until warming reentry. The two forward sensors nearest the bulkhead show slight warming. The aft sensors, closer to the telescope entrance aperture cool.

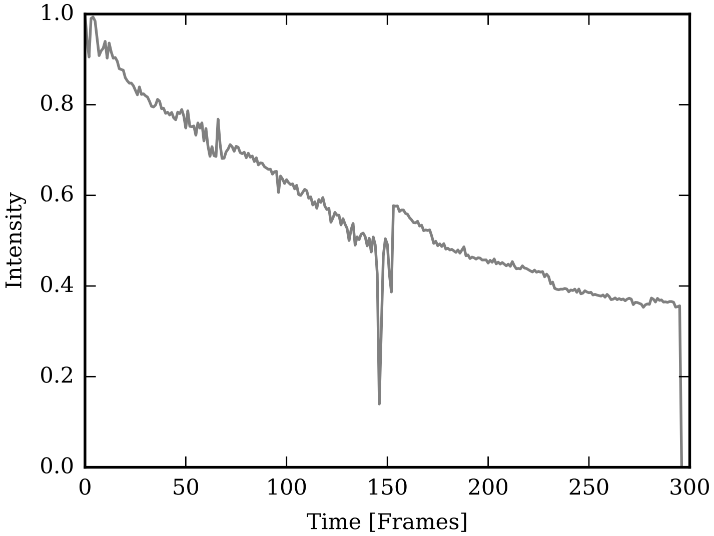

Fig. 5.22: Peak pixel value of the angle tracker full frame from shutter door open to shutter door close. The large drop and recover midway through the flight occurred during a repointing of the payload to increase the tilt into the interferometer.

5.6 Angle Tracker Results

The angle tracker camera images show the telescope drifted out of focus over the course flight 36.293. Fig. 5.22 shows the evolution of the brightest pixel in the angle tracker frame as a function of time. In the first half of the flight the peak intensity fell by a factor of two.

The simplified relation between pure focus Strehl and temperature shown in Fig. 5.2 limits the temperature change required to half the peak intensity. In the case where the initial PSF is near the so-called "diffraction limit" ($S \approx 0.8$), halving the Strehl would be a change in temperature of ≈ 0.75 degrees Fahrenheit. For realistic starting Strehl ratios, the temperature change required to decrease the intensity by a factor of two is smaller.

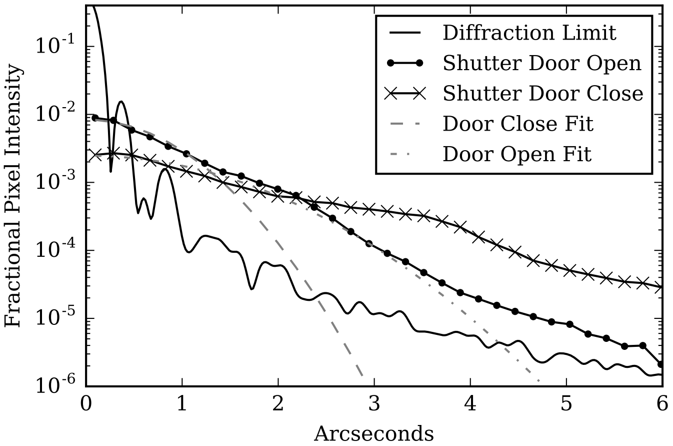

Fig. 5.23: Radial averages of the first PSF after the acquisition (dotted line) and the final PSF before the shutter door closed (x points). A gaussian function fit to each profile is shown as a dashed line. A polychromatic (500-600 nm) PSF shows the expected diffraction limited angle tracker performance in the absence of aberrations (solid line).

Fig. 5.23 shows the radial average of the first and last angle tracker exposure and a diffraction limited PSF. The Strehl ratio of first exposure is 0.05, calculated using the ratio of the peak fractional intensity of the first frame's background subtracted intensity to the peak of a diffraction-limited PSF. The diffraction limited PSF was calculated for the telescope with a central obscuration and sampled at the angle tracker camera plate scale. In the final image, the Strehl is 0.02 via the same approximation. Thus, from changes in the PSF alone, we expect the temperature change was at most 0.75 Fahrenheit (or 0.4 Celsius) in the first half of the flight and it is likely to be much smaller, given the measured Strehl places the change in the extremely low Strehl region.

The small change in the mean tube temperature, measured by onboard sensors, discussed subsequently strengthens the conclusion that the temperature drift in flight was small between Rigel acquisition and shutter door close.

5.7 Wavefront Sensor Results

This section details the analysis of unwrapped phase measurement to understand the stability of the measured wavefront error. While observing a distance point source, a wavefront sensor measurement of the deviation from a planar wavefront indicates the instrument state. Thus, wavefront sensor measurements recorded during the flight 36.293 observation of Rigel serve as a measure of system stability and wavefront sensor precision in space. For this analysis we use the initial consecutive set of 11 coarse-mode measurements recorded before repointing was attempted. The observations correspond to the best instrument focus and the highest visibility fringes.

5.7.1 Zernike Mode Fitting Results

Fig. 5.18 shows the fit of the first 30 Zernike polynomials versus time for the first contiguous set of coarse mode observations, which lasted ≈ 10 sec. Both trefoil terms are the largest aberrations after focus and astigmatism. Units are nanometers of wavefront error, calculated by assuming the phase error in radians is at the central wavelength of the VNC (675 nm). For these initial coarse mode measurements, the fits are relatively stable, with the exception of focus and astigmatism. Independently, in saved FPS frames, the telescope focus was observed to severely worsen over the duration of the flight.

5.7.2 Wavefront Sensor Precision

The removal of the Zernike polynomial aberration modes from the unwrapped phase data well subtracts the time varying wavefront components and the standard deviation of frame-to-frame residual provides an approximate measurement of the wavefront sensor precision. The residual after subtraction of the TTP modes, shown in the top row of Fig. 5.19, provides correction for changes in sheared wavefront tilt, focus, and astigmatism. The right columns shows the 1σ measurement-to-measurement variation, with the top right panel after TTP subtraction and the bottom right after Zernike mode subtraction. While the focus and astigmatism modes changed the most in flight, higher order aberrations also evolved in flight at the tens of nanometer scale. The bottom row Fig. 5.19 shows the residual after subtraction of higher order terms. The histograms in Fig. 5.20 show the standard deviation distribution of the residual across the unmasked WFS pixels as well as the 1σ distribution calculated from on the measured per pixel count rate for ideal $\pi/2$ steps (Wyant, 1975). The solid lines indicates gaussian kernel density estimations of the underlying distributions. The difference between the peaks of these distributions is ≈ 5 nm, although the measured standard deviation has a much longer tail. Possible causes of this discrepancy include low visibility due to the railed actuator, systematic errors in the fitting, electrical noise disturbing the DM actuator position, and evolution of higher-order aberrations as instrument temperature changes. Fitting errors are suggested by the morphology of the residual, where the edges are poorly subtracted but the central region has uniformly low error (Fig. 5.19, bottom right). Including these errors, the uncertainty in the phase is 13.2 ± 12.6 nm/pixel, measured by taking the mean and standard deviation of the standard deviation of the frame-to-frame residuals after Zernike mode subtraction.

5.8 Flight Science Results

The lack of VNC phase correction prevented flight science camera observation of the Rigel and ϵ Eri systems. However, the extensive in-flight data from other sensors allows estimation of the achievable nulling contrast and science products.

The total measured phase error in Fig. 5.19 exhibits less than one wave of phase error. This moderate total error (compared to the fringes in Fig. 5.1a), combined with the large contiguous regions of Zernike subtracted residual error below ten nanometers, implies that the DM was powered on and the actuators were responding appropriately.

Four wavefront sensor pixels sample each DM actuator; thus, the mean per actuator residual error was below 4 nm, even including the apparent fitting errors at the edges. Additionally, the per-actuator sensing error is significantly smaller, approximately 1 nm, for the central regions of the pupil. Flattening the RMS wavefront error between the arms to below 4 nm would have decreased the central star leakage to below $3 \times 10^{-4} L_\star$ with higher contrasts outside the PSF core. This VNC performance would likely have enabled testing for the presence of the 3AU dust ring around ϵ Eri.

The observed fringe visibility provides a first order estimate of the NPZT movement. The coherence length for a 150 nm bandpass at 675 nm is approximately 3 μm. The visibility was high and there were approximately two waves of error (one wave of displacement) across the first measurement (Fig. 5.12a and 5.14b). Thus, the central white light fringe was within ~ 2 μm of the NPZT limit, implying a total motion of no more than ~ 7 μm from the center of the NPZT range.

After the lack of sufficient NPZT piston range to initiate nulling, the next most science-limiting flight measurable is telescope focus. Fig. 5.23 shows the radial average of the first and last angle tracker PSF images of Rigel. The Full-Width-Half Maximum (FWHM) of the gaussian fit to the initial PSF is 1.6 arcseconds (dashed line) and at the end of the flight the FWHM increased to 2.84 arcseconds (dot-dash line). Furthermore, these FWHM measurements under-estimates the PSF size, as the gaussian fit fails capture the wings of the PSF in the last frame before the shutter door closed.

Given this telescope performance, despite high precision wavefront sensing providing the potential for high-contrast, excess detector noise for a large PSF and the inability to subtract speckles between PSFs of changing focus would have severely limited the science achievable. Even neglecting the change in focus and detector noise, since the Backman et al. (2009) proposed ϵ Eri warm ring diameter is two arcseconds, a $> 2''$ PSF would have been unable to resolve the science target.

The discrepancy between the *pysynphot* model results (Section 4.5.2) and flight 36.225 throughput was previously attributed to degradation of the primary mirror coating and thus the expected throughput rates were used to generate the simulated science results in Fig. 4.20. Since the WFS per pixel flux is indistinguishable between the two flights, Table 5.1 shows the corrected ϵ Eri brightness is approximately 30% lower than predicted, which would also decrease the dust count rate proportionally.

5.9 Conclusions

The road to exoplanet imaging from space has been slow. KenKnight (1977) proposed an internally apodized telescope to detect extrasolar planets and in 1978

Bracewell first proposed an interferometric method for detecting exoplanets in space. Laboratory validation of such proposals lagged by decades, not until Wallace et al. (2000) was deep (10^{-4}) interferometric nulling of starlight reported in the lab, and monochromatic laboratory validation of an internal coronagraph capable of imaging terrestrial planets at the 10^{-10} level was reported by Trauger & Traub (2007).

The PICTURE sounding rocket program, initiated in 2005 with the goal of imaging the exoplanet candidate ϵ Eri b (Shao et al., 2005), has advanced high-contrast exoplanet imaging by translating a variety of laboratory demonstrated technologies into spaceflight hardware. The program has demonstrated an FPS that provides precision pointing and active wavefront sensing at nanometer scale precision with a VNC that rearranges Bracewell's interferometer as an internal coronagraph with a single sheared telescope pupil.

PICTURE has also pointed to the limits of high-contrast science achievable in a short photon starved sounding rocket flight. This difficulty was underlined by the poor throughput performance, which may be attributable to the same coating degradation suggested in Section B.2. While better preservations of coatings may have somewhat increased throughput, to observe the ϵ Eri system at high SNR significantly longer observing times are required, motivating future high-contrast imaging either from orbital or high-altitude balloon platforms.

The cause for the NPZT railing is uncertain. The inflight measured DM and VNC temperatures are higher than the laboratory alignment temperature of NPZT, but overheating would have caused caused the NPZT to rail low and the encountered limit was at the high end of the range. If the temperature sensor reading was off by a few degrees, or if there were large gradients across the VNC assembly, and the DM was cold, the NPZT may have railed high due to temperature. Post-flight laboratory testing found the optimal NPZT position has shifted several microns compared to the prelaunch alignment. This shift is most likely due to motion of the 6-degrees-of-freedom (DOF) DM mount. Whether this shift occurred prior to the payload acquiring the target or upon re-entry and impact cannot be definitively determined absent more complete temperature sensor knowledge. However, as noted by Edeson et al. (2009), random vibration is the greatest contributor to optical bench instability in spacecraft, making the sounding rocket launch environment the most likely culprit for a few micron displacement. This suggests additional pre-launch vibration to ”relax” the optical assembly is required for future missions with micron-scale alignment tolerances. While the payload underwent random vibration before launch, the launch of a sounding rocket also subjects the payload to semi-constant acceleration which is difficult to replicate in testing and may have caused inelastic deformation or slippage of the DM mounting structure.

The PICTURE-B flight marks the first operation and measurement of a deformable mirror for high-contrast imaging in space. Despite the central white light fringe packet being out of range of the wavefront control system, this preliminary analysis of the WFS measurements finds that the DM surface was relatively stable.

The lack of a stable telescope PSF illustrates the challenges of constructing a passive optical bench which maintains stability in both varying thermal environments and 0g and 1g states. To address this unmet challenge the next generation of sub-orbital high-contrast imaging missions (e.g. Cook et al. (2015)) will employ active correction of telescope focus and other low-order errors before the coronagraph.

Appendix A

Useful Constants

- Solar Luminosity: $L_{\odot} = 3.8 * 10^{26}[watts] \approx 4 * 10^{26}[J/s]$
- Radius of the Sun: $R_{\odot} = 7 * 10^{8}[meters]$
- Gravitational constant: $G = 6.67 * 10^{-11}[\frac{m^3}{s^2 kg} = \frac{Nm^2}{kg^2}]$
- Electric constant (the permittivity of free space): $\epsilon_0 = 8.8 * 10^{-12}$ [Farads per meter]
- Magnetic constant (permeability of free space): $\mu_0 = 4\pi * 10^{-7}[Henry/M]$
- Electron Mass: $m_{electron} = 9.1 * 10^{-31}$ kg
- Thompson Cross section: $(\frac{8\pi}{3} r_e^2)$=$6.65 * 10^{-29}$ m^2
- 1 $parsec = 3 * 10^{16}$ [meters]
- 1 $radian$ = 206265 arcseconds
- $1ev = 1.6 * 10^{-19}$ Joules
- $hc = 1240$ [eV nm]
- $k_b = 1.38 * 10^{-23}[\frac{\mathrm{J}}{\mathrm{Kelvin}}]$
- $n_{0\ \mathrm{STP}} = 3 * 10^{25}$ [m^{-3}]
- 1 Barn=10^{-24}cm$^2 \approx \sigma_{Uranium}$

Appendix B

Leakage Budget

The leakage, or total fraction of stellar photons transmitted by a coronagraph, is a convenient metric of instrument performance independent of PSF shape. While contrast (C) is the ratio of intensity in a dark fringe pixel to the bright fringe PSF's maximum pixel intensity, leakage can be defined as the ratio of the integral of the dark fringe intensities over controllable spatial frequencies to the integral of the bright fringe PSF intensity over the same region. To convert contrast to leakage in an image plane measurement requires knowledge of the instrument bright fringe PSF (I_B) and the telescope resolution, which yields the ratio of the maximum intensity to the total stellar intensity. Given dark and bright fringe intensity maps (I_D, I_B) centered on the star, the leakage measured to the radius of the Outer Working Angle (OWA) is

$$L = \frac{\int_0^{OWA} I_D(r)dr}{\int_0^{OWA} I_B(r)dr} = \frac{\int_0^{OWA} C(x,y)\max(I_B(r))dr}{\int_0^{OWA} I_B(r)dr} \tag{B.1}$$

Thus, given a PSF and a total leakage, the number of stellar photons at a particular location in the image plane can be computed. Relations between various manufacturing errors and the leakage are derived the Appendix B. Table B.1 shows estimates of the design terms and the estimates of the as-built leakage for the PICTURE VNC.

The leakage, or total fraction of stellar photons transmitted by a coronagraph, is a convenient metric of instrument performance and is independent of PSF shape. Contrast (C) is the ratio of intensity in a dark fringe pixel to the bright fringe, PSF maximum intensity whereas leakage can be defined as the ratio of the integral of

Table B.1: Instrument design leakage (Hicks, 2012) and as-tested levels. Pointing error and RMS phase error are measured, other values are approximated. Starlight coherence is calculated for ϵ-Eridani and does not apply to laboratory measurements of a single mode fiber. Phase plate chromaticity is calculated using the optimized position of a single pair of phase plates to correct dispersion.

	Design Value	Lab Value		Design	Predicted Lab
Starlight Coherence, radius [as]	1.0e-03	0	L_{coh}	3.2e-06	0
Polarization Shift ϕ [rad]	1.7e-04	1.7e-04	L_{s-p}	1.8e-09	1.8e-09
Pupil Rotation [rad]	1.7e-04	1.7e-04	L_{α}	7.2e-09	7.2e-09
Pointing error σ_p [as]	1.0e-03	1.0e-03	L_p	2.9e-06	2.9e-06
Phase Plate Chromaticity [rad]	1.4e-02	1.4e-02	L_{chroma}	5.0e-05	5.0e-05
Birefringence [m]	4.0e-11	4.0e-09	L_B	3.5e-08	3.5e-04
Optical Path Difference [m]	1.0e-09	5.7e-09	$L_{\Delta\phi}$	2.2e-05	7.0e-04
Amplitude uniformity [σ_{amp}]	3.7e-03	9.7e-02	L_{amp}	1.7e-06	1.1e-03
Total				7.9e-05	2.2e-03
Measured Total					3.0e-03 ± 1.6e-03.

the dark fringe intensities over controllable spatial frequencies to the integral of the bright fringe PSF intensity over the same region. To convert contrast to leakage in an image plane measurement requires knowledge of the instrument bright fringe PSF (I_B) and the telescope resolution, which yields the ratio of the maximum intensity to the total stellar intensity. Given dark and bright fringe intensity maps (I_D, I_B) centered on the star, the leakage measured to the radius of the OWA is

$$L = \frac{\int_0^{OWA} I_D(r)dr}{\int_0^{OWA} I_B(r)dr} = \frac{\int_0^{OWA} C(x,y)\max(I_B(r))dr}{\int_0^{OWA} I_B(r)dr} \tag{B.2}$$

Thus, given a PSF and a total leakage, the number of stellar photons at a particular location in the image plane can be computed.

In order to quantify the major leakage terms, we shall derive expressions for the dominant error terms in a lateral shearing VNC, including: wavefront phase and amplitude error, birefringence, phase plate chromaticity, pointing error, polarization, pupil rotation, and star light coherence. Additionally, the expected values of these errors will be approximated and compared to measured total leakage. Serabyn (2000) also derived expressions for nuller errors in terms of null contribution (N_c), the ratio of the dark fringe to the bright fringe of a nulling coronagraph, which is analogous to the total leakage described herein. In the derivations that follow I expand on previous work by Hicks (2012) relating instrument error terms to measurable leakage reaching the image plane at a particular location.

Upon the combination of two beams of partially incoherent, quasimonochromatic light, I_1 and I_2, originating from points s_1 and s_2, the resultant intensity I is given by the interference equation (Born & Wolf, 1980, p. 507):

$$I = I_1 + I_2 + 2\sqrt{I_1}\sqrt{I_2}\cos(\beta_{12} - \Delta\phi)|\mu_{12}| \tag{B.3}$$

where μ_{12} is the complex degree of coherence between the points, defined in Sec. B.5; β_{12} is the effective phase difference due to the difference in coherence and equals the complex arguement (arg) of μ_{12}; $\Delta\phi$ is the phase difference, $\Delta\phi = 2\pi(s_2 - s_1)/\bar{\lambda}$.

The total leakage (L) or null depth (Serabyn, 2000) is equal to the ratio of the bright and dark outputs. When $\Delta\phi$ is small:

$$L = \frac{I_{min}}{I_{max}} = \frac{I_1 + I_2 + 2\sqrt{I_1}\sqrt{I_2}\cos(\beta_{12} - \Delta\phi + \pi)|\mu_{12}|}{I_1 + I_2 + 2\sqrt{I_1}\sqrt{I_2}\cos(\beta_{12} - \Delta\phi)|\mu_{12}|} \tag{B.4}$$

The remainder of this appendix will discuss the contribution of particular fabrication and environmental errors to the total leakage, since in the case that $L << 1$, the leakage can be split into components and added linearly (Serabyn, 2000).

Table B.1 shows the mission design leakage and total leakage terms using nominal design values (Hicks, 2012) as well as the expected, as-tested values from the current testbed. The leakage ratio of the total bright fringe PSF to the total dark fringe PSF was measured from unsaturated science camera frames by aperture photometry over a radius of 8.5 λ/D, the radius where uncorrectable phase error becomes notable.

B.1 Phase error

If the phase difference between the two arms varies from π, the null will not be complete. Eq. B.4 allows estimation of the leakage due to the root mean squared (RMS) phase error, $\Delta\phi$, at controllable spatial scales.

$$L_\phi = \frac{I_1 + I_2 + 2\sqrt{I_1}\sqrt{I_2}\cos\left(\pi - \Delta\phi\right)}{I_1 + I_2 + 2\sqrt{I_1}\sqrt{I_2}\cos\left(\Delta\phi\right)} = \frac{1 + \cos\left(\pi - \Delta\phi\right)}{1 + \cos\left(\Delta\phi\right)} \tag{B.5}$$

For small angles, a Taylor expansion gives

$$L_\phi = \frac{\Delta\phi^2}{4} \tag{B.6}$$

Since the science image is the Fourier transform of the pupil plane only those $\Delta\phi$ at low spatial frequencies will contribute measurable leakage. The deformable mirror allows correction of path length differences on spatial scales larger than the actuator Nyquist frequency (15 cycles/aperture for the 32×32 DM with a one-actuator buffer). Fig. 4.4 A1 shows the residual phase error. Fig. 4.4 B1 shows the same data low-pass filtered to the DM Nyquist frequency. In order to quantify the WFCS performance, measurements from multiple WFCS calibration sequences were recorded under the same conditions as the image plane measurements presented herein. The left panel of Fig. 4.10 shows the OPD of low-pass spatially filtered measurements versus time where the RMS phase difference is $\Delta\phi = \frac{2\pi}{\bar{\lambda}}\sqrt{(< OPD >^2 + \sigma_{OPD}^2)}$. The mean wavelength, $\bar{\lambda}$, equals 675 nm. The right panel shows a histogram of the same phase measurements. The average versus time of the RMS OPD measurements equals 5.7±2.6 nm, which represents the optical path length error at controllable spatial frequencies integrated over the two second control bandwidth.

B.2 Amplitude Error

A Lateral Shearing Interferometer (LSI) interferes spatially separated regions of the input beam, thus reflectivity variation across optical surfaces lead to mismatch between the sheared beams and prevent the amplitude of interfering beams from fully canceling. Eq. B.4 allows estimation of the leakage due to variations in the pupil illumination pattern by setting $I_1 = 1$ and $I_2 = 1 - \epsilon$, where ϵ is the fractional intensity variation.

$$L_{amp} = \frac{I_{min}}{I_{max}} = \frac{2 - \epsilon - 2\sqrt{1-\epsilon}}{(2 - \epsilon + 2\sqrt{1-\epsilon})} \tag{B.7}$$

In the tests described herein the optical train includes 12 reflective surfaces in each arm before the beams are recombined. With the exception of the gold-coated DM and NPZT mirrors, reflective coatings are specified as Denton FS-99 or equivalent protected silver. Two transmissive surfaces also contribute to potential amplitude errors. Limited data on the real-world uniformity of silver coating reflectivity exist in the literature; however, measurements of untarnished Denton FS-99 coated surfaces at the Hobby-Eberly Telescope have a standard deviation of 0.1%, while partially tarnished coatings stored under suboptimal conditions have standard deviations as large as 2.6% (Piche, 1999). The PICTURE optics have been similarly stored in non-humidity controlled environments across multiple years, thus as an upper limit I will assume a root mean squared error (RMSE) amplitude variation per optic equal to the tarnished Hobby-Eberly value. In Table B.1 I calculate the total amplitude leakage by assuming the contribution from each optic adds randomly and the optical train of each arm is independent of the other due to the shear between interfering regions.

B.3 Phase Plate Chromaticity

Assuming the single phase plates in the nuller arms are positioned for optimal dispersion, as a simplified case of the two plate treatment by Morgan et al. (2003), the phase error due to a difference in path length and glass dispersion is

$$\Delta\phi(\lambda) = 2\pi \left(\frac{dS}{\lambda} + \frac{n(\lambda) dT}{\lambda} \right) - \pi \tag{B.8}$$

λ is the wavelength, $n(\lambda)$ is the material dispersion, dT is the difference in phase plate thickness between the two arms, and dS is the difference in vacuum path length between the two arms. Applying Eq. B.6 to this phase error gives

$$L_D \approx \frac{(RMS(\Delta\phi(\lambda)))^2}{4} \tag{B.9}$$

The relative thickness, dT, of dispersive material in each arm was adjusted to high precision by independently rotating the phase plates relative to the optical axis. Using either the BK7 (Schott, 2012) or the fused silica (Malitson, 1965) dispersion curves between 600-750 nm we optimize for a π phase shift by solving the linear system of equations for dT and dS. Plugging the optimized dS and dT into Eq. B.8 gives the minimum phase shift versus wavelength shown in Fig. B.1. The RMS value of the chromatic phase error is 1.5 nm.

B.4 Pointing error

Spacecraft pointing jitter tilts the stellar wavefront with respect to the nuller and increases the leakage (Mendillo et al., 2012a). This leads to variation in wavefront tilt of magnitude $2\pi b\sigma_p/\lambda$ where again b is the baseline and σ_p is the RMSE of the pointing jitter in radians. This is divided by two since the single shearing interferometers is only concerned with tilts perpendicular to the fringe direction on

Fig. B.1: Phase shift as a function of wavelength for a single dispersive plate in each interferometer arm and rotated to the optimal dispersive OPD.

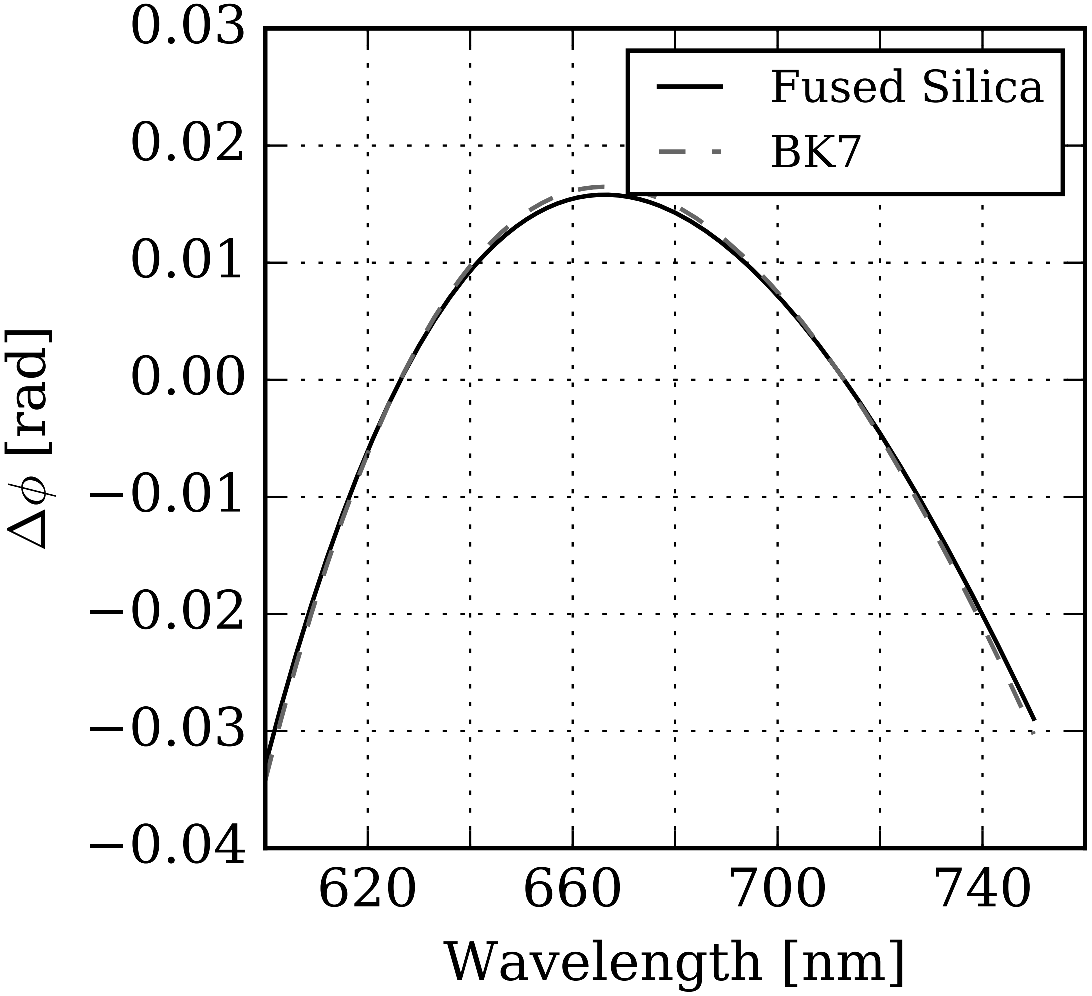

the sky (translation of the star along the fringe axis does not change the leakage). Thus, this phase error (Eq. B.6) gives a leakage of

$$L_p = \frac{1}{4}\left(\frac{\pi b \sigma_p}{\lambda}\right)^2 \tag{B.10}$$

In Table B.1 the leakage due to pointing jitter is calculated using the design value of one milliarcsecond, which is typically measured in the laboratory and is expected for a well focused telescope (Mendillo et al., 2012a).

B.5 Starlight Coherence

Unlike the coherent single mode fiber source used in the laboratory, starlight is only partially coherent. The mutual coherence coefficient μ_{12} between two points, separated by the baseline b can be derived using the Van Cittert-Zernike theorem (Born & Wolf, 1980, 511). A star can be treated as an extended quasimonochromatic source of average wavelength $\bar{\lambda}$ and radius ρ at a distance R and the degree of coherence is:

$$\mu_{12} = \frac{2J_1(v)}{v} e^{i\beta_{12}}, \tag{B.11}$$

where J_1 is a Bessel function of the first order and

$$v = \frac{2\pi}{\bar{\lambda}} \frac{\rho}{R} b, \tag{B.12}$$

where

$$\beta_{12} = \frac{2\pi}{\bar{\lambda}} \frac{b^2}{2R}. \tag{B.13}$$

For a 0.5 m telescope, the sheared PICTURE baseline is $b = 0.15$ m. For a star with an angular radius ($\alpha = \rho/R$) of 1 mas at the center of the PICTURE bandpass, $\mu_{12} = 0.999994$ and effective phase difference, $\beta_{12} = 10^{-12}$. Setting β_{12} to zero, and assuming other terms are negligible, from Eq. B.4 gives the dependence of leakage on coherence:

$$L = \frac{1 - |\mu_{12}|}{1 + |\mu_{12}|} \tag{B.14}$$

First order expansion about μ=1 gives:

$$L_{coh} = \frac{1}{2}(1 - |\mu_{12}|) = \frac{1}{2} - |\frac{J_1(2\pi\bar{\lambda}^{-1}\alpha b)}{2\pi\bar{\lambda}^{-1}\alpha b}|. \tag{B.15}$$

B.6 Birefringence

Birefringence, variation in the index of refraction about the optical axis, arises in isotropic transmissive optical materials due to mechanical stresses. The transmissive elements of the coronagraph are precision annealed glass (Corning, 2014) with a maximum birefringence below $0.1 nm/mm$. Each arm passes through a 10 mm thick beam splitter and a 10 mm thick phase plate, adding a maximum of two nanometers of phase error to each arm. Since birefringence results in a phase error, the total leakage due to the RMS birefringence across the pupil ($\Delta\phi_b$) is

$$L_b \approx \frac{\Delta\phi_b^2}{4} \tag{B.16}$$

Absent measurements of the post-assembly birefringence of the mounted transmissive elements, in Table B.1 this is conservatively estimated as the maximum birefringence of precision annealed glass. This is expected to be an upper limit as it much higher than the 0.04 nm error reported previously for a prototype of the PICTURE VNC (Samuele et al., 2007), which is used for the design value.

B.7 Polarization

Phase and intensity shifts arise between regions of the telescope pupil due to variations in the angle of incidence of parallel rays on curved optical surfaces. Solving the Fresnel formulae for a complex index of refraction gives the phase shift and reflectivity associated with variation in the angle of incidence Born & Wolf (1980). Numerical solutions for high-contrast imaging (Breckinridge & Oppenheimer, 2004) show that for simple metallic coatings differences in reflectivity and phase between polarization axes can generate significant unwanted pupil apodization, which requires multilayer overcoats to minimize (Balasubramanian et al., 2005). The effective phase difference between linear polarization axes, $(\Delta\phi_s - \Delta\phi_p)/2$, can be transformed into leakage directly via Eq. B.6. Thus,

$$L_{s-p} = \frac{(\Delta\phi_s - \Delta\phi_p)^2}{16} \tag{B.17}$$

In Table B.1, the expected polarization phase error contribution from the PICTURE design is 0.01° for both design and as-built instrument values since no new information is available on this term. The on-axis reflectivity variation for the telescope protected silver coatings [1] between the s and p polarization vectors in the PICTURE bandpass is approximately 0.01%. This amplitude variation contributes to the maximum design value of coating uniformity and negligible compared to the amplitude variation in the as-built leakage budget and thus will be neglected.

B.8 Pupil Rotation

Variation in the parallelism of reflecting optics imparts a rotation between interfered beams (Samuele et al., 2007; Serabyn, 2000). For small angles, the leakage contribution due to a rotation (α) is identical in form to phase error. Thus,

$$L_\alpha \approx \frac{\alpha^2}{4} \tag{B.18}$$

In Table B.1 expected value of 0.01° is for both the design and the as-built instrument leakage since no new information is available on this term.

B.9 Environmental Disturbances

Environmental disturbances primarily contribute to the phase error budget as changes in optical component position and, during laboratory testing, the refractive

---

[1] ISP Optics, Irvington NY, USA. Private Communication.

index of air. The residual phase error measured at the wavefront sensor includes contributions from disturbances above the 2 second bandwidth of the WFCS. wavefront control system. Lower frequency vibration are expected to couple poorly to the nuller optics through the stiff bonded glass optical assembly. Environmental disturbances are also minimized in calculating the leakage by selecting unsaturated images which reflect the best instantaneous system performance.

B.10 Summary

This section developed an extensive nuller leakage budget from a combination of design assumptions and measurements, and validated it by comparison to science camera measurements of nuller performance in the laboratory. Despite the unexpectedly large $\Delta\phi$ at controllable spatial frequencies, the measured phase error is insufficient to explain the measured leakage, and Table B.1 shows the expected uncorrected amplitude error, rather than phase error is likely the dominant contributor to leakage. Since the magnitude of several leakage terms, including amplitude, has been approximated rather than measured, the leakage budget presented is only one possible scenario. High spatial resolution measurements of the wavefront visibility and phase error would help break the degeneracy between various leakage terms. However, the low WFS camera sampling rate, $2f_a$, was chosen to maximize photons per pixel in order to minimize the time required to make phase error measurements in flight. Thus, the flight WFS prevents accurate assessment of the visibility due to aliasing of the high frequency DM print through surface error.

Appendix C

Radiative Transfer

Radiative transfer is essential to much of this dissertation. A few essential relations which appear repeatedly are summarized below. For thorough treatment see Rybicki & Lightman (1979). In cartesian (x, y, z) coordinates, intensity, I, is defined as energy per frequency per solid angle per area per time, or watts per Hertz per steradian per area:

$$\frac{dE}{dAdtd\nu d\Omega} = I_\nu(x, y, z, \theta, \phi, t) \cos\theta. \tag{C.1}$$

The fundamental equation of radiative transfer for light of intensity at a particular frequency, ν which has units [1/Hz]:

$$\boxed{\frac{dI_\nu}{ds} = j_\nu - \alpha I_\nu} \tag{C.2}$$

Where $\alpha = n\sigma$ is the absorption coefficient [1/m] and and j_ν is the spontaneous emission rate [1/s]. n is the number density of particles with cross section σ [m^2]. Sometimes it is useful to express the absorption in terms of mass density [kg/m^3], ρ via the opacity, κ [kg/m]:

$$\alpha = n\sigma = \rho\kappa_\nu. \tag{C.3}$$

The source function is:

$$S_\nu \equiv \frac{j_\nu}{\alpha_\nu}. \tag{C.4}$$

This is the ratio of spontaneous emission to total absorption. The solution to the equation of radiative transfer is found by multiplying both sides of Eq. C.2 by e^{τ} and marking variables of integration as τ':

$$I_\nu(\tau_\nu) = I_\nu(0)e^{-\tau_\nu} + \int_0^{\tau_\nu} S_\nu(\tau_\nu)e^{-(\tau_\nu - \tau_\nu')}d\tau'. \tag{C.5}$$

If S_ν is homogeneous, this simplifies to:

$$I_\nu(\tau) = I_\nu(0)e^{-\tau_\nu} + S_\nu(1 - e^{-\tau_\nu}). \tag{C.6}$$

References

Abdi, H., & Williams, L. J. 2010, Wiley Interdisciplinary Reviews: Computational Statistics, 2

Abramowitz, M., & Stegun, I. A. 2012, Handbook of Mathematical Functions: with Formulas, Graphs, and Mathematical Tables (Courier Corporation)

Absil, O., Eiroa, C., Augereau, J., et al. 2010, in ASP Conf Series, Vol. 430, 293

Absil, O., di Folco, E., Mérand, A., et al. 2008, Astronomy and Astrophysics, 487, 1041

Afraimovich, E. L., & Yasukevich, Y. V. 2008, Journal of Atmospheric and Solar-Terrestrial Physics, 70, 1949

Amara, A., & Quanz, S. P. 2012, Monthly Notices of the Royal Astronomical Society, 427, 948

Amara, A., Quanz, S. P., & Akeret, J. 2015, Astrophysics Source Code Library, ascl:1501.001

Anderson, D. N., Mendillo, M., & Herniter, B. 1986, Radio Science, 22, PP. 292

Anderson, J. D., & Meier, R. 1985, Planetary and Space Science, 33, 1179

Antonille, S., Content, D., Rabin, D., Wake, S., & Wallace, T. 2008, in Proc. SPIE, Vol. 7011, 28

Appleton, E. V., & Barnett, M. A. F. 1925, Proceedings of the Royal Society A: Mathematical, Physical and Engineering Sciences, 109, 621

Arrhenius, P. S. 1896, Philosophical Magazine Series 5, 41, 237

Asphaug, E. 2009, Annual Review of Earth and Planetary Sciences, 37, 413

Aumann, H. H. 1985, Publications of the Astronomical Society of the Pacific, 97, 885

Aumann, H. H., & Walker, R. G. 1977, Optical Engineering, 16, 166537

Aumann, H. H., Beichman, C. A., Gillett, F. C., et al. 1984, The Astrophysical Journal Letters, 278, L23

Austin, L., & Starke, H. 1902, Annalen der Physik, 314, 271

Backman, D., Marengo, M., Stapelfeldt, K., et al. 2009, ApJ, 690, 1522

Backman, D. E., & Paresce, F. 1993, in Protostars and Planets III, 1253–1304

Balasubramanian, K., Hoppe, D. J., Mouroulis, P. Z., Marchen, L. F., & Shaklan, S. B. 2005, in Proc. of SPIE, Vol. 5905, 59050H–59050H–11

Ballester, G. E., Sing, D. K., & Herbert, F. 2007, Nature, 445, 511

Bautz, M. W., Kissel, S. E., Prigozhin, G. Y., et al. 2004, in Proc. SPIE, Vol. 5501, 111–122

Bean, J. L., Benedict, G. F., Charbonneau, D., et al. 2008, Astronomy and Astrophysics, 486, 1039

Behnel, S., Bradshaw, R., Citro, C., et al. 2011, Computing in Science & Engineering, 13, 31

Belehaki, A., Stanislawska, I., & Lilensten, J. 2009, Space Science Reviews, 147, 271

Bell, K., & Stafford, R. 1992, Planetary and Space Science, 40, 1419

Benedict, G. F., McArthur, B. E., Gatewood, G., et al. 2007, ApJ, 132, 2206

Bennett, A. C., & Omidvar, K. 2001, Advances in Space Research, 27, 1685

Bernhardt, P. A., McCoy, R. P., Dymond, K. F., et al. 1998, Physics of Plasmas, 5, 2010

Beuzit. 2006, The ESO Messenger, 125, 2

Bibl, K., & Reinisch, B. W. 1978, Radio Science, 13, PP. 519

Bohlin, R. C., Sparks, W. M., Holm, A. V., Savage, B. D., & Snijders, M. A. J. 1980, Astronomy and Astrophysics, 85, 1

Bond, I. A., Udalski, A., Jaroszyski, M., et al. 2004, The Astrophysical Journal Letters, 606, L155

Born, M., & Wolf, E. 1980, Principles of Optics Electromagnetic Theory of Propagation, Interference and Diffraction of Light, 6th edn. (Pergamon Press)

Borucki, W. J., Koch, D., Basri, G., et al. 2003, in Proceedings of the Conference on Towards other Earths: DARWIN/TPF and the Search for Extrasolar Terrestrial Planets, Vol. 539, Heidelberg, Germany, 69–81

Bowyer, S., Kimble, R., Paresce, F., Lampton, M., & Penegor, G. 1981, Applied Optics, 20, 477

Bracewell, R. N. 1978, Nature, 274, 780

Branch, M., Coleman, T., & Li, Y. 1999, SIAM Journal on Scientific Computing, 21, 1

Breckinridge, J. B., & Oppenheimer, B. R. 2004, The Astrophysical Journal, 600, 1091

Breit, G., & Tuve, M. A. 1926, Physical Review, 28, 554

Broadfoot, A. L., Belton, M. J. S., Takacs, P. Z., et al. 1979, Science, 204, 979

Brown, R. A. 2012, New England Journal of Higher Education

Bruining, D. H. 1962, in Physics and Applications of Secondary Electron Emission, Pergamon Science Series: Electronics and Wavesa Series of Monographs (Pergamon), 27–51

Butler, R. P., Wright, J. T., Marcy, G. W., et al. 2006, The Astrophysical Journal, 646, 505

Carlson, R., & Judge, D. 1973, Planetary and Space Science, 21, 879

Carruthers, G. R., & Page, T. 1972, Science, 177, 788, articleType: research-article / Full publication date: Sep. 1, 1972 / Copyright I’ 1972 American Association for the Advancement of Science

—. 1976, Journal of Geophysical Research, 81, 1683

Chakrabarti, S., Mendillo, C. B., Cook, T. A., et al. 2016, Journal of Astronomical Instrumentation, 05, 1640004

Chakrabarti, S., Paresce, F., Bowyer, S., Kimble, R., & Kumar, S. 1983, Journal of Geophysical Research, 88, PP. 4898

Chapman, S. 1931, Proceedings of the Physical Society, 43, 26

Charbonneau, D., Brown, T. M., Latham, D. W., & Mayor, M. 2000, The Astrophysical Journal Letters, 529, L45

Charbonneau, D., Brown, T. M., Noyes, R. W., & Gilliland, R. L. 2002, The Astrophysical Journal, 568, 377

Charbonneau, D., Allen, L. E., Megeath, S. T., et al. 2005, The Astrophysical Journal, 626, 523

Chen, F. F. 1984, Introduction to Plasma Physics and Controlled Fusion (Boston, MA: Springer US)

Choquet, ., Pueyo, L., Hagan, J. B., et al. 2014, in Proc. SPIE, ed. J. M. Oschmann, M. Clampin, G. G. Fazio, & H. A. MacEwen, 914357

Christensen, A. B., Kayser, D. C., Pranke, J. B., et al. 1992, in Proc. SPIE, Vol. 1745

Christensen, A. B., Paxton, L. J., Avery, S., et al. 2003, Journal of Geophysical Research (Space Physics), 108, 1451

Clarke, J. T., Moos, H. W., Atreya, S. K., & Lane, A. L. 1980, The Astrophysical Journal Letters, 241, L179

Cleary, D. D., Meier, R. R., Gentieu, E. P., Feldman, P. D., & Christensen, A. B. 1989, Journal of Geophysical Research, 94, 17281

Conway, R. R. 1982, Journal of Geophysical Research: Space Physics, 87, 859

Cook, T., Chakrabarti, S., France, K., & Hicks, B. 2012, NASA RFI

Cook, T., Cahoy, K., Chakrabarti, S., et al. 2015, Journal of Astronomical Telescopes, Instruments, and Systems, 1, 044001

Corning. 2014, Corning Specialty Materials Product Information Sheet 7979, 7980 and 8655

Cotton, D. M., Cook, T., & Chakrabarti, S. 1994, Applied Optics, 33, 1958

Cotton, D. M., Stephan, A., Cook, T., et al. 2000, Applied Optics, 39, 3991

Cravens, T. E. 2004, Physics of Solar System Plasmas (Cambridge University Press)

Dalcanton, J., Seager, S., Aigrain, S., et al. 2015, arXiv:1507.04779 [astro-ph], arXiv: 1507.04779

Dalgarno, A., Henry, R., & Stewart, A. 1964, Planetary and Space Science, 12, 235

Defrère, D., Absil, O., den Hartog, R., Hanot, C., & Stark, C. 2010, Astronomy and Astrophysics, 509, 9

Defrère, D., Hinz, P., Mennesson, B., et al. 2013, Proceedings of the International Astronomical Union, 8, 332

Des Marais, D. J., Harwit, M. O., Jucks, K. W., et al. 2002, Astrobiology, 2, 153

Di Folco, E., Absil, O., Augereau, J.-C., et al. 2007, Astronomy and Astrophysics, 475, 243

Douglas, E. S., Mendillo, C. B., Cook, T. A., & Chakrabarti, S. 2016, arXiv:1607.00277 [astro-ph], arXiv: 1607.00277

Douglas, E. S., Smith, S. M., Stephan, A. W., et al. 2012, Journal of Geophysical Research, 117, 8 PP.

Douglas, E. S., Hewasawam, K., Mendillo, C. B., et al. 2015, in Proc. SPIE, Vol. 9605, 96051A–96051A–13

Dressing, C. D., & Charbonneau, D. 2013, The Astrophysical Journal, 767, 95

Dymond, K. F., Budzien, S. A., Thonnard, S. E., et al. 2001, AGU Fall Meeting Abstracts, 32, 0679

Dymond, K. F., McCoy, R. P., Thonnard, S. E., et al. 2000, Journal of Geophysical Research, 105, PP. 23,025

Edeson, R., Morris, N., Tatnall, A., & Aglietti, G. S. 2009, AIAA Journal, 47, 219

Einstein, A. 1905, Ann. Phys. Translation in to English: American Journal of Physics, v. 33, n. 5, May 1965, 17

—. 1936, Science, 84, 506

Esposito, L. W., & House, L. L. 1978, The Astrophysical Journal, 219, 1058

Evans, J. V. 1969, Proceedings of the IEEE, 57, 496

Evans, J. W., Macintosh, B., Poyneer, L., et al. 2006, Optics Express, 14, 5558

Farnsworth, P. T. 1934, Electron multiplier, u.S. Classification 315/3, 313/346.00R, 327/573, 313/356, 313/103.00R, 315/58, 313/285, 313/249; International Classification H01J43/00, H01J43/24; Cooperative Classification H01J43/24; European Classification H01J43/24

Feldman, P. D., Jr, D. E. A., Meier, R. R., & Gentieu, E. P. 1981, Journal of Geophysical Research, 86, PP. 3583

Fergus, R., Hogg, D. W., Oppenheimer, R., Brenner, D., & Pueyo, L. 2014, The Astrophysical Journal, 794, 161

Foreman-Mackey, D., Hogg, D. W., Lang, D., & Goodman, J. 2013, Publications of the Astronomical Society of the Pacific, 125, 306

Foreman-Mackey, D., Price-Whelan, A., Ryan, G., et al. 2014, triangle.py v0.1.1

Fox, M. W. 1994, Radio Science, 29, PP. 1473

Fried, D. L. 1965, Journal of the Optical Society of America, 55, 1427

Galkin, I. A., Reinisch, B. W., Huang, X. A., et al. 2014, AGU Fall Meeting Abstracts, 12

Geddes, G., Chakrabarti, S., Cook, T., Finn, S., & Douglas, E. 2015, Error Analysis of O+ Density Retrieved from Combined 83.4 nm and 61.7 nm EUV dayglow

Ghiglia, D. C., & Pritt, M. D. 1998, Two-dimensional phase unwrapping: theory, algorithms, and software (Wiley)

Ghiglia, D. C., & Romero, L. A. 1994, Journal of the Optical Society of America A, 11, 107

Giacconi, R., Branduardi, G., Briel, U., et al. 1979, The Astrophysical Journal, 230, 540

Gillies, R., van Eyken, A. P., spanswick, E., et al. 2015, in AGU Fall Meeting Abstracts (Agu)

Golini, D., Kordonski, W. I., Dumas, P., & Hogan, S. J. 1999, in Proc. SPIE, Vol. 3782, 80–91

Goodman, J., & Weare, J. 2010, Communications in Applied Mathematics and Computational Science, 5, 65

Greaves, J. S., Holland, W. S., Moriarty-Schieven, G., et al. 1998, The Astrophysical Journal Letters, 506, L133

Grogan, K., Dermott, S. F., & Durda, D. D. 2001, Icarus, 152, 251

Guyon, O., Pluzhnik, E. A., Kuchner, M. J., Collins, B., & Ridgway, S. T. 2006, The Astrophysical Journal Supplement Series, 167, 81

Haguenauer, P., & Serabyn, E. 2006, Applied Optics, 45, 2749

Harbers, G., Kunst, P. J., & Leibbrandt, G. W. R. 1996, Applied optics, 35, 6162

Hatzes, A. P., Cochran, W. D., McArthur, B., et al. 2000, The Astrophysical Journal, 544, L145

Hedin, A. E. 1991, Journal of Geophysical Research, 96, 1159

Hedin, A. E., Biondi, M. A., Burnside, R. G., et al. 1991, Journal of Geophysical Research, 96, PP. 7657

Heinze, A. N., Hinz, P. M., Kenworthy, M., et al. 2010, arXiv.org, 1003.5323

Henry, R. J. W. 1967, Planetary and Space Science, 15, 1747

Herráez, M. A., Burton, D. R., Lalor, M. J., & Gdeisat, M. A. 2002, Applied Optics, 41, 7437

Hicks, B., Cook, T., Lane, B., & Chakrabarti, S. 2009, Applied Optics, 48, 4963

Hicks, B., Oram, K., Lewis, N., et al. 2013, in Proc. SPIE, Vol. 8864, 886408–886408–11

Hicks, B. A. 2012, PhD thesis, Boston University, Boston, MA, USA

Hill, J. M. 1990, in Proc. SPIE, Vol. 1236, 86–107

Hinkley, S., Oppenheimer, B. R., Zimmerman, N., et al. 2011, Publications of the Astronomical Society of the Pacific, 123, 74

Hinteregger, H. E., Fukui, K., & Gilson, B. R. 1981, Geophysical Research Letters, 8, 1147

Hinz, P. M. 2009, in AIP Conference Proceedings, Vol. 1158 (AIP Publishing), 313–317

Hinz, P. M., Angel, J. R. P., Hoffmann, W. F., et al. 1998, Nature, 395, 251

Hinz, P. M., Angel, J. R. P., Woolf, N. J., Hoffmann, W. F., & McCarthy, Jr., D. W. 1999, in ASP Conf Series, Vol. 194, 401

Holstein, T. 1947, Physical Review, 72, 1212

Holt, J. M., Goncharenko, L. P., Rideout, W., & Palo, S. 2006, AGU Fall Meeting Abstracts, 13, 1165

Hunten, D., Roach, F., & Chamberlain, J. 1956, Journal of Atmospheric and Terrestrial Physics, 8, 345

Janson, M., Bergfors, C., Goto, M., Brandner, W., & Lafrenière, D. 2010, The Astrophysical Journal Letters, 710, L35

Janson, M., Quanz, S. P., Carson, J. C., et al. 2015, Astronomy and Astrophysics, 574, A120

Janson, M., Brandner, W., Henning, T., et al. 2007, The Astronomical Journal, 133, 2442

Janson, M., Brandt, T. D., Kuzuhara, M., et al. 2013, The Astrophysical Journal Letters, 778, L4

Jee, M. J., Blakeslee, J. P., Sirianni, M., et al. 2007, Publications of the Astronomical Society of the Pacific, 119, 1403

Johnson, C. Y. 1966, Journal of Geophysical Research, 71, 330

Jones, E., Oliphant, T., & Peterson, P. 2001, http://www. scipy. org/

Jovanovic, N., Martinache, F., Guyon, O., et al. 2015, Publications of the Astronomical Society of the Pacific, 127, 890

Kalas, P., Graham, J. R., Chiang, E., et al. 2008, Science, 322, 1345

Kaltenegger, L., Selsis, F., Fridlund, M., et al. 2010, Astrobiology, 10, 89

Kamalabadi, F., Karl, W. C., Semeter, J. L., et al. 1999, Radio Science, 34, 437

Kayser, D. C., Chater, W. T., Christensen, A. B., et al. 1989, Development of the RAIDS (Remote Atmospheric and Ionospheric Detector System) Extreme Ultraviolet Wedge and Strip Detector, Tech. rep., DTIC Document

Kelley, M. C. 2009, The earth's ionosphere : plasma physics and electrodynamics (Amsterdam; Boston: Academic Press)

Kelly, J. D., Heinselman, C. J., & Valentic, T. 2006, AGU Fall Meeting Abstracts, 21

Kelsall, T., Weiland, J. L., Franz, B. A., et al. 1998, The Astrophysical Journal, 508, 44

KenKnight, C. E. 1977, Icarus, 30, 422

Kennedy, G. M., Wyatt, M. C., Bailey, V., et al. 2014, arXiv:1412.0675 [astro-ph], arXiv: 1412.0675

Kirby, K., Constantinides, E. R., Babeu, S., Oppenheimer, M., & Victor, G. A. 1979, Atomic Data and Nuclear Data Tables, 23, 63

Krist, J. 1995, in ASP Conf Series, Vol. 77, 349

Krist, J. E. 2004, in Proc. SPIE, Vol. 5487, 1284–1295

Krist, J. E. 2007, in Proc. SPIE, Vol. 6675, 66750P–66750P–9

Ku, H. 1966, Journal of Research of the National Bureau of Standards, Section C: Engineering and Instrumentation, 70C, 263

Kumar, S., Chakrabarti, S., Paresce, F., & Bowyer, S. 1983, Journal of Geophysical Research, 88, PAGES 9271

Labeyrie, A. 1995, Astronomy and Astrophysics, 298, 544

Lafrenière, D., Jayawardhana, R., & Kerkwijk, M. H. v. 2008, The Astrophysical Journal Letters, 689, L153

Lafrenière, D., Marois, C., Doyon, R., Nadeau, D., & Artigau, . 2007, The Astrophysical Journal, 660, 770

Lallo, M. D., Makidon, R. B., Casertano, S., & Krist, J. E. 2006, in SPIE Astronomical Telescopes+ Instrumentation (International Society for Optics and Photonics), 62701N–62701N

Lammer, H., Bredehöft, J. H., Coustenis, A., et al. 2009, The Astronomy and Astrophysics Review, 17, 181

Lawrence, R. S., Little, C. G., & Chivers, H. J. 1964, Proceedings of the IEEE, 52, 4

Lawson, P. R., Belikov, R., Cash, W., et al. 2013, in SPIE Optical Engineering+ Applications (International Society for Optics and Photonics), 88641F–88641F

Lebreton, J., van Lieshout, R., Augereau, J.-C., et al. 2013, Astronomy & Astrophysics, 555, A146, arXiv: 1306.0956

Lei, J., Liu, L., Wan, W., Zhang, S.-R., & Holt, J. M. 2004, Geophysical Research Letters, 31, 14804

Levine, B. M., Aguayo, F., Bifano, T., et al. 2006, in Proc. SPIE, ed. J. C. Mather, H. A. MacEwen, & M. W. M. de Graauw, 62651A–62651A–13

Lewis, N. K., Showman, A. P., Fortney, J. J., et al. 2010, The Astrophysical Journal, 720, 344

Link, R., Evans, J. S., & Gladstone, G. R. 1994, Journal of Geophysical Research, 99, PP. 2121

Lockheed. 1979, Systems level feasibility study for the detection of extra-solar planets. Volume 2 Apodized Telescope (APODS), Tech. rep., LOCKHEED PALO ALTO RESEARCH LABORATORY

Lowrance, P. J., Schneider, G., Kirkpatrick, J. D., et al. 2000, The Astrophysical Journal, 541, 390

Lozi, J., Cassaing, F., Le Duigou, J.-M., et al. 2011, in Proc. SPIE, Vol. 8151, eprint: arXiv:1109.3131, 81510B

Luu, J. X., & Jewitt, D. C. 2002, Annual Review of Astronomy and Astrophysics, 40, 63

Lyon, R. G., Clampin, M., Woodruff, R., et al. 2006, IAU Colloquim, 200

MacGregor, M. A., Wilner, D. J., Andrews, S. M., Lestrade, J.-F., & Maddison, S. 2015, The Astrophysical Journal, 809, 47

Macintosh, B. A., Graham, J. R., Palmer, D. W., et al. 2008, in Proc. SPIE, Vol. 7015, 701518

MacKay, D. J. 2003, Information theory, inference and learning algorithms (Cambridge university press)

Mahajan, V. N. 1983, Journal of the Optical Society of America, 73, 860

Males, J. R., Close, L. M., Morzinski, K. M., et al. 2014, The Astrophysical Journal, 786, 32

Malitson, I. H. 1965, JOSA, 55, 1205

Marengo, M., Megeath, S. T., Fazio, G. G., et al. 2006, A Spitzer/IRAC Search for Substellar Companions of the Debris Disk Star epsilon Eridani, arXiv e-print astro-ph/0605187, astrophys.J.647:1437-1451,2006

Marengo, M., Stapelfeldt, K., Werner, M. W., et al. 2009, The Astrophysical Journal, 700, 1647

Martin, C., Jelinsky, P., Lampton, M., Malina, R. F., & Anger, H. O. 1981, Review of Scientific Instruments, 52, 1067

Martin, H. M. 1987, Publications of the Astronomical Society of the Pacific, 99, 1360

Matthews, B. C., Krivov, A. V., Wyatt, M. C., Bryden, G., & Eiroa, C. 2014, arXiv preprint arXiv:1401.0743

May, B. 2008, A Survey of Radial Velocities in the Zodiacal Dust Cloud (Springer Science & Business Media)

Mayor, M., & Queloz, D. 1995, Nature, 378, 355

McCarthy, D. J., & Facey, T. A. 1982, in Proc. SPIE, Vol. 0330, 139–143

McCoy, R. P., Jr, D. E. A., & Chakrabarti, S. 1985, Journal of Geophysical Research, 90, PP. 12,257

McMahan, L. 1982, in Technology for Space Astrophysics (Danbury, CT: American Institute of Aeronautics and Astronautics)

Meier, R. R. 1991, Space Science Reviews, 58, 1

Mende, S. B., Heetderks, H., Frey, H. U., et al. 2000, Space Science Reviews, 91, 243

Mendillo, C. B. 2013, PhD thesis, Boston University, Boston, MA, USA

Mendillo, C. B., Chakrabarti, S., Cook, T. A., Hicks, B. A., & Lane, B. F. 2012a, Applied Optics, 51, 7069

Mendillo, C. B., Hicks, B. A., Cook, T. A., et al. 2012b, in Proc. SPIE, Vol. 8442

Mikhailov, A. V., Leschinskaya, T. Y., Miro, G., & Depuev, V. K. 2000, Annals of Geophysics, 43

Millan-Gabet, R., Serabyn, E., Mennesson, B., et al. 2011, The Astrophysical Journal, 734, 67

Morgan, R. M., Burge, J. H., & Woolf, N. J. 2003, in Proc. SPIE, Vol. 4838, 644–655

Morzinski, K. M., Norton, A. P., Evans, J. W., et al. 2012, in SPIE MOEMS-MEMS, 825304–825304

Nesvorný, D., Jenniskens, P., Levison, H. F., et al. 2010, The Astrophysical Journal, 713, 816

Nielsen, E. L., Close, L. M., Biller, B. A., Masciadri, E., & Lenzen, R. 2008, The Astrophysical Journal, 674, 466

Noll, R. J. 1976, Journal of the Optical Society of America, 66, 207

NRL, N. R. L. 2010, RAIDS Newsletter, Newletter 6, Naval Research Laboratory

Offner, A. 1963, Applied Optics, 2, 153

Oort, J. H. 1950, Bulletin of the Astronomical Institutes of the Netherlands, 11, 91

Oppenheimer, B. R., & Hinkley, S. 2009, arXiv preprint arXiv:0903.4466

Pawellek, N., Krivov, A. V., Marshall, J. P., et al. 2014, The Astrophysical Journal, 792, 65

Perrin, M., Long, J., Douglas, E., et al. 2016, Astrophysics Source Code Library, ascl:1602.018

Perrin, M. D., Sivaramakrishnan, A., Makidon, R. B., Oppenheimer, B. R., & Graham, J. R. 2003, The Astrophysical Journal, 596, 702

Perrin, M. D., Soummer, R., Elliott, E. M., Lallo, M. D., & Sivaramakrishnan, A. 2012, in Proc. SPIE, Vol. 8442, 84423D–84423D–11

Perez, F., & Granger, B. 2007, Computing in Science Engineering, 9, 21

Piche, F. 1999, SAC Mirrors Reflectivity Measurements, Tech. rep., The University of Texas at Austin, McDonald Observatory

Pickles, A. 1998, Publications of the Astronomical Society of the Pacific, 110, 863, articleType: research-article / Full publication date: July 1998 / Copyright Ĩ 1998 The University of Chicago Press

Picone, J. M. 2008, Journal of Geophysical Research (Space Physics), 113, 09306

Picone, J. M., Hedin, A. E., Drob, D. P., & Aikin, A. C. 2002, Journal of Geophysical Research, 107, 16 PP.

Picone, J. M., Meier, R. R., Kelley, O. A., et al. 1997, Journal of Geophysical Research, 102, 2441

Postma, J., Hutchings, J. B., & Leahy, D. 2011, arXiv:1105.5361

Powell, M. J. D. 1964, The Computer Journal, 7, 155

Poyneer, L. A., & Dillon, D. 2008, in Proc. SPIE, Vol. 6888, 68880H–68880H–10

Poyneer, L. A., De Rosa, R. J., Macintosh, B., et al. 2014, arXiv:1407.2278 [astro-ph], 91480K, arXiv: 1407.2278

Proffitt, C. R., Sahu, K., Livio, M., et al. 2004, The Astrophysical Journal, 612, 481

Rao, S. R., Wallace, J. K., Samuele, R., et al. 2008, in Proc. SPIE, Vol. 6888, 68880B–68880B

Refsdal, B., Doe, S., Ng, D., et al. 2011, in Astronomical Data Analysis Software and Systems XX. ASP Conference Proceedings, Vol. 442 (San Francisco: Astronomical Society of the Pacific), 687–690

Reidemeister, M., Krivov, A. V., Stark, C. C., et al. 2011, Astronomy & Astrophysics, 527, A57

Reinisch, B. W., Galkin, I. A., Khmyrov, G. M., et al. 2009, Radio Science, 44

Rideout, W., & Coster, A. 2006, GPS Solutions, 10, 219

Risbeth, & Garriott. 1969, Introduction to Ionospheric Physics (Academic Press)

Roberge, A., Chen, C. H., Millan-Gabet, R., et al. 2012, Publications of the Astronomical Society of the Pacific, 124, 799

Rodriguez, D. R., & Zuckerman, B. 2012, The Astrophysical Journal, 745, 147

Roth, E. M. 1964, Space-cabin Atmosphere: Engineering trade-offs of one-versus two-gas systems, Vol. 4 (Scientific and Technical Information Division, National Aeronautics and Spcae Administration)

Rowland, H. A. 1882, The Observatory, 5, 224

Rybicki, G. B., & Lightman, A. P. 1979, Radiative Processes in Astrophysics (John Wiley & Sons)

Sakao, T., Narukage, N., Suematsu, Y., et al. 2014, in Proc. SPIE, Vol. 9144, 91443D–91443D–8

Sambridge, M., & Mosegaard, K. 2002, Reviews of Geophysics, 40, 1009

Samuele, R., Wallace, J., Schmidtlin, E., et al. 2007, in 2007 IEEE Aero. Conf., 1 –7

Sarazin, M., & Roddier, F. 1990, Astronomy and Astrophysics, 227, 294

Schneider, G. 2014, arXiv:1412.8421 [astro-ph], arXiv: 1412.8421

Schneider, G., & Stobie, E. 2002, in ASP Conf Series, Vol. 281, 382

Schneider, G., Silverstone, M. D., Hines, D. C., et al. 2006, The Astrophysical Journal, 650, 414

Schneider, G., Grady, C. A., Hines, D. C., et al. 2014, The Astronomical Journal, 148, 59

Schott, A. G. 2012, Optical Glass, Data Sheets

Schunk, R. W., Scherliess, L., Sojka, J. J., et al. 2004, Radio Science, 39, RS1S02

Seager, S. 2014, Proceedings of the National Academy of Sciences, 111, 12634

Serabyn, E. 2000, in Proc. SPIE, Vol. 4006, 328–339

Serabyn, E., Wallace, J. K., Hardy, G. J., Schmidtlin, E. G. H., & Nguyen, H. T. 1999, Applied Optics, 38, 7128

Shao, M., Green, J. J., Lane, B., et al. 2005, Proceedings of the International Astronomical Union, 1, 525

Shao, M., Wallace, J. K., Levine, B. M., & Liu, D. T. 2004, in Proc. SPIE, Vol. 5487, 1296–1303

Siegmund, O. H. W. 2003, in Proc. SPIE, Vol. 4854, 181–190

Siegmund, O. H. W., Lampton, M., Bixier, J., et al. 1986, Journal of the Optical Society of America A, 3, 2139

Silburt, A., Gaidos, E., & Wu, Y. 2015, The Astrophysical Journal, 799, 180

Sirk, M. M., Vallerga, J. V., Finley, D. S., Jelinsky, P., & Malina, R. F. 1997, The Astrophysical Journal Supplement Series, 110, 347

Smith, B. A., & Terrile, R. J. 1984, Science, 226, 1421

Smith, E. R. 1976, Physical Review A, 13, 1058

Soummer, R., Pueyo, L., & Larkin, J. 2012, The Astrophysical Journal Letters, 755, L28

Soummer, R., Pueyo, L., Sivaramakrishnan, A., & Vanderbei, R. J. 2007, Optics Express, 15, 15935

Soummer, R., Perrin, M. D., Pueyo, L., et al. 2014, The Astrophysical Journal, 786, L23

Spergel, D., Gehrels, N., Baltay, C., et al. 2015, ArXiv e-prints, 1503, 3757

Stark, C. C., & Kuchner, M. J. 2008, ApJ, 686, 637

Stark, C. C., Roberge, A., Mandell, A., & Robinson, T. D. 2014, arXiv:1409.5128 [astro-ph], arXiv: 1409.5128

Steffen, J. H., Fabrycky, D. C., Agol, E., et al. 2012, Monthly Notices of the Royal Astronomical Society

Stephan, A. W., Budzien, S. A., Bishop, R. L., et al. 2009, in Proc. SPIE (SPIE), 74380Y–74380Y–10

Stephan, A. W., Christensen, A. B., Minschwaner, K., et al. 2011, Proceedings of SPIE, 8148, 814804

Stephan, A. W., Finn, S. C., Cook, T. A., Chakrabarti, S., & Budzien, S. A. 2015, in AAS/AGU Triennial Earth-Sun Summit, Vol. 1

Stephan, A. W., Picone, J. M., Budzien, S. A., et al. 2012, Journal of Geophysical Research: Space Physics, 117, n/a

Strickland, D., Bishop, J., Evans, J., et al. 1999, Journal of Quantitative Spectroscopy and Radiative Transfer, 62, 689

Strickland, D., & Donahue, T. 1970, Planetary and Space Science, 18, 661

Struve, O. 1952, The Observatory, 72, 199

STScI development Team. 2013, Astrophysics Source Code Library, 1303.023

The Astropy Collaboration, Robitaille, T. P., Tollerud, E. J., et al. 2013, Astronomy & Astrophysics, 558, A33

Thomas, J. O. 1963, Science, 139, 229

Thomas, S., Poyneer, L., Savransky, D., et al. 2012, in Proc. SPIE, ed. B. L. Ellerbroek, E. Marchetti, & J.-P. Véran, 844714–844714–12

Traub, W. A., Chen, P., Kern, B., & Matsuo, T. 2008, in Proc. SPIE, ed. J. M. Oschmann, Jr., M. W. M. de Graauw, & H. A. MacEwen, 70103S–70103S–12

Traub, W. A., & Oppenheimer, B. R. 2010, in Exoplanets (Tucson, AZ, USA: University of Arizona Press), 111–156, seager, S., ed

Trauger, J. T., & Traub, W. A. 2007, Nature, 446, 771

Turnbull, M. C., Traub, W. A., Jucks, K. W., et al. 2006, The Astrophysical Journal, 644, 551

Vallerga, J. V., McPhate, J. B., Martin, A. P., et al. 2001, in Proc. SPIE, Vol. 4498, 141–151

VanderPlas, J. 2014, arXiv:1411.5018 [astro-ph], arXiv: 1411.5018

Vickers, J. V. 1996, PhD thesis, UC Berkeley

Wadsworth, F. L. O. 1896, The Astrophysical Journal, 3, 47

Wallace, J. K., Bartos, R., Rao, S., Samuele, R., & Schmidtlin, E. 2006, in Proc. SPIE, Vol. 6272, 62722L–62722L–7

Wallace, K., Hardy, G., & Serabyn, E. 2000, Nature, 406, 700

Waskom, M., Olga Botvinnik, drewokane, et al. 2016, Zenodo

Wildt, R. 1940, The Astrophysical Journal, 91, 266

Williams, J. P., & Cieza, L. A. 2011, Annual Review of Astronomy and Astrophysics, 49, 67, arXiv: 1103.0556

Williams, M. B., Sealock, R. M., Majewski, S., & Weisenberger, A. G. 1998, IEEE Transactions on Nuclear Science, 45, 195

Witasse, O., Cravens, T., Mendillo, M., et al. 2008, Space Science Reviews, 139, 235

Wiza, L. J. 1979, Nuclear Instruments and Methods, 162, 587

Wolszczan, A., & Frail, D. A. 1992, Nature, 355, 145

Wood, B. E., Müller, H.-R., Zank, G. P., & Linsky, J. L. 2002, The Astrophysical Journal, 574, 412

Woods, T. N., Rottman, G. J., Bailey, S. M., Solomon, S. C., & Worden, J. R. 1998, Solar Physics, 177, 133

Woolf, N. J., Smith, P. S., Traub, W. A., & Jucks, K. W. 2002, The Astrophysical Journal, 574, 430

Wyant, J. C. 1975, Applied Optics, 14, 2622

—. 2011, Phase-Shifting Interferometry

Wyant, J. C., & Creath, K. 1992, in Applied optics and optical engineering. Vol. 11: [...], ed. R. Kingslake & R. R. Shannon (New York: Acad. Press), 28–39

Wyatt, M. C. 2008, Annual Review of Astronomy and Astrophysics, 46, 339

Yamazaki, A., Tashiro, S., Nakasaka, Y., et al. 2002, Geophysical Research Letters, 29, 4 PP.

Yonezawa, T. 1959, Journal of Atmospheric and Terrestrial Physics, 15, 89

Yuhas, C. 2012, Sounding Rocket Program Update to the Heliophysics Subcommittee

Zechmeister, M., Kürster, M., Endl, M., et al. 2013, Astronomy and Astrophysics, 552, 78

Zhang, S.-R., Holt, J. M., van Eyken, A. P., et al. 2005, Geophysical Research Letters, 32, 20102

Curriculum Vitae

Ewan S. Douglas

Citations: Google Scholar, ADS Database

Education

Present: Ph.D. Candidate, Astronomy, **Boston University**, Boston, MA. *Adviser*: S. Chakrabarti.

M.A. Astronomy, 2011, **Boston University**, Boston, MA

B.S. Physics, cum laude, 2008, **Tufts University**, Medford, MA. *Adviser*: R. Tobin.

Study-Abroad: Tufts-in-Ghana, University of Ghana, Fall 2007.

Professional History

Boston University, Center for Space Physics. Graduate Research Assistant, 2009–Present.

California Institute of Technology, LIGO Hanford Observatory, Operational Specialist, 2008–2009.

Teaching

Astronomy Camp. Counselor. (University of Arizona).

Boston University. Teaching Fellow, Astronomy 101, “The Solar System”, Spring 2010.

Honors and Awards

Massachusetts Space Grant Fellowship, 2014, 2015, 2016.

Invited Talks

Star and Planet Formation Seminar Series, STScI, Baltimore, MD. 29 Jan 2016.

Special Seminar, Harvard-Smithsonian Center for Astrophysics, Cambridge, Ma. 20 Apr 2016.

Organizations and Service

American Astronomical Society. *Junior Member.*

American Geophysical Union. *Member.*

SPIE. *Member.*

Journal of Applied Remote Sensing. *Reviewer.* 2016.

Citable Software Contributions

Perrin, M., J. Long, **E. Douglas**, A. Sivaramakrishnan, C. Slocum, and others. 2016. "POPPY: Physical Optics Propagation in PYthon." Astrophysics Source Code Library, February, ascl:1602.018.

Douglas, E., 2016. Poppy_example_notebooks: Initial Release, with Finished Microscope Example. doi:10.5281/zenodo.50106

Douglas, E., 2016. Poppy_nulling: Initial Release. doi:10.5281/zenodo.56408

Publications and Presentations

Submitted Scientific Publications

Geddes, G., **E.S. Douglas**, S. Finn, T.A. Cook, S. Chakrabarti. "Inverting OII 83.4 nm Dayglow Profiles Using Markov Chain Radiative Transfer". J. Geo. Res.

Selected Scientific Publications (Refereed)

Chakrabarti, S., and 5 co-authors. 2016. "Planet Imaging Coronagraphic Technology Using a Reconfigurable Experimental Base (PICTURE-B:) the Second in the Series of Suborbital Exoplanet Experiments", Journal of Astronomical Instrumentation. doi:10.1142/S2251171716400043

Li, Zi., and 11 co-authors. 2016. "Radiometric Calibration of a Dual-Wavelength, Full-Waveform Terrestrial Lidar", Sensors. doi:10.3390/s16030313.

Howe, G., and 8 co-authors. 2015.“Capabilities and Performance of DWEL, the Dual-Wavelength Echidna Lidar”, J. of Applied Remote Sensing. doi:10.1117/1.JRS.9.095979.

Cook, T., and 15 co-authors. 2015. “Planetary Imaging Concept Testbed Using a Recoverable Experiment-Coronagraph (PICTURE C)”, J. Astron. Telesc. Instrum. Syst. doi:10.1117/1.JATIS.1.4.044001.

Douglas, E. S., and 10 co-authors. 2014. “Finding Leaves in the Forest: The Dual-Wavelength Echidna Lidar (DWEL)", Geosci. Rem. Sensing Let. doi:10.1109/LGRS.2014.2361812.

Douglas, E. S., and 8 co-authors. 2012. “Evaluation of Ionospheric Densities Using Coincident OII 83.4 nm Airglow and the Millstone Hill Radar." J. Geo. Res. doi:10.1029/2012JA017574.

Conference Proceedings

Douglas, E. S., C. B. Mendillo, T. A. Cook, and S. Chakrabarti 2016. Wavefront Sensing in Space from the PICTURE-B Sounding Rocket. Proc. SPIE. http://arxiv.org/abs/1607.00277

Douglas, E. S. and 11 co-authors. 2015. “End-to-end simulation of high-contrast imaging systems - methods and results for the PICTURE mission family." Proc. SPIE. doi:10.1117/12.2187262.

Mendillo, C. B., and 15 co-authors. 2015. “The Low-Order Wavefront Sensor for the PICTURE-C Mission." Proc. SPIE. doi:10.1117/12.2188238.

Li, Z., **E. Douglas**, and 17 co-authors. 2013. “Separating leaves from trunks and branches with dual-wavelength terrestrial lidar scanning", IEEE Int. Geosci and Rem. Sens. Symp.
doi:10.1109/IGARSS.2013.6723554.

Douglas, E. S. and 14 co-authors. 2012. “DWEL: A dual-wavelength Echidna lidar for ground-based forest scanning." IEEE Int. Geosci and Rem. Sens. Symp. doi:10.1109/LGRS.2014.2361812.

LIGO Collaboration Publications (Refereed)

Abadie, J., and 714 co-authors.“Directional Limits on Persistent Gravitational Waves Using LIGO S5 Science Data.” Phys. Rev. Lett, 107, no. 27 (2011): 271102.

Abadie, J., and 768 co-authors. “Search for Gravitational Wave Bursts from Six Magnetars.” Astrophysical J. Lett 734 (2011): L35.

Abadie, J., and 749 co-authors. “Beating the Spin-down Limit on Gravitational Wave Emission from the Vela Pulsar.” Astrophysical J., 737, no. 2 (2011): 93.

Abadie, J., and 544 co-authors. “Calibration of the LIGO Gravitational Wave Detectors in the Fifth Science Run.” Nucl. Instr. and Meth. in Phy, Res. Sec. A: 624, no. 1 (2010): 223-240.

Abadie, J., and 539 co-authors. “First Search for Gravitational Waves from the Youngest Known Neutron Star.” Astrophysical J., 722, no. 2 (2010): 1504-1513.

Abadie, J., and 711 co-authors. “Predictions for the Rates of Compact Binary Coalescences Observable by Ground-based Gravitational-wave Detectors.” Class. and Quant. Grav. 27, no. 17 (2010): 173001.

Selected Conference Presentations

Douglas, E. S.. 2014, “Imaging the ϵ-Eridani system in visible light from a sounding rocket", (presented at NExScI Sagan Exoplanet Summer Workshop, July 2014).

Douglas, E. S., et al. 2014, “Status of the PICTURE Sounding Rocket to Image the Epsilon Eridani Circumstellar Environment", (presented at AAS Meeting #224, June 2014).

Douglas, E. S., et al. 2014, “Modeling of Expected PICTURE Observations of Exozodiacal Dust Around Epsilon Eridani", (presented at AAS Meeting #223, January 2014).

Douglas, E. S., et al. 2012. “Ionospheric observations with RAIDS, an extensive comparison of O+ 83.4 nm emission to ground based observations",#SA51B-2189 (presented at the AGU Fall Meeting 2012).

Douglas, E. S., et al. 2012. “Further Comparison of RAIDS observations to a radar-fed model of OII 83.4 nm emission" (presented at 2012 CEDAR, 26 June 2012).

Douglas, E. S., D. Pallamraju, and S. Chakrabarti, “Coordinated investigations of daytime redline optical emissions and incoherent scatter radar measurements from Sondrestromfjord, Greenland”, #SA41A-1717 (presented at the AGU Fall Meeting 2010).

Telegrams

Leonard, D. C. et al. (2015a), ASASSN-15lo is a Post-Maximum Normal Type Ia Supernova, ATEL, 7675, 1.

Leonard, D. C. et al. (2015b), ASASSN-15lu is a Type Ia Supernova, ATEL, 7707, 1.

Leonard, D. C. et al. (2015c), Optical Spectroscopy of PSN J15044078+ 1237436, ATEL, 7690, 1.

Leonard, D. C. et al. (2015d), PSN J11473508+ 5558147 is a Type Ib Supernova Near Maximum Light, ATEL, 7680, 1.

Wiggins, P. et al. (2015), Supernova 2015Q in NGC 3888= Psn J11473508+ 5558147, CBET, 4128, 1.

Rachubo, A. A. et al. (2013), Spectroscopy of PSN J00513484+ 2943149 in UGC 525, ATEL, 5176, 1.

Elenin, L. et al. (2013), Supernova 2013do in UGC 12137= Psn J22395067+ 3812443, CBET, 3571, 2.

Howerton, S. et al. (2013), Supernova 2013dq in UGC 525= Psn J00513484+ 2943149, CBET, 3573, 1.

Leonard, D. C. et al. (2011a), Spectroscopy of PSN J19583553+ 0236163, ATEL, 3450, 1.

Leonard, D. C. et al. (2011b), Supernova 2011dv in NGC 6078= PSN J16120400+ 1412330., CBET, 2755, 2.

Leonard, D. C. et al. (2011c), Supernova 2011dw in PGC 58436= PSN J16313945+ 4129229., CBET, 2756, 2.